A theoretical investigation of fiber phase sensitive amplifiers for applications

Thèse de doctorat de l'université Paris-Saclay

École doctorale n° 572, Ecole Doctorale Ondes et Matière (EDOM)
Spécialité de doctorat : Physique
Unité de recherche : Université Paris-Saclay, ENS Paris-Saclay, LuMIn
91190, Gif-sur-Yvette, France
Référent : ENS Paris-Saclay

**Thèse présentée et soutenue en visioconférence totale à Gif-sur-Yvette,
le 27/01/2021, par**

Debanuj CHATTERJEE

Composition du Jury

Dr. Isabelle LEDOUX-RAK Professeur, ENS Paris-Saclay	Présidente
Dr. Arnaud MUSSOT Professeur, PhLAM, Université de Lille	Rapporteur & Examinateur
Dr. Thierry CHARTIER Professeur, ENSSAT, Université de Rennes 1	Rapporteur & Examinateur
Dr. Christophe FINOT Professeur, Université de Bourgogne	Examinateur
Dr. Ihsan FSAIFES Ingénieur de researche, Ecole Polytechnique	Examinateur
Dr. Fabien BRETENAKER Directeur, LuMIn, ENS Paris-Saclay	Directeur de thèse

Thèse de doctorat

NNT : 2021UPASP008

École Normale Supérieure Paris-Saclay

Doctoral Thesis

A Theoretical Investigation of Fiber Phase Sensitive Amplifiers for Applications

---

Author:
Debanuj Chatterjee

Supervisor:
Dr. Fabien Bretenaker

A thesis submitted in fulfillment of the requirements
for the degree of Doctor of Philosophy

in the

LuMIn,
Department of Physics, ENS Paris-Saclay

27th January, 2021

Declaration of Authorship

I, Debanuj CHATTERJEE, declare that this thesis titled, “” and the works presented in it are my own. I confirm that:

- This work was done wholly or mainly while in candidature for a research degree at this University.
- Where any part of this thesis has previously been submitted for a degree or any other qualification at this University or any other institution, this has been clearly stated.
- Where I have consulted the published work of others, this is always clearly attributed.
- Where I have quoted from the work of others, the source is always given. With the exception of such quotations, this thesis is entirely my own work.
- I have acknowledged all main sources of help.
- Where the thesis is based on work done by myself jointly with others, I have made clear exactly what was done by others and what I have contributed myself.

Signature :

Debanuj Chatterjee

Date : February 11, 2021

Place : Paris, France.

"Total obscurity. Bilbo in Gollum's tunnel.

A mathematician's first steps into unknown territory constitute the first phase of a familiar cycle. After the darkness comes a faint, faint glimmer of light, just enough to make you think that something is there, almost within reach, waiting to be discovered...

Then, after the faint, faint glimmer, if all goes well, you unravel the thread - and suddenly it's broad daylight! You're full of confidence, you want to tell anyone who will listen about what you've found. And then, after day has broken, after the sun has climbed high into the sky, a phase of depression inevitably follows. You lose all faith in the importance of what you've achieved. Any idiot could have done what you've done, go find yourself a more worthwhile problem and make something of your life. Thus the cycle of mathematical research."

Cédric Villani

ÉCOLE NORMALE SUPÉRIEURE PARIS-SACLAY

Abstract

Faculty of Sciences
Department of Physics

Doctor of Philosophy

by Debanuj CHATTERJEE

Fiber optic parametric amplifiers (FOPA) are promising for tomorrow's communication systems. In particular, fiber phase sensitive amplifiers offer attractive functionalities like low noise and high gain which makes it a potential candidate for applications in microwave photonic links. This thesis provides a theoretical investigation of such fiber phase sensitive amplifiers aimed towards applications.

The first part of the thesis is dedicated towards development of an analytical model for propagation of seven CW waves through a FOPA. The system was solved exactly when nonlinear effects of the fiber are not strong. The developed model unravelled the important role of the higher order waves in determining the amplification performance of the FOPA. Strategies were formulated to enhance the amplification and the possibility of a phase sensitive frequency conversion with just two pump waves was also predicted.

In the second part of this thesis, the possibility of introducing a fiber phase sensitive amplifier in a microwave photonic link for analog signal distribution was investigated. A numerical model was utilized to simulate how the RF nonlinearities in a microwave photonic link are amplified by the FOPA. The performance of the link when the FOPA attains a gain saturation was also studied. The study revealed the possibility of RF nonlinearity mitigation using the fiber nonlinearity. Implementation of such techniques could lead to realization of long-range and highly linear microwave photonic links for antenna remoting applications.

Résume

Les amplificateurs paramétriques à fibre optique (FOPA) sont prometteurs pour les systèmes de communication de demain. En particulier, les amplificateurs sensibles à la phase à base de fibres offrent des fonctionnalités intéressantes comme un faible bruit et un gain élevé, ce qui en fait des candidats potentiels pour des applications dans les liaisons photoniques micro-ondes. Cette thèse propose une étude théorique de tels amplificateurs sensibles à la phase destinés à certaines applications.

La première partie de la thèse est consacrée au développement d'un modèle analytique pour la propagation de sept ondes continues à travers un FOPA. Les sept ondes sont : deux pompes puissantes, un signal dégénéré avec le complémentaire, deux complémentaires d'ordre supérieur et deux pompes d'ordre supérieur. Nous obtenons une solution analytique valable lorsque les effets non linéaires de la fibre ne sont pas trop forts. Dans ce régime faiblement non linéaire, nous montrons que le système peut être analysé en décomposant les sept ondes couplées en trois sous-systèmes à quatre ondes. Alors que le sous-système contenant le signal et le sous-système contenant les deux complémentaires d'ordre supérieur sont couplés l'un à l'autre, le sous-système contenant les pompes d'ordre supérieur est découplé des deux premiers. Ce découplage nous permet de trouver une solution analytique. Le modèle développé révèle le rôle important des ondes d'ordre supérieur dans la détermination des performances d'amplification du FOPA. Des stratégies sont formulées pour améliorer l'amplification. La possibilité d'une conversion de fréquence sensible à la phase avec seulement deux ondes de pompe est également prédite. Un tel modèle analytique de la propagation des ondes dans une fibre non linéaire est également pertinent pour le calcul du bruit quantique d'un amplificateur sensible à la phase à fibre à double pompe.

Dans la deuxième partie de cette thèse, la possibilité d'introduire un amplificateur sensible à la phase (PSA) dans une liaison photonique hyperfréquence pour la distribution de signaux analogiques est étudiée. Un modèle numérique est utilisé pour simuler comment les non-linéarités du signal RF dans la liaison photonique hyperfréquence sont amplifiées par le FOPA. La non-linéarité de la liaison est quantifiée par les produits d'intermodulation d'ordre 3 générés à partir de deux fréquences RF. Le modèle numérique est d'abord validé par comparaison avec des résultats expérimentaux obtenus précédemment. Nous observons que dans le cas où le signal utile est transféré à la liaison par un modulateur d'intensité standard, le PSA non saturé n'améliore ni ne dégrade la distorsion de la liaison. Dans certaines conditions, saturer le gain du PSA permet d'améliorer la dynamique de la liaison. D'autre part, dans le cas d'un modulateur d'intensité parfaitement linéaire, la distorsion générée par le PSA est très faible négligeable en l'absence de saturation du gain. En revanche, la saturation du gain mène à une distorsion significative du signal. La mise en œuvre de telles techniques pourrait conduire à la réalisation de liaisons photoniques hyperfréquences à longue portée et hautement linéaires pour les applications de déport d'antenne.

Acknowledgements

This thesis without the acknowledgements would leave it highly incomplete.

Fisrt, I would like to thank my supervisor Dr. Fabien Bretenaker for giving me the opportunity to study for a PhD at ENS Paris-Saclay. I am deeply grateful to him for the highly-competent guidance and the great support that pushed me forward.

I also thank the reviewers of my thesis, Dr. Arnaud Mussot and Dr. Thierry Chartier for their crtical and encouraging reviews that undoubtedly helped in improving the quality of this thesis. I am also thankful to the other members of the jury, i.e., Dr. Isabelle Ledoux-Rak, Dr. Christophe Finot and Dr. Ihsan Fsaifes for examining my thesis.

A special thanks to my closest colleagues Dr. Chitram Banerjee, Yousra Bouasria and Dr. Yifan Sun for all the love, support and help that they provided throughout my PhD. I would like to express my gratitude to Dr. Fabienne Goldfarb for all the help she provided specially when I started my PhD. I would also like to thank my colleagues and co-workers Dr. Hui Lui, Dr. Grégory Gredat, Dr. Paul Bouteyre, Dr. Pascal Neveu, Syrine Guefrachhe and Dr. Sara Mitiche for everything I learnt from them and the enormous assistance in the lab. I would like to thank Dr. Weilin Xie for the important discussions and for his simulations that helped me advance with my research. I also thank my dear friends Vikash Chowdhury, Subha Jana, Amy Dubey, Aman,... (this list can go on) for bearing me.

Finally, I want to thank my family, Samarnath Chatterjee, Bharati Chatterjee and Debanjana Chatterjee for their continuous support and inspiration.

Contents

Declaration of Authorship **iii**

Abstract **vii**

Résume **ix**

Acknowledgements **xi**

General Introduction **1**

1 Introduction **5**
- 1.1 Historical Perspective of FOPA . . . 6
  - 1.1.1 Total Internal Reflection of Light (17th-19th Century CE) . . . 6
  - 1.1.2 Birth of Fiber Optic Communication Systems (1900-1979 CE) . . . 7
  - 1.1.3 Growth of Nonlinear Fiber Optics (1980-1999 CE) . . . 8
  - 1.1.4 Emergence of Fiber Optic Amplifiers (1980-1999 CE) . . . 9
  - 1.1.5 FOPA State-of-the-Art (2000-2020 CE) . . . 11
- 1.2 Properties of Optical Fibers . . . 12
  - 1.2.1 Profile . . . 12
  - 1.2.2 Loss . . . 13
  - 1.2.3 Dispersion . . . 14
    - 1.2.3.1 Material Dispersion . . . 14
    - 1.2.3.2 Waveguide Dispersion . . . 15
    - 1.2.3.3 Dispersion Parameter D . . . 15
    - 1.2.3.4 Dispersion Regimes . . . 15
  - 1.2.4 Nonlinearity . . . 16
- 1.3 Microwave Photonic Link . . . 17
  - 1.3.1 Principle . . . 17
  - 1.3.2 Historical Perspective and Overview . . . 18
  - 1.3.3 PSA in a Microwave Photonic Link . . . 20

2 **Analytical 7-Wave Model** **23**
2.1 Introduction . . . 25
2.2 Analytical 3-Wave Model . . . 26
2.2.1 Configurations . . . 26
2.2.2 Approximations . . . 27
2.2.3 Wave Evolution Equations . . . 28
2.2.4 Signal Gain : Degenerate Pump Configuration . . . 29
2.2.5 Signal Gain : Non-Degenerate Pump Configuration . . . 31
2.2.6 PIA vs PSA . . . 32
2.3 Analytical 4-Wave Model . . . 33
2.3.1 Configuration . . . 33
2.3.2 Approximations . . . 33
2.3.3 Linear Phase Mismatch . . . 34
2.3.4 Wave Evolution Equations . . . 35
2.3.5 Solution of Equations . . . 36
2.3.6 Stability of Solution . . . 40
2.3.7 Limitations . . . 41
2.4 Analytical 7-Wave Model . . . 42
2.4.1 Configuration . . . 43
2.4.2 Approximations . . . 43
2.4.3 Linear Phase Mismatch . . . 43
2.4.3.1 Validity of Second Order Approximation . . . 43
2.4.4 Wave Evolution Equations . . . 44
2.4.5 Subsystems of the Analytical 7-Wave Model . . . 46
2.4.6 Coupled Signal and HOI Evolution (Subsystems 1 and 2) . . . 46
2.4.7 Maximum Signal Gain . . . 59
2.4.8 Phase Sensitive Frequency Conversion (PSFC) . . . 59
2.4.9 Input Signal Phase for Maximum Signal Gain . . . 63
2.4.10 HOP Evolution (Subsystem 3) . . . 65
2.4.11 Comparison of Analytical 3- and 7-Wave Models with Numerical 7-Wave Model . . . 71
2.4.12 Physical Interpretation . . . 74
2.4.13 Limitations . . . 78
2.4.14 PSA Noise Figure . . . 78
2.5 Conclusion . . . 78

3 **Nonlinear Schrödinger Equation** **81**
3.1 Introduction . . . 82
3.1.1 Input Electric Field . . . 82
3.1.2 Dispersion . . . 83
3.1.3 Derivation of NLSE . . . 84
3.1.4 Change of Reference Frame . . . 84
3.1.5 Attenuation of the Medium . . . 85

3.1.6 Calculation of Parameters . . . 85
3.2 Numerical Model . . . 87
3.2.1 SSFM Algorithm . . . 88
3.2.1.1 Dispersion . . . 89
3.2.1.2 Nonlinearity . . . 91
3.2.1.3 Final Form of Algorithm . . . 91
3.2.2 Step Size . . . 91
3.2.3 Spectral Leakage . . . 93
3.3 Verification of Numerical Model . . . 94
3.3.1 Parameters . . . 95
3.3.1.1 Numerical parameters . . . 95
3.3.1.2 System parameters . . . 95
3.3.2 PIA . . . 96
3.3.2.1 Experiment . . . 97
3.3.2.2 Results . . . 99
3.3.3 PSA . . . 99
3.4 Discussion and Conclusion . . . 100
3.4.1 Comparison of Models . . . 100
3.4.2 Conclusion . . . 102

4 PSA in a Microwave Photonics Link **103**
4.1 Scheme . . . 106
4.1.1 Electro-Optic Conversion : Phase Modulator . . . 107
4.1.1.1 Pockels Effect . . . 107
4.1.1.2 Phase Modulator . . . 107
4.1.1.3 Input Field . . . 107
4.1.1.4 Modulator Voltage . . . 108
4.1.1.5 Input RF Power . . . 108
4.1.1.6 Half Wave Voltage V_π . . . 109
4.1.1.7 Output Field . . . 109
4.1.2 Electro-Optic Conversion : Mach-Zehnder Modulator . . . 109
4.1.2.1 Output Field . . . 110
4.1.2.2 Amplitude Modulation . . . 111
4.1.3 Opto-RF Conversion . . . 111
4.2 Two-Tone Test . . . 113
4.2.1 MZM Output Power . . . 114
4.2.2 Part of Total Optical Power at Fundamental Frequency . . . 118
4.2.3 Part of Total Optical Power at IMD3 Frequency . . . 120
4.2.4 SFDR . . . 122
4.3 Numerical Model . . . 124
4.3.1 Model Outline . . . 124
4.3.2 Experimental Setup . . . 124
4.3.3 Experimental Validation . . . 126

4.4 AM vs PM 127
    4.4.1 AM 127
    4.4.2 PM 129
    4.4.3 Simulation Results 130
4.5 Saturation Behaviour : Standard Intensity Modulator 131
    4.5.1 Scan of Input RF Power 132
    4.5.2 Scan of Input Signal Power 134
    4.5.3 Scan of Input Pump Power 136
    4.5.4 Scan of Input Signal Phase 137
    4.5.5 SFDR 138
    4.5.6 Discussion 140
4.6 Saturation Behaviour : Linear Intensity Modulator 141
4.7 Physical Interpretation 142
4.8 Conclusion 148

5 Perspectives and Conclusion **151**
5.1 Perspectives 152
    5.1.1 Frequency Comb PSA 152
    5.1.2 Quantum Noise using a 7-Wave Model 153
5.2 Conclusion 154

A Solution of the Analytical 3-wave Model **157**
A.1 Degenerate Pump Configuration 157
A.2 Non-degenerate Pump Configuration 160

B Coupled Equations for the 7-Wave Model **163**

C Signal and HOI Evolution in Analytical 7-wave Model **167**

D *Mathematica* Code to Calculate b_{ij} Coefficients in Equation (C.14) **171**

E MATLAB Code to Simulate Input and Output Spectrum of a HNLF **181**

F Optical Power in an Electromagnetic Field **185**
F.1 One Erequency 185
F.2 Three Frequencies 187

G Properties of Bessel Functions of the First Kind **191**

H SFDR of a Microwave Photonic Link with PSA **193**

List of Abbreviations

PSA	**P**hase **S**ensitive **A**mplifier/**A**mplification
PIA	**P**hase **I**nsensitive **A**mplifier/**A**mplification
FOPA	**F**iber **O**ptics **P**arametric **A**mplifier
SVA	**S**lowly **V**arying **A**mplitude
HNLF	**H**ighly **N**on**L**inear **F**iber
SPM	**S**elf **P**hase**M**odulation
XPM	**C**ross **P**hase**M**odulation
FWM	**F**our **W**ave**M**ixing
EDFA	**E**rbium **D**oped **F**iber **Amplifier**
ASE	**A**mplified **S**pontaneous **E**mission
CW	**C**ontinuous **W**ave
NLSE	**N**on**L**inear **S**chrödinger **E**quation
ADC	**A**nalog-to-**D**igital **C**onvertor
SBS	**S**timulated **B**rillouin **S**cattering
MZM	**M**ach-**Z**ehnder **M**odulator
ESA	**E**lectrical **S**pectrum **A**nalyzer
TLS	**T**unable **L**aser **S**ource
C	**C**irculator
OSA	**O**ptical **S**pectrum **A**nalyzer
BPF	**B**and **P**ass **F**ilter
FBG	**F**iber **B**ragg **G**rating
PZT	**P**ie**Z**oelectric **T**ransducer
PD	**P**hoto**D**etector
RF	**R**adio **F**requency
IMD3	**3**rd order **I**nter-**M**odulation
AM	**A**mplitude **M**odulation
PM	**P**hase **M**odulation
RFA	**R**adio **F**requency **A**mplifier
3wm	**3**-**W**ave **M**odel
4wm	**4**-**W**ave **M**odel
7wm	**7**-**W**ave **M**odel

nwm	*n* **W**ave **M**odel
WDM	**W**avelength **D**ivision **M**ultiplexing

Dedicated to Prof. Trilokeshwar Shonku…

General Introduction

Background and Motivation

In the past few decades we witnessed a revolution in communication and information technologies. The advent of high-speed internet connectivity enabled a plethora of customized services at our fingertips. This was a major step forward in terms of technological progress that truly transformed our society. But needless to say, such mammoth transformation owes a great deal to the development of modern optical technologies, in particular optical fiber technology. Optical fibers, which are specially engineered silica based cables that can carry light waves with encoded information enabled high-speed and voluminous data-transmission links between far-away locations of trans-oceanic scales. One of the most important and essential components for such long distance communication systems are the optical amplifiers. Optical amplifiers boost the information carrying signal periodically to compensate for the incurred fiber losses along the transmission length. As one might imagine, the optical amplification process is a key determinant of the performance and capability of such communication systems and networks. This motivates us to investigate the physics of optical amplifiers and identify different avenues of applications towards ameliorating modern communication systems for better performance.

This thesis focuses on a particular kind of emerging optical amplifiers known as the phase sensitive amplifiers (PSA), especially its implementation in optical fiber based systems. Such kind of optical amplifiers has received considerable attention recently due to its ability to generate the so-called "squeezed states of light" that exhibit noiseless amplification properties. PSA's outperform conventional optical amplifiers and are regarded as a promising candidate for the future of optical amplifiers in next generation optical and photonic systems. In this thesis we investigate some of the basic properties of such amplifiers and evaluate their potential for implementation in analog signal transmission systems.

Modern-day analog transmission links such as radio-over-fiber systems are at the fore-front of current state-of-the-art technologies for applications such as antenna remoting, internet-of-things, 5G data connectivity, high-performance radar, etc. These systems try to employ signal distribution using optical fibers rather than traditional coaxial cables and are often referred to as microwave photonic links. Optical fibers are preferred in these systems due to their numerous advantages over coaxial cables such as low loss, high bandwidth, immunity to electromagnetic interference etc. However, use of optical fibers for analog signal transmission comes with a down side. The electric to optical signal conversion at the transmitter end and subsequent optical to electrical signal conversion at the receiver end accompany large signal losses. Therefore, the possibility of integrating a PSA in such signal distribution architecture is an interesting option to explore. Indeed such endeavours are expected to meet numerous challenges. For example fiber-based PSA's being highly nonlinear systems hold the risk of degrading the global distortion performance of the link when integrated within the microwave photonic link. Therefore a comprehensive study on the impact of PSA introduction on the performance of a microwave photonic link is worth pursuing.

Contribution

This thesis primarily focuses on analyzing the fundamental mechanisms of light amplification by a PSA. To this aim, we introduce the existing theoretical models of light propagation through a fiber phase sensitive amplifier, *viz.* the n-wave models ($n = 3, 4, 7$) and the nonlinear Schrödinger equation (NLSE) model. We use a matrix-based approach to find an exact solution for the 7-wave model when the PSA is weakly nonlinear. We also analyze the system in terms of coupled oscillatory subsystems and project perspectives on design of optimized low-noise optical parametric amplifiers.

To probe a PSA system under strongly nonlinear conditions, we utilize a robust numerical model based on the NLSE approach. We use this numerical model to investigate the effect of PSA insertion in a microwave photonic link. More precisely, we investigate how the nonlinearities generated from the electro-optic conversion in a microwave photonic link are amplified by the PSA. We also explore more extreme scenarios like a PSA operating under gain saturation. Subsequently we interpret the results and develop a physical picture for the same.

Thesis Outline

Here we provide a broad outline of the organization of this thesis. A summary of chapter wise contents is presented below.

Chapter 1

This chapter is primarily motivated towards developing a broad overview of the scope and goals of this thesis. In the first part of this chapter we provide a historical perspective of development of optical fiber technologies with a focus on research related to fiber optic amplifiers. Then in the later part, we discuss the development of microwave photonic links and envisage how fiber optic amplifiers can provide the possibility of their performance enhancement.

Chapter 2

In this chapter we develop an analytical model to describe propagation of multiple continuous wave (CW) lights through a nonlinear optical fiber. In particular, we consider propagation of 3, 4 and 7 CW waves. The theoretical model is motivated towards understanding the phase sensitive amplification functionality of a nonlinear fiber. Using the developed 7-wave analytical model we analyze the role of higher order waves in the optical amplification process and project some perspectives related to design optimization of low-noise and high-gain phase sensitive fiber optic parametric amplifiers.

Chapter 3

This chapter introduces the nonlinear Schrödinger equation (NLSE) that governs the propagation of a continuous distribution of frequencies through a nonlinear fiber. We briefly discuss the associated theory and describe a numerical formalism (split step Fourier method or SSFM) to simulate propagation of multiple CW waves through a nonlinear fiber using the NLSE. We also validate the numerical approach with experimental data and compare the results with some simple cases where analytical results are available.

Chapter 4

In this chapter, first we describe different parts of a microwave photonic link and discuss the sources of distortion in the link. We also describe the two-tone test which is often used to evaluate how "noisy" the link is. Then we use a NLSE based numerical model to investigate how the incorporation of a PSA into a microwave photonic link affects the effective link distortion. We validate the numerical results with available experimental data. Furthermore, we use the numerical model to investigate the link performance under extreme situations. For example we consider a microwave photonic link with a PSA which is gain saturated. These investigations reveal interesting results showing the possibility of developing PSA-integrated microwave photonic links with high linearity. We also try to develop a simple physical picture to analyze the obtained results.

Chapter 5

This chapter provides a brief overview of the different perspectives generated from the investigations performed in this thesis. For example we project some ideas related to extending the analytical 7-wave to a more generalized n-wave model. We also highlight the potential application of this model to calculate the noise figure of a fiber phase sensitive amplifier. Finally we summarize the different results obtained through the investigations in this research and provide a global conclusion of the thesis.

Chapter 1

Introduction

Contents

1.1 Historical Perspective of FOPA 6
1.1.1 Total Internal Reflection of Light (17th-19th Century CE) . . 6
1.1.2 Birth of Fiber Optic Communication Systems (1900-1979 CE) 7
1.1.3 Growth of Nonlinear Fiber Optics (1980-1999 CE) 8
1.1.4 Emergence of Fiber Optic Amplifiers (1980-1999 CE) 9
1.1.5 FOPA State-of-the-Art (2000-2020 CE) 11
1.2 Properties of Optical Fibers 12
1.2.1 Profile 12
1.2.2 Loss 13
1.2.3 Dispersion 14
1.2.4 Nonlinearity 16
1.3 Microwave Photonic Link 17
1.3.1 Principle 17
1.3.2 Historical Perspective and Overview 18
1.3.3 PSA in a Microwave Photonic Link 20

The field of fiber optics traces its transformation from a 19th century parlour trick to the foundation of our global communication network. However this revolutionary technology is far from attaining its maximum potential. Exploring aspects of nonlinear fiber optical systems and harnessing their capabilities for superior communication systems represent the core motivation of this thesis.

This introductory chapter aims at providing a broad overview of the history, characteristics, scope and applications of fiber optic parametric amplifiers (FOPA) in modern-day communication systems with an emboldened focus on microwave photonics applications. In Section 1.1 we first start off by discussing the historical context of development of fiber optics in general and then fiber optical parametric amplifiers in particular. We also briefly discuss the physical properties of a FOPA that are key to its operation. Then in Section 1.3 we move on to microwave systems and in particular microwave photonic links which are often employed for efficient distribution of analog signals. Furthermore, in this section we explore the possibility of incorporation of a FOPA within a microwave photonic link for its range improvement. We also envisage the possible outcomes with respect to the link's distortion characteristics for such an architecture.

1.1 Historical Perspective of FOPA

Optical amplifiers play an important role in numerous scientific and technological disciplines such as optical communication, imaging, sensing, spectroscopy, etc. The entire digital revolution with the development of high-speed internet infrastructure would not have been possible without optical amplifiers which are being used in virtually all long-haul optical fiber transmission links. However the trails of this success story trace back farther in time than one expects to imagine.

1.1.1 Total Internal Reflection of Light (17th-19th Century CE)

Optical fibers are typically made up of an optically transparent core (generally silica or glass) and light is confined inside the core by the phenomenon of total internal reflection which causes the fiber to act as a waveguide. Let us start by exploring the history of understanding the phenomenon of total internal reflection of light.

The concept of total internal reflection of light was known to humankind even back in the 17th century. Following Kepler's and Descartes' pioneering work on the theory of refraction of light, Huygens was the first to discuss total internal reflection of light with considerable comprehension in his book "Treatise on Light". Newton, a contemporary, rejected Huygens' wave theory of light in advocacy for his corpuscular theory. Nevertheless both the wave and corpuscular picture had problems of their own. It was much later, in the first half of the 19th century that Fresnel developed a wave-based theory of polarized light that laid a firm foundation to the theory of total internal reflection of light.

Guiding of light by refraction, the principle that makes fiber optics work, was first demonstrated by Daniel Colladon in Paris in the early 1840s [1][1]. Ironically, Colladon's demonstrations were not intended to guide light, but to show how water streams break up while falling from a height. An illustration of the setup he used to focus light from an arc lamp into a narrow jet of leaking water is shown in Fig. 1.1. Another contemporary physicist, Jacques Babinet also discovered this effect independently [4], however he too failed to recognize the worth of the light guiding principle. This idea caught the common eye decades later when it was used to create gorgeous illuminated fountains at many of the great Victorian exhibitions.

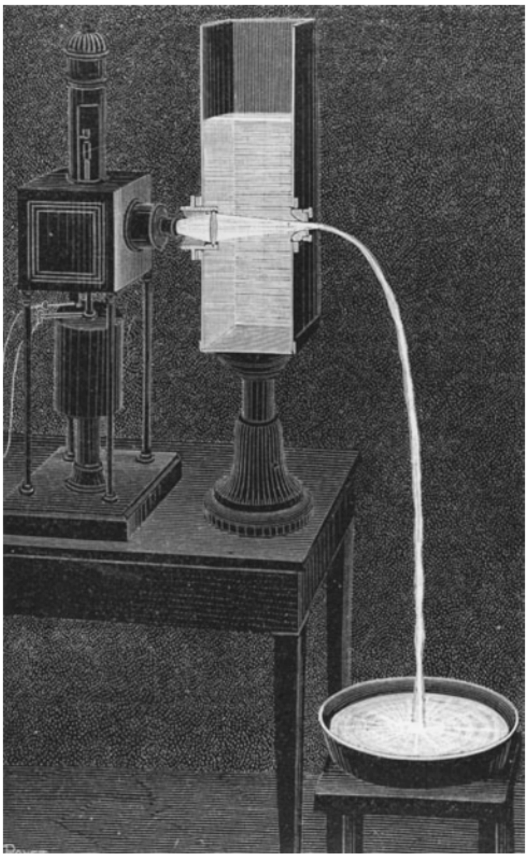

Figure 1.1. Colladon's fountain sparkles with light from an arc lamp, illustrated in his 1884 article. (courtesy : Ref. [3])

1.1.2 Birth of Fiber Optic Communication Systems (1900-1979 CE)

Although the potential of fiber optics was not realized for a long time, a breakthrough in the 1950s, with the advent of cladded glass fibers, led to a considerable improvement in the light carrying capacity of glass fibers [5, 6]. During the 1960's, a rapid development ensued in the field of fiber optics that was centered around development of image transmission systems using a bundle of glass fibers. At this

---

[1] John Tyndall is often given the credit for inventing light guiding by total internal reflection, however Colladon demonstrated it a dozen years before him [2].

period, it was Kapany who popularized the term "Fiber optics" [7] and also wrote the first book [8] on it to broaden the visibility of the new field.

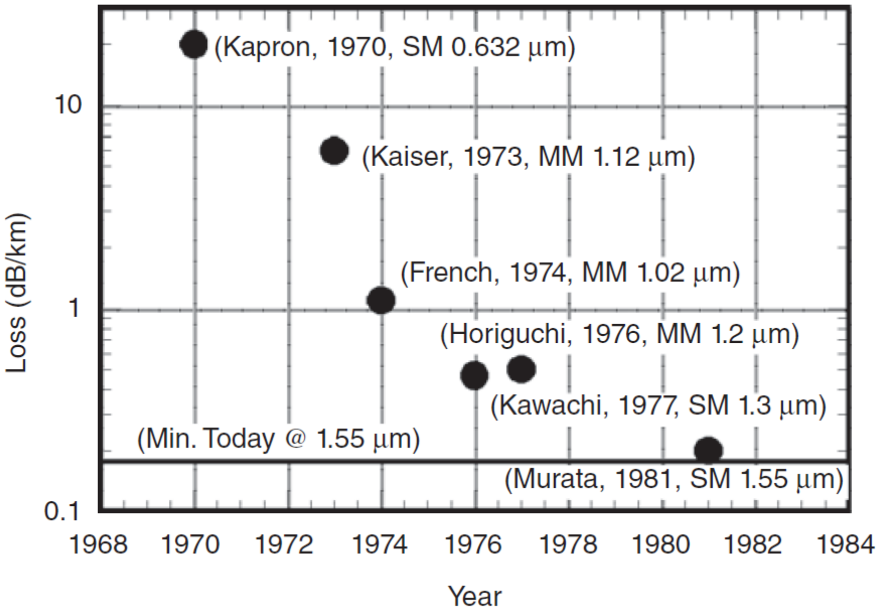

Figure 1.2. Reported losses in optical fiber over time for single mode (SM) and multimode (MM) fibers at various wavelengths (Kapron, 1970 [9]; Kaiser, 1973 [10]; French *et al.*, 1974 [11]; Horiguchi, 1976 [12]; Kawachi, 1977 [13]; and Murata and Inagaki, 1981 [14]). (courtesy : Ref. [15])

One big obstacle still was the high loss (> 1000 dB/km) associated with the transmission. Charles K. Kao and George A. Hockham were the first to pioneer the idea that optical fiber attenuation could be reduced below 20 dB/km making it a promising communication medium [16][2]. In the next decade, developments in the fabrication technology led to the realization of that dream [9]. Subsequent developments even made it possible to decrease the fiber attenuation to as low as 0.2 dB/km [11, 14, 17] in the 1.55 μm wavelength window. Evolution of the fiber losses through time is shown in Fig. 1.2. By the end of the 70s, the losses in such fibers were only limited by the fundamental process of Rayleigh scattering. Also developments in chemical engineering in research centers like CSELT and Corning led to an increase in the manufacturing speed of optical fibers making it an economically viable technology for communication systems[3].

1.1.3 Growth of Nonlinear Fiber Optics (1980-1999 CE)

The increase in accessibility to low-loss silica fibers was a watershed event in the history of optical fiber technology as it facilitated the development of a new and dynamic field of research related to nonlinear effects in optical fibers. Thus in the 1970s

---

[2] Kao received the Nobel Prize in Physics in 2009 for this contribution.

[3] Turin in Italy was the first metropolis where fiber optic cables were deployed in 1977.

and 80s there was an emergence of research-boom in phenomena related to nonlinear fiber optics. Raman and Brillouin scattering processes [18–20], optically induced birefringence [21], parametric four-wave mixing [22–24], self-phase modulation [25], generation of soliton pulses [26, 27], etc. were gaining significant attention during this time. These developments cascaded into exploration of other exotic nonlinear optical phenomena like generation and control of ultrashort optical pulses [28, 29], pulse-compression [30–33], optical switching [34–36], etc. Major developments in this period can also be found in Refs. [37, 38].

1.1.4 Emergence of Fiber Optic Amplifiers (1980-1999 CE)

Development of long distance fiber optic communication channels increased the demand for periodic signal amplifiers or repeaters. Initially these repeaters were working in the electrical domain, meaning an optical-electrical-optical conversion was necessary at each repeating event. This was a major bottleneck for the noise performance and efficiency of the communication channels. Thus the requirement of a better amplification technique was imminent.

- **EDFA**
  Just before the beginning of the 90s, research on fibers doped with rare-earth elements was a major focal point for building optical amplifiers and lasers. This led to a significant breakthrough with respect to communication technologies with the advent of erbium-doped fiber amplifiers (EDFA) in 1987 [39–41]. It paved the way for development of broadband and highly efficient optical communication systems. A remarkable property of the EDFA is that its transition energy is coincident with the low-loss spectral window of conventional optical fibers, leading to the simultaneous amplification of large number of waves at different wavelengths carrying information independently, eliminating the necessity of per-channel amplification of signals. Also the requirement of optical-electrical-optical conversion at repeaters for long distance communication was now eliminated as the optical signal could now be amplified directly in the optical domain (see Fig. 1.3).

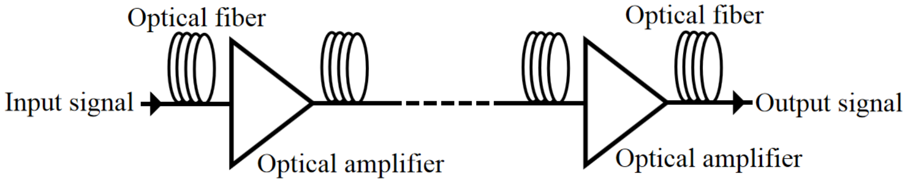

Figure 1.3. Scheme of a long distance fiber optic communication system.

- **Parametric Amplifiers**
  In nonlinear optics, the nonlinear susceptibility of the medium leads to a coupling between the different waves propagating through it. This leads to an

exchange of photons from one wave to the other. Therefore under a suitable configuration, a strong pump wave can provide energy to a co-propagating signal wave leading to a signal-amplification effect. Although this effect was demonstrated by Stolen *et al.* in 1974 [22], the full potential of this kind of optical amplification was not realized until the advent of lasers at 1.3 μm wavelength in the 1980s.

The first important step towards the development of fiber optic parametric amplifiers based on four wave mixing processes was arguably[4] the work by Pocholle *et al.* in 1985 [43]. A cardinal property of these new class of amplifiers was that under certain initial conditions[5], the gain of the signal depended on the relative phase between the different waves (for example signal, idler and pump(s)) injected into the fiber (which itself acted as an amplifier). Phase sensitive gain in an optical fiber was observed for the first time by Bar-Joseph *et al.* in 1986 [44].

The process of optical amplification in a quantum mechanical sense is based on stimulated emission of photons in the same quantum state as an incoming photon. However, there is another process that can occur with a non-zero probability called spontaneous emission of photons. In contrast to stimulated emission, spontaneously emitted photons have random properties for their quantum state. Spontaneous emission therefore becomes a key source of noise in optical amplifiers [45].

The principles of quantum optics predict that ordinary amplifiers, which amplify all the quadratures of a light mode with the same gain, lead to a degradation of the signal-to-noise ratio, due to the coupling of the amplified mode with vacuum modes [46]. EDFA is an example of such an amplifier. This degradation, characterized by the amplifier noise figure, cannot be smaller than 3 dB when the gain is large. Alternatively to such phase insensitive amplifiers (PIA's), Caves showed that a phase sensitive amplifier (PSA) can amplify the signal without degrading the signal-to-noise ratio [47]. Similar conclusions were also drawn by Yamamoto and Haus in the 1980s[6] [49]. This meant that the noise figure of a PSA is supposed to be 0 dB[7]. These interesting insights sparked a spontaneous awakening in the fiber optic research community [50].

Low noise figure phase sensitive amplifiers were first demonstrated in $\chi^{(2)}$ media by Levenson *et al.* in the 1980s where they broke the 3 dB noise figure limit [51]. Also Marhic *et al.* [52] used a fiber Sagnac interferometer to realize

---

[4] There were similar works by Washio *et al.* [42].

[5] For example, when a non-zero signal, idler and pump is injected at the input of the fiber. A detailed discussion on this topic is presented in Chapter 2.

[6] Ironically, it was found out that these results were already known by Gordon even in the 1960s [48].

[7] Here we consider a homodyne detection scheme.

parametric gain with degenerate FWM. The first $\chi^{(3)}$-based[8] parametric amplification with a noise figure of 1.8 dB (with a similar structure as Marhic *et al.*) was observed by Imajuku *et al.* in 1999 [53][9]. These developments set the stage for the emergence of a new genre of fiber optic amplifiers; ones with high gain and ultra-low noise properties.

1.1.5 FOPA State-of-the-Art (2000-2020 CE)

Although research in the 1980s and 90s proved the potential of FOPAs, its effective use was constrained by two challenges. First, active occurrence of SBS prevented the use of large pump powers for signal amplification. Second, the fiber nonlinearity was quite weak to deliver a high gain by using a short (few 100 m) length fiber. Use of longer fibers were impractical due to the varying dispersion of longer fibers stemming from manufacturing imperfections [59].

The solution to the second problem was achieved by the following modifications : GeO_2 doping in the fiber, reducing core radius and using a W-shaped refractive index profile of the fiber [60]. These developments marked the emergence of a new kind of fiber : highly nonlinear fiber (HNLF), with an order of magnitude improvement in the nonlinearity. Hansryd *et al.* utilized HNLF's to develop fiber-based parametric amplifier with continuous wave pumping and a significant gain [61, 62]. The other problem, i.e. with SBS was by-passed by using a phase modulated pump leading to an increased Brillouin threshold [63–66]. Further, alteration of the core radius led to techniques to shift the zero dispersion wavelength of the fiber from the value given by the material dispersion of silica [67]. The HNLF thus became an explorable platform for FOPA research in the first and second decades of the 2000s.

High gain parametric amplification (although phase insensitive) [68] with a large bandwidth [69] was demonstrated in 2006-7. Fundamental noise properties of these amplifiers were investigated in Refs. [70–72].

The first decade of the 2000s also saw a growth in the research related to the theoretical understanding of FOPA's. Marhic *et al.* investigated the dependence of FOPA gain spectrum on the medium dispersion [73]. A flatter gain spectrum of a two pump configuration compared to a one pump case was theoretically predicted [74] and experimentally realized [75]. The quantum properties of parametric amplifiers were studied in the seminal work of McKinstrie *et al.* [76–78].

Around 2005, FOPA's with PSA configuration started attracting the spotlight [78–80]. Signal regeneration capabilities of a PSA was demonstrated by Crussore *et al.* [81–83] and later studied by Slavík *et al.* [84, 85]. This led to the development of the copier PSA setup, introduced by Tang *et al.* [86]. It is based on the principle : copying of the signal to a conjugate idler wave using a parametric stage, and then at a second stage, another parametric amplifier becomes phase sensitive due to the presence of

---

[8] Silica fiber is an example of a $\chi^{(3)}$ medium.

[9] Although here we did not cover all the important developments in the field, an interested reader can look up Refs. [54–58] for a more comprehensive overview.

the signal and the idler waves. Such architectures were explored experimentally in the context of quadrature phase shift keyed (QPSK) data transmission by Tong *et al.* [87, 88].

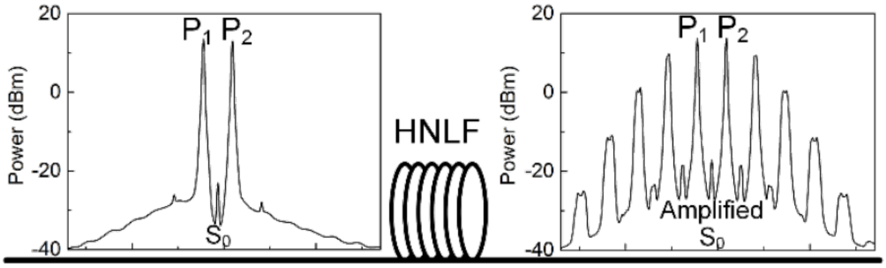

Figure 1.4. Experimental results of the power spectrum of input and output of a highly nonlinear fiber (HNLF) showing high-order waves generated by FWM processes at the output. P_1 and P_2 are the two pumps and S_0 is the signal. (courtesy : Ref. [89])

One crucial challenge for PSA operation of a FOPA originates from the cascaded FWM processes generating parasitic sidebands. In Fig. 1.4 we show the example of two pumps (P_1 and P_2) and a signal (S_0) being launched inside a HNLF. In the output spectrum, we see higher order waves apart from the two pumps and the signal being originated. These extra higher order waves deplete the available gain of the amplifier. To reduce this detrimental effect, efforts in theoretical [76, 90] and numerical [91, 92] investigation have been made to analyze the complex dynamics of the different FWM processes generating these sidebands. Most of these models are based on propagation of multiple CW waves through a HNLF. However, a complete analytical model to deal with more than four waves is still unavailable [45]. This is a problem that we embark on in this thesis and discuss in detail in Chapter 2.

1.2 Properties of Optical Fibers

In this section we introduce some general properties of optical fibers. We will use some of these concepts extensively in the later chapters.

1.2.1 Profile

An optical fiber consists of a central glass core with a surrounding cladding whose refractive index n_c is slightly lower than the core index n_1. These fibers are also known as step-index fibers. Another class of fibers, commonly known as graded-index fibers have a gradual variation of refractive index from the core to the periphery [93]. In Fig. 1.5 we show the scheme of a step-index (a) and graded-index (b) fiber.

In this discussion we confine ourselves only to step-index fibers. Two parameters that characterize a step-index fiber are the relative core–cladding index difference Δ defined as :

$$\Delta = \frac{n_1 - n_c}{n_1}, \tag{1.1}$$

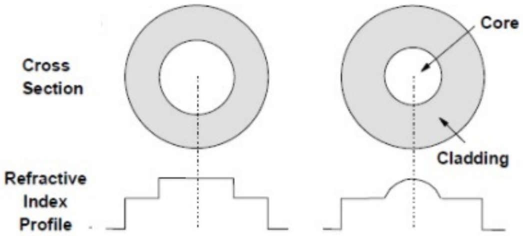

Figure 1.5. Transverse refractive index variation of a step-index and graded index fiber. (courtesy : Test and Measurement World)

where n_1 and n_c are the refractive indices of the core and the cladding of the fiber respectively. The second one is V defined as :

$$V = k_0 a (n_1^2 - n_c^2)^{\frac{1}{2}}, \tag{1.2}$$

where $k_0 = \frac{2\pi}{\lambda}$, a is the core radius and λ is the wavelength of light. The number of light modes supported by the fiber is given by the value of V. For a step-index fiber, the fiber supports only one mode when $V < 2.405$ [58]. These fibers are called single mode fibers. On the other hand, fibers designed to achieve a $V > 2.405$ can support more than one modes and hence called multimode fibers. In general, the main difference between single and multimode fibers is core radius a (smaller for single mode and larger for multimode fibers respectively). In this thesis all the discussions pertain to the case of single mode fibers.

1.2.2 Loss

Transmission of optical signals inside a fiber is accompanied with losses. If P_{in} is the input power launched into a fiber of length L, the transmitted power P_{out} is given by :

$$P_{out} = P_{in} e^{-\alpha L}, \tag{1.3}$$

where α is the fiber attenuation coefficient. As one might expect, the fiber losses are highly dependent on the wavelength of operation. In Fig. 1.6 we show the loss spectrum of a state-of-the-art silica fiber with a low loss window of several hundred nanometers (depending on acceptable attenuation). The losses are minimum in the C-band reaching as low as 0.2 dB/km, whereas being much larger near the visible spectrum.

There are several factors that contribute to the loss mechanism of a material. Rayleigh scattering and material absorption are however the dominant contributors. The Rayleigh scattering loss varies as λ^{-4} and is dominant at shorter wavelengths. As this loss is intrinsic to the fiber, it sets the ultimate limit on fiber loss [58].

Coming to material absorption, silica glass exhibits electronic resonances in the ultraviolet region, and vibrational resonances in the far-infrared region (beyond 2 μm). However in the 0.5 to 2 μm window it shows very low absorption. Nevertheless, even a small amount of impurity can lead to a significant absorption in this

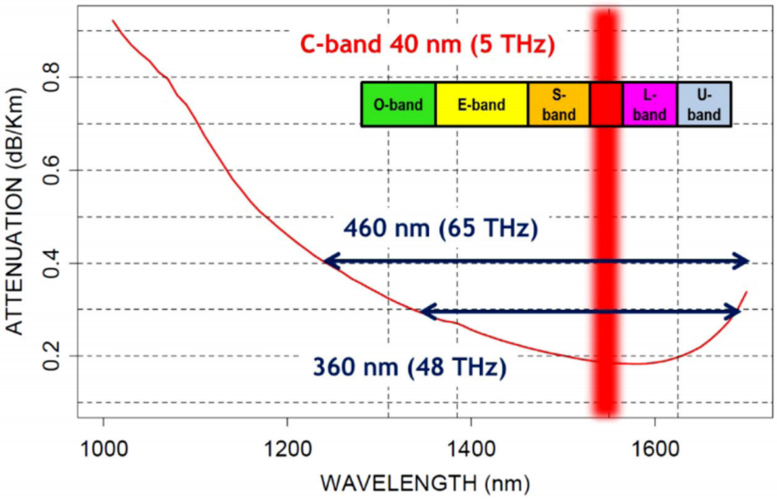

Figure 1.6. Typical attenuation spectrum for a state-of-the-art silica fiber. The different amplification bands (O, E, S, C, L and U) are indicated. The C-band is highlighted in red. (courtesy : Ref. [45])

window. In silica fibers, a significant source of such impurities are OH- ions. They lead to losses due to their vibrational absorption peaks. However state-of-the-art fiber fabrication techniques can reduce such impurities significantly [94].

Among other factors that may contribute to losses are bending of the fiber and scattering of light at the core–cladding interface.

1.2.3 Dispersion

Refractive index of a medium in general depends on the wavelength of the light. Such wavelength dependence of the refractive index accounts for the dispersive effects of the medium. The dispersion arises from two main sources : 1. material composition of the medium (material dispersion), and 2. geometric distribution of refractive index of the medium (waveguide dispersion).

1.2.3.1 Material Dispersion

On a fundamental level, the frequency dependence of the refractive index is related to the characteristic resonance frequencies for oscillation of bound electrons in the medium driven by the external electromagnetic radiation. Far from the medium resonance frequency, the refractive index n can be approximated by the Sellemeier equation as [58] :

$$n^2(\omega) = 1 + \sum_{j=1}^{m} \frac{B_j \omega_j^2}{\omega_j^2 - \omega^2}, \tag{1.4}$$

where ω_j is the j-th resonance frequency and B_j is its strength. ω_j's and B_j's can be obtained by fitting an experimentally obtained dispersion curve to Equation (1.4).

1.2.3.2 Waveguide Dispersion

Waveguide dispersion is the result of the geometric distribution of refractive index of the medium that leads to wavelength dependence of the propagation constant of the optical waveguide. For example, in the case of a single mode fiber, the larger the wavelength, the more the fundamental mode will spread from the core into the cladding causing the fundamental mode to propagate faster. Thus by altering the refractive index profile of the waveguide, we can design waveguides with a preferred dispersion profile. For example, see Ref. [95].

1.2.3.3 Dispersion Parameter *D*

An alternative way to mathematically represent dispersion is through the Taylor expansion of the mode propagation constant $\beta(\omega)$ around a chosen central frequency ω_c.

$$\beta(\omega) = \sum_{n=0}^{\infty} \frac{1}{n!} \left(\frac{d^n\beta}{d\omega^n} \right)_{\omega=\omega_c} (\omega - \omega_c)^n = \sum_{n=0}^{\infty} \frac{1}{n!} \beta^{(n)}(\omega_c)(\omega - \omega_c)^n, \tag{1.5}$$

where $\frac{d^n\beta}{d\omega^n} = \beta^{(n)}$. We note here that for a pulse, $\beta^{(1)}(\omega_c)$ is the inverse of the group velocity and $\beta^{(2)}(\omega_c)$ is the group velocity dispersion.

Often the dispersion of a fiber is expressed in terms of the dispersion parameter D, which is related to β as :

$$D = \frac{d\beta^{(1)}}{d\lambda_c}, \tag{1.6}$$

where λ_c is the central wavelength corresponding to ω_c. The variation of D with wavelength can often be approximated as linear and the slope for the relation, i.e. dispersion slope D', is provided by the manufacturer. The wavelength for which $D = 0$ is known as the zero dispersion wavelength of the fiber and is denoted by λ_{ZDW}. These topics are re-discussed in detail in Chapter 2. We should note here that near the zero dispersion wavelength, cubic terms in the Taylor expansion of β become important.

1.2.3.4 Dispersion Regimes

For wavelengths below the zero dispersion wavelength of the fiber ($\beta_2 > 0$), the fiber is said to exhibit normal dispersion. In the normal dispersion regime, high-frequency (blue-shifted) components of an optical pulse travel slower than low-frequency (red-shifted) components. In contrast, the opposite occurs in the anomalous dispersion regime, where the wavelength is more than the zero dispersion wavelength of the fiber ($\beta_2 < 0$). The anomalous dispersion regime is interesting for the study of nonlinear effects related to optical solitons which are generated through a balance between the dispersive and nonlinear effects of the fiber.

1.2.4 Nonlinearity

When an electromagnetic field is incident on a material, the material acquires an induced polarization due to action of the external electric field. For a homogeneous dielectric medium, this polarization $\vec{P}$ (which is the density of induced dipole moments) is related to $\vec{E}$ through the susceptibility χ of the medium as :

$$\vec{P} = \epsilon_0 \sum_{k=1}^{\infty} \chi^{(k)} \vec{E}^k, \tag{1.7}$$

where $\chi^{(k)}$ models the k-th order nonlinearity of the medium[10] and ϵ_0 is the vacuum permittivity. Note that for a time-varying electric field, this result is true in the frequency domain.

Maxwell's equations in a non-magnetic, charge-free medium (like silica fiber) leads to the following differential equation [56]:

$$\nabla^2 \vec{E} - \frac{1}{c^2}\frac{\partial^2 \vec{E}}{\partial t^2} = \frac{1}{c^2}\frac{\partial^2 \vec{P}}{\partial t^2}, \tag{1.8}$$

where c is the speed of light in vacuum. It should be noted that for most practical purposes, $\vec{E}$ and $\vec{P}$ are considered to be in the same direction. Thus using a scalar version of Equation (1.8) often suffices. The important thing to note in Equation (1.8) is that depending on $\vec{P}$ (that depends on χ), the differential equation can exhibit linear or nonlinear dynamics. For the case of vacuum, $\vec{P} = \vec{0}$ that leads to the wave equation which has sinusoidal solutions. For the first order case, when $\chi^{(1)} \neq 0$ and $\chi^{(k)} = 0$ for $k > 1$, we have the case of a linear system. For cases when $\chi^{(2)} \neq 0$, nonlinear effects such as second harmonic generation and sum frequency generation are observed. For $\chi^{(3)} \neq 0$ also, the system shows nonlinearities and exhibits effects like four wave mixing, self phase modulation and cross phase modulation [58].

From Equation (1.7) we can say that when the medium does not have an inversion symmetry (for example a crystal), the nonlinearity will arise from $\chi^{(2)}$ (and higher even order terms), whereas when the material has an inversion symmetry (for example an amorphous material like silica), all the even order terms will be 0, and the nonlinearity will come from $\chi^{(3)}$ (and higher odd order terms) [45].

In this discussion we only confine ourselves to the discussion of silica fiber, which is a $\chi^{(3)}$ medium. The third order nonlinearity $\chi^{(3)}$ manifests in most cases as a power-dependent refractive index where the intensity dependent refractive index $n(\omega, I)$ is given by [58] :

$$n(\omega, I) = n_0(\omega) + n_2 I, \tag{1.9}$$

where n_0 is the linear part of the refractive index and n_2 is the second order nonlinear refractive index. I is the intensity of the wave. This is also known as the Kerr-effect. If the index increases with optical power, the media is said to be self-focusing, since an intense beam can induce its own waveguide, and thus suppress diffraction

---

[10] Note that $\chi^{(k)}$ is a tensor of rank $k+1$ in general [58].

[96]. The intensity dependence of the refractive index leads to a large number of interesting nonlinear effects. We will study the implications of these effects further in Chapter 2.

1.3 Microwave Photonic Link

Microwave photonics has been defined as the study of photonic devices operating at microwave frequencies and their application to microwave and optical systems [97]. It combines the two worlds : microwaves (with frequency roughly a few to a hundred GHz) and photonics (roughly a few hundred THz) [98]. In this section, we will discuss a few aspects of microwave photonic links which are playing a crucial role in modern-day communication systems.

1.3.1 Principle

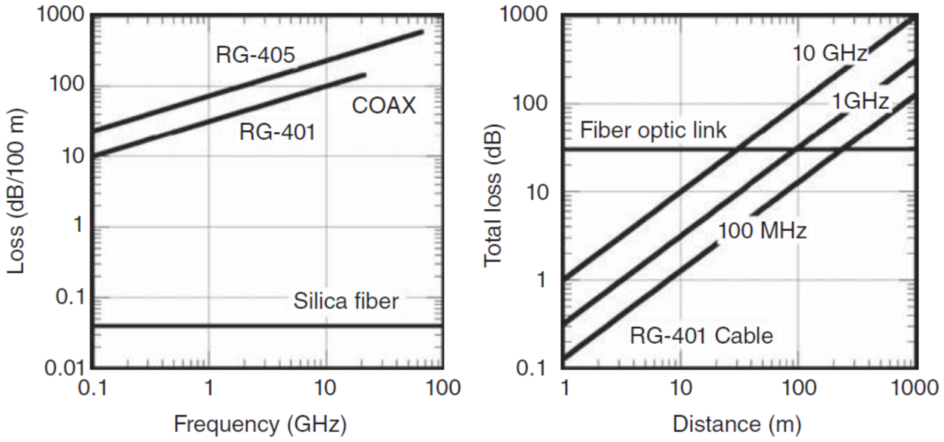

(a) (b)

Figure 1.7. Loss as a function of (a) frequency including only propagation loss in the cable for RG-401, RG-405 and silica fiber and (b) propagation distance for RG-401 at three frequencies. In (b), the fiber optic loss includes a 30 dB fixed loss due to E/O and O/E conversion. (courtesy : Ref. [15])

The core idea behind the functioning of a microwave photonics system is explained as follows. Optical fiber communication links provide numerous advantages compared to its coaxial counterpart, like larger bandwidth, faster transmission, immunity to electromagnetic interference, lower loss, etc. Figure 1.7 shows the comparison of losses between coaxial cables and optical fibers. Two kinds of coaxial cables are considered : RG-401 (larger diameter) and RG-405 (smaller diameter). It can be seen from Fig. 1.7 (a) that higher frequencies lead to much higher (three to four orders of magnitude) losses for coaxial cables compared to silica fiber. From Fig. 1.7 (b) we see that the E/O and O/E conversion accounts for a high loss in the fiber case compared to the coaxial fibers. Nevertheless, when the propagation distance is large, the fiber easily outperforms coaxial cables.

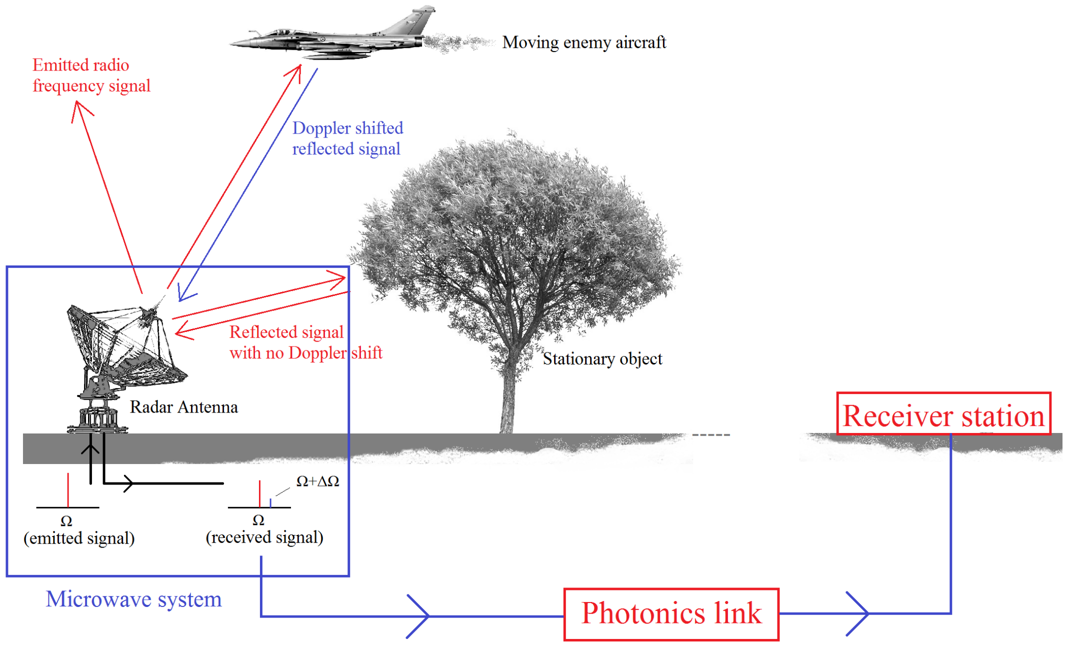

Figure 1.8. Illustration of a microwave photonic link in a radar-based system to track an enemy aircraft. The radar antenna picks up a Doppler shifted microwave signal which is sent to a receiver station via a photonic link.

To enjoy the benefits of optical fiber links, microwave signals are used to modulate an optical carrier and the information is imprinted on the optical signal. This process is also called the electric-to-optical (E/O) conversion. The modulated optical carrier is then transmitted through a fiber optic link. At the receiver end, the modulated optical carrier is demodulated (optical-to-electric or O/E conversion) to retrieve back the original microwave signal [99].

Figure 1.8 shows an example of a microwave photonic link in a radar system. The radar antenna, in order to detect an airborne threat, emits microwave radiation in all directions in an airspace. The existence of a moving object in the airspace would reflect back some of the microwave radiation with a Doppler shift, to the radar antenna. The microwave circuitry at the antenna filters out the background and feeds the Doppler shifted received signal to an electro-optic modulator. The modulator modulates an optical signal utilizing Pockels effect [100]. Then this modulated signal is transmitted through a fiber optic link to a receiver station. At the receiver, a photodetector demodulates the signal to retrieve back the original radar signal.

1.3.2 Historical Perspective and Overview

Microwave photonics is a multidisciplinary field encompassing optical, microwave, and electrical engineering. This field originated as a result of the need to solve complex radio engineering problems with the aid of optical technologies [15]. Although the field of microwave photonics was not formally recognized until the late 1980s and the early 1990s [101], the development of optical communication systems in the 1960s, can arguably be called the inception period for microwave photonics technologies [102]. With the availability of laser sources, an important question floating around at that time was, how to modulate the output of a laser source at a high rate? The answer to this came from the development of electro-optic modulators [100, 103]. In 1971, Standley *et al.* achieved modulation with frequencies as high as 11 GHz [104]. This development opened the possibility for using information carrying electrical signals to modulate an optical carrier that in turn can carry the information over a distance.

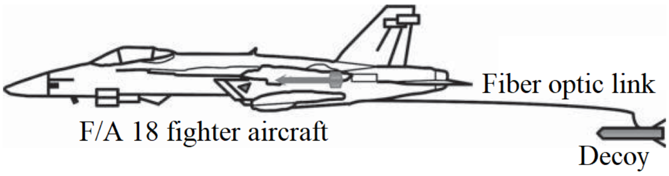

Figure 1.9. A depiction of an RF towed decoy (ALE-55) with a fiber optic link from a F/A 18 aircraft. (courtesy : Ref. [15])

For implementation in communication systems, early plans for signal transmission, were based on free-space optics and gas lenses, however with the realization of the potential of low-loss optical fiber transmission [9, 16], fibers rapidly became the preferred choice.

Early microwave analog transmission links had very high electrical input to electrical output losses (>40 dB). However in the 1990s, using external modulation it was possible to demonstrate microwave photonic links displaying gain without the use of electrical amplification [105]. Further developments ensued with the introduction of interferometric modulators using $LiNbO_3$ and GaAs [106–108].

For detection of signals, high speed photodetectors were designed to provide the useful microwave detection bandwidth [109, 110] in the 1960s. Later in the 70s and 80s, more advanced detectors were available [111, 112].

One instance of application of fiber optic links in microwave systems was in the military technology. Fiber optic links were employed in an airborne towed decoy called ALE-55, of F/A 18 fighter aircrafts (see Fig. 1.9) [113]. In the early designs, a receiving antenna on the decoy detected a threat, amplified, and then retransmitted a higher power return signal to the aircraft. However, due to the size limitations due to aerodynamic constraints of the decoy, only a limited amount of signal processing could be performed in the decoy. Introducing a fiber optic cable to connect the aircraft and the decoy makes it possible to perform sophisticated signal processing, remoting processed signals to the decoy where amplification and transmission occur. This allowed the decoy to be used effectively in defeating a threat by suppressing enemy radar functionalities and seducing an approaching missile away from the aircraft. Use of fiber optics also minimized the size of the decoy considerably making its integration into aircrafts more robust.

A more recent application of microwave photonics technology is in the field of radio astronomy. The Greenbank Telescope, located in West Virginia in the USA, is the world's largest fully steerable single antenna (see Fig. 1.10) [114, 115]. It operates in the range 0.1 to 115 GHz. The huge parabolic antenna, with a 100 m diameter is used for the detection of atomic and molecular emission lines often produced near blackholes or those where the measurement of weak, spatially extended spectral lines can be used to detect new organic molecules in space. The facility uses an analog fiber optic link for remoting signals to a processing station [116] which was demonstrated to be useful by Payne *et al.* [117].

Figure 1.10. A picture of the Greenbank telescope, in West Virginia, USA. (courtesy : Hauser Spouser)

The application domains of microwave photonics technology is multi-faceted and spans military, industrial, and academic sectors. Other applications include radio-over-fiber for wireless communications, signal routing and true time delay beamforming in arrays, optical signal processing, filtering, waveform synthesis, optoelectronic oscillators for precision generation of RF signals, optical clocks for precision timing, etc. [15].

1.3.3 PSA in a Microwave Photonic Link

In a microwave photonic system, often the received RF signals by the antenna are quite weak. Examples of such systems are radio telescopes collecting signals that originate at astronomical distances and are thus very low power. Also high precision radars require the capability to detect very weak reflections from enemy aircrafts at a distance. In such systems, the RF signal requires a pre-amplification before being sent to the processing station. This amplification can be performed in the optical domain, i.e. in the optical link of the system. As one can expect, a high noise performance optical amplifier is required for such sensitive application. Thus a FOPA in a PSA configuration immediately comes to our mind for such a role. Furthermore, utilization of a PSA can offer the possibility of realizing other functionalities such as optical filtering through phase sensitive amplification and de-amplification [118], wideband photonic assisted radio-over-fiber systems [119], microwave photonic frequency measurement [120], etc. A schematic representation of a microwave photonic link with a PSA is shown in Fig. 1.11.

The possibility of noiseless amplification in PSA's has been extensively studied in the context of digital optical communication systems [54, 55, 57, 62, 121]. But such links are constrained by the bandwidth of analog-to-digital converters (ADC) and therefore are not suitable for applications requiring a wide bandwidth. This makes the resort to analog microwave photonic links inevitable. Preliminary studies on performance of analog links with respect to modulation formats [122], signal multicasting [123] and PSA inclusion in a link [118, 124–126] were performed, however the possibility of incorporating a PSA within an analog microwave photonic link needs further exploration. Integration of a PSA in a microwave photonic link comes with different challenges too. We discuss these issues and formulate a direction of studying these problems in the following.

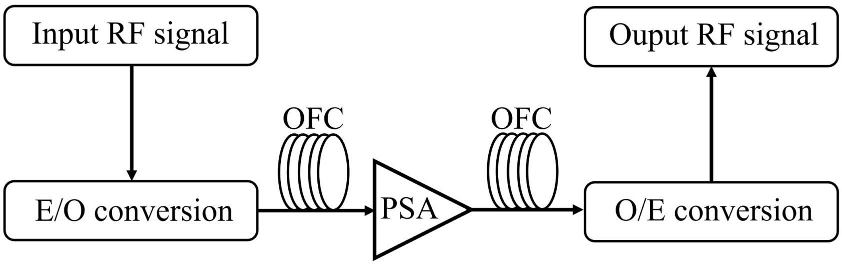

Figure 1.11. Scheme of a microwave photonic link with a PSA. OFC : optical fiber cable; PSA : phase sensitive amplifier.

Apart from other implementation challenges, the first question that we ask here is : Does the optical amplifier introduce extra distortions into the link? At first sight this question might sound baseless, however it is relevant as we explain in the following.

In a microwave photonic link, the electro-optic conversion is a nonlinear process that often leads to nonlinearities in the optical domain to be transmitted by the optical link. Therefore, when we use an optical amplifier to amplify the optical signal, the optical amplifier should also amplify the generated nonlinearities. Thus depending on the interplay between the electro-optic nonlinearities and the PSA-generated nonlinearities, the effective distortion of the microwave photonic link is determined [127]. Although generation and mitigation of nonlinearities by a PSA has been studied for digital links [84, 128–133], in the case of analog links, it is still a topic of ongoing research [134].

Thus these questions about the impact of PSA inclusion, on the linearity of the link will be addressed in a greater detail in Chapter 4 of this thesis. We will also explore the link dynamics under PSA gain saturation and look for conditions where the PSA nonlinearities can be used to mitigate electro-optic nonlinearities leading to a highly linearized link.

Chapter 2

Analytical 7-Wave Model

Contents

2.1 Introduction 25

2.2 Analytical 3-Wave Model 26

2.2.1 Configurations 26

2.2.2 Approximations 27

2.2.3 Wave Evolution Equations 28

2.2.4 Signal Gain : Degenerate Pump Configuration 29

2.2.5 Signal Gain : Non-Degenerate Pump Configuration 31

2.2.6 PIA vs PSA 32

2.3 Analytical 4-Wave Model 33

2.3.1 Configuration 33

2.3.2 Approximations 33

2.3.3 Linear Phase Mismatch 34

2.3.4 Wave Evolution Equations 35

2.3.5 Solution of Equations 36

2.3.6 Stability of Solution 40

2.3.7 Limitations 41

2.4 Analytical 7-Wave Model 42

2.4.1 Configuration 43

2.4.2 Approximations 43

2.4.3 Linear Phase Mismatch 43

2.4.4 Wave Evolution Equations 44

2.4.5 Subsystems of the Analytical 7-Wave Model 46

2.4.6 Coupled Signal and HOI Evolution (Subsystems 1 and 2) . . 46

2.4.7 Maximum Signal Gain 59

2.4.8 Phase Sensitive Frequency Conversion (PSFC) 59

2.4.9 Input Signal Phase for Maximum Signal Gain 63

2.4.10 HOP Evolution (Subsystem 3) 65

2.4.11 Comparison of Analytical 3- and 7-Wave Models with Numerical 7-Wave Model . . . 71
2.4.12 Physical Interpretation . . . 74
2.4.13 Limitations . . . 78
2.4.14 PSA Noise Figure . . . 78

2.5 Conclusion . . . 78

2.1 Introduction

In this chapter we introduce the mechanism of continuous wave (CW) light propagation through a fiber acting as an optical parametric amplifier. We discuss a multi-wave model that can be employed to describe the dynamics of the system for different configurations of operation. In this discussion we confine ourselves to the situations where all the waves are launched into the parametric amplifier with the same linear state of polarization and remain in that state along the entire length of the fiber. This assumption allows us to consider a single component of the electric field vector and hence use a scalar description for the model [56].

Propagation of light in a fiber optic parametric amplifier (FOPA) is chiefly addressed through two classes of models [58] : a) n-wave models and b) nonlinear Schrödinger equation (NLSE) based models. The n-wave models[1] deal with the propagation of n discrete CW waves, whereas the NLSE based models describe the propagation of a pulse with a continuous distribution of frequencies. This chapter is devoted solely for the description of n-wave models. More specifically, we focus on the case when $n = 3, 4$ and 7. A NLSE based model is described in the next chapter.

The n-wave model is often used with $n = 4$, also known as the 4-wave model. This model consists of four waves : two pumps, a signal and an idler. The 4-wave model is solvable analytically under certain approximations and is well studied in the scientific literature [45, 56, 58, 76, 135]. In the special case where the signal and the idler waves have the same frequency, the 4-wave model becomes the 3-wave model. This is often the preferred configuration in digital communication systems [87]. However, the consideration of just three or four waves is often not sufficient to describe the dynamics of a FOPA. Indeed, complex four wave mixing (FWM) processes can lead to generation of more sideband waves than injected at the input of the fiber. These sideband waves influence the evolution of all the other waves inside the FOPA. Thus often the 4-wave model is extended to a higher ($n > 4$) number of waves to account for the influence of the extra sideband waves. For example a 6-wave model is investigated in [76, 136] and a 7-wave model is investigated in [91, 137, 138]. However extending the 4-wave model for a large n is restricted by the fact that the number of FWM terms in the coupled differential equations of the n waves grows as $\sim n^3$ [90]. Thus with growing n, the n-wave model becomes intractable very soon, the highest achieved value of n so far being $n = 24$ [92].

This chapter is organized as follows. In Section 2.2 we introduce the most basic analytical model to describe CW light propagation through a FOPA considering only three waves, i.e. the analytical 3-wave model. Then in Section 2.3 we move to an analytical 4-wave model and use a matrix approach for solving the system. Then in Section 2.4 we consider a more complicated analytical model considering propagation of seven waves, i.e. the analytical 7-wave model.

---

[1] The n-wave model is often referred to as multi-wave model.

2.2 Analytical 3-Wave Model

The 3-wave model is a special case of the 4-wave model where either two of the pumps or the signal and idler are degenerate. This model provides the simplest description of light propagation through a $\chi^{(3)}$ fiber capturing the physics of dispersive and nonlinear effects of a FOPA [56]. The 4-wave model in general and the 3-wave model in particular are quite extensively studied in the context of amplification and wavelength conversion in digital communication systems [61, 62, 139–143]. In this section we discuss the different aspects of an analytical 3-wave model and understand the amplification and wavelength conversion capabilities of a FOPA.

2.2.1 Configurations

Considering the allocation of frequency of the pump(s) and signal (and/or idler), FOPA's can be operated in different configurations. The most general scenario consists of two pumps and a signal and an idler, with all the waves having different frequencies (see Fig. 2.1). This configuration corresponds to the 4-wave model. The different interacting frequencies are related as :

$$\omega_{P1} + \omega_{P2} = \omega_s + \omega_i, \tag{2.1}$$

where ω_{P1} and ω_{P2} are the pump frequencies and ω_s and ω_i are the signal and idler frequencies respectively. Equation (2.1) guarantees the energy conservation associated with the interaction processes between the different waves [144, 145].

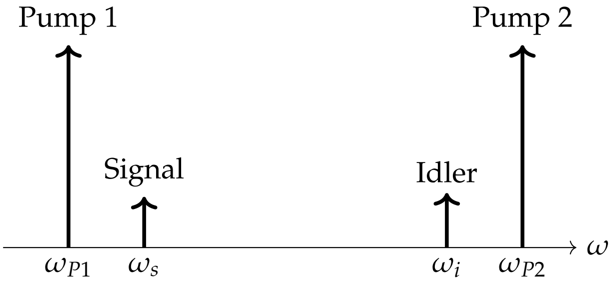

Figure 2.1. General configuration of a FOPA without considering any sidebands. ω_s, ω_i, ω_{P1} and ω_{P2} are the frequencies of the signal, idler, pump 1 and pump 2 waves respectively. The height of the arrows represent intensity of the waves (not to scale).

While Fig. 2.1 shows the most general configuration, FOPA's are broadly operated in two common configurations [54]: a) degenerate pumps and non-degenerate signal and idler, b) non-degenerate pumps and degenerate signal and idler (see Fig 2.2). These configurations correspond to the 3-wave model. In the field of digital communication systems, the non-degenerate pump configuration is often preferred due to its flat and broad gain spectrum when the signal is close to the zero dispersion wavelength of the fiber [74, 75, 146–150], which is attractive for wavelength division multiplexing (WDM) systems [151] and wavelength converters [152].

Also, the non-degenerate pump configuration benefits from other advantages such as non-requirement of producing an idler wave at the input of the fiber to achieve PSA operation and obtaining the same signal gain with a lower individual pump power compared to the degenerate pump configuration [58]. However, the degenerate pump configuration has a simpler dynamics compared to the non-degenerate pump configuration but with a less flat gain spectrum [153].

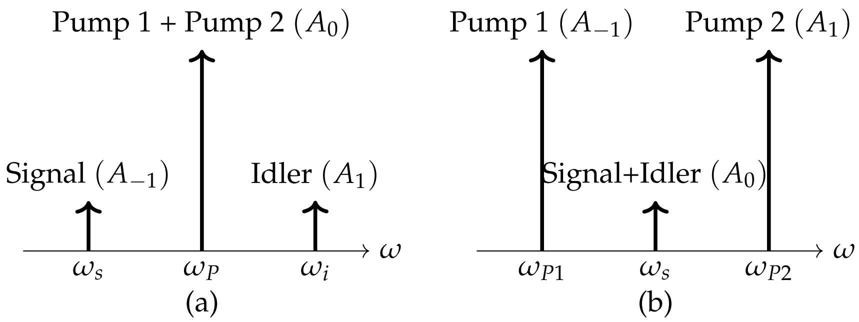

Figure 2.2. Configurations of a FOPA in a 3-wave model : (a) Degenerate pumps and non-degenerate signal and idler. (b) Degenerate signal and idler and non-degenerate pumps. We introduce a simplified notation A_0 and $A_{\pm 1}$ for the different waves for convenience. ω is frequency and the height of the arrows represents intensity (not to scale).

2.2.2 Approximations

In this subsection we list the approximations considered for the calculation of wave evolution through the FOPA in a degenerate wave configuration. Here first we define the real electric field $E(z,t)$ with $2N+1$ components with indices running from $-N$ to N, as :

$$E(z,t) = \sum_{n=-N}^{N} A_n e^{i(\beta_n z - \omega_n t)} + c.c., \tag{2.2}$$

where A_n is the complex amplitude and ω_n is the frequency of the wave with index n. The corresponding propagation constant for the n-th wave is given by β_n (or $\beta(\omega_n)$). For the 3-wave model, $N = 1$. Here we have not considered the transverse profile of the mode as we consider it to be a constant within a characteristic radius r_0 of the fiber and 0 outside that radius.

Now we list the considered approximations as [56][2]:

- The attenuation of the fiber is neglected, i.e. $\alpha = 0$ where α is the attenuation coefficient of the fiber.
- The amplitudes of the electric fields A_k's, of the considered waves are assumed to vary little over the length scale of the wavelengths of the waves. This is also

---

[2] Here we do not mention that the waves are co-polarized as it is understood from the previous discussion.

called the slowly varying amplitude (SVA) approximation and is written as :

$$\left|\frac{d^2A_k}{dz^2}\right| \ll \left|\beta_k \frac{dA_k}{dz}\right| . \tag{2.3}$$

- Along the length of the fiber, the power(s) of the pump(s) are much larger than those of the other waves i.e. signal and/or idler in this case. This can also be referred as the strong pump approximation.
- The pump power(s) are considered almost undepleted along the length of the fiber. The undepleted pump powers are given by $|A_{\pm1}(z)|^2 = P$. This is also known as the non-pump depletion approximation.
- For the case of a non-degenerate pump configuration, the input pump powers are the same, i.e. $|A_1(0)|^2 = |A_{-1}(0)|^2$.

2.2.3 Wave Evolution Equations

The differential equations for the $2k+1$ slowly varying complex amplitudes, A_j's with $j = -k$ to k are given as [56] :

$$\frac{dA_j}{dz} = i\gamma\Big[|A_j|^2A_j + 2\sum_{l\neq j=-k}^{k}|A_l|^2A_j + \sum_{\substack{m,n,p=-k,\\ \omega_m+\omega_n-\omega_p=\omega_j}}^{k} A_mA_nA_p^*e^{i\Delta\beta_{mnpj}z}\Big], \tag{2.4}$$

where $\Delta\beta_{mnpj} = \beta_m + \beta_n - \beta_p - \beta_j$ and γ is the nonlinear coefficient of the fiber. The three terms on the right-hand side of Equation (2.4) respectively correspond to: 1. the interaction of one wave, A_j with itself, which is called self-phase modulation (SPM); 2. the interaction between two waves, A_l and A_j, which is called cross-phase modulation (XPM); 3. the interaction between four waves, A_m, A_n, A_p and A_j, which is called four wave mixing (FWM). Here $\Delta\beta_{klmn}$'s account for the linear phase mismatch of the four interacting waves in a FWM process. We note here that the SPM and XPM interactions between the waves only account for a phase shift of the waves, while the FWM interactions lead to an exchange of energy between the different waves [56, 58]. Thus utilizing the FWM interaction, one can design high-gain optical amplifiers where energy is pumped from a strong pump wave to a weak signal wave [151].

Solving Equation (2.4) for all the $2k+1$ (for degenerate wave configuration) waves with proper initial conditions determines how the fields evolve along the FOPA. While considering the 3-wave model, i.e. $j = -1, 0$ and 1, we can write down the equations for the field evolution of the different waves as :

$$\frac{dA_1}{dz} = i\gamma\Big(|A_1|^2A_1 + 2(|A_{-1}|^2 + |A_0|^2)A_1 + A_0^2A_{-1}{}^*e^{i\Delta\beta_{00-11}z}\Big), \tag{2.5}$$

$$\frac{dA_{-1}}{dz} = i\gamma\left(|A_{-1}|^2 A_{-1} + 2(|A_1|^2 + |A_0|^2)A_{-1} + A_0^2 A_1{}^* e^{i\Delta\beta_{001-1}z}\right), \tag{2.6}$$

$$\frac{dA_0}{dz} = i\gamma\left(|A_0|^2 A_0 + 2(|A_1|^2 + |A_{-1}|^2)A_0 + 2A_1 A_{-1} A_0{}^* e^{i\Delta\beta_{1-100}z}\right). \tag{2.7}$$

While considering a non-degenerate pump configuration, $A_{\pm 1}$ represent the amplitudes of the pumps and A_0 represents the amplitude of the degenerate signal and idler (see Fig. 2.2 (b)). However for a degenerate pump configuration, A_1 and A_{-1} represent the amplitudes of the signal and idler respectively and A_0 represents the amplitude of the degenerate pump (see Fig. 2.2 (a)).

2.2.4 Signal Gain : Degenerate Pump Configuration

For the degenerate pump configuration, the signal is characterized by A_{-1} (see Fig. 2.2 (a)). Solving Equations (2.5), (2.6) and (2.7) we find the gain of the signal $G_{-1} = \frac{|A_{-1}(L)|^2}{|A_{-1}(0)|^2}$ where L is the length of the fiber as [58, 135] (see Appendix A) :

$$\begin{aligned} G_{-1} =& 1 + \left(1 + \frac{\kappa^2 + 4\gamma^2 P^2 \vartheta^2 - 4\kappa\gamma P\vartheta\cos(\Theta)}{4g^2}\right)\sinh^2(gL) \\ &+ \frac{\gamma P\vartheta\sin(\Theta)}{g}\sinh(2gL), \end{aligned} \tag{2.8}$$

where P is the input (undepleted) power of the pump. Θ is the relative phase difference between the signal, pump and the idler and is given by :

$$\Theta = 2\phi_0 - \phi_{-1} - \phi_1, \tag{2.9}$$

where ϕ_{-1}, ϕ_0 and ϕ_1 are the phases of the signal, pump and idler respectively at the input of the fiber (see Equation (2.2)). κ is the nonlinear phase mismatch given by:

$$\kappa = \Delta\beta_{00-11} - 2\gamma P. \tag{2.10}$$

For this configuration $\Delta\beta_{001-1}$ is given by [58]:

$$\Delta\beta_{001-1} = 2\beta(\omega_0) - \beta(\omega_1) - \beta(\omega_{-1}) \approx \beta^{(2)}(\omega_{-1} - \omega_0)^2 + \frac{1}{12}\beta^{(4)}(\omega_{-1} - \omega_0)^4, \tag{2.11}$$

where $\beta^{(2)}$ and $\beta^{(4)}$ are the second and fourth derivative of the propagation constant with respect to the frequency ω_0. A detailed discussion on the calculation of $\beta^{(2)}$ and $\beta^{(4)}$ is provided in Subsection 3.1.6. This expression of $\Delta\beta_{klmn}$ is derived by truncating the Taylor series expansions of the $\beta(\omega_i)$'s (for $i = 0, 1, -1$) around ω_0 after four terms. We should keep in mind that it is only valid for a ω_0 close to ω_{-1}. ω_0 is often called the central frequency denoted by ω_c. Also we note that due to the symmetrical position of ω_1 and ω_{-1} with respect to ω_0, the first and third order terms in the Taylor series expansion of β_1 and β_{-1} cancel out. Also in Equation (2.8),

g, which is known as the parametric gain coefficient [58], is given by :

$$g^2 = (\gamma P)^2 - \left(\frac{\kappa}{2}\right)^2. \tag{2.12}$$

The parameter ϑ is given by :

$$\vartheta = \sqrt{\frac{P_1(0)}{P_{-1}(0)}}, \tag{2.13}$$

where $P_1(0)$ and $P_{-1}(0)$ are the powers of the idler and the signal at the input of the fiber respectively. For $\vartheta = 0$, the FOPA acts as a phase insensitive amplifier (PIA) and for $\vartheta = 1$ (or rather any other non-zero value of ϑ) it behaves as a phase sensitive amplifier (PSA).

- $\boldsymbol{\vartheta = 0}$:

  For the case of PIA, there is no idler at the input of the fiber. Thus using $\vartheta = 0$, we get the PIA gain ${G_{-1}}^{PIA}$ from Equation (2.8) as :

  $$ {G_{-1}}^{PIA} = 1 + \left(1 + \frac{\kappa^2}{4g^2}\right)\sinh^2(gL). \tag{2.14}$$

  We should note here that the gain ${G_{-1}}^{PIA}$ does not depend on the relative phase of the signal and pump (see Fig. 2.3 (in blue)).

  Another important feature of this configuration is that even when there is just the signal and the pump at the input of the fiber, an idler is generated at the output of the fiber. This PIA-generated idler is located at the symmetrically opposite side of the spectrum with respect to the pump and its phase is conjugate of the signal phase. Such spontaneous generation of an idler has many applications such as dispersion compensation and wavelength conversion in a WDM system [154].

- $\boldsymbol{\vartheta = 1}$:

  For the special PSA case of equal amplitudes of signal and idler at the input of the FOPA, i.e. $\vartheta = 1$, we get the signal gain G_{-1} from Equation (2.8) as :

  $$\begin{aligned} G_{-1} =& 1 + \left(1 + \frac{\kappa^2 + 4\gamma^2P^2 - 4\kappa\gamma P\cos(\Theta)}{4g^2}\right)\sinh^2(gL) \\ &+ \frac{\gamma P\sin(\Theta)}{g}\sinh(2gL). \end{aligned} \tag{2.15}$$

  We should note here that the gain G_{-1} depends on the relative phase of the signal, pump and idler, i.e. Θ. A plot of the PSA gain G_{-1} as a function of the relative phase Θ is shown in Fig. 2.3 (in red). In the plot, P=20 dBm, L=200 m, γ =11.3 $\mathrm{W}^{-1}\mathrm{km}^{-1}$, λ_{-1}=1546.9 nm, λ_0=1547.1 nm, zero dispersion wavelength of the fiber[3]. λ_{ZDW}=1547 nm and dispersion slope of the fiber D_1=0.017 ps/nm^2/km[4]. Thus we see from Equation (2.8) and Fig. 2.3, that G_{-1} is a periodic sinusoidal function with respect to Θ with a period of 2π. So if G_{-1} is maximized for $\Theta = \Theta_m$, then G_{-1} is minimum for $\Theta = \Theta_m + \pi$. In fact one can show that $G_{-1,\max} = \frac{1}{G_{-1,\min}}$ where $G_{-1,\max}$ and $G_{-1,\min}$ are the maximum and minimum PSA gains respectively [155, 156].

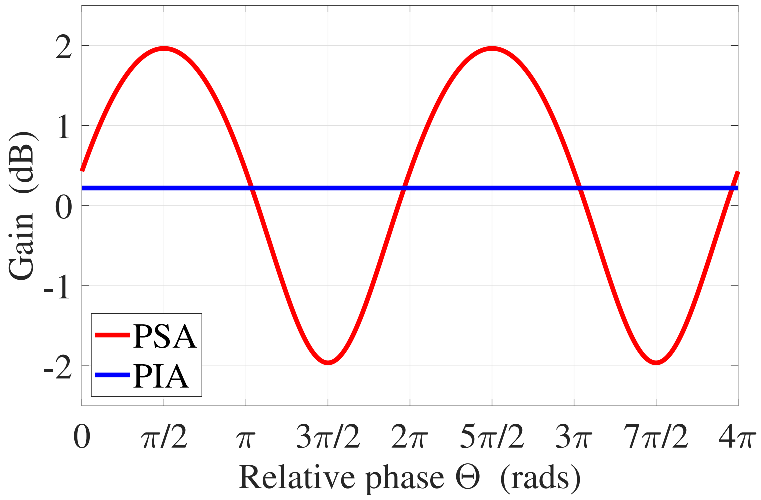

Figure 2.3. PSA (red) and PIA (blue) gain of signal using the 3-wave model as a function of the relative phase between the pump, signal and idler $\Theta = \theta_s + \theta_i - 2\theta_P$ where θ_s, θ_i and θ_P are the phases of the signal, idler and pump respectively at the input of the fiber. A degenerate pump configuration is considered. $P = 20$ dBm, $L = 200$ m, $\gamma = 11.3\ \mathrm{W}^{-1}\mathrm{km}^{-1}$, $\lambda_{-1} = 1546.9$ nm, $\lambda_0 = 1547.1$ nm, $\lambda_{ZDW} =$ 1547 nm and $D_1 = 0.017$ ps/nm^2/km.

From Equations (2.14) and (2.15), we see that the PSA configuration can provide a larger gain than the PIA configuration, however since the PSA gain is sensitive to the relative phase between the pump, signal and idler, all the waves must be phase locked to provide a stable gain. Such phase stabilization can be obtained by the use of feedback loops as illustrated in Ref. [155].

2.2.5 Signal Gain : Non-Degenerate Pump Configuration

For the non-degenerate pump configuration (see Fig. 2.2 (b)), the signal gain $G_0 = \frac{|A_0(L)|^2}{|A_0(0)|^2}$ where L is the length of the fiber, is given by solving Equations (2.5), (2.6) and (2.7) as [58, 135] (see Appendix A) :

$$\begin{aligned} G_0 =& 1 + \left(1 + \frac{\frac{\kappa^2}{4} + 4\gamma^2P^2 - 2\kappa\gamma P\cos(\Theta)}{g^2}\right)\sinh^2(gL) \\ &+ \frac{2\gamma P\sin(\Theta)}{g}\sinh(2gL), \end{aligned} \tag{2.16}$$

---

[3] The zero dispersion wavelength is the wavelength at which the dispersion parameter D of the fiber becomes zero. We will revisit this in Subsection 3.1.6.

[4] These parameters correspond to the ones used for a standard HNLF in [155].

where the parametric gain coefficient g is given by :

$$g^2 = 4\gamma^2 P^2 - \frac{\kappa^2}{4}. \tag{2.17}$$

In this case κ is given by :

$$\kappa = \Delta\beta_{1-100} - 2\gamma P, \tag{2.18}$$

where $\Delta\beta_{1-100}$ is the linear phase mismatch given by :

$$\Delta\beta_{1-100} = \beta(\omega_1) + \beta(\omega_{-1}) - 2\beta(\omega_0). \tag{2.19}$$

Marhic *et al.* showed that using a Taylor series expansion of $\beta(\omega)$ around $\omega_c \approx \omega_0$, we can write [140]:

$$\Delta\beta_{1-100} = 2\sum_{n=1}^{\infty} \frac{1}{(2n)!} \left(\frac{d^{2n}\beta}{d\omega^{2n}}\right)_{\omega=\omega_c} \left[(\omega_0 - \omega_c)^{2n} - \left(\frac{\omega_1 - \omega_{-1}}{2}\right)^{2n}\right], \tag{2.20}$$

Thus when $\omega_c = \omega_0$, we get :

$$\Delta\beta_{1-100} = -2\sum_{n=1}^{\infty} \frac{1}{(2n)!} \left(\frac{d^{2n}\beta}{d\omega^{2n}}\right)_{\omega=\omega_c} \left(\frac{\omega_1 - \omega_{-1}}{2}\right)^{2n}. \tag{2.21}$$

Thus tailoring $\omega_1 - \omega_{-1}$, $\beta^{(2)}$ and $\beta^{(4)}$, one can obtain a configuration with a flat and broad gain spectrum for the FOPA when the signal wavelength is close to the zero dispersion wavelength of the FOPA [140]. This property of the non-degenerate pump FOPA makes it a promising candidate for WDM systems.

We note here that the degenerate and non-degenerate pump FOPA's both have the same form of solution for the signal gain, however they differ with respect to the parameters κ and g. Thus the spectral dependences of the gain are different for the two cases.

2.2.6 PIA vs PSA

We saw from Equation (2.8) that the signal gain for PIA is independent of the relative phase of the pump and the signal and for PSA it depends on the relative phase. It turns out that this phase sensitivity has implications on the quantum noise properties of a FOPA. Caves showed that the quantum noise figure, which is the ratio of signal to noise ratio between the input and output of the FOPA, for a FOPA in PIA configuration is limited by 3 dB whereas for PSA it can be as small as 0 dB [47]. This means a FOPA in PSA configuration can act as a noiseless amplifier without degrading the signal-to-noise ratio after amplification [51, 155].

2.3 Analytical 4-Wave Model

In the previous section we dealt with the analytical 3-wave model for non-degenerate and degenerate pump configurations. In the non-degenerate pump case, the 3-wave model becomes a special case of the 4-wave model when the signal and the idler are degenerate. In this section we provide a matrix based approach to solve the system with two pumps and non-degenerate signal and idler [56].

2.3.1 Configuration

The configuration of the 4-wave model is similar to the 3-wave model however with a non-degenerate signal and idler. In Fig. 2.4 we show such a configuration. The two pumps are labelled A_1 and A_{-1}, the signal and idler are labelled A_{q_s} and A_{q_i} respectively. $\Delta\omega_{PP}$ is the frequency separation between the pumps.

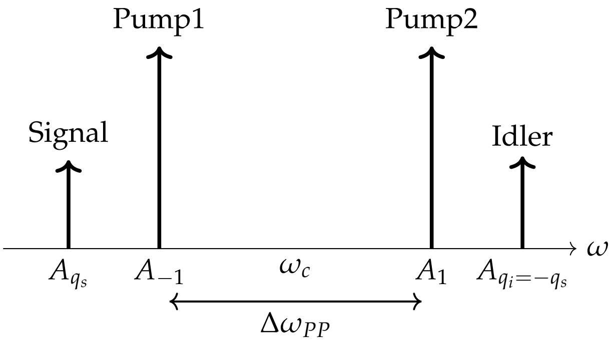

Figure 2.4. Configuration of a dual pump FOPA with non-degenerate signal and idler and non-degenerate pumps. ω is frequency. The two pumps are labelled A_1 and A_{-1}, the signal and idler are labelled A_{q_s} and A_{q_i} respectively. $\Delta\omega_{PP}$ is the frequency separation between the pumps. (not to scale)

For reasons that we discuss later, here we treat the signal (or idler) index q_s (or q_i) as a parameter, where $q_{s/i}$ is defined by :

$$q_{s/i} = \frac{2(\omega_{s/i} - \omega_c)}{\Delta\omega_{PP}}, \tag{2.22}$$

where ω_s (or ω_i) is the frequency of the signal (or idler), $\Delta\omega_{PP}$ is the frequency separation between the two pumps and ω_c is the central frequency chosen to be the average frequency of all the considered waves. Note that since the signal and the idler are located symmetrically with respect to the central frequency, we have $q_i = -q_s$. Also, if we replace the signal (or idler) frequency by the pump frequencies in Equation (2.22), we get $q_P = 1$ (or -1), which are indeed the pump indices.

2.3.2 Approximations

The considered approximations for this analytical model are the same as for the analytical 3-wave model described previously (see Section 2.2). However, here we impose an additional approximation :

- Dispersion terms are kept till the second order, i.e. $\beta^{(n)} = 0$ for $n > 2$.

This approximation will simplify the coupled differential equations for the A_i's considerably as we will see subsequently.

2.3.3 Linear Phase Mismatch

The linear phase mismatch $\Delta\beta_{klmn}$ between four interacting waves at frequencies ω_k, ω_l, ω_m and ω_n is given by :

$$\Delta\beta_{klmn} = \beta(\omega_k) + \beta(\omega_l) - \beta(\omega_m) - \beta(\omega_n), \tag{2.23}$$

where $\beta(\omega_j)$, $(j = k, l, m, n)$ is the propagation constant at frequency ω_j. We can also rewrite it by performing a Taylor series expansion of $\beta(\omega)$ around the central frequency ω_c as :

$$\beta(\omega) = \sum_{n=0}^{\infty} \frac{1}{n!} \left(\frac{d^n\beta}{d\omega^n}\right)_{\omega=\omega_c} (\omega - \omega_c)^n. \tag{2.24}$$

Here we consider $\frac{d^n\beta}{d\omega^n} = \beta^{(n)}$ till $n = 2$ in the Taylor series expansion [76, 157]. Thus considering a second order approximation, we write :

$$\beta(\omega) \approx \beta(\omega_c) + \left(\frac{d\beta}{d\omega}\right)_{\omega_c} (\omega - \omega_c) + \left(\frac{d^2\beta}{d\omega^2}\right)_{\omega_c} \frac{(\omega - \omega_c)^2}{2}. \tag{2.25}$$

Next we calculate $\Delta\beta_{mnkj}$ by using Equation (2.25) in Equation (2.23) as :

$$\begin{aligned} \Delta\beta_{mnkj} &= \beta(\omega_m) + \beta(\omega_n) - \beta(\omega_k) - \beta(\omega_j) \\ &= \left(\frac{d\beta}{d\omega}\right)_{\omega_c} (\omega_m + \omega_n - \omega_k - \omega_j) \\ &+ \frac{1}{2}\left(\frac{d^2\beta}{d\omega^2}\right)_{\omega_c} \left({\omega_m}^2 + {\omega_n}^2 - {\omega_k}^2 - {\omega_j}^2 - 2\omega_c(\omega_m + \omega_n - \omega_k - \omega_j)\right). \end{aligned} \tag{2.26}$$

By imposing the energy conservation condition for the FWM between waves at frequencies ω_m, ω_n, ω_k and ω_j [58], i.e. $\omega_m + \omega_n - \omega_k - \omega_j = 0$, we have :

$$\begin{aligned} \Delta\beta_{mnkj} &= \frac{1}{2}\left(\frac{d^2\beta}{d\omega^2}\right)_{\omega_c} ({\omega_m}^2 + {\omega_n}^2 - {\omega_k}^2 - {\omega_j}^2) \\ &= \frac{\beta^{(2)}(\omega_c)}{2}({\omega_m}^2 + {\omega_n}^2 - {\omega_k}^2 - {\omega_j}^2). \end{aligned} \tag{2.27}$$

To simplify the calculation, we make the following change of variable as in Equation (2.22) :

$$q = \frac{2(\omega - \omega_c)}{\Delta\omega_{PP}}, \tag{2.28}$$

where ω_c is the central frequency, which is chosen to be the average of all the frequencies. $\Delta\omega_{PP}$ is the frequency separation of the two pumps. This variable transformation makes the calculation of $\Delta\beta_{mnkj}$ much easier as now the frequencies are expressed in terms of their relative position with respect to the central frequency ω_c. For example, in a dual pump configuration, with a degenerate signal and idler, the signal frequency becomes the central frequency and $q = 0$ for the signal in such a case.

Now we compute ${q_m}^2 + {q_n}^2 - {q_k}^2 - {q_j}^2$ as :

$$ {q_m}^2 + {q_n}^2 - {q_k}^2 - {q_j}^2 = \frac{{\omega_m}^2 + {\omega_n}^2 - {\omega_k}^2 - {\omega_j}^2 - 2\omega_0(\omega_m + \omega_n - \omega_k - \omega_j)}{\left(\frac{{\Delta\omega_{PP}}^2}{4}\right)}. \quad (2.29) $$

Thus we have :

$$ {\omega_m}^2 + {\omega_n}^2 - {\omega_k}^2 - {\omega_j}^2 = \frac{{\Delta\omega_{PP}}^2}{4}({q_m}^2 + {q_n}^2 - {q_k}^2 - {q_j}^2), \quad (2.30) $$

where we have used the fact that $\omega_m + \omega_n - \omega_k - \omega_j = 0$. Hence we can write :

$$ \Delta\beta_{mnkj} = \frac{\beta^{(2)}(\omega_c){\Delta\omega_{PP}}^2}{8}({q_m}^2 + {q_n}^2 - {q_k}^2 - {q_j}^2) = C({q_m}^2 + {q_n}^2 - {q_k}^2 - {q_j}^2), \quad (2.31) $$

where C is given by :

$$ C = \frac{\beta^{(2)}(\omega_c){\Delta\omega_{PP}}^2}{8} = \frac{\beta^{(2)}(\omega_c)\pi^2 c^2 \Delta\lambda_{PP}^2}{2\left(\lambda_c + \frac{\Delta\lambda_{PP}}{2}\right)^2\left(\lambda_c - \frac{\Delta\lambda_{PP}}{2}\right)^2}. \quad (2.32) $$

Here λ_c is the central wavelength corresponding to the central frequency ω_c and $\Delta\lambda_{PP}$ is the pump-pump wavelength separation.

To illustrate a simple example, we consider the term $\Delta\beta_{1-100}$ which arises in the coupled equations in the analytical 3-wave model for a non-degenerate pump configuration (see Equation (2.7)). Using Equation (2.31) we compute :

$$ \Delta\beta_{1-100} = C\left(1^2 + (-1)^2 - 0^2 - 0^2\right) = 2C. \quad (2.33) $$

Therefore, the linear phase mismatch terms can be evaluated conveniently when we know C[5].

2.3.4 Wave Evolution Equations

Similar to the analytical 3-wave model, using Equation (2.4) we write the evolution equations for A_1, A_{-1}, A_{q_s} and A_{-q_s} (or A_{q_i}) as :

$$ \frac{dA_1}{dz} = i\gamma\left(|A_1|^2 A_1 + 2(|A_{-1}|^2 + |A_{-q_s}|^2 + |A_{q_s}|^2)A_1 + 2A_{-q_s}A_{q_s}{A_{-1}}^* e^{i\Delta\beta_{-q_s q_s -11} z}\right), \quad (2.34) $$

---

[5] The calculation of $\beta^{(2)}$ is required for evaluating C and is shown in Subsection 3.1.6 in Chapter 3.

$$\frac{dA_{-1}}{dz} = i\gamma\Big(|A_{-1}|^2 A_{-1} + 2(|A_1|^2 + |A_{-q_s}|^2 + |A_{q_s}|^2) A_{-1} + 2A_{-q_s} A_{q_s} {A_1}^{*} e^{i\Delta\beta_{-q_s q_s 1 -1} z} \Big), \tag{2.35}$$

$$\frac{dA_{-q_s}}{dz} = i\gamma\Big(|A_{-q_s}|^2 A_{-q_s} + 2(|A_1|^2 + |A_{-1}|^2 + |A_{q_s}|^2) A_{-q_s} + 2A_1 A_{-1} {A_{q_s}}^{*} e^{i\Delta\beta_{1 -1 q_s -q_s} z} \Big), \tag{2.36}$$

$$\frac{dA_{q_s}}{dz} = i\gamma\Big(|A_{q_s}|^2 A_{q_s} + 2(|A_1|^2 + |A_{-1}|^2 + |A_{-q_s}|^2) A_{q_s} + 2A_1 A_{-1} {A_{-q_s}}^{*} e^{i\Delta\beta_{1 -1 -q_s q_s} z} \Big), \tag{2.37}$$

where we have replaced the indices m, n, k and j in the $\Delta\beta_{mnkj}$ terms with 1, -1, q_s and $-q_s$ accordingly. It is important to note here that this set of equations is valid when $|q_s| \neq 3$. That is because when $|q_s| = 3$, we need to consider an extra FWM process that leads to a slight modification of the equations. We will deal with such a special case later while describing the analytical 7-wave model. Also note that $|q_s| = 0$ leads to the equations for a 3-wave model with non-degenerate pump configuration (see Subsection 2.2.5).

Invoking the strong pump approximation, in particular, neglecting the terms that contain less than two pump terms in Equations (2.34)-(2.37), we get :

$$\frac{dA_1}{dz} = i\gamma 3PA_1, \tag{2.38}$$

$$\frac{dA_{-1}}{dz} = i\gamma 3PA_{-1}, \tag{2.39}$$

$$\frac{dA_{q_s}}{dz} = i\gamma\Big(4PA_{q_s} + 2A_1 A_{-1} {A_{-q_s}}^{*} e^{i\Delta\beta_{1 -1 -q_s q_s} z} \Big), \tag{2.40}$$

$$\frac{dA_{-q_s}}{dz} = i\gamma\Big(4PA_{-q_s} + 2A_1 A_{-1} {A_{q_s}}^{*} e^{i\Delta\beta_{1 -1 q_s -q_s} z} \Big), \tag{2.41}$$

where we have replaced the undepleted pump powers $|A_{\pm 1}|^2$ by P.

2.3.5 Solution of Equations

The solutions to Equations (2.38) and (2.39) are given by :

$$A_{\pm 1} = \sqrt{P} e^{i\gamma 3Pz}, \tag{2.42}$$

where we consider the phases of the pumps at the input of the fiber to be 0[6]. Thus injecting this solution into Equations (2.40) and (2.41) we can write a matrix-form equation as :

$$\frac{d}{dz}\begin{bmatrix} A_{q_s} \\ A_{-q_s}{}^* \end{bmatrix} = i\gamma P \begin{bmatrix} 4 & 2e^{i(6\gamma P+2C(1-q_s{}^2))z} \\ -2e^{-i(6\gamma P+2C(1-q_s{}^2))z} & -4 \end{bmatrix} \begin{bmatrix} A_{q_s} \\ A_{-q_s}{}^* \end{bmatrix}, \tag{2.43}$$

where we have used Equation (2.31) to calculate $\Delta\beta_{1-1-q_s q_s}$ and $\Delta\beta_{1-1q_s-q_s}$. The form of Equation (2.43) is the same as used to describe the dynamics of an oscillating pendulum of variable length or that of a child's swing pumped by the squatting and rising motion of the child [45, 158]. We note that the coefficient matrix in Equation (2.43) depends on z with oscillating terms. Thus depending on the phase of this oscillation, A_{q_s} will be either amplified or de-amplified.

In order to get rid of the z-dependence from the coefficient matrix in Equation (2.43), we do the following transformation of variables :

$$A_{\pm q_s} = B_{\pm q_s} e^{i(3\gamma P+C(1-q_s{}^2))z}. \tag{2.44}$$

To simplify the notation, we now denote q_s as q and we will follow this notation henceforth. With the transformed variables $B_{\pm q}$, Equation (2.43) can be rewritten as :

$$\frac{d}{dz}\begin{bmatrix} B_q \\ B_{-q}{}^* \end{bmatrix} = i\gamma P \begin{bmatrix} 1-F_q & 2 \\ -2 & -(1-F_q) \end{bmatrix} \begin{bmatrix} B_q \\ B_{-q}{}^* \end{bmatrix}, \tag{2.45}$$

where F_q is given by :

$$F_q = \frac{C(1-q^2)}{\gamma P}. \tag{2.46}$$

F_q is basically the ratio between the dispersion and nonlinearity of the fiber. We also note from Equation (2.45) that the trace of the coefficient matrix is 0. This means that, after integration along z, the transfer matrix relating the input ($B_q(0)$, $B^*_{-q}(0)$) and output ($B_q(L)$, $B^*_{-q}(L)$) modes (where L is the fiber length) has a unit determinant. This also means that the 2×2 transfer matrix relating the input and output modes is symplectic [159].

One way to solve Equation (2.45) is to note that the equation is of the form $\frac{d\mathbf{B}}{dz} = \mathbf{MB}$ where $\mathbf{M}$ is the coefficient matrix. Therefore the solution can be written as :

$$\mathbf{B} = e^{\mathbf{M}z}. \tag{2.47}$$

Since in this case $\mathbf{M}^2$ is diagonal, i.e. :

$$\mathbf{M}^2 = -\gamma P(3 + 2F_q + F_q{}^2)\mathbf{I}, \tag{2.48}$$

where $\mathbf{I}$ is the identity matrix, all even powers of $\mathbf{M}$ (i.e. $\mathbf{M}^{2n}$) will be proportional

---

[6] This assumption is reasonable because for the case of a PSA, only the relative phase between the pumps and the signal determines the signal gain.

to **I** and all odd powers of **M** (i.e. $\mathbf{M}^{2n+1}$) will be proportional to **M**. Thus the final solution can be expressed as :

$$\mathbf{B} = \cos(\gamma P \mu_q z)\mathbf{I} + i\frac{\sin(\gamma P \mu_q z)}{\mu_q}\mathbf{M}, \tag{2.49}$$

where μ_q is given by :

$$\mu_q = (-3 - 2F_q + F_q^2)^{\frac{1}{2}} \ . \tag{2.50}$$

Although the above approach provides an easy way to solve the system, however we introduce here a slightly more rigorous way to obtain the solution using the traditional eigenvalue method. The eigensystem (eigenvalues : λ_1 and λ_2, eigenvectors : $\mathbf{V_1}$ and $\mathbf{V_2}$) for the coefficient matrix in Equation (2.45) is given by :

$$\lambda_1 = -i\gamma P \ \mu_q, \quad \lambda_2 = i\gamma P \ \mu_q, \tag{2.51}$$

$$\mathbf{V_1} = \begin{bmatrix} \frac{\eta_q + \mu_q}{2} \\ 1 \end{bmatrix}, \ \mathbf{V_2} = \begin{bmatrix} \frac{\eta_q - \mu_q}{2} \\ 1 \end{bmatrix}, \tag{2.52}$$

where μ_q and η_q are given by :

$$\eta_q = -1 + F_q \ , \ \ \mu_q = (-3 - 2F_q + F_q^2)^{\frac{1}{2}} \ . \tag{2.53}$$

Note that for $q = 0$, i.e. the 3-wave model, μ_0 is related to the parametric gain coefficient introduced in the last section (see Equation (2.17)), as:

$$g^2 = -\gamma^2 P^2 {\mu_0}^2. \tag{2.54}$$

The solution of Equation (2.43) is given by :

$$\begin{bmatrix} B_q(z) \\ B_{-q}{}^*(z) \end{bmatrix} = \begin{bmatrix} \cos(\gamma P \mu_q z) - \frac{\eta_q}{\mu_q} i \sin(\gamma P \mu_q z) & \frac{2}{\mu_q} i \sin(\gamma P \mu_q z) \\ -\frac{2}{\mu_q} i \sin(\gamma P \mu_q z) & \cos(\gamma P \mu_q z) + \frac{\eta_q}{\mu_q} i \sin(\gamma P \mu_q z) \end{bmatrix} \begin{bmatrix} B_q(0) \\ B_{-q}{}^*(0) \end{bmatrix}. \tag{2.55}$$

Obtaining the full solution, now we consider a simple case, i.e. $q = 0$ corresponding to the 3-wave model in non-degenerate pump configuration. To visualize the solution, in Fig. 2.5 we plot the maximum signal gain (by scanning the signal input phase) as a function of $\delta\lambda_{ofs}$ i.e. the signal wavelength offset from the zero dispersion wavelength of the fiber and the pump-pump wavelength separation $\Delta\lambda_{PP}$. The considered parameters are : $L = 500$ m, $P = 20$ dBm, $\gamma = 11.3$ W^{-1}km^{-1}, zero dispersion wavelength $\lambda_{ZDW} = 1547.5$ nm and dispersion slope of fiber $D' = 0.017$ ps/nm^2/km. From Fig. 2.5 we see that for small values of $\Delta\lambda_{PP}$ (<10 nm), the gain is large and the profile is flatter. However for larger values of $\Delta\lambda_{PP}$ (>10 nm), the gain decreases and shows oscillating behaviour. Of course, for the system to act as an amplifier, a large signal gain is desirable.

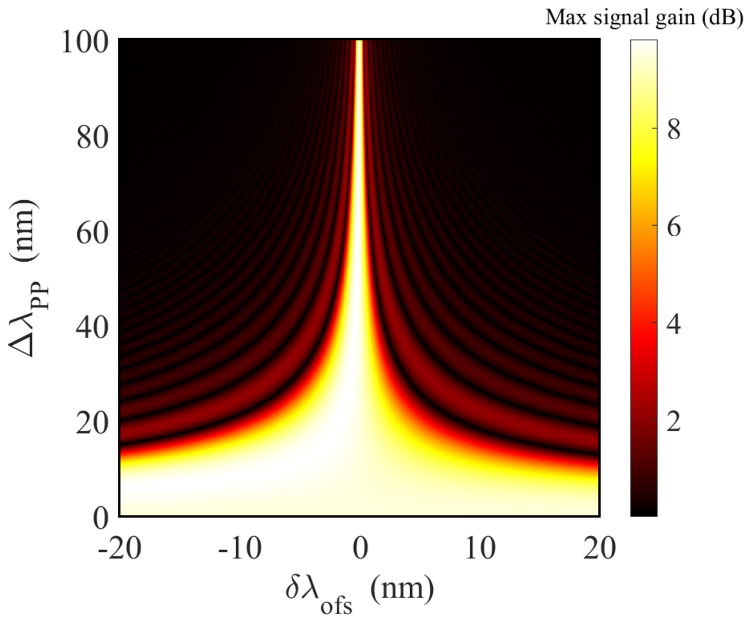

Figure 2.5. Maximum signal gain vs $\delta\lambda_{ofs}$ vs $\Delta\lambda_{PP}$ in a FOPA considering a 3-wave model with non-degenerate pump configuration. $\delta\lambda_{ofs} = \lambda_0 - \lambda_{ZDW}$ where λ_0 is the signal wavelength and λ_{ZDW} is the zero dispersion wavelength. $L = 500$ m, $P = 20$ dBm, $\gamma = 11.3\ \mathrm{W}^{-1}\mathrm{km}^{-1}$, $\lambda_{ZDW} = 1547.5$ nm and dispersion slope of fiber $D^{'} = 0.017\ \mathrm{ps/nm^2/km}$.

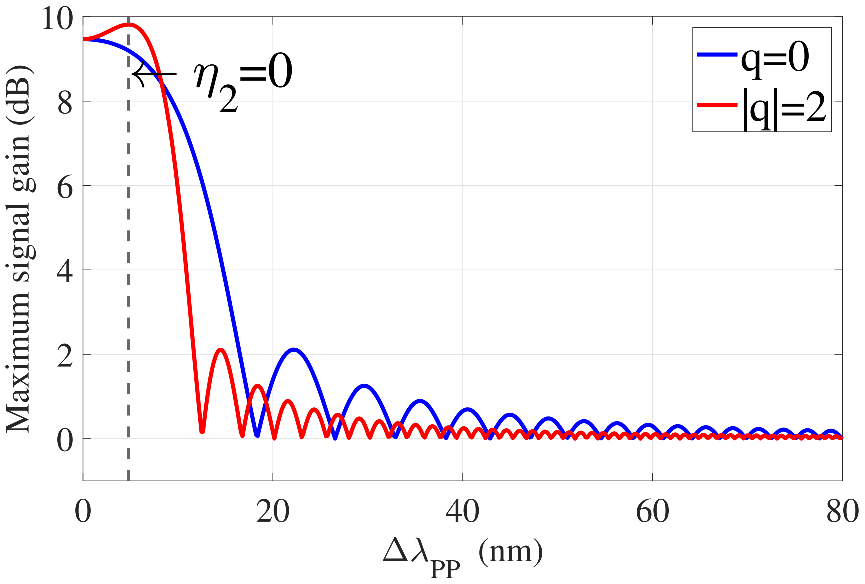

Figure 2.6. Maximum signal gain vs $\Delta\lambda_{PP}$ in a FOPA considering a 4-wave model with non-degenerate pump configuration for $q = 0$ (blue) and $|q| = 2$ (red). Parameters are same as Fig. 2.5.

Subsequently in Fig. 2.6, we compare the maximum PSA gains for $q = 0$ and $|q| = 2$ as a function of $\Delta\lambda_{PP}$. From Fig. 2.6 we see that unlike the flatter gain spectrum for the $q = 0$ case, when $|q| = 2$, the spectrum has a bulge near $\Delta\lambda_{PP} = 5$ nm. In general, this peak appears where $\eta_q = -1 + \frac{C(1-q^2)}{\gamma P} = 0$ ($\eta_2 = 0$ here). In the anomalous dispersion region (where C is negative), this is possible only when $|q| > 1$. Physically, this peak appears due to the efficient FWM process that leads to conversion of two pump photons into a signal and idler photon. Thus when the signal is located between the two pumps ($|q| < 1$), the gain spectrum is flatter compared to the bulged spectrum when the signal is outside the two pumps ($|q| > 1$).

2.3.6 Stability of Solution

The stability of the solutions can be related to the trace of the transfer matrix (denoted as $\mathbf{T}$) in Equation (2.55). When $|Tr(\mathbf{T})| > 2$ the solution is unstable or hyperbolic and when $|Tr(\mathbf{T})| < 2$ the solution is stable or oscillatory [159]. In our case, this means when μ_q is real, the solution is stable and when it is imaginary, the solution is unstable. In the stable solution regime, the modes oscillate at a frequency $\gamma P \mu_q$. However we should note that it is a very slow oscillation often not completing even a half cycle for $\gamma PL < 0.5$. In the unstable regime the modes grow exponentially.

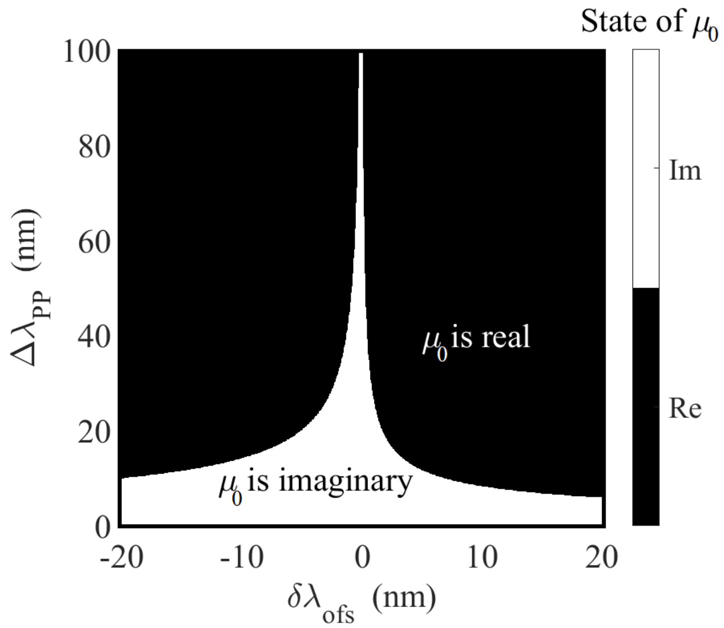

Figure 2.7. State of μ_0 (real (black) or imaginary (white)) vs $\delta\lambda_{ofs}$ vs $\Delta\lambda_{PP}$. Parameters are same as in Fig. 2.5.

μ_q depends on the dispersion, nonlinearity of the fiber and the wavelength allocation of the system and therefore the stability of the solution too. In Fig. 2.7 we plot the state (real or imaginary) of μ_0 i.e. $q = 0$. The utilized parameters are the same as in Fig. 2.5. Fig. 2.7 bears a striking similarity with Fig 2.5. We see from Fig. 2.7 that the region where μ_0 is imaginary, or the solution is unstable, shows a large maximum gain for the signal in Fig 2.5. Similarly, the region where μ_0 is real, or the solution is stable, shows a smaller maximum gain for the signal in Fig 2.5.

For the more general case (i.e. not considering $q = 0$), we find from Equations (2.46) and (2.53) that μ_q is imaginary when :

$$F_0 = \frac{C}{\gamma P} \begin{cases} \in \left(-\frac{1}{1-q^2}, \frac{3}{1-q^2}\right) & \text{when } q < 1, \\ \in \left(\frac{3}{1-q^2}, -\frac{1}{1-q^2}\right) & \text{when } q > 1. \end{cases} \tag{2.56}$$

In Fig. 2.8 we show the region (blue shaded) in the F_0-q plane where ${\mu_q}^2 < 2$, or

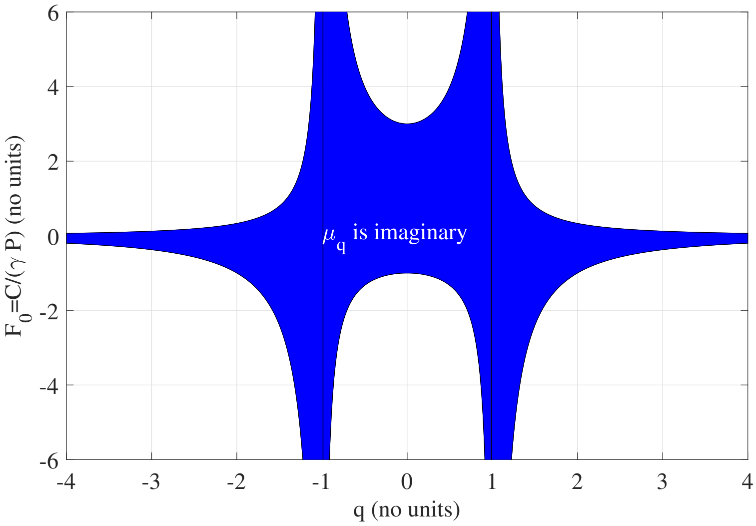

Figure 2.8. Plot showing the region in the F_0-q plane where ${\mu_q}^2 < 2$, or μ_q is imaginary (shaded blue region).

μ_q is imaginary. Therefore, the signal shows a hyperbolic solution in this region. Note that near the pumps ($|q| = 1$), the bandwidth of hyperbolic signal solution is quite large compared to when the signal is away from the pumps. This provides us an estimate of an operating bandwidth where the nonlinear fiber can efficiently act as an amplifier with a large gain. Although the analytical 4-wave model has been investigated extensively [56], for example Tanemure *et al.* provided a similar analysis however in terms of eigenmodes of the system [160], the system stability analysis with respect to the frequency allocation of the waves is original to the best of our knowledge.

2.3.7 Limitations

The analytical 4-wave model does not take into account the higher order waves that are generated due to FWM processes in the FOPA. These higher order waves can be amplified significantly through the FOPA and often play an important role in influencing the signal gain [91].

The solution of the analytical 4-wave model was obtained by considering the non-pump depletion approximation. However, when the length of the FOPA is large, this approximation breaks down. Although the differential equations, i.e. Equations (2.34)-(2.37) are still solvable including pump depletion into the model, but the solutions are expressed in terms of Jacobian elliptic functions [161, 162] and are complicated to deal with. Also while taking pump depletion into account, we can only solve for the powers of the different waves and their associated phases cannot be obtained [56].

In this model we neglected the higher order terms ($n > 2$) in the Taylor series expansion of $\beta(\omega)$ in our calculation. In certain cases, for example when the wavelength of the considered waves are close (within a few nanometers) to the zero dispersion wavelength, higher order treatment is solicited for accurate results [58].

A special case of the developed model arises when $|q| = 3$ (or $|q_s| = 3$) i.e. the pump-pump wavelength separation is equal to the pump-signal wavelength separation. This specific situation was not dealt with in this discussion and it will be addressed later in the analytical 7-wave model (see Subsubsection 2.4.10).

2.4 Analytical 7-Wave Model

When a signal and two strong pumps are launched in a FOPA, due to cascaded FWM processes multiple sidebands are generated that deteriorate the signal gain predicted by the analytical 3-wave model. Thus consideration of multiple waves in the model becomes necessary [91]. In order to investigate more accurately such a situation, we derive an analytical 7-wave model, with a configuration as depicted in Fig. 2.9.

In the scientific literature the n-wave models with $n > 4$ have been studied mostly in the context of PSA noise figure investigation [76, 157]. However non-existence of a full analytical solution of the n-wave model provides scope for further investigation [45].

McKinstrie *et al.* [76] and Marhic *et al.* [163] analyzed the 6-wave model analytically, however for some limited cases. Their analysis does not incorporate the dependence of signal gain on the fiber dispersion. Vedadi *et al.* [164] also analyzed the 6-wave model, however did not provide a full analytical solution considering arbitrary initial conditions for the different waves. Tanemura studied the 6-wave model in terms of the system eignemodes [160]. We should also mention that the system of equations for the 7-wave system turns out to be different compared to the 6-wave system due to the symmetry of the degenerate signal and idler. Numerical approaches were also used to analyze the n-wave model for $n > 6$ [91, 92, 165, 166]. More recently Inoue developed a semi-analytical model to solve for the two pumps and higher order pumps (HOP's) numerically while incorporating their effects on the signal and higher order idlers (HOI's) analytically [157]. In our group, Bouasria *et al.* computed the noise figure within the 7-wave model framework but using a semi-quantum approach due to the absence of a full analytical solution for the classical system with seven waves [166].

Although an analytical approach is often constrained by approximations, nevertheless, an analytical description will help us gain insight into the dynamics of the FOPA and can be helpful in calculating the noise figure as done in Refs. [76, 157, 166]. Therefore, in this section we develop an analytical 7-wave model taking into account the effect of fiber dispersion up to second order. Such an approach is original to the best of our knowledge.

2.4.1 Configuration

The 7-wave model is mostly employed considering a dual pump configuration with degenerate signal and idler [91, 92]. The amplitudes of the two pumps are labelled A_1 and A_{-1}, the signal is labelled A_0, the two so-called higher order idlers (HOI's) are labelled A_2 and A_{-2} and the two so-called higher order pumps (HOP's) are labelled A_3 and A_{-3} (see Fig. 2.9).

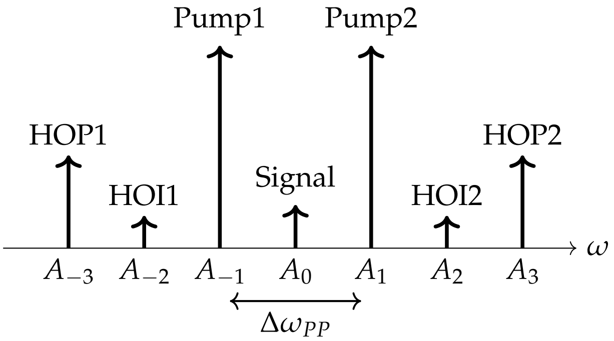

Figure 2.9. Configuration of a dual pump FOPA with degenerate signal and idler and non-degenerate pumps. ω is frequency. The two pumps are labelled A_1 and A_{-1}, the signal is labelled A_0, two higher order idlers (HOI) are labelled A_2 and A_{-2} and two higher order pumps (HOP) are labelled A_3 and A_{-3}. The height of the arrows represent intensity. $\Delta\omega_{PP}$ is the frequency difference between the pumps. (not to scale)

2.4.2 Approximations

The approximations for this model are exactly the same as for the analytical 4-wave model, which are listed in Subsections 2.2.2 and 2.3.2. We just clarify the fact, that the strong pump approximation here means that that pumps are much stronger than all the other waves, i.e. signal, HOI's and the HOP's throughout the length of the fiber.

2.4.3 Linear Phase Mismatch

The linear phase mismatch $\Delta\beta_{klmn}$ between four interacting waves at frequencies ω_k, ω_l, ω_m and ω_n was already derived in the discussion of the analytical 4-wave model and is given by (see Subsection 2.3.3) :

$$\Delta\beta_{mnkj} = \frac{\beta^{(2)}(\omega_c)\Delta\omega_{PP}{}^2}{8}({q_m}^2 + {q_n}^2 - {q_k}^2 - {q_j}^2) = C({q_m}^2 + {q_n}^2 - {q_k}^2 - {q_j}^2). \quad (2.57)$$

2.4.3.1 Validity of Second Order Approximation

In Subsection 2.3.3 the linear phase mismatch terms were calculated considering a second order approximation. In this subsection we investigate the validity of that second order approximation of $\beta(\omega)$ as shown in Equation (2.25) to calculate $\Delta\beta_{klmn}$'s. To do so, we plot in Fig 2.10 several $\Delta\beta_{klmn}$'s ($\Delta\beta_{1-100}$ (in red), $\Delta\beta_{1-2-10}$

(in blue), $\Delta\beta_{-101-2}$ (in magenta) and $\Delta\beta_{10-12}$ (in green)) considering second (solid line) and fourth (dotted line) order approximation[7] of the Taylor series expansion of $\beta(\omega)$, as a function of $\Delta\lambda_{PP}$. We considered a non-degenerate pump configuration with the central wavelength λ_c at the signal wavelength $\lambda_0 = 1557.5$ nm. A standard HNLF was considered with a zero dispersion wavelength $\lambda_{ZDW} = 1547.5$ nm and a dispersion slope $D' = 0.017$ ps.nm^{-2}.km^{-1}. From Fig 2.10 we see that for

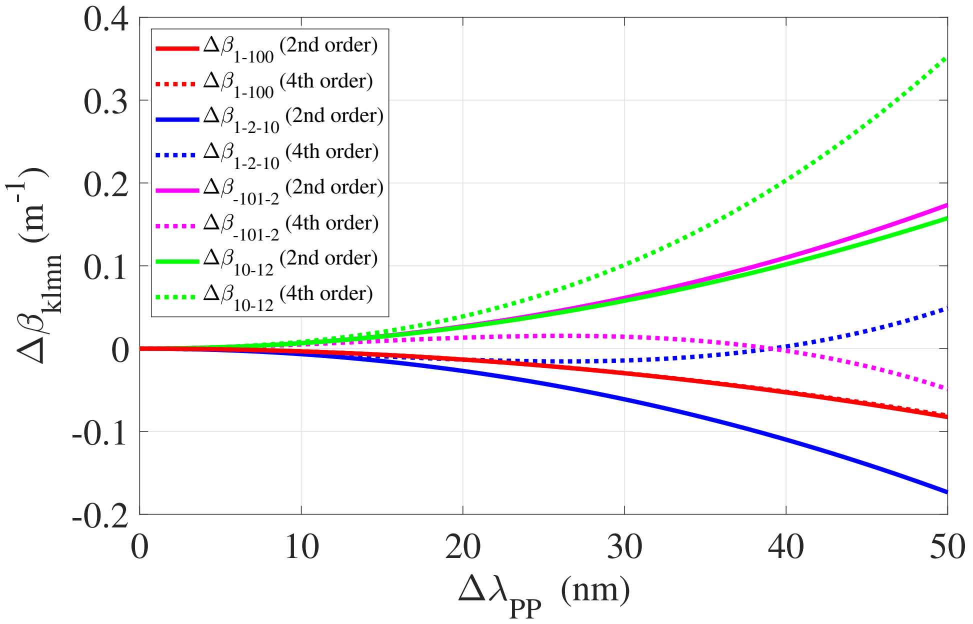

Figure 2.10. Plot of $\Delta\beta_{klmn}$'s ($\Delta\beta_{1-100}$ (in red), $\Delta\beta_{1-2-10}$ (in blue), $\Delta\beta_{-101-2}$ (in magenta) and $\Delta\beta_{10-12}$ (in green)) considering second (solid line) and fourth (dotted line) order approximation of the Taylor series expansion of $\beta(\omega)$, as a function of $\Delta\lambda_{PP}$.

small values of $\Delta\lambda_{PP}$ (<5 nm), all the different curves are clustered around 0. However for larger values of $\Delta\lambda_{PP}$ (>10 nm), all the curves branch out and the values of $\Delta\lambda_{PP}$ from the second order approximation deviate from that of the fourth order approximation. We also note here, that the deviation between the second and fourth order approaches is negligible for $\Delta\beta_{1-100}$ which corresponds to the FWM process considered in the analytical 3-wave model.

2.4.4 Wave Evolution Equations

The evolution of the amplitudes of the seven waves along the fiber is described by a set of seven coupled equations [58, 138] (see Equation (2.4)). For example, the equation of evolution of the signal considering all the SPM, XPM and FWM terms,

---

[7] Liu considered a fifth order approach for $\Delta\lambda_{PP} < 50$ nm [167]. However Marhic *et al.* in Ref. [140] considered a fourth order approach for a similar situation.

is given by :

$$\begin{aligned}\frac{dA_0}{dz} = i\gamma\Big\{ &[|A_0|^2 A_0 + 2\sum_{j=-3,j\neq 0}^{3} |A_j|^2] A_0 + A_{-1}^2 A_{-2}^* e^{i\Delta\beta_{-1-1-20}} + A_1^2 A_2^* e^{i\Delta\beta_{1120}} \\ &+ 2A_{-1}A_1A_0^* e^{i\Delta\beta_{-1100}} + 2A_{-1}A_3A_2^* e^{i\Delta\beta_{-1320}} + 2A_{-1}A_{-2}A_{-3}^* e^{i\Delta\beta_{-1-2-30}} + 2A_{-1}A_2A_1^* e^{i\Delta\beta_{-1210}} \\ &+ 2A_1A_{-3}A_{-2}^* e^{i\Delta\beta_{1-3-20}} + 2A_1A_{-2}A_{-1}^* e^{i\Delta\beta_{1-2-10}} + 2A_1A_2A_3^* e^{i\Delta\beta_{1230}} + 2A_{-3}A_2A_{-1}^* e^{i\Delta\beta_{-32-10}} \\ &+ 2A_{-3}A_3A_0^* e^{i\Delta\beta_{-3300}} + 2A_{-2}A_2A_0^* e^{i\Delta\beta_{-2200}} + 2A_3A_{-2}A_1^* e^{i\Delta\beta_{3-210}} \Big\}. \end{aligned} \tag{2.58}$$

A complete set of all the coupled differential equations for the seven waves is provided in Appendix B and can be found in Refs. [89, 168].

In the special case where the pump powers remain much higher than the other waves all along the fiber, or in other words with the strong pump approximation, many terms of Equation (2.58) can be neglected as they do not contain the pump terms. In such a case, we retrieve a simpler set of differential equations governing the evolution of the waves. Thus we can write down the equations of evolution of the slowly varying amplitudes of the signal (A_0), the HOI's (A_2 and A_{-2}) and the HOP's (A_3 and A_{-3}) as :

$$\begin{aligned}\frac{dA_0}{dz} = i\gamma\Big(&2|A_1|^2 A_0 + 2|A_{-1}|^2 A_0 + 2A_1A_{-1}{A_0}^* e^{i\Delta\beta_{1-100z}} + 2A_1A_{-2}{A_{-1}}^* e^{i\Delta\beta_{1-2-10z}} \\ &+ {A_{-1}}^2{A_{-2}}^* e^{i\Delta\beta_{-1-1-20z}} + 2A_{-1}A_2{A_1}^* e^{i\Delta\beta_{-1210z}} + {A_1}^2{A_2}^* e^{i\Delta\beta_{1120z}}\Big),\end{aligned} \tag{2.59}$$

$$\begin{aligned}\frac{dA_{-2}}{dz} = i\gamma\Big(&2|A_{-1}|^2 A_{-2} + 2|A_1|^2 A_{-2} + 2A_{-1}A_0{A_1}^* e^{i\Delta\beta_{-101-2z}} \\ &+ {A_{-1}}^2{A_0}^* e^{i\Delta\beta_{-1-10-2z}} + 2A_{-1}A_1{A_2}^* e^{i\Delta\beta_{-112-2z}}\Big),\end{aligned} \tag{2.60}$$

$$\begin{aligned}\frac{dA_2}{dz} = i\gamma\Big(&2|A_{-1}|^2 A_2 + 2|A_1|^2 A_2 + 2A_1A_0{A_{-1}}^* e^{i\Delta\beta_{10-12z}} \\ &+ {A_1}^2{A_0}^* e^{i\Delta\beta_{1102z}} + 2A_{-1}A_1{A_{-2}}^* e^{i\Delta\beta_{-11-22z}}\Big),\end{aligned} \tag{2.61}$$

$$\frac{dA_{-3}}{dz} = i\gamma\Big(2|A_{-1}|^2 A_{-3} + 2|A_1|^2 A_{-3} + {A_{-1}}^2{A_1}^* e^{i\Delta\beta_{-1-11-3z}} + 2A_{-1}A_1{A_3}^* e^{i\Delta\beta_{-113-3z}}\Big), \tag{2.62}$$

$$\frac{dA_3}{dz} = i\gamma\Big(2|A_{-1}|^2 A_3 + 2|A_1|^2 A_3 + {A_1}^2{A_{-1}}^* e^{i\Delta\beta_{11-13z}} + 2A_{-1}A_1{A_{-3}}^* e^{i\Delta\beta_{-11-33z}}\Big). \tag{2.63}$$

where we have kept only those terms which contain at least two pump waves. We have not provided the equations for the pumps here, as we already solved them in the analytical 4-wave model. Thus we directly write down the solution for the pumps (A_1 and A_{-1}) as (see Equation (2.42)) :

$$A_{\pm 1} = \sqrt{P} e^{i\gamma 3Pz}. \tag{2.64}$$

We make a note here that although for the analytical 7-wave model, the pump equations get slightly modified compared to that of the analytical 4-wave model, we still retrieve the same solution after neglecting terms in the differential equation that contain less than three pump terms.

2.4.5 Subsystems of the Analytical 7-Wave Model

With the strong pump approximation as described before, the 7-wave model can be broken down into three subsystems. They are three 4-wave models with different values of q_s, i.e. 1. $q_s = 0$ (subsystem 1, Fig. 2.11 (a)), 2. $|q_s| = 2$ (subsystem 2, Fig. 2.11 (b)) and 3. $|q_s| = 3$ (subsystem 3, Fig. 2.11 (c)). All the three subsystems share the two common pumps.

It is important to note from Equations (2.59)-(2.63) that the HOP evolution equations get decoupled from the signal and HOI evolution equations. Therefore we can solve subsystems 1 and 2 (signal and HOI's) separately from subsystem 3 (HOP's).

For convenience, we provide a table (Table 2.1) of the different approximations and initial conditions that will consider for different cases while performing the calculations.

Table of Cases for Calculation

Calculation	**Case**	**$\Delta\beta_{klm}$**	**Initial condition**
Signal and HOI equations	Case 1	$\Delta\beta_{klm} = 0$	$A_2(0) = A_{-2}(0) = 0$
	Case 2	$\Delta\beta_{klm} \neq 0$	$A_2(0) = A_{-2}(0) \neq 0$
	Case 3	$\Delta\beta_{klm} \neq 0$	$A_2(0) = A_{-2}(0) = 0$
	Case 4	$\Delta\beta_{klm} \neq 0$	$A_2(0) \neq A_{-2}(0)$
Input signal phase for maximum signal gain	Case 1	$\Delta\beta_{klm} = 0$	$A_2(0) = A_{-2}(0) = 0$
	Case 2	$\Delta\beta_{klm} \neq 0$	$A_2(0) = A_{-2}(0) = 0$
HOP equations	Case 1	$\Delta\beta_{klm} = 0$	$A_3(0) = A_{-3}(0)$=0
	Case 2	$\Delta\beta_{klm} \neq 0$	$A_3(0) \neq A_{-3}(0)$
	Case 3	$\Delta\beta_{klm} \neq 0$	$A_3(0) = A_{-3}(0) \neq 0$
	Case 4	$\Delta\beta_{klm} \neq 0$	$A_3(0) = A_{-3}(0) = 0$

Table 2.1. Table of approximations and initial conditions considered for the respective calculations.

2.4.6 Coupled Signal and HOI Evolution (Subsystems 1 and 2)

Using Equation (2.31), we calculate all the $\Delta\beta_{klmn}$'s in Equations (2.59), (2.60) and (2.61) as :

$$\Delta\beta_{klmn} = C({q_k}^2 + {q_l}^2 - {q_m}^2 - {q_n}^2), \tag{2.65}$$

where C is given by Equation (2.32). Note that for the 7-wave model, for the signal $q = 0$, for the HOI's $q = \pm 2$ and for the HOP's $q = \pm 3$. Thus we list here the

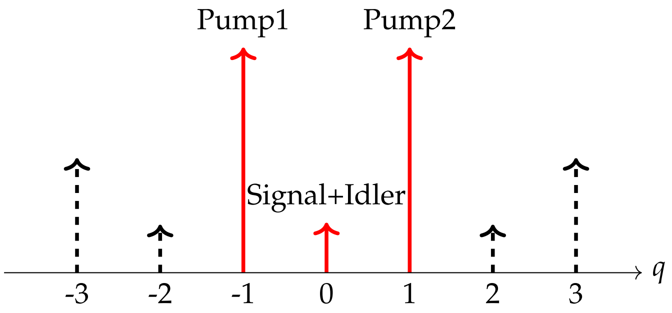

(a) Subsystem 1 ($q_s = 0$).

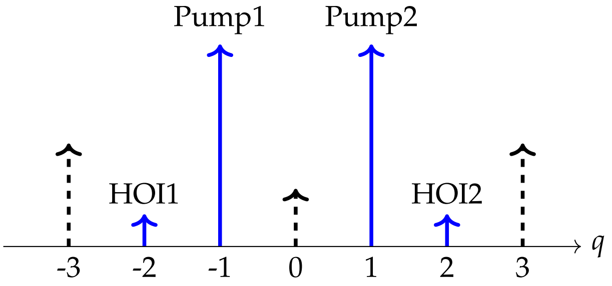

(b) Subsystem 2 ($|q_s| = 2$).

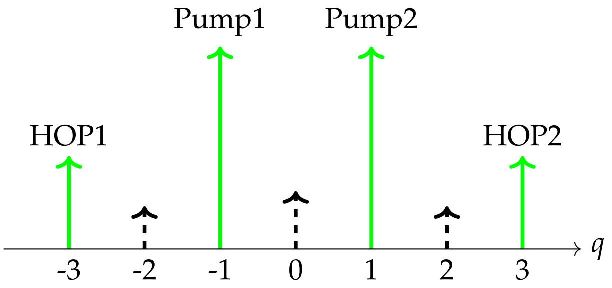

(c) Subsystem 3 ($|q_s| = 3$).

Figure 2.11. (a) Subsystem 1 ($|q_s| = 0$ in a 4-wave model) in red, (b) subsystem 2 ($|q_s| = 2$ in a 4-wave model) in blue and (c) subsystem 3 ($|q_s| = 3$ in a 4-wave model) in green for describing the 7-wave model. Dashed arrows represent the waves that are not in the subsystem. (not to scale)

different $\Delta\beta_{klmn}$'s as :

$$\begin{gathered}\Delta\beta_{1-100} = 2C, \quad \Delta\beta_{1-210} = 4C, \quad \Delta\beta_{-1-1-20} = -2C, \quad \Delta\beta_{-1210} = 4C, \quad \Delta\beta_{1120} = -2C, \\ \Delta\beta_{-101-2} = -4C, \quad \Delta\beta_{-1-10-2} = -2C, \quad \Delta\beta_{-112-2} = -6C, \\ \Delta\beta_{10-12} = -4C, \quad \Delta\beta_{1102} = -2C, \quad \Delta\beta_{-11-22} = -6C.\end{gathered} \tag{2.66}$$

Plugging in all the $\Delta\beta_{klmn}$'s in Equations (2.59), (2.60) and (2.61), and using $|A_1|^2 = |A_{-1}|^2 = P$ and $A_1 = A_{-1} = \sqrt{P}e^{i3\gamma Pz}$, we can write Equations (2.59), (2.60) and

(2.61) in a matrix form as :

$$\frac{d}{dz}\begin{bmatrix} A_0 \\ {A_0}^* \\ A_2 \\ {A_2}^* \\ A_{-2} \\ {A_{-2}}^* \end{bmatrix} = i\gamma P \begin{bmatrix} 4 & 2e^{i(6\gamma P+2C)z} & 2e^{i4Cz} & e^{i(6\gamma P-2C)z} & 2e^{i4Cz} & e^{i(6\gamma P-2C)} \\ -2e^{-i(6\gamma P+2C)z} & -4 & -e^{-i(6\gamma P-2C)z} & -2e^{-i4Cz} & -e^{-i(6\gamma P-2C)z} & -2e^{-i4Cz} \\ 2e^{-i4Cz} & e^{i(6\gamma P-2C)z} & 4 & 0 & 0 & 2e^{i(6\gamma P-6C)z} \\ -e^{-i(6\gamma P-2C)z} & -2e^{i4Cz} & 0 & -4 & -2e^{-i(6\gamma P-6C)z} & 0 \\ 2e^{-i4Cz} & e^{i(6\gamma P-2C)z} & 0 & 2e^{i(6\gamma P-6C)z} & 4 & 0 \\ -e^{-i(6\gamma P-2C)z} & -2e^{i4Cz} & -2e^{-i(6\gamma P-6C)z} & 0 & 0 & -4 \end{bmatrix} \begin{bmatrix} A_0 \\ {A_0}^* \\ A_2 \\ {A_2}^* \\ A_{-2} \\ {A_{-2}}^* \end{bmatrix}. \tag{2.67}$$

This is an equation of the form $\frac{d\mathbf{A}}{dz} = \mathbf{M}(z)\mathbf{A}$, where $\mathbf{M}$ represents a coefficient matrix. We note here that $\mathbf{M}$ depends on z. However, as we show later, it is possible to get rid of the z-dependence of $\mathbf{M}$ by performing an appropriate transformation of variables. Let us call the coefficient matrix after the variable transformation $\mathbf{M}^{'}$. Now, for simplicity let us assume $\mathbf{M}^{'}$ is a linear function of C[8]. We also see that $\mathbf{M}^{'}$ for the set of differential equations represented in Equation (2.67) is 6×6 in dimension. Thus finding an expression for the eigenvalues of $\mathbf{M}^{'}$ is equivalent to finding the roots of a 6th degree polynomial in C. But a general closed form expression for the roots of a polynomial with degree more than four does not exist [169]. Hence we cannot apply the eigenvalue method [170] to solve the set of coupled linear differential equations represented in Equation (2.67) without reducing the dimension of the transfer matrix or making some approximation.

- **Case 1 : $\Delta\beta_{klmn} = 0$, $A_2(0) = A_{-2}(0) = 0$:**

  Often in the case of PSA based microwave photonic links, the frequency separation of the pumps and the signal is small (~ GHz) [118, 124, 125, 171]. For such cases, using Equation (2.31) we can make the approximation $C \approx 0$ and thus $\Delta\beta_{klmn} \approx 0$ [76]. Hence we arrive at a simpler form of Equation (2.67) as :

$$\frac{d}{dz}\begin{bmatrix} A_0 \\ {A_0}^* \\ A_2 \\ {A_2}^* \\ A_{-2} \\ {A_{-2}}^* \end{bmatrix} = i\gamma P \begin{bmatrix} 4 & 2e^{i6\gamma Pz} & 2 & e^{i6\gamma Pz} & 2 & e^{i6\gamma Pz} \\ -2e^{-i6\gamma Pz} & -4 & -e^{-i6\gamma Pz} & -2 & -e^{-i6\gamma Pz} & -2 \\ 2 & e^{i6\gamma Pz} & 4 & 0 & 0 & 2e^{i6\gamma Pz} \\ -e^{-i6\gamma Pz} & -2 & 0 & -4 & -2e^{-i6\gamma Pz} & 0 \\ 2 & e^{i6\gamma Pz} & 0 & 2e^{i6\gamma Pz} & 4 & 0 \\ -e^{-i6\gamma Pz} & -2 & -2e^{-i6\gamma Pz} & 0 & 0 & -4 \end{bmatrix} \begin{bmatrix} A_0 \\ {A_0}^* \\ A_2 \\ {A_2}^* \\ A_{-2} \\ {A_{-2}}^* \end{bmatrix}. \tag{2.68}$$

  In order to get rid of the exponential terms from Equation (2.68), we perform a transformation of variables as done for the analytical 4-wave model (see Equation (2.44) with $C = 0$)[9] :

$$A_j = B_j e^{i3\gamma Pz}, \tag{2.69}$$

---

[8] This means all the elements of $\mathbf{M}^{'}$ are linear in C which we show later in this subsection.

[9] We should note here that the method shown to solve the equations for the analytical 3-wave model in Appendix A becomes complicated to deal with in this case as now we have a large number of terms on the right hand side of the coupled equations.

where $j = 0, 2, -2$. Thus we have :

$$\frac{d}{dz}\begin{bmatrix} B_0 \\ B_0{}^* \\ B_2 \\ B_2{}^* \\ B_{-2} \\ B_{-2}{}^* \end{bmatrix} = i\gamma P \begin{bmatrix} 1 & 2 & 2 & 1 & 2 & 1 \\ -2 & -1 & -1 & -2 & -1 & -2 \\ 2 & 1 & 1 & 0 & 0 & 2 \\ -1 & -2 & 0 & -1 & -2 & 0 \\ 2 & 1 & 0 & 2 & 1 & 0 \\ -1 & -2 & -2 & 0 & 0 & -1 \end{bmatrix} \begin{bmatrix} B_0 \\ B_0{}^* \\ B_2 \\ B_2{}^* \\ B_{-2} \\ B_{-2}{}^* \end{bmatrix}. \tag{2.70}$$

We can write an analytical solution for this coupled set of differential equations as :

$$\begin{aligned} B_0(z) = {} & a_0\left(\cos(\theta_0)\cos(\sqrt{3}\gamma Pz) + \frac{\sin(\theta_0)}{\sqrt{3}}\sin(\sqrt{3}\gamma Pz)\right) \\ & + ia_0\left(\sin(\theta_0)\cos(\sqrt{3}\gamma Pz) + \sqrt{3}\cos(\theta_0)\sin(\sqrt{3}\gamma Pz)\right), \end{aligned} \tag{2.71}$$

$$B_2(z) = B_{-2}(z) = a_0\left(-\frac{\sin(\theta_0)}{\sqrt{3}}\sin(\sqrt{3}\gamma Pz) + i\sqrt{3}\cos(\theta_0)\sin(\sqrt{3}\gamma Pz)\right), \tag{2.72}$$

where the initial conditions for A_0, A_2 and A_{-2} are given by :

$$A_0(z=0) = a_0 e^{i\theta_0}, A_2(z=0) = A_{-2}(z=0) = 0. \tag{2.73}$$

Also we write the solution for the power of the signal $P_0 = |A_0|^2$ and HOI's $P_{-2} = |A_{-2}|^2$, $P_2 = |A_2|^2$ as :

$$\begin{aligned} P_0(z) = {} & a_0{}^2\Bigg[\cos^2(\sqrt{3}\gamma Pz) + \frac{\sin^2(\sqrt{3}\gamma Pz)}{3}\left(1 + 8\cos^2(\theta_0)\right) \\ & + \frac{4}{\sqrt{3}}\cos(\sqrt{3}\gamma Pz)\sin(\sqrt{3}\gamma Pz)\sin(2\theta_0)\Bigg], \end{aligned} \tag{2.74}$$

$$P_2(z) = P_{-2}(z) = \frac{a_0{}^2}{3}\sin^2(\sqrt{3}\gamma Pz)\left(1 + 8\cos^2(\theta_0)\right). \tag{2.75}$$

- **Case 2 : $\Delta\beta_{klmn} \neq 0$, $A_2(0) = A_{-2}(0) \neq 0$:**

In the case where $\Delta\beta_{klmn}$'s are non-negligible, we can make a different assumption to solve Equation (2.67). We note here that Equations (2.60) and (2.61) are basically the same differential equation with the indices 2 and -2 exchanged. Hence by symmetry we can say that A_2 and A_{-2} will have the same solutions provided they have the same initial conditions. Thus for the case of same initial conditions of A_2 and A_{-2} we can replace A_2 in Equation (2.60) with A_{-2}. Also, using $|A_1|^2 = |A_{-1}|^2 = P$ and $A_1 = A_{-1} = \sqrt{P}e^{i3\gamma Pz}$, we can write

Equation (2.59) and (2.60) in a matrix form as :

$$\frac{d}{dz}\begin{bmatrix} A_0 \\ {A_0}^* \\ A_{-2} \\ {A_{-2}}^* \end{bmatrix} = i\gamma P \begin{bmatrix} 4 & 2e^{i(6\gamma P+2C)z} & 4e^{i4Cz} & 2e^{i(6\gamma P-2C)z} \\ -2e^{-i(6\gamma P+2C)z} & -4 & -2e^{-i(6\gamma P-2C)z} & -4e^{-i4Cz} \\ 2e^{-i4Cz} & e^{i(6\gamma P-2C)z} & 4 & 2e^{i(6\gamma P-6C)z} \\ -e^{-i(6\gamma P-2C)z} & -2e^{i4Cz} & -2e^{-i(6\gamma P-6C)z} & -4 \end{bmatrix} \begin{bmatrix} A_0 \\ {A_0}^* \\ A_{-2} \\ {A_{-2}}^* \end{bmatrix}. \tag{2.76}$$

In order to remove the exponentials from Equation (2.76) we do the following transformation of variables (see Equation (2.44) with $q = 0$ and $q = -2$) :

$$\begin{aligned} A_0 &= B_0 e^{i(3\gamma P+C)z}, \\ A_{-2} &= B_{-2} e^{i(3\gamma P-3C)z}. \end{aligned} \tag{2.77}$$

Hence we get :

$$\frac{d}{dz}\begin{bmatrix} B_0 \\ {B_0}^* \\ B_{-2} \\ {B_{-2}}^* \end{bmatrix} = i\gamma P \begin{bmatrix} 1-F_0 & 2 & 4 & 2 \\ -2 & -(1-F_0) & -2 & -4 \\ 2 & 1 & 1-F_2 & 2 \\ -1 & -2 & -2 & -(1-F_2) \end{bmatrix} \begin{bmatrix} B_0 \\ {B_0}^* \\ B_{-2} \\ {B_{-2}}^* \end{bmatrix}, \tag{2.78}$$

where F_q is given by (see Equation (2.46)) :

$$F_q = \frac{C(1-q^2)}{\gamma P}, \tag{2.79}$$

where $q = 0, 2$. Equation (2.78) is a coupled linear differential equation of the form :

$$\frac{d\mathbf{B}}{dz} = \mathbf{M}'\mathbf{B},$$

where $\mathbf{M}'$ is the coefficient matrix given by :

$$\mathbf{M}' = i\gamma P \begin{bmatrix} 1-F_0 & 2 & 4 & 2 \\ -2 & -(1-F_0) & -2 & -4 \\ 2 & 1 & 1-F_2 & 2 \\ -1 & -2 & -2 & -(1-F_2) \end{bmatrix}. \tag{2.80}$$

From Equation (2.78) we can say that subsystem 1 and 2 are coupled through the coefficient matrix $\mathbf{M}'$. We can describe the coupling by breaking the coefficient matrix into four 2×2 block matrices $\mathbf{M_{11}}$, $\mathbf{M_{12}}$, $\mathbf{M_{21}}$, and $\mathbf{M_{22}}$ given as :

$$\begin{aligned} \mathbf{M_{11}} &= i\gamma P \begin{bmatrix} 1-F_0 & 2 \\ -2 & -(1-F_0) \end{bmatrix}, \quad \mathbf{M_{12}} = i\gamma P2 \begin{bmatrix} 2 & 1 \\ -1 & -2 \end{bmatrix}, \\ \mathbf{M_{21}} &= i\gamma P \begin{bmatrix} 2 & 1 \\ -1 & -2 \end{bmatrix}, \quad \mathbf{M_{22}} = i\gamma P \begin{bmatrix} 1-F_2 & 2 \\ -2 & -(1-F_2) \end{bmatrix}. \end{aligned} \tag{2.81}$$

The diagonal blocks $\mathbf{M_{11}}$ and $\mathbf{M_{22}}$ are the coefficient matrices for a 4-wave model with $q = 0$ and $|q| = 2$ respectively (see Equation (2.45)). On the other hand, off-diagonal blocks $\mathbf{M_{12}}$ and $\mathbf{M_{21}}$ describe how the two subsystems interact with each other.

To simplify our expressions in the following calculations, here we define a few parameters :

$$\eta = -1 - F_0 \,, \tag{2.82}$$

$$\nu_q = \sqrt{3 - 2F_q + {F_q}^2} \,, \tag{2.83}$$

where $|q| = 0, 2$. We note here that ν_0 and ν_2 are always real numbers as ${\nu_0}^2 = 3 - 2F_0 + {F_0}^2 > 0$ and ${\nu_2}^2 = 3 + 6F_0 + 9{F_0}^2 > 0$ for all values of F_0[10]. Hence the eigenvalues λ_1, λ_2, λ_3 and λ_4 of $\mathbf{M}'$ are given by :

$$\lambda_1 = -i\gamma P\,\nu_0, \quad \lambda_2 = i\gamma P\,\nu_0, \quad \lambda_3 = -i\gamma P\,\nu_2, \quad \lambda_4 = i\gamma P\,\nu_2. \tag{2.84}$$

The corresponding eigenvectors $\mathbf{V_1}$, $\mathbf{V_2}$, $\mathbf{V_3}$ and $\mathbf{V_4}$ of $\mathbf{M}$ are :

$$\mathbf{V_1} = \begin{bmatrix} \eta - \nu_0 \\ \eta + \nu_0 \\ 1 \\ 1 \end{bmatrix}, \quad \mathbf{V_2} = \begin{bmatrix} \eta + \nu_0 \\ \eta - \nu_0 \\ 1 \\ 1 \end{bmatrix}, \quad \mathbf{V_3} = \begin{bmatrix} \frac{-6}{\nu_2 - 3\eta} \\ \frac{6}{\nu_2 - 3\eta} \\ \frac{\nu_2 + 3\eta}{\nu_2 - 3\eta} \\ 1 \end{bmatrix}, \quad \mathbf{V_4} = \begin{bmatrix} \frac{6}{\nu_2 + 3\eta} \\ \frac{-6}{\nu_2 + 3\eta} \\ \frac{\nu_2 - 3\eta}{\nu_2 + 3\eta} \\ 1 \end{bmatrix}. \tag{2.85}$$

Thus, the solution of Equation (2.78) can be written as :

$$\mathbf{B}(z) = C_1 e^{\lambda_1 z}\mathbf{V_1} + C_2 e^{\lambda_2 z}\mathbf{V_2} + C_3 e^{\lambda_3 z}\mathbf{V_3} + C_4 e^{\lambda_4 z}\mathbf{V_4}, \tag{2.86}$$

where C_1, C_2, C_3 and C_4 are constants which can be determined from the initial conditions. We write down the initial conditions as :

$$B_0(z = 0) = a_0 e^{i\theta_0}, \tag{2.87}$$

$$B_{-2}(z = 0) = a_{-2} e^{i\theta_{-2}}. \tag{2.88}$$

---

[10] It can be easily checked that the minimum values of the quadratic expressions $3 - 2F_0 + {F_0}^2$ and $3 + 6F_0 + 9{F_0}^2$ are 2. Hence they are positive for all values of F_0.

Using these initial conditions in Equation (2.86) and solving the resulting system of linear equations, we find :

$$
\begin{aligned}
C_1 &= \frac{a_0\cos(\theta_0)}{2\eta} - i\left(\frac{a_0\sin(\theta_0)}{2\nu_0} + \frac{a_{-2}\sin(\theta_{-2})}{\nu_0\eta}\right),\\
C_2 &= \frac{a_0\cos(\theta_0)}{2\eta} + i\left(\frac{a_0\sin(\theta_0)}{2\nu_0} + \frac{a_{-2}\sin(\theta_{-2})}{\nu_0\eta}\right),\\
C_3 &= \frac{-(\nu_2-3\eta)a_0\cos(\theta_0)}{2\nu_2\eta} + \frac{(\nu_2-3\eta)a_{-2}\cos(\theta_{-2})}{2\nu_2} + i\frac{(\nu_2-3\eta)a_{-2}\sin(\theta_{-2})}{6\eta},\\
C_4 &= \frac{-(\nu_2+3\eta)a_0\cos(\theta_0)}{2\nu_2\eta} + \frac{(\nu_2+3\eta)a_{-2}\cos(\theta_{-2})}{2\nu_2} - i\frac{(\nu_2+3\eta)a_{-2}\sin(\theta_{-2})}{6\eta}.
\end{aligned}
\tag{2.89}
$$

Hence using Equation (2.89) in Equation (2.86) we get :

$$
\begin{aligned}
B_0(z) = {} & \left[-\frac{\eta}{\nu_0}a_0\sin(\theta_0) - \frac{2}{\nu_0}a_{-2}\sin(\theta_{-2})\right]\sin(\gamma P\nu_0 z) + a_0\cos(\theta_0)\cos(\gamma P\nu_0 z)\\
& + i\Bigg(\frac{\nu_0}{\eta}a_0\cos(\theta_0)\sin(\gamma P\nu_0 z) + \left[a_0\sin(\theta_0) + \frac{2}{\eta}a_{-2}\sin(\theta_{-2})\right]\cos(\gamma P\nu_0 z)\\
& + \left[-\frac{6}{\eta\nu_2}a_0\cos(\theta_0) + \frac{6}{\nu_2}a_{-2}\cos(\theta_{-2})\right]\sin(\gamma P\nu_2 z) - \frac{2}{\eta}a_{-2}\sin(\theta_{-2})\cos(\gamma P\nu_2 z)\Bigg),
\end{aligned}
\tag{2.90}
$$

$$
\begin{aligned}
B_{-2}(z) = {} & \left[-\frac{1}{\nu_0}a_0\sin(\theta_0) - \frac{2}{\nu_0\eta}a_{-2}\sin(\theta_{-2})\right]\sin(\gamma P\nu_0 z) + \frac{1}{\eta}a_0\cos(\theta_0)\cos(\gamma P\nu_0 z)\\
& + \frac{\nu_2}{3\eta}a_{-2}\sin(\theta_{-2})\sin(\gamma P\nu_2 z) + \left[-\frac{1}{\eta}a_0\cos(\theta_0) + a_{-2}\cos(\theta_{-2})\right]\cos(\gamma P\nu_2 z)\\
& + i\Bigg(\left[\frac{3}{\nu_2}a_0\cos(\theta_0) - \frac{3\eta}{\nu_2}a_{-2}\cos(\theta_{-2})\right]\sin(\gamma P\nu_2 z) + a_{-2}\sin(\theta_{-2})\cos(\gamma P\nu_2 z)\Bigg).
\end{aligned}
\tag{2.91}
$$

From the above equation, we see that the solution depends on the input amplitude of the HOI's. This means that it might be possible to have a larger signal gain by injecting HOI's at the input of the fiber. We also see that the solution acquires two oscillation frequencies $\gamma P\nu_0$ and $\gamma P\nu_2$ however these frequencies are different from the characteristic oscillation frequencies of subsystems 1 and 2 given by $\gamma P\mu_0$ and $\gamma P\mu_2$ (see Equation (2.55)). ν_q and μ_q are related as :

$$
{\mu_q}^2 = {\nu_q}^2 - 6. \tag{2.92}
$$

Note that ${\nu_q}^2$ is larger than ${\mu_q}^2$. Since $\gamma P\nu_q$ is also the parametric gain coefficient of the system, a larger value indicates a larger growth rate of the signal compared to the 4-wave model (when μ_q is real). Furthermore we note that unlike the case of the analytical 4-wave model, where the solutions can be oscillatory or hyperbolic depending on μ_q is real or imaginary respectively, here the solutions are always oscillatory as ν_q is always real.

- **Case 3 : $\Delta\beta_{klmn} \neq 0$, $A_2(0) = A_{-2}(0) = 0$:**

For many practical scenarios, we can use $A_2(0) = A_{-2}(0) = a_{-2} = 0$. Thus we can write down a simpler form of Equations (2.90) and (2.91) as :

$$\begin{aligned} B_0(z) &= -\frac{\eta}{\nu_0} a_0 \sin(\theta_0) \sin(\gamma P \nu_0 z) + a_0 \cos(\theta_0) \cos(\gamma P \nu_0 z) \\ &+ i \left(\frac{\nu_0}{\eta} a_0 \cos(\theta_0) \sin(\gamma P \nu_0 z) + a_0 \sin(\theta_0) \cos(\gamma P \nu_0 z) - \frac{6}{\eta \nu_2} a_0 \cos(\theta_0) \sin(\gamma P \nu_2 z) \right), \end{aligned} \tag{2.93}$$

$$\begin{aligned} B_{-2}(z) = &-\frac{1}{\nu_0} a_0 \sin(\theta_0) \sin(\gamma P \nu_0 z) + \frac{1}{\eta} a_0 \cos(\theta_0) \cos(\gamma P \nu_0 z) \\ &- \frac{1}{\eta} a_0 \cos(\theta_0) \cos(\gamma P \nu_2 z) + i \left(\frac{3}{\nu_2} a_0 \cos(\theta_0) \sin(\gamma P \nu_2 z) \right). \end{aligned} \tag{2.94}$$

One can check for completeness that when we consider $\Delta\beta_{klmn} = 0$, Equations (2.93) and (2.94) lead to Equations (2.71) and (2.72) respectively. The corresponding powers P_0 and P_{-2} are given by :

$$\begin{aligned} P_0(z) = {a_0}^2 \Bigg[&\left(\cos(\gamma P \nu_0 z) \cos(\theta_0) - \frac{\eta}{\nu_0} \sin(\gamma P \nu_0 z) \sin(\theta_0) \right)^2 \\ &+ \left(\cos(\gamma P \nu_0 z) \sin(\theta_0) + \frac{\nu_0}{\eta} \sin(\gamma P \nu_0 z) \cos(\theta_0) - \frac{6}{\eta \nu_2} \sin(\gamma P \nu_2 z) \cos(\theta_0) \right)^2 \Bigg], \end{aligned} \tag{2.95}$$

$$\begin{aligned} P_{-2}(z) = {a_0}^2 \Bigg[&\left(\frac{1}{\eta} \cos(\gamma P \nu_0 z) \cos(\theta_0) - \frac{1}{\eta} \cos(\gamma P \nu_2 z) \cos(\theta_0) - \frac{1}{\nu_0} \sin(\gamma P \nu_0 z) \sin(\theta_0) \right)^2 \\ &+ \left(\frac{3}{\nu_2} \sin(\gamma P \nu_2 z) \cos(\theta_0) \right)^2 \Bigg]. \end{aligned} \tag{2.96}$$

From Equations (2.95) and (2.96) we see that the powers of the signal and the HOI's depend on the power and phase of the waves at the input of the fiber ensuring its functioning as a PSA.

In Fig. 2.12 we plot the dependence of the PSA gain $G_0 = \frac{P_0(L)}{{a_0}^2}$ on the relative phase between the pumps and the signal $\Theta = 2\theta_0$. The parameters used are : $P = 20$ dBm, $L = 500$ m, $\gamma = 11.3\ \mathrm{W}^{-1}\mathrm{km}^{-1}$, $\lambda_0 = 1557.5$ nm, $\lambda_1 = 1556.5$ nm, $\lambda_{ZDW} = 1547.5$ nm and $D' = 0.017\ \mathrm{ps/nm^2/km}$.

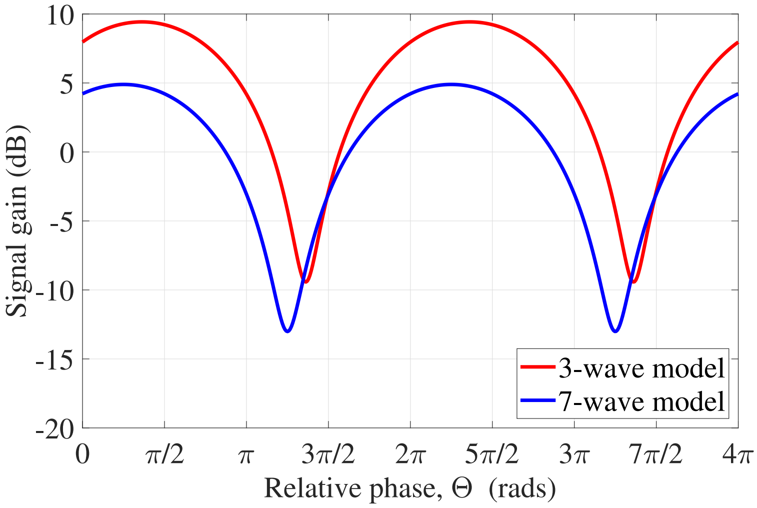

Figure 2.12. PSA gain of signal using the 3-wave model (red) and 7-wave model (blue) as a function of the relative phase between the pump, signal and idler Θ. A non-degenerate pump configuration is considered with $\Delta\beta_{klmn} \neq 0$, $A_2(0) = A_{-2}(0) = 0$ (Case 3). $P = 20$ dBm, $L = 500$ m, $\gamma = 11.3$ W^{-1}km^{-1}, $\lambda_0 = 1557.5$ nm, $\lambda_1 = 1556.5$ nm, $\lambda_{ZDW} = 1547.5$ nm and $D^{'} = 0.017$ ps/nm^2/km.

We see from Fig. 2.12 that with the 2 nm pump-pump wavelength separation, the 3-wave and 7-wave analytical models differ significantly with respect to the gain dependence on input signal phase. In particular, the two models predict different maximum signal gains. This can be more clearly seen in Fig. 2.13 (a) where we plot the maximum signal gains from the 3- and 7-wave analytical models as a function of $\Delta\lambda_{PP}$. The parameters used are the same as used for Fig.2.12 except for the wavelength separation of the pumps, which is a variable for Fig 2.13. As already seen from Fig. 2.12, in Fig. 2.13 (a) we see that for small values of $\Delta\lambda_{PP}$ (<10 nm), the 3- and 7-wave models differ substantially. On the other hand, for large values of $\Delta\lambda_{PP}$ (>30 nm) the two models converge.

Coming back to Equation (2.95), we see that the output power of the signal depends primarily on the coefficients $\eta^2/{\nu_0}^2$, ${\nu_0}^2/\eta^2$, $36/(\eta^2{\nu_2}^2)$ and $6\nu_0/(\eta^2\nu_2)$ as the other terms are all sinusoids bounded between -1 and 1. These coefficients are functions of $\Delta\lambda_{PP}$. To understand the dependence of the signal gain on these coefficients, we plot their logarithms in Fig. 2.13 (b). We see from Fig. 2.13 (b), that at 8.28 nm (shown in grey dashed line), ${\nu_0}^2/\eta^2$,$36/(\eta^2{\nu_2}^2)$ and $6\nu_0/(\eta^2\nu_2)$ attain a large value. They become much smaller when either $\Delta\lambda_{PP}$ is low (<5 nm) or large (>40 nm). This divergence is due to η going to 0 which arises when the dispersion (C) and the nonlinearity (γP) of the fiber cancel each other. This is also reflected on the maximum gain spectrum of the signal, i.e. for lower and larger values of $\Delta\lambda_{PP}$, the maximum gain is much lower compared to that at an intermediate value ($\approx$ 9.6 nm). Moreover we see from Fig. 2.13 (b) that for large values of $\Delta\lambda_{PP}$ (>40 nm), $\eta \approx \nu_0$ and $\frac{6}{(\eta\nu_2)} \ll \frac{\nu_0}{\eta}$.

In that limit, we can write from Equation (2.95) :

$$P_0(z) \approx {a_0}^2 \left[\cos^2(\gamma P \nu_0 z + \theta_0) + \sin^2(\gamma P \nu_0 z + \theta_0)\right] = {a_0}^2. \tag{2.97}$$

Thus the maximum gain G_0 (in dB) is expected to asymptotically approach 0 for large $\Delta\lambda_{PP}$'s. This is what we also see in Fig. 2.13 (a).

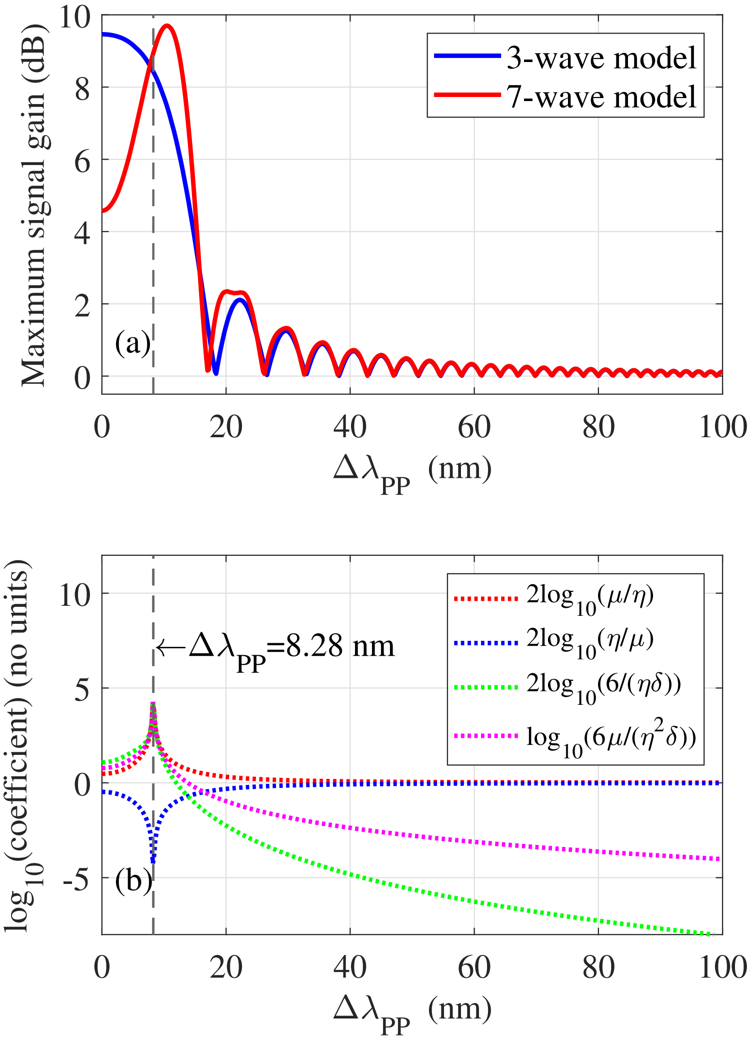

Figure 2.13. (a) Plot of maximum PSA gain of signal using the 3-wave (blue) and 7-wave (red) analytical models as a function of $\Delta\lambda_{PP}$. (b) Plot of the twice log of coefficients of different terms in Equation (2.95), *viz.* $2\log_{10}(\nu_0/\eta)$ (red dotted line), $2\log_{10}(\eta/\nu_0)$ (blue dotted line), $2\log_{10}(6/(\eta\nu_2))$ (green dotted line) and $\log_{10}(6\nu_0/(\eta^2\nu_2))$ (magenta dotted line), as a function of pump-pump wavelength separation $\Delta\lambda_{PP}$. A non-degenerate pump configuration is considered with $\Delta\beta_{klmn} \neq 0$, $A_2(0) = A_{-2}(0) = 0$ (Case 3). $P = 20$ dBm, $L = 500$ m, $\gamma = 11.3$ W^{-1}km^{-1}, $\lambda_0 = 1557.5$ nm, $\lambda_{ZDW} = 1547.5$ nm and $D^{'} = 0.017$ ps/nm^2/km.

- **Case 4 : $\boldsymbol{\Delta\beta_{klmn} \neq 0, A_2(0) \neq A_{-2}(0)}$:**

In the last discussion we had considered $A_2(0) = A_{-2}(0)$ to obtain Equations (2.90) and (2.91). However to obtain a more general solution, we first look at the explicit dependence of A_2 on A_{-2}. Thus we define the quantity δ_2 as :

$$\delta_2 = A_{-2} - A_2. \tag{2.98}$$

Now using Equations (2.60) and (2.61) along with $|A_1|^2 = |A_{-1}|^2 = P$ we get :

$$\frac{d\delta_2}{dz} = \frac{dA_{-2}}{dz} - \frac{dA_2}{dz} = i\gamma P(4\delta_2 - 2e^{i(6\gamma P-6C)z}\delta_2^*). \tag{2.99}$$

This can be written down in a matrix-form as :

$$\frac{d}{dz}\begin{bmatrix} \delta_2 \\ {\delta_2}^* \end{bmatrix} = i\gamma P \begin{bmatrix} 4 & -2e^{i(6\gamma P-6C)z} \\ 2e^{-i(6\gamma P-6C)z} & -4 \end{bmatrix} \begin{bmatrix} \delta_2 \\ {\delta_2}^* \end{bmatrix}. \tag{2.100}$$

Thus when $A_2(0) \neq A_{-2}(0)$, we can use $A_2(z) = A_{-2}(z) - \delta_2(z)$ and express Equation (2.67) as :

$$\begin{aligned} \frac{d}{dz}\begin{bmatrix} A_0 \\ {A_0}^* \\ A_{-2} \\ {A_{-2}}^* \end{bmatrix} &= i\gamma P \begin{bmatrix} 4 & 2e^{i(6\gamma P+2C)z} & 4e^{i4Cz} & 2e^{i(6\gamma P-2C)z} \\ -2e^{-i(6\gamma P+2C)z} & -4 & -2e^{-i(6\gamma P-2C)z} & -4e^{-i4Cz} \\ 2e^{-i4Cz} & e^{i(6\gamma P-2C)z} & 4 & 2e^{i(6\gamma P-6C)z} \\ -e^{-i(6\gamma P-2C)z} & -2e^{i4Cz} & -2e^{-i(6\gamma P-6C)z} & -4 \end{bmatrix} \begin{bmatrix} A_0 \\ {A_0}^* \\ A_{-2} \\ {A_{-2}}^* \end{bmatrix} \\ &+ i\gamma P \begin{bmatrix} -2e^{i4Cz}\delta_2 - e^{i(6\gamma P-2C)z}\delta_2^* \\ 2e^{-i4Cz}\delta_2^* + e^{-i(6\gamma P-2C)z}\delta_2 \\ -2e^{i(6\gamma P-6C)z}\delta_2^* \\ 2e^{-i(6\gamma P-6C)z}\delta_2 \end{bmatrix}. \end{aligned} \tag{2.101}$$

We perform the transformation of variables (see Equation (2.44)) as :

$$\begin{aligned} A_q &= B_q e^{i(3\gamma P+C(1-q^2))z}, \\ \tilde{\delta_2} &= B_{-2} - B_2 = e^{-i(3\gamma P-3C)z}\delta_2, \end{aligned} \tag{2.102}$$

where $q = 0, 2, -2$. Invoking these transformations in Equation (2.101) we get :

$$\frac{d}{dz}\begin{bmatrix} B_0 \\ {B_0}^* \\ B_{-2} \\ {B_{-2}}^* \end{bmatrix} = i\gamma P \begin{bmatrix} 1-F_0 & 2 & 4 & 2 \\ -2 & -(1-F_0) & -2 & -4 \\ 2 & 1 & 1-F_2 & 2 \\ -1 & -2 & -2 & -(1-F_2) \end{bmatrix} \begin{bmatrix} B_0 \\ {B_0}^* \\ B_{-2} \\ {B_{-2}}^* \end{bmatrix} + i\gamma P \begin{bmatrix} -2\tilde{\delta_2} - \tilde{\delta_2}^* \\ 2\tilde{\delta_2}^* + \tilde{\delta_2} \\ -2\tilde{\delta_2}^* \\ 2\tilde{\delta_2} \end{bmatrix}. \tag{2.103}$$

Equation (2.103) is a coupled linear inhomogeneous differential equation of the form :

$$\frac{d\mathbf{B}}{dz} = \mathbf{M}'\mathbf{B} + \mathbf{N},$$

where $\mathbf{M}'$ is the coefficient matrix of the homogeneous part and $\mathbf{N}$ is the inhomogenity term. Solving Equation (2.100) we get the explicit z-dependence of

$\tilde{\delta_2}$ as :

$$\tilde{\delta_2}(z) = \left(\frac{-i\eta_2 \sin(\gamma P \mu_2 z)}{\mu_2} + \cos(\gamma P \mu_2 z)\right)\tilde{\delta_2}(0) - \left(\frac{2i \sin(\gamma P \mu_2 z)}{\mu_2}\right)\tilde{\delta_2}^*(0), \tag{2.104}$$

where η_2 and μ_2 can be obtained from Equation (2.53) with $|q| = 2$. From Equation (2.104) we see that when $B_2(0) = B_{-2}(0)$ (or $A_2(0) = A_{-2}(0)$), i.e. $\tilde{\delta_2}(0) = 0$ we get $\tilde{\delta_2}(z) = 0$ i.e. $B_2(z) = B_{-2}(z)$ (or $A_2(z) = A_{-2}(z)$) as expected. The solution to Equation (2.103) is given by :

$$\mathbf{B}(z) = \mathbf{F}(z)\mathbf{F}(0)^{-1}\mathbf{B}(0) + \int_0^z \mathbf{F}(z)\mathbf{F}(s)^{-1}\mathbf{N}(s)ds \tag{2.105}$$

where the first term on the right hand side represents the solution when $\tilde{\delta_2}(0) = 0$ which is given by Equations (2.90) and (2.91), and the second term arises due to the inhomogenity of the system. The full solution of the system is derived in Appendices C and D. Thus we provide the solution for $B_0(z)$, $B_{-2}(z)$ and $B_2(z)$ as :

$$\begin{aligned}
B_0(z) = B_0(0)&\left(\cos(\gamma P\nu_0 z) + \frac{i(\eta^2+{\nu_0}^2)}{2\eta\nu_0}\sin(\gamma P\nu_0 z) - \frac{3i}{\eta\nu_2}\sin(\gamma P\nu_2 z)\right)\\
&+ B_0^*(0)\left(\frac{i(-\eta^2+{\nu_0}^2)}{2\eta\nu_0}\sin(\gamma P\nu_0 z) - \frac{3i}{\eta\nu_2}\sin(\gamma P\nu_2 z)\right)\\
&+ B_{-2}(0)\left(\frac{1}{2\eta}\cos(\gamma P\nu_0 z) - \frac{1}{2\eta}\cos(\gamma P\nu_2 z) + \frac{i}{2\nu_0}\sin(\gamma P\nu_0 z) + \frac{3i}{2\nu_2}\sin(\gamma P\nu_2 z)\right)\\
&+ B^*_{-2}(0)\left(-\frac{1}{2\eta}\cos(\gamma P\nu_0 z) + \frac{1}{2\eta}\cos(\gamma P\nu_2 z) - \frac{i}{2\nu_0}\sin(\gamma P\nu_0 z) + \frac{3i}{2\nu_2}\sin(\gamma P\nu_2 z)\right)\\
&+ B_2(0)\left(\frac{1}{2\eta}\cos(\gamma P\nu_0 z) - \frac{1}{2\eta}\cos(\gamma P\nu_2 z) + \frac{i}{2\nu_0}\sin(\gamma P\nu_0 z) + \frac{3i}{2\nu_2}\sin(\gamma P\nu_2 z)\right)\\
&+ B_2^*(0)\left(-\frac{1}{2\eta}\cos(\gamma P\nu_0 z) + \frac{1}{2\eta}\cos(\gamma P\nu_2 z) - \frac{i}{2\nu_0}\sin(\gamma P\nu_0 z) + \frac{3i}{2\nu_2}\sin(\gamma P\nu_2 z)\right),
\end{aligned} \tag{2.106}$$

$$\begin{aligned}
B_{-2}(z) = {} & B_0(0)\left(\frac{1}{2\eta}\cos(\gamma P\nu_0 z) - \frac{1}{2\eta}\cos(\gamma P\nu_2 z) + \frac{i}{2\nu_0}\sin(\gamma P\nu_0 z) + \frac{3i}{2\nu_2}\sin(\gamma P\nu_2 z)\right) \\
& + B_0^*(0)\left(\frac{1}{2\eta}\cos(\gamma P\nu_0 z) - \frac{1}{2\eta}\cos(\gamma P\nu_2 z) - \frac{i}{2\nu_0}\sin(\gamma P\nu_0 z) + \frac{3i}{2\nu_2}\sin(\gamma P\nu_2 z)\right) \\
& + B_{-2}(0)\bigg(\frac{1}{2}\cos(\gamma P\nu_2 z) + \frac{1}{2}\cos(\gamma P\mu_2 z) + \frac{i}{2\eta\nu_0}\sin(\gamma P\nu_0 z) \\
& - \frac{i(3\eta^2+2\eta+1)}{2\eta\nu_2}\sin(\gamma P\nu_2 z) - \frac{i(2+3\eta)}{2\mu_2}\sin(\gamma P\mu_2 z)\bigg) \\
& + B_{-2}^*(0)\left(-\frac{i}{2\eta\nu_0}\sin(\gamma P\nu_0 z) + \frac{i(2\eta+1)}{2\eta\nu_2}\sin(\gamma P\nu_2 z) - \frac{i}{\mu_2}\sin(\gamma P\mu_2 z)\right) \\
& + B_2(0)\bigg(\frac{1}{2}\cos(\gamma P\nu_2 z) - \frac{1}{2}\cos(\gamma P\mu_2 z) + \frac{i}{2\eta\nu_0}\sin(\gamma P\nu_0 z) \\
& - \frac{i(3\eta^2+2\eta+1)}{2\eta\nu_2}\sin(\gamma P\nu_2 z) + \frac{i(2+3\eta)}{2\mu_2}\sin(\gamma P\mu_2 z)\bigg) \\
& + B_2^*(0)\left(-\frac{i}{2\eta\nu_0}\sin(\gamma P\nu_0 z) + \frac{i(2\eta+1)}{2\eta\nu_2}\sin(\gamma P\nu_2 z) + \frac{i}{\mu_2}\sin(\gamma P\mu_2 z)\right),
\end{aligned} \tag{2.107}$$

$$\begin{aligned}
B_{2}(z) = {} & B_0(0)\left(\frac{1}{2\eta}\cos(\gamma P\nu_0 z) - \frac{1}{2\eta}\cos(\gamma P\nu_2 z) + \frac{i}{2\nu_0}\sin(\gamma P\nu_0 z) + \frac{3i}{2\nu_2}\sin(\gamma P\nu_2 z)\right) \\
& + B_0^*(0)\left(\frac{1}{2\eta}\cos(\gamma P\nu_0 z) - \frac{1}{2\eta}\cos(\gamma P\nu_2 z) - \frac{i}{2\nu_0}\sin(\gamma P\nu_0 z) + \frac{3i}{2\nu_2}\sin(\gamma P\nu_2 z)\right) \\
& + B_{-2}(0)\bigg(\frac{1}{2}\cos(\gamma P\nu_2 z) - \frac{1}{2}\cos(\gamma P\mu_2 z) + \frac{i}{2\eta\nu_0}\sin(\gamma P\nu_0 z) \\
& - \frac{i(3\eta^2+2\eta+1)}{2\eta\nu_2}\sin(\gamma P\nu_2 z) + \frac{i(2+3\eta)}{2\mu_2}\sin(\gamma P\mu_2 z)\bigg) \\
& + B_{-2}^*(0)\left(-\frac{i}{2\eta\nu_0}\sin(\gamma P\nu_0 z) + \frac{i(2\eta+1)}{2\eta\nu_2}\sin(\gamma P\nu_2 z) + \frac{i}{\mu_2}\sin(\gamma P\mu_2 z)\right) \\
& + B_2(0)\bigg(\frac{1}{2}\cos(\gamma P\nu_2 z) + \frac{1}{2}\cos(\gamma P\mu_2 z) + \frac{i}{2\eta\nu_0}\sin(\gamma P\nu_0 z) \\
& - \frac{i(3\eta^2+2\eta+1)}{2\eta\nu_2}\sin(\gamma P\nu_2 z) - \frac{i(2+3\eta)}{2\mu_2}\sin(\gamma P\mu_2 z)\bigg) \\
& + B_2^*(0)\left(-\frac{i}{2\eta\nu_0}\sin(\gamma P\nu_0 z) + \frac{i(2\eta+1)}{2\eta\nu_2}\sin(\gamma P\nu_2 z) - \frac{i}{\mu_2}\sin(\gamma P\mu_2 z)\right),
\end{aligned} \tag{2.108}$$

where η is given by Equation (C.8), ν_0 and ν_2 are given by Equation (C.9) (with $q = 0$ and 2) and μ_2 is given by Equation (2.53) (with $q = 2$). While for the analytical 4-wave model, the solution had hyperbolic terms (when parametric gain coefficient $i\gamma P\mu_q$ is real), in contrast, for the analytical 7-wave model, the signal solution is always sinusoidal, and attains a resonance when $\eta \to 0$. Thus the analytical 7-wave model indicates that the mechanism of signal instability relies on the balance between the dispersion and nonlinearity of the fiber ($\eta = 0 \implies C + \gamma P = 0$) which is fundamentally different from the analytical 4-wave model.

Thus, now we have a formalism to relate the input and output fields of A_0, A_2 and A_{-2} with a linear matrix under the strong pump approximation.

Comparing Equation (2.91) with Equation (2.107) we see that when the HOI's are not equal at the input of the fiber, the solution of the HOI's acquire a third frequency of oscillation $\gamma P \mu_2$, apart from $\gamma P \nu_0$ and $\gamma P \nu_2$. This means, while the signal would lead to an oscillatory stable solution always, the HOI's have terms in the solution that can show hyperbolic evolution with z when μ_2 is imaginary.

One important observation from this analysis is that, while for the analytical 3- or 4-wave models, the modulation instability of the signal originates from the hyperbolic terms in the solution, that arise only when μ_q is imaginary, however for the analytical 7-wave model, the signal modulation instability is a consequence of the resonance corresponding to $\eta \rightarrow 0$. Thus for the analytical 7-wave model, the mechanism of instability relies on the balance between the dispersion and nonlinearity of the fiber ($C + \gamma P = 0$).

2.4.7 Maximum Signal Gain

Using the most general case (Case 4 : $\Delta\beta_{klmn} \neq 0, A_2(0) \neq A_{-2}(0)$) of the analytical 7-wave model, in Fig. 2.14 we plot the maximum signal gain as a function of pump-pump wavelength separation for different values of r_{-2} and r_2, where r_{-2} and r_2 are the ratios of power of the HOI's to the power of the signal at the input of the fiber. They are given by :

$$r_{-2} = \frac{|B_{-2}(0)|^2}{|B_0(0)|^2}, \quad r_2 = \frac{|B_2(0)|^2}{|B_0(0)|^2}. \tag{2.109}$$

We see from Fig. 2.14 that injecting the HOI's at the input of the fiber leads to a strong improvement of the maximum signal gain (about 5 dB with $\gamma PL = 0.5$, and $r_{-2} = r_2 = 1$). This is because from Equation (2.106) we have seen that the signal wave depends on the input amplitude of the HOI's. Thus a non-zero value of input HOI powers leads to an enhancement of the maximum signal gain.

2.4.8 Phase Sensitive Frequency Conversion (PSFC)

One interesting feature of this system is its phase sensitive nature. Let us consider an example. Suppose we consider the case where only HOI1 is injected at the input. In such a case, we can ask the question : Can we generate either the signal or the HOI2 at the fiber output depending on the input phase of HOI1? Such a functionality is known as phase sensitive frequency conversion (PSFC) [45] and is well studied in the scientific literature [82, 84, 133, 172].

Since from Equations (2.106)-(2.108) it is not obvious that this system is capable of a PSFC operation, in Fig. 2.15 we plot the output powers of signal, HOI1 and HOI2 as a function of input phase of HOI1 at the fiber input. We consider only HOI1 at the input of the fiber with a power $P_{-1}(0) = -20$ dBm. We see that even if only

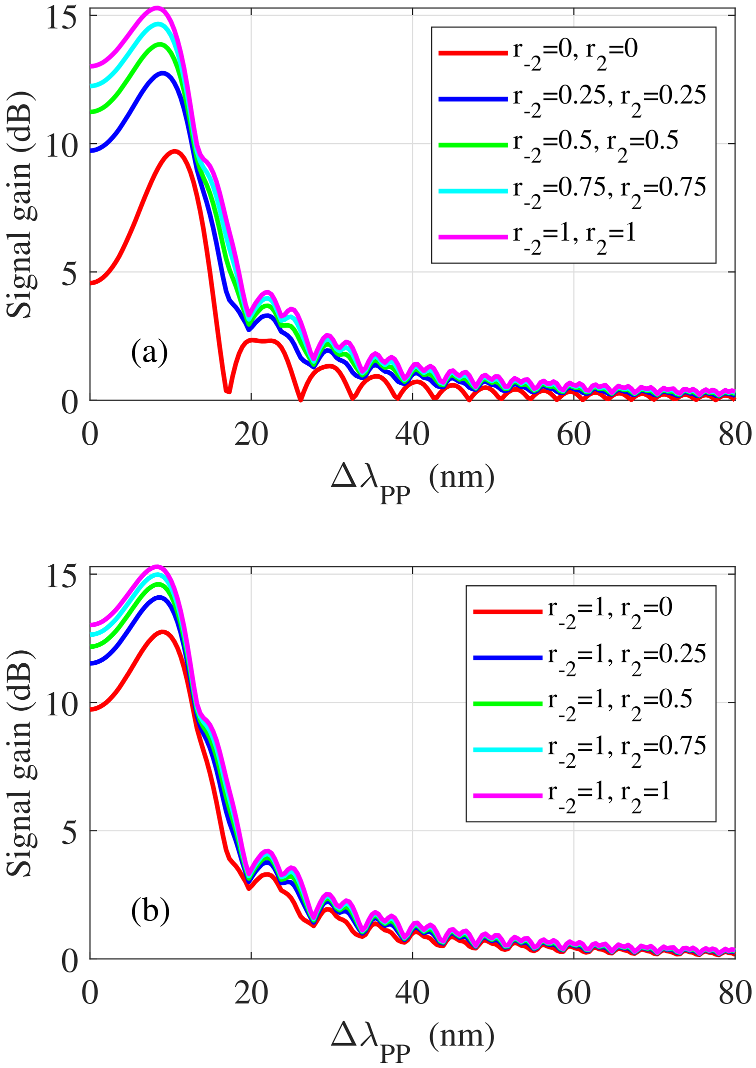

Figure 2.14. Plot of maximum gain of signal using the analytical 7-wave model as a function of $\Delta\lambda_{PP}$ for different values of r_{-2} and r_2. (a) $r_{-2} = r_2$ (b) $r_{-2} = 1$. Parameters : $P_0 = -20$ dBm, $P = 20$ dBm, $L = 500$ m, $\gamma = 11.3$ W^{-1}km^{-1}, $\lambda_0 = 1557.5$ nm, $\lambda_{ZDW} = 1547.5$ nm and $D' = 0.017$ ps/nm^2/km.

HOI1 is launched at the input, all the three waves show phase sensitivity. The most interesting case arises around $\Delta\lambda_{PP} = 7.5$ nm (see Fig. 2.15 (c)). In this case, when the input phase of HOI1 is near $\frac{\pi}{4}$, the signal is efficiently generated at the output while HOI2 is not. On the other hand, when the input phase of HOI1 is near $\frac{3\pi}{4}$, HOI2 is efficiently generated at the output while not the signal (see Fig. 2.16). This implies, the system is capable of phase sensitive frequency conversion i.e. conversion of HOI1 to either signal or HOI2 depending on the initial phase of HOI1.

With hindsight, we note that the phase sensitive operation of our system is subtle. Let us first analyze how the system evolves at the initial part of the fiber. This means we look at the solutions of $B_0(z)$ and $B_2(z)$ when z is small. First, we ignore all the terms with coefficients $B_0(0)$, $B_0^*(0)$, $B_2(0)$ and $B_2^*(0)$ in Equations (2.106) and (2.108) as they are 0. We also make the approximations $\cos(\gamma P \nu_0 z) \approx 1$, $\cos(\gamma P \nu_2 z) \approx 1$, $\sin(\gamma P \nu_0 z) \approx \gamma P \nu_0 z$, $\sin(\gamma P \nu_2 z) \approx \gamma P \nu_2 z$ and $\sin(\gamma P \mu_2 z) \approx \gamma P \mu_2 z$ since z is

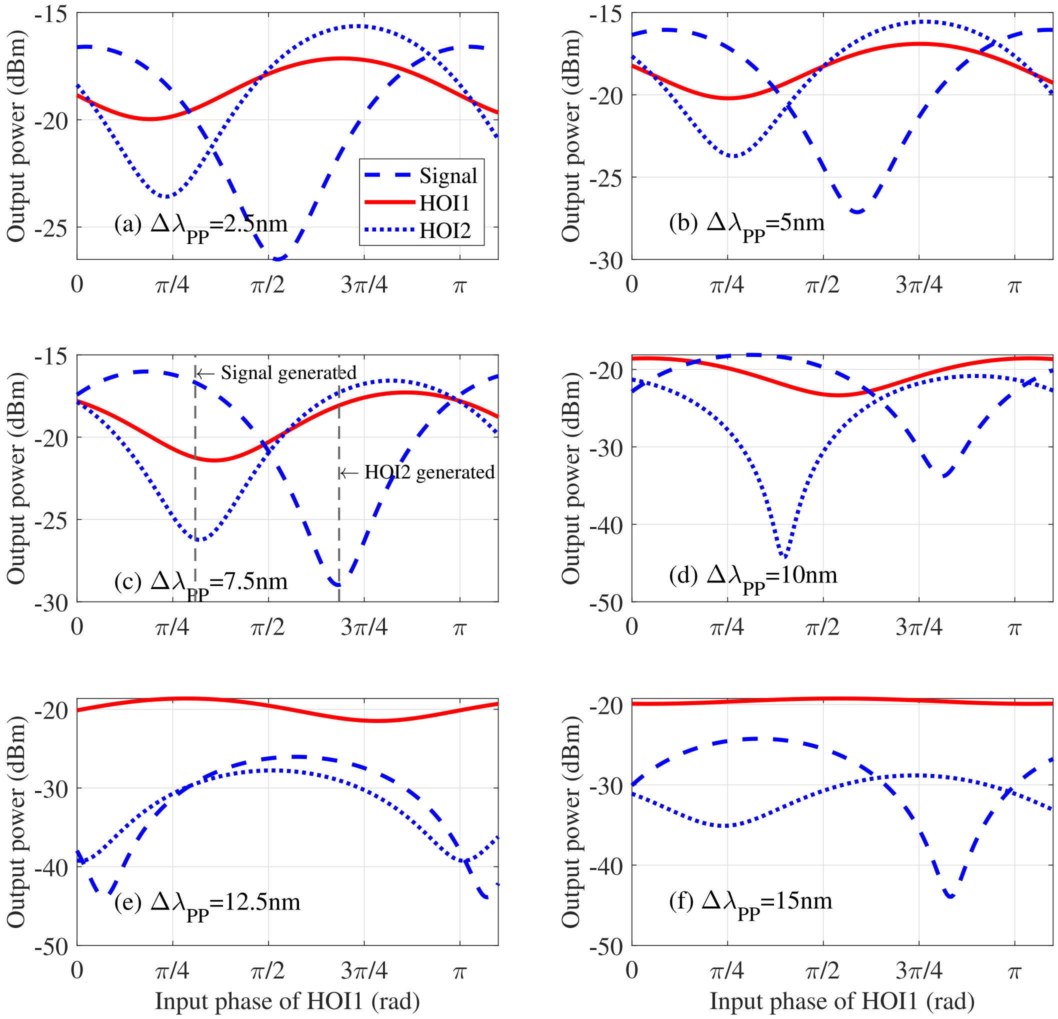

Figure 2.15. Plot of output powers of signal (blue dashed), HOI1 (red solid) and HOI2 (blue dotted) using the analytical 7-wave model as a function of input phase of HOI1 at the fiber input. Only HOI1 is launched at the input. Different values of $\Delta\lambda_{PP}$ are considered : (a) $\Delta\lambda_{PP} = 2.5$ nm, (b) $\Delta\lambda_{PP} = 5$ nm, (c) $\Delta\lambda_{PP} = 7.5$ nm, (d) $\Delta\lambda_{PP} = 10$ nm, (e) $\Delta\lambda_{PP} = 12.5$ nm and (f) $\Delta\lambda_{PP} = 15$ nm. Parameters : $P = 20$ dBm, $P_{-1}(0) = -20$ dBm, $L = 500$ m, $\gamma = 11.3$ W^{-1}km^{-1}, $\lambda_0 = 1557.5$ nm, $\lambda_{ZDW} = 1547.5$ nm and $D^{'} = 0.017$ ps/nm^2/km.

small. After a few steps of simplifications, Equations (2.106) and (2.108) give :

$$B_2(z) \approx |B_{-2}(0)|e^{-i\theta_{-2}}\frac{i(2\eta+1)\gamma P}{2\eta}z, \tag{2.110}$$

$$B_0(z) \approx |B_{-2}(0)|\gamma P(-\sin(\theta_{-2}) + 3i\cos(\theta_{-2}))z, \tag{2.111}$$

where θ_{-2} is the initial phase of B_{-2}. We note from the above equations that $|B_2(z)|$ does not depend on θ_{-2} whereas $|B_0(z)|$ does. This means at the initial part of the fiber, the signal is phase sensitively generated by HOI1, but not HOI2.

Let us now look at the situation when z is non negligible compared to $(\gamma P\nu_q)^{-1}$ and $(\gamma P\mu_q)^{-1}$. In such a case, to simplify the equations, we make a special choice of

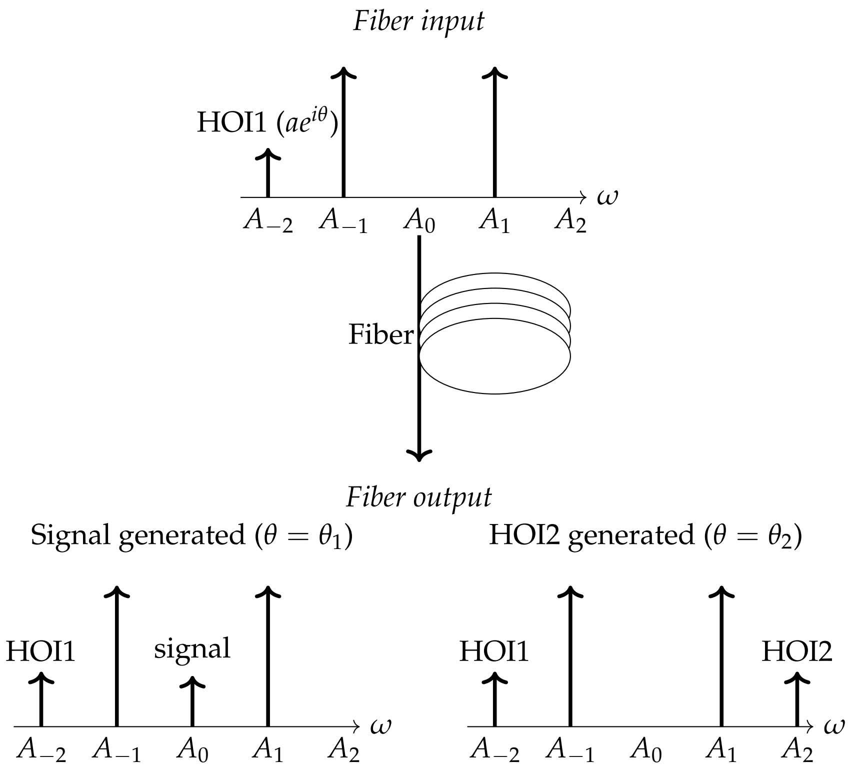

Figure 2.16. An illustration of phase sensitive frequency conversion where either signal or HOI2 is generated at the fiber output depending on the initial phase $\theta = \theta_1$ or $\theta = \theta_2$ of HOI1 respectively.

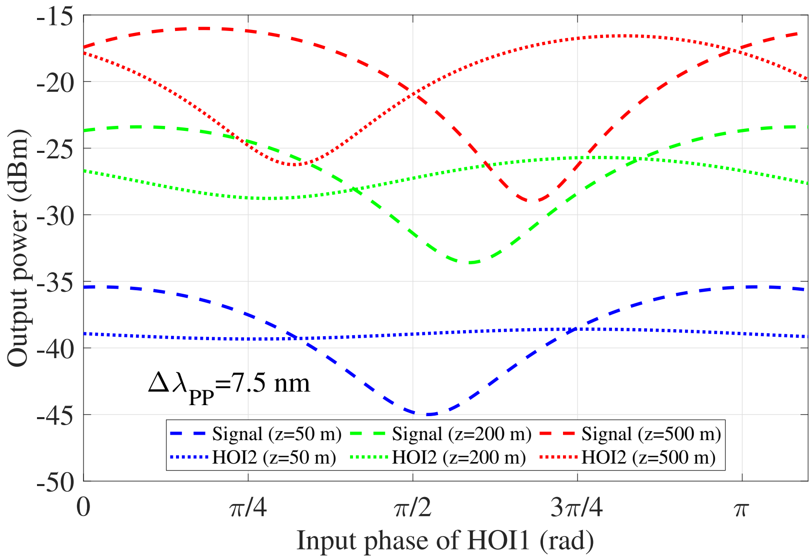

Figure 2.17. Plot of output powers of signal (dashed) and HOI2 (dotted) using the analytical 7-wave model as a function of input phase of HOI1 at the fiber input. Plots are made at different lengths of the fiber : 50 m (blue), 200 m (green) and 500 m (red). Only HOI1 is launched at the input. $\Delta\lambda_{PP} = 7.5$ nm. Other parameters are same as Fig. 2.15

η, i.e. $\eta \approx 0$ (which is approximately the case for Fig. 2.15 (c)). We remind the reader that this condition also leads to a large PSA gain as we observed in Fig. 2.13 (a). In this case, as η is small, we keep only those terms in Equations (2.106) and (2.108) that contain η or $\sqrt{\eta}$ in the denominator. Thus we get :

$$B_0(z) \approx |B_{-2}(0)|\frac{i}{\eta}\left(\cos(\gamma P\nu_0 z) - \cos(\gamma P\nu_2 z)\right)\sin(\theta_{-2}), \tag{2.112}$$

$$\begin{aligned} B_2(z) \approx |B_{-2}(0)|\frac{1}{\eta}\left(\frac{\sin(\gamma P\nu_2 z)}{\nu_2} - \frac{\sin(\gamma P\nu_0 z)}{\nu_0}\right)\sin(\theta_{-2}) \\ + |B_{-2}(0)|\frac{2i\sin(\gamma P\mu_2 z)}{\sqrt{\eta}\sqrt{3\eta+4}}\cos(\theta_{-2}), \end{aligned} \tag{2.113}$$

where we have used ${\mu_2}^2 = \eta(3\eta+4)$. We clearly see from the above equations, that both $B_0(z)$ and $|B_2(z)|$ depend on θ_{-2}. This is also reproduced in Fig. 2.17 where we plot the output powers of signal (dashed) and HOI2 (dotted) using the analytical 7-wave model (using Equations (2.106) and (2.108)) as a function of input phase of HOI1 at the fiber input. Plots are made for different distances inside the fiber, i.e. 50 m (blue), 200 m (green) and 500 m (red). We see that after propagating a small length (blue curve (z =50 m) in Fig. 2.17), the signal power shows phase sensitivity, whereas the HOI2 power remains almost insensitive to the input HOI1 phase θ_{-2} (as already seen from Equations (2.111) and (2.110)). On the other hand, at larger propagation distances (green and red curves (z = 200 and 500 m) in Fig. 2.17) we find both the signal and HOI2 become sensitive to θ_{-2} as understood from Equations (2.112) and (2.113).

One should notice here, that even for a 500 m propagation distance, the maxima and minima of output powers of signal and HOI2, with respect to input phase of HOI1, do not coincide exactly at the same value of input HOI1 phase. This implies, that the PSFC process in this system is an imperfect one. However, it might be possible to further optimize the PSFC performance utilizing Equations (2.112) and (2.113).

PSFC functionality has also been studied for PSA systems with four pump waves [173] and three pump waves [138]. However in our case, we predict a single stage PSFC mechanism with just two pump waves, which opens new perspectives for design of optical frequency converters.

2.4.9 Input Signal Phase for Maximum Signal Gain

- **Case 1 : $\Delta\beta_{klmn} = 0$, $A_2(0) = A_{-2}(0) = 0$:**

  To find the input phase of the signal that leads to a maximum PSA signal gain, we first equate the partial derivative of P_0 (as given in Equation (2.74)) with respect to θ_0 to 0. Thus we get :

$$\frac{\partial P_0}{\partial \theta_0} = {a_0}^2 \sin(\sqrt{3}\gamma Pz)\frac{8}{\sqrt{3}}\cos(2\theta_0)\left(\cos(\sqrt{3}\gamma Pz) - \frac{\sin(\sqrt{3}\gamma Pz)}{\sqrt{3}}\tan(2\theta_0)\right) = 0. \tag{2.114}$$

Assuming $\sin(\sqrt{3}\gamma Pz)$ and $\cos(2\theta_0)$ to be non-zero, we have :

$$\theta_0 = \frac{1}{2}\tan^{-1}\left(\frac{\sqrt{3}}{\tan(\sqrt{3}\gamma Pz)}\right). \tag{2.115}$$

In order to find the condition of a maximum (and not minimum), we perform the second partial derivative of P_0 with respect to θ_0 :

$$\frac{\partial^2 P_0}{\partial {\theta_0}^2} = -{a_0}^2\frac{16}{3}\sin(\sqrt{3}\gamma Pz)\cos(2\theta_0)\left(\sqrt{3}\cos(\sqrt{3}\gamma Pz_0)\tan(2\theta_0) + \sin(\sqrt{3}\gamma Pz)\right) \tag{2.116}$$

Injecting the value of θ_0 from Equation (2.115) into Equation (2.116) we get :

$$\frac{\partial^2 P_0}{\partial {\theta_0}^2} = -{a_0}^2\frac{16}{3}\cos(2\theta_0)(2\cos^2(\sqrt{3}\gamma Pz) + 1) \tag{2.117}$$

Thus for $\frac{\partial^2 P_0}{\partial {\theta_0}^2}$ to be negative, θ_0 should be in the interval $\left(n\pi - \frac{\pi}{4}, n\pi + \frac{\pi}{4}\right)$.

- **Case 2 : $\boldsymbol{\Delta\beta_{klmn} \neq 0}$, $\boldsymbol{A_2(0) = A_{-2}(0) = 0}$:**

As before, we equate the partial derivative of P_0 with respect to θ_0 to 0 :

$$\frac{\partial P_0}{\partial \theta_0} = \left[\frac{\nu_2({\nu_0}^2 - \eta^2)\sin(\gamma P\nu_0 z) - 6\nu_0\sin(\gamma P\nu_2 z)}{(\nu_0\nu_2\eta)^2}\right]\left[-2\nu_0\nu_2\eta\cos(\gamma P\nu_0 z)\cos(2\theta_0)\right.$$
$$\left. + \left(\nu_2({\nu_0}^2 + \eta^2)\sin(\gamma P\nu_0 z) - 6\nu_0\sin(\gamma P\nu_2 z)\right)\sin(2\theta_0)\right] = 0. \tag{2.118}$$

Here we assume :

$$\frac{\nu_2({\nu_0}^2 - \eta^2)\sin(\gamma P\nu_0 z) - 6\nu_0\sin(\gamma P\nu_2 z)}{(\nu_0\nu_2\eta)^2} \neq 0. \tag{2.119}$$

Thus solving Equation (2.118) for θ_0, we get :

$$\theta_0 = \frac{1}{2}\tan^{-1}\left(\frac{2\nu_0\nu_2\eta\cos(\gamma P\nu_0 z)}{\nu_2({\nu_0}^2 + \eta^2)\sin(\gamma P\nu_0 z) - 6\nu_0\sin(\gamma P\nu_2 z)}\right), \tag{2.120}$$

where we also assumed $\cos(2\theta_0) \neq 0$. In order to find the condition of a maximum (and not minimum), we perform the second partial derivative of P_0 with respect to θ_0 :

$$\frac{\partial^2 P_0}{\partial {\theta_0}^2} = \left[\frac{\nu_2({\nu_0}^2-\eta^2)\sin(\gamma P\nu_0 z)-6\nu_0\sin(\gamma P\nu_2 z)}{(\nu_0\nu_2\eta)^2}\right]\Big[4\nu_0\nu_2\eta\cos(\gamma P\nu_0 z)\tan(2\theta_0) \\ +2\nu_2({\nu_0}^2+\eta^2)\sin(\gamma P\nu_0 z)-12\nu_0\sin(\gamma P\nu_2 z)\Big]\cos(2\theta_0). \tag{2.121}$$

Replacing the value of θ_0 form Equation (2.120) in Equation (2.121), we get :

$$\frac{\partial^2 P_0}{\partial {\theta_0}^2} = \left[\frac{\Big(\nu_2({\nu_0}^2-\eta^2)\sin(\gamma P\nu_0 z)-6\nu_0\sin(\gamma P\nu_2 z)\Big)8\cos^2(\gamma P\nu_0 z)}{\nu_2({\nu_0}^2+\eta^2)\sin(\gamma P\nu_0 z)-6\nu_0\sin(\gamma P\nu_2 z)} \right. \\ \left. +\frac{2\Big(\big(\nu_2{\nu_0}^2\sin(\gamma P\nu_0 z)-6\nu_0\sin(\gamma P\nu_2 z)\big)^2-{\nu_2}^2\eta^4\sin^2(\gamma P\nu_0 z)\Big)}{(\nu_0\nu_2\eta)^2}\right]\cos(2\theta_0) \\ = K\cos(2\theta_0), \tag{2.122}$$

where K is the pre-factor of $\cos(2\theta_0)$. Thus when K is positive, $\cos(2\theta_0)$ should be negative and vice versa for P_0 to attain a maximum. This translates to :

$$\theta_0 \in \begin{cases} \left(n\pi-\frac{\pi}{4}, n\pi+\frac{\pi}{4}\right) & \text{if } K<0 \\ \left[\frac{2n+1}{2}\pi-\frac{\pi}{4}, \frac{2n+1}{2}\pi+\frac{\pi}{4}\right] & \text{if } K\geq 0 \end{cases} \tag{2.123}$$

where $n \in \mathbb{Z}$.

2.4.10 HOP Evolution (Subsystem 3)

As we have noted before, under the strong pump approximation, or when the FOPA is weakly nonlinear[11], the HOP's get decoupled from the signal and the HOI's which can be seen from the following equations (same as Equations (2.62) and (2.63)) :

$$\frac{dA_{-3}}{dz} = i\gamma\Big(2|A_{-1}|^2A_{-3}+2|A_1|^2A_{-3}+{A_{-1}}^2{A_1}^*e^{i\Delta\beta_{-1-11-3}z}+2A_{-1}A_1{A_3}^*e^{i\Delta\beta_{-113-3}z}\Big), \tag{2.124}$$

$$\frac{dA_3}{dz} = i\gamma\Big(2|A_{-1}|^2A_3+2|A_1|^2A_3+{A_1}^2{A_{-1}}^*e^{i\Delta\beta_{11-13}z}+2A_{-1}A_1{A_{-3}}^*e^{i\Delta\beta_{-11-33}z}\Big). \tag{2.125}$$

We should note here that Equations (2.124) and (2.125) are similar to the equations of a signal and idler in the analytical 4-wave model (see Equations (2.36) and (2.37)), except for the third term on the right hand side that accounts for a FWM process which contains a product of three pump amplitudes. In fact this is the most important term as all the other terms are products of less than three pump amplitudes.

---

[11] A discussion on the strength of the nonlinearity of the FOPA is provided in Subsection 2.4.12.

This extra term arises only because in this case, the wavelength separation between the HOP's with its nearest pump is equal to the pump-pump wavelength separation (see Fig. 2.11 (c)).

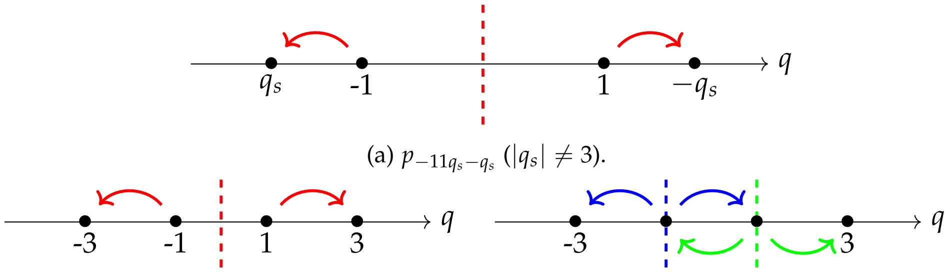

(a) $p_{-11q_s-q_s}$ ($|q_s| \neq 3$).

(b) p_{-11-33} ($|q_s| = 3$).

(c) $p_{-1-11-3}$, p_{11-13} ($|q_s| = 3$).

Figure 2.18. Illustrations of different symmetry axes (dashed lines) and corresponding FWM processes (curved arrows) for : (a) 4-wave model with $|q_s| \neq 3$, (b,c) 4-wave model with $|q_s| = 3$. Each FWM process corresponds to a symmetry axis of the same color. The FWM processes with wave indices a, b, c and d are denoted as p_{abcd} ($p_{-11q_s-q_s}$ in red, $p_{-1-11-3}$ in blue and p_{11-13} in green). The arrow directions are always opposite on different sides of the symmetry axis but can have reverse directions depending on the direction of energy transfer.

In fact the symmetry of the frequency allocation of the waves is important to find out all the possible FWM processes of the system. This is because each FWM process should respect energy conservation with respect to the four involved photons and thus each such process corresponds to a symmetry axis that divides the four photons on the frequency axis. To provide a simple example of such a scenario, consider the analytical 4-wave model. The signal index is given by q_s. When $|q_s| = 3$, a FWM between two pump1 photons, a signal photon and a pump2 photon is possible since $2\hbar\omega_{-1} - \hbar\omega_{-3} - \hbar\omega_1 = 0$ (see blue curved arrows in Fig. 2.18 (c)). However this FWM process is not possible when $|q_s| \neq 3$ (see Fig. 2.18 (a)). Thus depending on the allocation of frequencies of the involved waves, some FWM processes are possible while others are not.

- **Case 1 : $\boldsymbol{\Delta\beta_{klmn} = 0, A_3(0) = A_{-3}(0) = 0}$:**

  In the case where $\Delta\beta_{klmn} \approx 0$, as proceeding for the signal and HOI case, we can simplify the equations and write the solution for the power of the HOP's $P_3 = |A_3|^2$ and $P_{-3} = |A_{-3}|^2$ as :

$$P_3(z) = P_{-3}(z) = \frac{P}{9}\left[\cosh^2(\sqrt{3}\gamma Pz) - 2\cosh(\sqrt{3}\gamma Pz) + 3\sinh^2(\sqrt{3}\gamma Pz) + 1\right], \tag{2.126}$$

  where the initial conditions for A_3 and A_{-3} are given by :

$$A_3(0) = A_{-3}(0) = 0. \tag{2.127}$$

- **Case 2 :** $\boldsymbol{\Delta\beta_{klmn} \neq 0, A_3(0) \neq A_{-3}(0)}$ **:**

In the case where the $\Delta\beta_{klmn}$'s are non-negligible, using Equation (2.31) we can calculate all the $\Delta\beta_{klmn}$'s appearing in Equations (2.124) and (2.125) as :

$$\Delta\beta_{-1-11-3} = -8C, \quad \Delta\beta_{-113-3} = -16C, \quad \Delta\beta_{11-13} = -8C, \quad \Delta\beta_{-11-33} = -16C. \tag{2.128}$$

Now, using the pump equations and Equation (2.128), we can write Equations (2.124) and (2.125) in a compact matrix-form as :

$$\frac{d}{dz}\begin{bmatrix} A_3 \\ A_{-3}{}^* \end{bmatrix} = i\gamma P \begin{bmatrix} 4 & 2e^{i(6\gamma P-16C)z} \\ -2e^{-i(6\gamma P-16C)z} & -4 \end{bmatrix}\begin{bmatrix} A_3 \\ A_{-3}{}^* \end{bmatrix} + \begin{bmatrix} i\gamma P^{\frac{3}{2}} e^{i(3\gamma P-8C)z} \\ -i\gamma P^{\frac{3}{2}} e^{-i(3\gamma P-8C)z} \end{bmatrix}. \tag{2.129}$$

In order to remove the exponential terms from Equation (2.129), we do the following transformation of variables (see Equation (2.44)) :

$$A_q = B_q e^{i(3\gamma P + C(1-q^2))z}, \tag{2.130}$$

where q=3,-3. Thus we can write :

$$\frac{d}{dz}\begin{bmatrix} B_3 \\ B_{-3}{}^* \end{bmatrix} = i\gamma P \begin{bmatrix} 1-F_3 & 2 \\ -2 & -(1-F_3) \end{bmatrix}\begin{bmatrix} B_3 \\ B_{-3}{}^* \end{bmatrix} + \begin{bmatrix} i\gamma P^{\frac{3}{2}} \\ -i\gamma P^{\frac{3}{2}} \end{bmatrix}, \tag{2.131}$$

where F_3 is given by Equation (2.46) with $|q| = 3$. Thus again we have an equation of the form :

$$\frac{d\mathbf{B}}{dz} = \mathbf{M}'\mathbf{B} + \mathbf{N}. \tag{2.132}$$

This is a first order inhomogeneous differential equation. Note that the homogeneous part of Equation (2.131) gives the equation that the analytical 4-wave model would have predicted (see Equation (2.45)). Therefore we know the solution to the homogeneous part (see Equation (2.55)). In fact, since the inhomogeneous part is a constant, solving this system is quite straightforward. Therefore we write the solution of this system as :

$$\begin{aligned} \begin{bmatrix} B_3(z) \\ B_{-3}{}^*(z) \end{bmatrix} = & \\ & \begin{bmatrix} \cos(\gamma P\mu_3 z) - \frac{\eta_3}{\mu_3} i\sin(\gamma P\mu_3 z) & \frac{2}{\mu_3} i\sin(\gamma P\mu_3 z) \\ -\frac{2}{\mu_3} i\sin(\gamma P\mu_3 z) & \cos(\gamma P\mu_3 z) + \frac{\eta_3}{\mu_3} i\sin(\gamma P\mu_3 z) \end{bmatrix}\begin{bmatrix} B_3(0) \\ B_{-3}{}^*(0) \end{bmatrix} \\ & + \sqrt{P}\begin{bmatrix} \frac{-(2+\eta_3)}{\mu_3^2}\cos(\gamma P\mu_3 z) + \frac{2+\eta_3}{\mu_3^2} + \frac{i}{\mu_3}\sin(\gamma P\mu_3 z) \\ \frac{-(2+\eta_3)}{\mu_3^2}\cos(\gamma P\mu_3 z) + \frac{2+\eta_3}{\mu_3^2} - \frac{i}{\mu_3}\sin(\gamma P\mu_3 z) \end{bmatrix}, \end{aligned} \tag{2.133}$$

where μ_3 and η_3 are given by Equation (2.53) with $|q| = 3$. We note that the first term on the right hand side of Equation (2.133) is the solution of the homogeneous system and the second term originates due to the inhomogenity in

Equation (2.131). It is also interesting to notice that the second term has a prefactor of $\sqrt{P}$, meaning it is the dominant term in the solution. This also means that if we scan the signal frequency, then for $|q_s| = 3$, suddenly we should observe a strong increase in the wave amplitude due to the extra symmetry of the configuration.

- **Case 3 : $\boldsymbol{\Delta\beta_{klmn} \neq 0, A_3(0) = A_{-3}(0) \neq 0}$:**

We now move to a simpler case where the two HOP's are equal at the fiber input. We use the initial conditions for B_3 and B_{-3} as :

$$B_3(0) = a_3 e^{i\theta_3}, \tag{2.134}$$

$$B^*_{-3}(0) = a_3 e^{-i\theta_3}, \tag{2.135}$$

where $a_{\pm 3}$ and $\theta_{\pm 3}$ are the amplitudes and phases of $B_{\pm 3}$ at the input. Thus we have :

$$\begin{aligned} B_3(z) = B_{-3}(z) = i\frac{a_3}{\mu_3}\left[-\eta_3 e^{i\theta_3} + 2e^{-i\theta_3}\right]\sin(\gamma P\mu_3 z) + a_3 e^{i\theta_3}\cos(\gamma P\mu_3 z) \\ + i\frac{\sqrt{P}}{\mu_3}\sin(\gamma P\mu_3 z) - \frac{\sqrt{P}(2+\eta_3)}{{\mu_3}^2}\cos(\gamma P\mu_3 z) + \frac{\sqrt{P}(2+\eta_3)}{{\mu_3}^2}, \end{aligned} \tag{2.136}$$

Thus from the above equation we conclude that when $a_3 \neq 0$, the output power of the HOP's are expected to oscillate with respect to θ_3 around an average value given by the last three terms of the right hand side, that are independent of θ_3. In Fig. 2.19 we plot the output powers (left axis) of the HOP's as a function of their input phases θ_3 for two different values of the input HOP powers : $|a_3|^2 = 1$ mW (red solid line) and $|a_3|^2 = 0$ mW (blue dashed line). Here we have considered a rescaled unit system where the modulus square of the complex amplitudes give the power in Watts. The corresponding gain (for $|a_3|^2 = 1$ mW) is shown in the right axis.

We see from Fig. 2.19 that when $a_3 = 0$, a constant output HOP power is obtained, however when $a_3 \neq 0$, we find the output HOP power to be dependent on its input phase θ_3[12]. We also find from Fig. 2.19 that for a small input HOP power of 1 mW, a gain of around 77 dB was obtained. Such a high gain can be attributed to efficient FWM processes between the pumps and the HOP's in the fiber. This lets us wonder whether we can use a configuration (like subsystem 3) to achieve high gain PSA functionality. A similar strategy is also proposed

---

[12] The output power of the HOP's depend on the phase difference between the pumps and the HOP's too. In our case, the HOP's are considered to have the same phase θ_3 at the input, and the pump phases at the input are assumed to be 0.

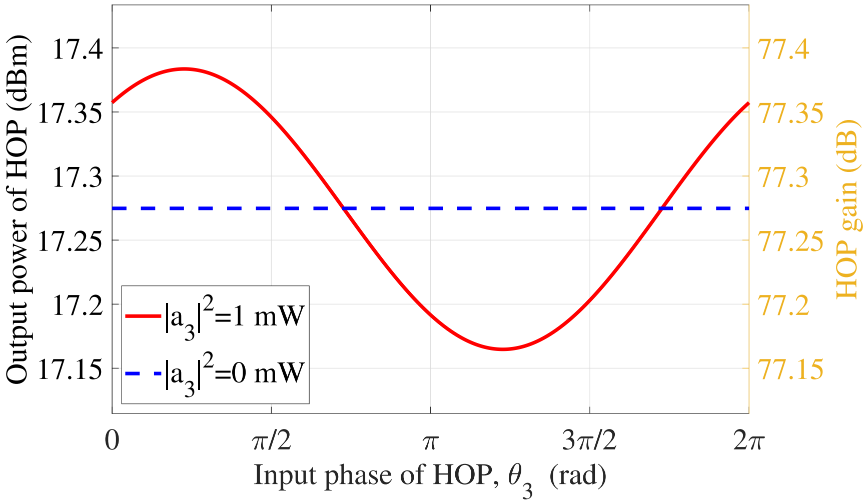

Figure 2.19. Plot of output power (left axis) and gain (right axis, except for when $|a_3|^2 = 0$) of HOP's using the analytical 7-wave model as a function of its input phase θ_3 for two different input powers : $|a_3|^2 = 0$ mW (blue dashed line) and $|a_3|^2 = 1$ mW (red solid line). At the fiber input, the HOP fields are considered equal. $P = 20$ dBm, $\gamma = 11.3\ \mathrm{W}^{-1}\mathrm{km}^{-1}$, $\lambda_0 = 1557.5$ nm, $\lambda_{ZDW} = 1547.5$ nm, $D^{'} = 0.017$ ps/nm^2/km and $L = 500$ m.

in Ref. [174]. A comprehensive analysis of the nonlinear dynamics of such a system can be found in [175].

- **Case 4 : $\boldsymbol{\Delta\beta_{klmn} \neq 0, A_3(0) = A_{-3}(0) = 0}$:**

For most practical purposes we can use $A_3(0) = A_{-3}(0) = a_3 = 0$ to get a simpler form of the expression for $B_{\pm 3}(z)$. Thus from Equation (2.136) using $a_3 = 0$, we have :

$$B_3(z) = B_{-3}(z) = i\frac{\sqrt{P}}{\mu_3}\sin(\gamma P\mu_3 z) - \frac{\sqrt{P}(2+\eta_3)}{{\mu_3}^2}\cos(\gamma P\mu_3 z) + \frac{\sqrt{P}(2+\eta_3)}{{\mu_3}^2}. \tag{2.137}$$

The corresponding powers $P_{\pm 3}(z)$ are given as :

$$\begin{aligned} P_3(z) = P_{-3}(z) &= \frac{P}{{\mu_3}^2}\sin^2(\gamma P\mu_3 z) - \frac{P(2+\eta_3)^2}{{\mu_3}^4}\cos^2(\gamma P\mu_3 z) \\ &+ \frac{2P(2+\eta_3)^2}{{\mu_3}^4}\cos(\gamma P\mu_3 z) - \frac{P(2+\eta_3)^2}{{\mu_3}^4}. \end{aligned} \tag{2.138}$$

As we have seen before in the case of the analytical 4-wave model, here also, depending on whether ${\mu_3}^2$ is non-negative or negative, $P_3(z)$ will be either sinusoidal or hyperbolic in nature respectively. Consequently in Fig. 2.20 we plot ${\mu_3}^2$ as a function of $\Delta\lambda_{PP}$ for $\gamma = 11.3\ (\mathrm{W.km})^{-1}$, $P = 20$ dBm, $\lambda_0 = 1557.5$ nm (or $\delta\lambda_{ofs} = \lambda_0 - \lambda_{ZDW} = 10$ nm), $\lambda_{ZDW} = 1547.5$ nm and dispersion slope of the fiber $D^{'} = 0.017$ ps/nm^2/km. From Fig. 2.20 we see that ${\mu_3}^2 \geq 0$ for

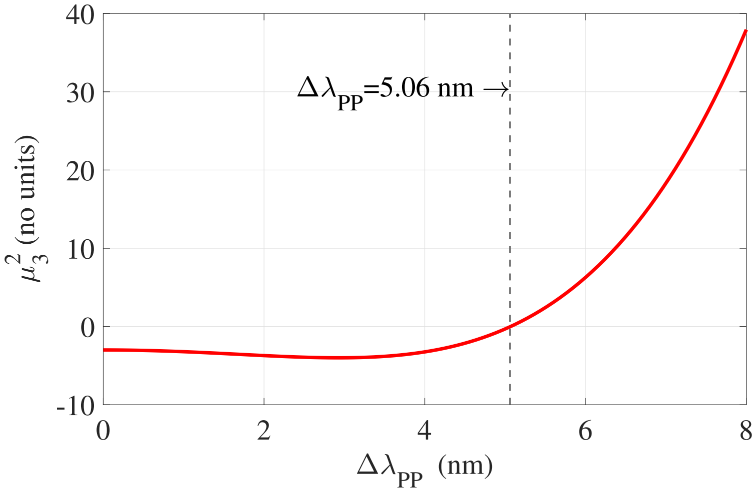

Figure 2.20. Plot of $\mu_3{}^2$ as a function of $\Delta\lambda_{PP}$. The vertical grey dashed line shows the position where $\mu_3{}^2 = 0$. A non-degenerate pump configuration is considered. $P = 20$ dBm, $\gamma = 11.3$ W^{-1}km^{-1}, $\lambda_0 = 1557.5$ nm, $\lambda_{ZDW} = 1547.5$ nm and $D' = 0.017$ ps/nm^2/km.

$\Delta\lambda_{PP} \geq 5.06$ nm and $\mu_3{}^2 < 0$ for $\Delta\lambda_{PP} < 5.06$ nm.

Here we can also ask the question that, can there be a situation, where the output HOP powers are zero at the output of the fiber? This also means that the terms on the right hand side of Equation (2.137) add up to zero. Thus equating both the real and imaginary parts to zero, we obtain the following condition to be satisfied :

$$\begin{cases} \frac{-(2+\eta_3)}{\mu_3{}^2}\Big(\cos(\gamma P \mu_3 L) - 1\Big) = 0, \ \frac{\sin(\gamma P \mu_3 L)}{\mu_3} = 0 & \text{when } \mu_3{}^2 \geq 0, \\ \frac{-(2+\eta_3)}{\mu_3{}'^2}\Big(\cosh(\gamma P \mu_3{}' L) - 1\Big) = 0, \ \frac{\sinh(\gamma P \mu_3{}' L)}{\mu_3{}'} = 0 & \text{when } \mu_3{}^2 < 0, \end{cases} \tag{2.139}$$

where $\mu_3{}' = \sqrt{-\mu_3{}^2}$. Hence we see that when $\mu_3{}^2 < 0$, Equation (2.139) does not have a solution as $\sinh(aL)/L$ is a strictly positive function of L for an arbitrary positive a. However, when $\mu_3{}^2 > 0$, we have a solution as :

$$\gamma P \mu_3 L = 2n\pi, \tag{2.140}$$

where $n \in \mathbb{Z}\backslash\{0\}$. We note here that, n cannot take the value 0 because that would mean $\mu_3 = 0$, thus we have $\lim_{\mu_3 \to 0} \frac{\sin(\gamma P \mu_3 L)}{\mu_3} = \gamma P L \neq 0$. In Fig. 2.21 we plot in dashed line, $\gamma P \mu_3 L - 2n\pi$ (right axis) as a function of $\Delta\lambda_{PP}$ when $\mu_3{}^2 > 0$ for n =1 (red), 2 (blue), 3 (green), 4 (magenta) and 5 (black). The roots of all these curves correspond to a situation where $B_3(L) = 0$ (or $P_3(L) = 0$). This phenomenon is also reflected in the dips in the plot of output power of the HOP's (left axis, shown in red solid line) in Fig. 2.21. Grey dashed lines are used to show the concurrency of the dips of output HOP powers with the roots of Equation (2.140).

The above discussion suggests that by tailoring the pump-pump wavelength separation and/or $\gamma P L$, it is possible to achieve a PSA with suppressed HOP's

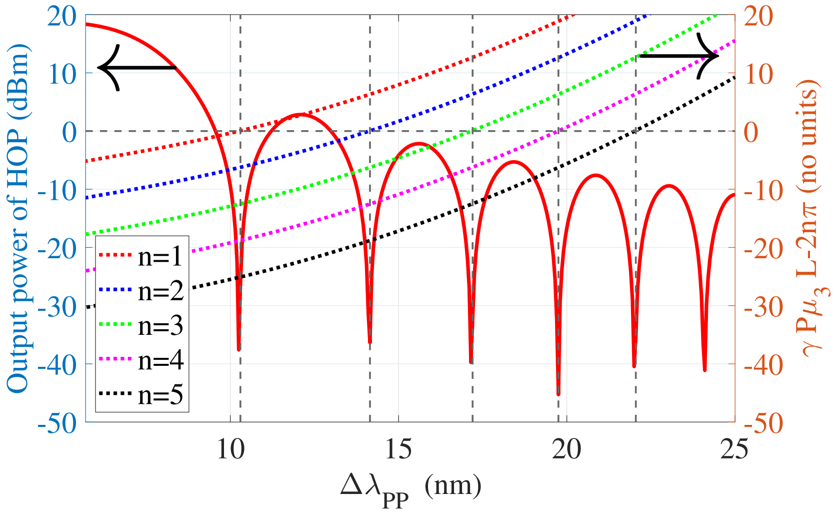

Figure 2.21. Plot of output HOP powers considering $\Delta\beta_{klmn} \neq 0$, $A_3(0) = A_{-3}(0) = 0$ as a function of $\Delta\lambda_{PP}$ (red solid line). Plot of $\gamma P \mu_3 L - 2n\pi$ as a function of $\Delta\lambda_{PP}$ when ${\mu_3}^2 > 0$ in dotted line for $n = 1$ (red), 2 (blue), 3 (green), 4 (magenta) and 5 (black). Grey dashed lines are for visual aid. $L = 500$ m. Other parameters are same as in Fig. 2.20.

at the output when the strong pump approximation is valid. Such an operation might be useful due to the detrimental nature of the HOP's often observed in FOPA operations specially when the pump-pump wavelength separation is small [92].

Thus so far we derived the analytical expressions of all the seven waves in a 7-wave model to describe the CW light propagation in a FOPA. These solutions are only valid when the pump waves are much stronger than the other waves along the fiber. To understand the validity of this model, we will compare these results with the corresponding 7-wave numerical model (considering all the FWM terms) in the next subsection.

2.4.11 Comparison of Analytical 3- and 7-Wave Models with Numerical 7-Wave Model

In our approach to develop the analytical 7-wave model, we only considered the terms that contain at least two pump amplitudes [56] to obtain a linear system of coupled differential equations that we can solve. This limits the validity of our model. With the increase of either the pump power, fiber length or the nonlinear coefficient, the FOPA starts behaving more and more nonlinearly. When the nonlinearity becomes strong, the generated sidebands i.e. $A_{\pm 2}$ and $A_{\pm 3}$ become important to describe the dynamics of the FOPA. In such cases the developed analytical approach becomes inapplicable.

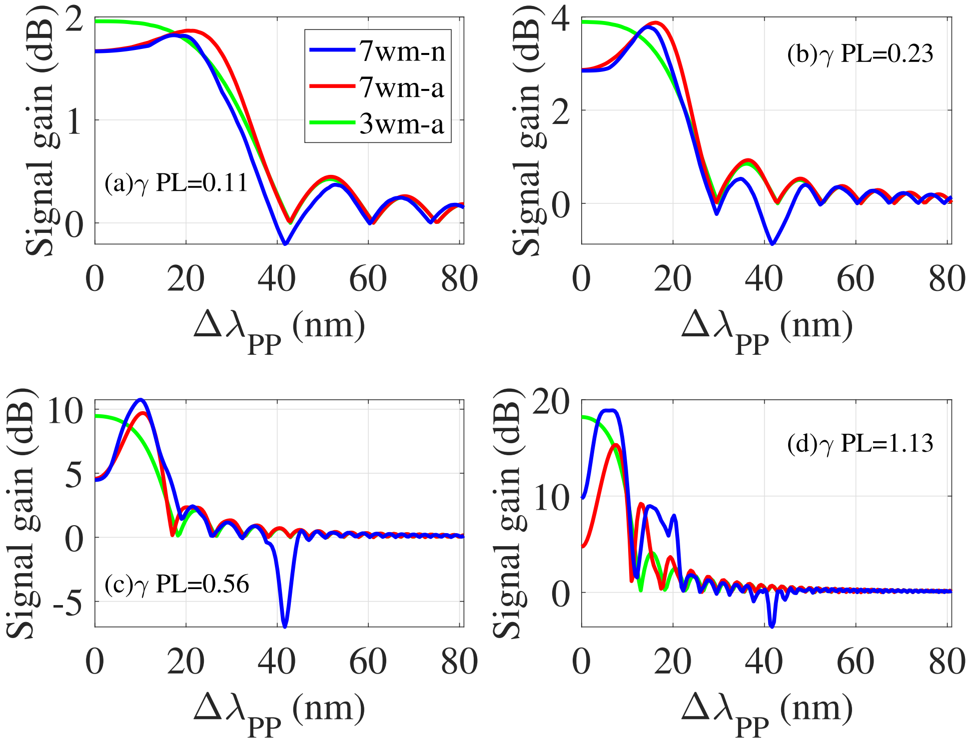

Figure 2.22. Plot of maximum signal gain for a dual-pump PSA as a function of the pump-pump wavelength separation $\Delta\lambda_{PP}$ solving the 3- and 7-wave models (green and red solid lines respectively) analytically and 7-wave model (blue solid line) numerically for different values of γPL : (a) 0.11, (b) 0.23, (c) 0.56 and (d) 1.13. 7wm-n : numerical 7-wave model; 7wm-a : analytical 7-wave model; 3wm-a : analytical 3-wave model. Other parameters are provided in Table 2.2.

In contrast to an analytical approach, using a numerical approach, one can solve the set of seven coupled nonlinear differential equations[13], without making any approximation [91]. In fact Qian *et al.* numerically solved the coupled equations for a dual pump PSA for as large as 27 waves [92]. Nevertheless, an analytical approach might help us gain a better insight of the physics of the system.

In order to validate our approach, we compare the dependence of maximum signal gain (with respect to input signal phase) of a dual-pump FOPA on the pump-pump wavelength separation, calculated using the analytical 3- and 7-wave models and numerical 7-wave model for different fiber lengths (see Fig. 2.22). For the numerical 7-wave model we neglected the fiber attenuation and used the coupled equations provided in Appendix B. Also note that the different fiber lengths correspond to different values of γPL (0.11 for $L = 100$ m, 0.23 for $L = 200$ m, 0.56 for $L = 500$ m and 1.13 for $L = 1000$ m) or the nonlinear phase. This quantity is a characteristic of the nonlinearity of the system.

From Figs. 2.22 (a), (b), (c) and (d) we see that all the three models predict approximately the same signal gain for a large pump-pump wavelength separation

---

[13] The differential equation for the signal is given in Equation (2.58). A complete set of seven coupled equations is given in in Appendix B.

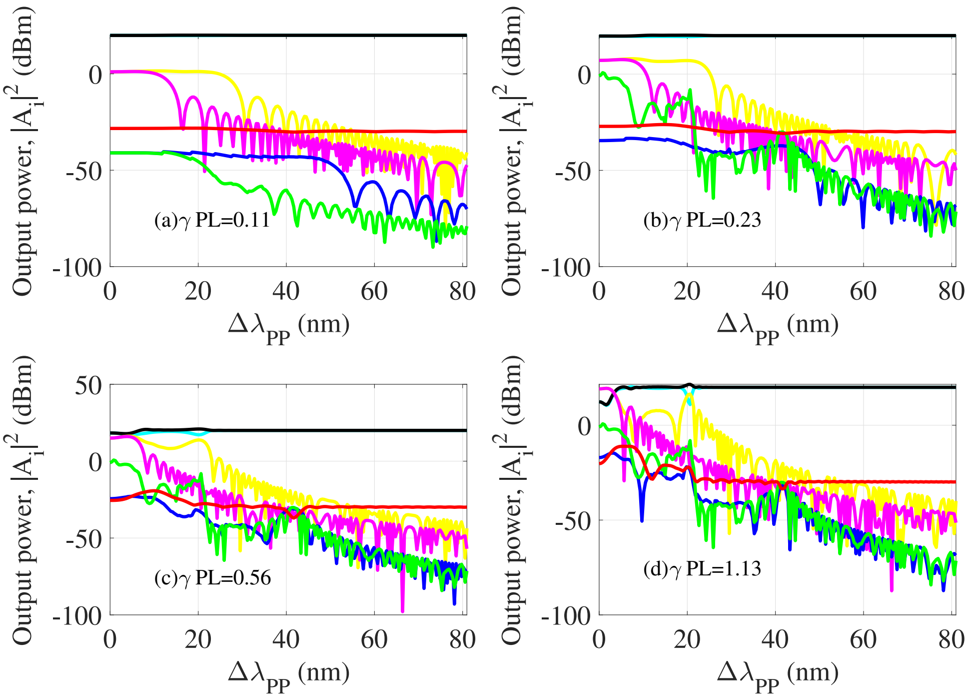

Figure 2.23. Plot of output power of the different waves $|A_i|^2$ (signal (red), pumps (black and cyan), HOI's (blue and green), HOP's (yellow and magenta)) with pump-pump wavelength separation for different values of γPL : (a) 0.11, (b) 0.23, (c) 0.56 and (d) 1.13. The numerical 7-wave model is considered. Other parameters are provided in Table 2.2.

($\Delta\lambda_{PP} > 60$ nm). The deviation between the analytical 7-wave model and the numerical 7-wave model however thins out for larger pump-pump separations. We also see, when the pump-pump wavelength separation is low ($\Delta\lambda_{PP} < 10$ nm), the analytical 3-wave model deviates significantly from the 7-wave numerical model, but for $\gamma PL < 0.5$, the analytical 7-wave model predicts almost the same signal gain as the numerical 7-wave model.

We point out here that the analytical 3- and 7-wave models described in Sections 2.2 and 2.4 respectively, do not take into account pump depletion, whereas their numerical counterparts do. For the numerical approach, we numerically solve the seven coupled differential equations (obtained from Equation (2.4)) for the seven waves and scan the input signal phase to get the maximum gain[14]. The only approximations considered in the numerical model are : 1. fiber attenuation coefficient α was set to zero, and 2. dispersion terms were considered till the second order (similar to the analytical 4- and 7-wave models).

Following Xie *et al.* who predicted the possibility of attaining a higher signal gain (compared to the 3-wave model) in the anomalous dispersion region [91], we restrict our analysis to the anomalous dispersion region ($\delta\lambda_{ofs} = \lambda_0 - \lambda_{ZDW} > 0$). The parameters used for this simulation are provided in the Table 2.2.

We also plot in Fig. 2.23, the output powers of the different waves as a function

---

[14] This numerical model is also discussed in Ref. [89].

System Parameter List			
HNLF	**Parameter**	**Value**	**Unit**
Standard	Input signal power : P_0	-30	dBm
	Input pump power : P	20	dBm
	Signal wavelength : λ_0	1557.5	nm
	Zero dispersion wavelength of HNLF : λ_{ZDW}	1547.5	nm
	Nonlinear coefficient of HNLF : γ	11.3	$(\text{W.km})^{-1}$
	Wavelength offset from zero dispersion wavelength : $\delta\lambda_{ofs} = \lambda_0 - \lambda_{ZDW}$	10	nm
	Dispersion slope of HNLF : $D^{'}$	0.017	$\text{ps.nm}^{-2}.\text{km}^{-1}$

Table 2.2. Table of system parameters used to compare the analytical 7-wave model with the numerical 7-wave model.

of $\Delta\lambda_{PP}$ for different values of γPL considering the numerical 7-wave model. From Fig. 2.23 (a) and (b) (i.e. $\gamma PL < 0.5$), we see that for the whole range of pump-pump wavelength separation, the pumps remain undepleted at the output of the fiber as all the other waves are much weaker than the pumps. This ensures us the validity of the strong pump approximation. However on the other hand, in Figs. 2.23 (c) and (d) (i.e. $\gamma PL > 0.5$) we find that when $\Delta\lambda_{PP}$ is less than about 25 nm, the HOP's become comparable in power to the pumps at the fiber output. This implies that, as γPL increases (typically >0.5), the analytical 7-wave model starts becoming inaccurate as the HOP's (see magenta and yellow curves in Figs. 2.23 (c) and (d)) become comparable to the pump waves at the fiber output.

2.4.12 Physical Interpretation

In this subsection we provide a physical interpretation of how the seven waves interact in a nonlinear fiber in terms of FWM processes. We consider the analytical 7-wave model, and analyze the case where only the signal and the two pumps are launched at the input of the fiber. We have seen that the differential equation of the signal wave evolution in a FOPA, considering a 7-wave model, consists of 22 FWM processes (see Equation (2.58)). However, when the length of the FOPA is small, we can assume that the pumps have a much larger power than the signal, HOI's and the HOP's. Thus we can neglect the terms that do not contain two pumps, and arrive at a simpler equation that can be solved analytically (see Equations (2.59), (2.60) and (2.61)).

As discussed before, the evolution of the HOP's turn out to be independent of the signal and the HOI's under the strong pump approximation, and are well understood (see Subsection 2.4.10). The situation is however more complicated for the signal and HOI's, as their evolution are coupled through several FWM processes. To analyze this, first we define the effective phase mismatch term κ_{kmnl} as [91] :

$$\kappa_{kmnl} = \gamma P_{kmnl} - \Delta\beta_{kmnl}, \tag{2.141}$$

where γP_{kmnl} is the nonlinear phase mismatch and P_{kmnl} is given by :

$$P_{kmnl} = P_k + P_m - P_n - P_l, \tag{2.142}$$

where P_i is the power of the wave at frequency ω_i at the end of the fiber ($i = k, l, m$ and n). The effective phase mismatch κ_{kmnl} provides an estimate of the efficiency of the FWM process p_{klmn} occurring between the waves at frequencies ω_k, ω_l, ω_m and ω_n (see Fig. 2.24) [135]. A small value ($\approx$ 0) of the effective phase mismatch implies a highly efficient FWM between the corresponding waves whereas larger values indicate inefficient FWM [58].

For the simplest case, i.e. the 3-wave model, the only effective phase mismatch term κ_{1-100} (see corresponding process p_{1-100} in Fig. 2.24 (a)) is given by :

$$\kappa_{1-100} = \gamma P_{1-100} - \Delta\beta_{1-100} \approx \gamma 2P - 2C, \tag{2.143}$$

where we have invoked the non-pump depletion approximation considering the output pump powers to be much larger than the power of the other waves ($P_1 + P_{-1} - P_0 - P_0 \approx 2P$). We calculated $\Delta\beta_{klmn}$ using Equation (2.31). In the case of the analytical 7-wave model, the considered phase mismatch terms are given by (see corresponding processes in Figs. 2.24 (a), (b) and (c)) :

$$\kappa_{1-100} \approx \gamma 2P - 2C, \quad \kappa_{1-2-10} \approx -4C, \quad \kappa_{-1-1-20} \approx \gamma 2P + 2C. \tag{2.144}$$

For the sake of brevity, here we have not listed κ_{1-1-20} and κ_{1120} as they are just the symmetrically opposite processes corresponding to κ_{1-2-10} and $\kappa_{-1-1-20}$ respectively.

We note from Equation (2.32) that $C \propto \Delta\lambda_{PP}^2 \left(\lambda_0 - \frac{\Delta\lambda_{PP}}{2}\right)^{-2} \left(\lambda_0 + \frac{\Delta\lambda_{PP}}{2}\right)^{-2}$. Thus when $\Delta\lambda_{PP}$ is small, $C \propto \Delta\lambda_{PP}^2$. Thus we see from Equation (2.144) that when $\Delta\lambda_{PP}$ is small (< 3 nm), κ_{1-2-10} is also small ($\approx$ 0) as it is independent of P (see Fig. 2.25). Note that κ_{1-2-10} correspond to a FWM process involving two pumps, signal and a HOI (see fig. 2.24 (b)). Thus we can argue, that for a small pump-pump wavelength separation, the large difference between the maximum signal gain from the analytical 3- and 7-wave models (see Fig. 2.13 (a)) is because p_{1-2-10} is not accounted for in the analytical 3-wave model. The FWM process p_{1-2-10} leads to conversion of one pump1 and one signal photon into one HOI1 and one pump2 photon. Thus an efficient occurrence of this process leads to depletion of the maximum gain of the signal at low pump-pump separation (see dip in maximum signal gain in Fig. 2.13 (a) from the analytical 7-wave model for $\Delta\lambda_{PP} \approx 0$).

The effective phase mismatch terms that were not accounted for in the analytical 7-wave model (in Equation (2.144)) but considered in the numerical 7-wave model, are given as (not considering symmetrically opposite terms) :

$$\begin{gathered}\kappa_{-1320} \approx \gamma P - 6C,\ \ \kappa_{-1-2-30} \approx \gamma P + 4C,\ \ \kappa_{-32-10} \approx -\gamma P - 12C, \\ \kappa_{-3300} \approx -18C,\ \ \kappa_{-2200} \approx -8C. \end{gathered} \tag{2.145}$$

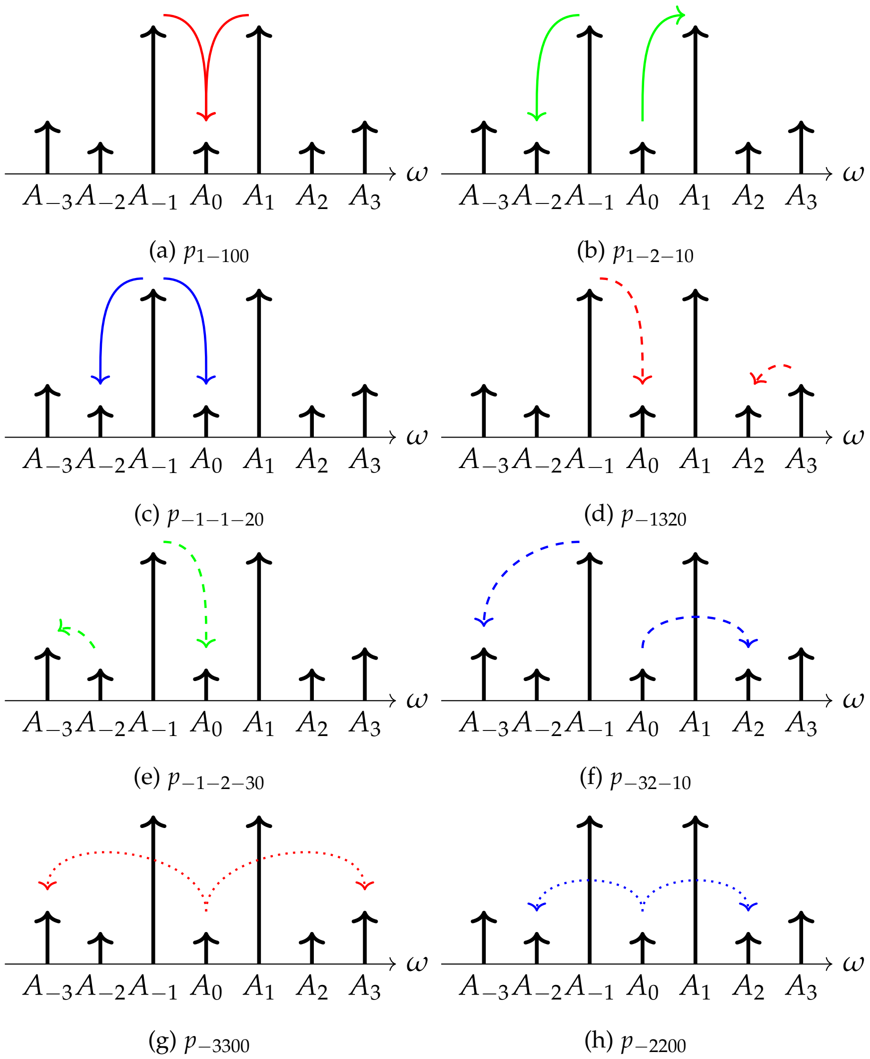

(a) p_{1-100} (b) p_{1-2-10}

(c) $p_{-1-1-20}$ (d) p_{-1320}

(e) $p_{-1-2-30}$ (f) p_{-32-10}

(g) p_{-3300} (h) p_{-2200}

Figure 2.24. An illustration of the different FWM processes in a FOPA. The processes are labelled p_{klmn} where the involved waves are at frequencies ω_k, ω_l, ω_m and ω_n. (a), (b) and (c) are the processes used in the analytical 7-wave model. The analytical 3-wave model considers only (a). The direction of the arrows show the direction of energy flow obtained from the numerical 7-wave model simulation [91].

From Equation (2.145) we see that when the pump-pump wavelength separation $\Delta\lambda_{PP}$ is small (< 10 nm), i.e. C is small, the only effective phase mismatch terms that are small (≈ 0) are κ_{-3300} and κ_{-2200} (see corresponding processes in Figs. 2.24 (g) and (h)). But these two processes, which lead to conversion of two signal photons into a HOI1 (HOP1) and a HOI2 (HOP2) photons, involve no pumps. Thus for a small length of the fiber, these processes will not have a strong influence on the signal evolution. Hence, the analytical 7-wave model converges with the numerical

7-wave model for a short length of the fiber, when the pump-pump wavelength separation is small (see Fig. 2.22 (a) and (b)).

In Fig. 2.25 we plot the product of the effective phase mismatch κ_{kmnl} (corresponding to a FWM processe p_{kmnl}) and the fiber length L, as a function of the pump-pump wavelength separation $\Delta\lambda_{PP}$. We consider $\gamma PL = 0.11$ and $\delta\lambda_{ofs} = 10$ nm. An absolute value of $\kappa_{kmnl}L$ near 0 implies an efficient FWM whereas an absolute value close to or larger than π implies low efficiency of the process p_{kmnl} [91]. Other parameters are same as in Table 2.2.

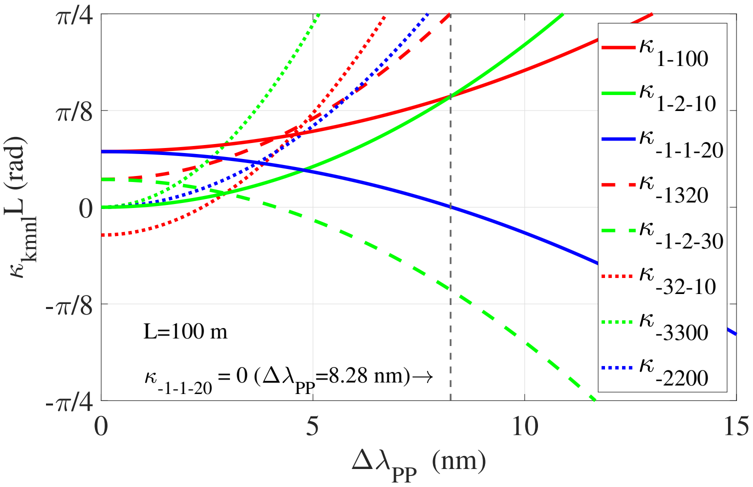

Figure 2.25. Plot of $\kappa_{kmnl}L$ corresponding to different FWM processes p_{kmnl}, as a function of the pump-pump wavelength separation $\Delta\lambda_{PP}$ for $L = 100$ m, $\gamma = 11.3$ (W.km)$^{-1}$, $P = 20$ dBm and $\delta\lambda_{ofs} = 10$ nm. κ_{1-100} (red solid line) corresponds to the only FWM process considered in the 3-wave model p_{1-100}. κ_{1-100}, κ_{1-2-10} (green solid line) and $\kappa_{-1-1-20}$ (blue solid line) correspond to the processes considered in the analytical 7-wave model. κ_{1-100}, κ_{1-2-10}, $\kappa_{-1-1-20}$, κ_{-1320} (red dashed line), $\kappa_{-1-2-30}$ (green dashed line), κ_{-32-10} (blue dashed line), κ_{-3300} (red dotted line) and κ_{-2200} (blue dotted line) correspond to the processes considered in the numerical 7-wave model. The colour coding of the arrows are consistent with Fig. 2.25.

From Fig. 2.25 we see that for small values of pump-pump wavelength separation, ($\Delta\lambda_{PP} < 6$ nm), process p_{1-2-10} is the most efficient process (we neglect p_{-3300} and p_{-2200} as they do not contain pump terms). This explains the fact that at low (< 5 nm) values of $\Delta\lambda_{PP}$ the 3-wave model deviates from the 7-wave analytical and numerical models (see Fig 2.22). For 5 nm$< \Delta\lambda_{PP} < 15$ nm, the most dominant process is $p_{-1-1-20}$ (and p_{1120}) (see Fig. 2.24 (c)). Near $\Delta\lambda_{PP} \approx 8$ nm (or $\eta \approx 0$), we see $\kappa_{-1-1-20} \approx 0$ (see blue solid line in Fig. 2.25). This process leads to an efficient generation of the signal (for $\Delta\lambda_{PP} \approx 8$ nm) and is responsible for the large gain peak seen in Fig. 2.22 (see red curves). For $\Delta\lambda_{PP}$ larger than 15 nm, all the processes start to lose efficiency. Therefore, contribution from all the FWM processes must be accounted for to obtain an accurate signal gain. However, in the case of very large pump-pump wavelength separation, i.e. $\Delta\lambda_{PP} > 60$ nm, the HOI's and the HOP's are very weak due to the inefficiency of the processes that generate them. Thus in such a case, the analytical 3-wave model is enough to describe the dynamics.

2.4.13 Limitations

The analytical 7-wave model developed here is valid for a limited range of scenarios. The limitations are more or less the same as for the analytical 3- and 4-wave model. The only advantage of the analytical 7-wave model is that it considers the effect of the presence of the HOI's in the signal evolution.

The analytical 7-wave model is valid only when the nonlinear phase γPL is small (<0.5) and the pump-pump wavelength separation $\Delta\lambda_{PP}$ is either small (<5 nm) or large (>60 nm). For larger values of γPL (>0.5), the signal, HOI's and HOP's can have large gains (typically for small values of $\Delta\lambda_{PP}$ (<5 nm)) leading to a significant depletion of the pumps and hence making the analytical 7-wave model invalid (see Fig. 2.22 (d)).

In this model we neglected the higher order terms ($n > 2$) in the Taylor series expansion of $\beta(\omega)$. In certain cases, for example with larger values of $\Delta\lambda_{PP}$ (typically >5nm) or when the wavelength of the considered waves are close (within a few nanometers) to the zero dispersion wavelength, higher order treatment is solicited for accurate results [58].

2.4.14 PSA Noise Figure

A FOPA in a PSA configuration can act as an amplifier without degrading the signal to noise ratio (SNR) [47]. Further, due to the broad gain spectrum of dual pump FOPA's, they are attractive candidates for low noise optical amplification [88, 155, 176][15]. However, due to the non-existence of a general solution of the 7-wave model (or n-wave model), a full quantum treatment of calculating the NF is difficult to achieve [157]. Thus, the developed 7-wave analytical model might be useful to calculate the noise figure (NF) of a dual pump PSA with a full quantum treatment considering seven interacting waves.

2.5 Conclusion

In this chapter we developed a formalism to describe propagation of seven CW waves through a nonlinear fiber. We considered the fiber acting as a FOPA and considered a dual-pump with degenerate signal and idler configuration. We fragmented the 7-wave system into three subsystems, one with the signal, one with the HOI's and one with the HOP's. The HOP subsystem decouples from the signal and HOI's when the pumps are strong.

The HOP's show strong amplification due to an efficient FWM between the two pumps to generate the HOP's. The dynamics of the coupled signal and HOI's turns out to be more complex and is similar to that of two coupled oscillators.

---

[15] The 3dB limit of noise figure of a PIA was surpassed by several investigations in the context of fiber phase sensitive amplification [53, 177]. Recently, Liu *et al.* demonstrated the low-noise performance of a PSA-based hybrid optical amplifier with a noise figure lower than 3 dB [176].

From the developed model, we found that in the analytical 7-wave model, the maximum PSA gain of the signal shows a resonance when the dispersive and nonlinear effects of the fiber achieve a balance in the anomalous dispersion region. Moreover we found that the solution of the analytical 7-wave model is always sinusoidal, however with a larger parametric gain coefficient than the 4-wave model. This change in the gain coefficient is mediated by the coupling of the signal with the HOIs. This is different from the analytical 4-wave model where the high PSA gain of the signal is not due to a large gain coefficient, rather due to the hyperbolic nature of the obtained solution.

The analytical 7-wave model predicts the maximum signal gain accurately (as verified with a numerical approach with less stringent assumptions) when γPL is less than 0.5. We also found that the HOI's play an important role in the system evolution. In particular, its coupling with the signal leads to a change in the signal gain which is unaccounted for in the analytical 3-wave model.

Using the developed model, we explored PSA configurations with non-zero HOI powers at the input of the fiber. We found a significant increase in the maximum signal gain for such configurations.

We also described how the system can be used as a PSFC by launching just HOI1 at the input, to generate either signal or HOI2 at the output depending on the input phase of HOI1.

These developments not only open new perspectives in the development of modern PSA based technologies, but also gives us a better insight into the physics of interaction of multiple CW waves within a nonlinear medium.

Chapter Highlights

From the developed analytical 7-wave model, we found out the following results.

- **Decoupling of HOPs :** The subsystem containing the HOPs, decouples from the other two subsystems, i.e. from the signal and the HOIs when the pumps are assumed to be much stronger than the other waves. Thus the HOPs can be analyzed separately, independently of the signal and the HOIs.
- **Large Amplification of HOPs :** The HOPs exhibit a very strong amplification due to an efficient FWM mechanism that involves two pumps and a HOP. This FWM is possible as the pump-pump wavelength separation is equal to the pump-HOP wavelength separation.
- **Phase Sensitive Frequency Conversion (PSFC) :** We found that a dual-pump PSA system can be used as a PSFC by launching just HOI1 at the fiber input, to generate either signal or HOI2 at the output depending on the input phase of HOI1.
- **Signal Modulation Instability :** While for the analytical 3-wave model, the modulation instability of the signal originated from the solution having hyperbolic terms (when parametric gain coefficient $\gamma P \mu_0$ is imaginary), in contrast, for the analytical 7-wave model, the signal modulation instability is mainly due to the larger value of the parametric gain coefficient $\gamma P \nu_0$ compared to $\gamma P \mu_0$, which is a result of the coupling of the HOIs with the signal.
- **Validity of the Analytical Model :** The analytical 7-wave model predicts the maximum signal gain for a dual-pump PSA accurately (as verified with a numerical approach considering all FWM terms) when the nonlinear phase γPL is less than 0.5 rads.

Chapter 3

Nonlinear Schrödinger Equation

Contents

3.1 Introduction . . . 82
- 3.1.1 Input Electric Field . . . 82
- 3.1.2 Dispersion . . . 83
- 3.1.3 Derivation of NLSE . . . 84
- 3.1.4 Change of Reference Frame . . . 84
- 3.1.5 Attenuation of the Medium . . . 85
- 3.1.6 Calculation of Parameters . . . 85

3.2 Numerical Model . . . 87
- 3.2.1 SSFM Algorithm . . . 88
- 3.2.2 Step Size . . . 91
- 3.2.3 Spectral Leakage . . . 93

3.3 Verification of Numerical Model . . . 94
- 3.3.1 Parameters . . . 95
- 3.3.2 PIA . . . 96
- 3.3.3 PSA . . . 99

3.4 Discussion and Conclusion . . . 100
- 3.4.1 Comparison of Models . . . 100
- 3.4.2 Conclusion . . . 102

3.1 Introduction

In the previous chapter we looked at situations where we dealt with propagation of at most seven CW waves through a nonlinear fiber. However, with the n-wave model, for higher number of waves, i.e. more than seven waves, the coupled set of differential equations that determine the propagation of different waves becomes enormously complicated. This is because with the increase in number of waves, the number of terms originating from the four wave mixing of the different waves increases as $\sim n^3$ [90]. Thus it becomes very difficult to tackle the problem analytically or numerically. This brings us to the requirement of an alternative approach.

In contrast to the n-wave model, the nonlinear Schrödinger equation (NLSE) can describe the propagation of a continuous spectrum of waves through a nonlinear fiber [56, 58, 178–181]. Thus for scenarios with large number of waves, it becomes much more convenient to numerically simulate the wave propagation using a NLSE based approach.

In real life, indeed there are situations which require to deal with a large number of waves. An example of such a situation is a wavelength division multiplexing (WDM) system [182]. Also, in the case of fiber phase sensitive amplifiers, the pump waves are often modulated to suppress stimulated Brillouin scattering (SBS) [63–66]. Analysis of the propagation of such modulated CW waves through a nonlinear fiber inevitably requires a NLSE based model, since it can handle simultaneous evolution of multiple waves through a nonlinear fiber.

This chapter is organized as follows. Section 3.1 focuses on a general description of NLSE explaining all the different terms in the equation. Then in Section 3.2 a numerical model based on split-step Fourier method is discussed to solve the NLSE. Then in Section 3.3 the numerical model is validated with analytical solutions and experimental data for the simple case of three wave propagation through a fiber. Finally, in Section 3.4 a comparison between the n-wave models developed in Chapter 2 and the numerical NLSE model is provided with respect to their validity regimes. Also the key points of this chapter are summarized.

3.1.1 Input Electric Field

In the most general case, when we consider N discrete frequency CW waves at the input of the nonlinear fiber. The real electric field $E(0,t)$ at the input can be written as :

$$E(0,t) = \sum_{k=1}^{N} A_k e^{-i\omega_k t} + c.c. \,, \tag{3.1}$$

where A_k is the complex amplitude of the wave component at frequency ω_k and $c.c.$ denotes complex conjugate. When all the wave components in the input field are centered close to a central frequency ω_c, we can approximate the real electric field

$E(z,t)$ inside the fiber in the form :

$$E(z,t) = A(z,t)e^{i(\beta_c z - \omega_c t)} + c.c.\,, \tag{3.2}$$

where β_c is the propagation constant at the central frequency ω_c. We can also see from the above equation that for $z = 0$, we can write the real electric field $E(0,t)$ as :

$$E(0,t) = A(0,t)e^{-i\omega_c t} + c.c.\,. \tag{3.3}$$

We define the Fourier transform of the complex amplitude $A(z,t)$ at $z = 0$ as :

$$A(0,t) = \frac{1}{\sqrt{2\pi}} \int_{\Omega=-\infty}^{\infty} B(0,\Omega)e^{-i\Omega t} d\Omega, \tag{3.4}$$

where we have used $\Omega = \omega - \omega_c$ and we have considered the symmetric version of Fourier transform. The advantage of using the Fourier transform is the fact that when we consider only dispersive effects of the fiber, we can evaluate the evolution of $B(0,\Omega)$ in the fiber just by multiplying a phase to it.

3.1.2 Dispersion

In a dispersive medium, the waves at different frequencies propagate with different speeds. We look at the dispersion of our medium given by the quantity $\beta(\omega)$, which is the propagation constant of a wave at frequency ω. $\beta(\omega)$ can be written as a Taylor series expansion around a central frequency ω_c as :

$$\beta(\omega) = \sum_{n=0}^{\infty} \frac{\beta^{(n)}}{n!}(\omega - \omega_c)^n = \beta_c + \sum_{n=1}^{\infty} \frac{\beta^{(n)}}{n!}\Omega^n, \tag{3.5}$$

where $\beta_c = \beta(\omega_c)$, $\Omega = \omega - \omega_c$ and $\beta^{(n)} = \frac{d^n\beta}{d\omega^n}$ at $\omega = \omega_c$. Physically, ω_c/β_c is the phase velocity of the wave component at the central frequency ω_c. $1/\beta^{(1)}$ is the group velocity of the wave. $\beta^{(2)}$ is known as the group velocity dispersion.

In the case of linear propagation, i.e. when we consider only dispersion and no nonlinearity of the fiber, propagation of the complex amplitude in the Fourier domain means only addition of a phase to the initial complex amplitude as we mentioned before. The added phase of a wave at frequency Ω is the wave-vector $\beta(\omega_c + \Omega)$ times the propagation distance z. Considering the initial form of the electric field as defined in Equation (3.2), we can write $A(z,t)$ as :

$$\begin{aligned} A(z,t) &= \frac{1}{\sqrt{2\pi}} \int_{\Omega=-\infty}^{\infty} B(z,\Omega)e^{-i\Omega t} d\Omega \\ &= \frac{1}{\sqrt{2\pi}} \int_{\Omega=-\infty}^{\infty} B(0,\Omega)e^{i\beta(\omega_c+\Omega)z - i\Omega t} d\Omega. \end{aligned} \tag{3.6}$$

3.1.3 Derivation of NLSE

In order to solve for $A(z,t)$, we need to find how its dependence on the position or z, is related to its dependence on time or t. So we start off by taking the partial derivative of $A(z,t)$ with respect to z :

$$\frac{\partial A}{\partial z} = \frac{1}{\sqrt{2\pi}} \int B(0,\Omega) i\beta(\omega_c + \Omega) e^{i\beta(\omega_c+\Omega))z - i\Omega t} d\Omega. \tag{3.7}$$

Using Equation (3.5), we have :

$$\frac{\partial A}{\partial z} = i\frac{1}{\sqrt{2\pi}} \int B(0,\Omega) \left(\sum_{n=0}^{\infty} \frac{\beta^{(n)}}{n!} \Omega^n \right) e^{i\beta(\omega_c+\Omega)z - i\Omega t} d\Omega. \tag{3.8}$$

Now if we take the mth derivative of $A(z,t)$ with respect to t, we get :

$$\frac{\partial^m A}{\partial t^m} = \frac{1}{\sqrt{2\pi}} \int B(0,\Omega) (-i\Omega)^m e^{i\beta(\omega_c+\Omega))z - i\Omega t} d\Omega. \tag{3.9}$$

Comparing Equation (3.8) and Equation (3.9), we find :

$$\frac{\partial A}{\partial z} - \sum_{n=1}^{\infty} \frac{i^{n+1}\beta^{(n)}}{n!} \frac{\partial^n A}{\partial t^n} = 0. \tag{3.10}$$

In the case of optical fibers, $\beta^{(n)}$'s can be neglected for $n > 4$ [58]. Thus we terminate our series at $n = 4$.

So far we have only introduced linear propagation of light considering dispersive effects of a fiber. However, for a nonlinear fiber, we also need to account for the Kerr nonlinearity effects. We introduce this nonlinearity, i.e. $i\gamma|A|^2 A$ as a perturbation term on the right hand side of Equation (3.10) [56] [1]. Thus we have :

$$\frac{\partial A}{\partial z} - \sum_{n=1}^{4} \frac{i^{n+1}\beta^{(n)}}{n!} \frac{\partial^n A}{\partial t^n} - i\gamma|A|^2 A = 0. \tag{3.11}$$

In Equation (3.11), the first and second terms on the left hand side represent the space and time dependence of the complex amplitude A respectively, while the third term arises from the nonlinearity of the fiber.

3.1.4 Change of Reference Frame

At this point, a common technique to simplify Equation (3.11) is to make a change of reference frame from t to $T = t - \beta^{(1)} z$ which is also known as a retarded time frame [58]. This means we change our reference frame from the lab reference frame to one that travels at the group velocity v_g of the wave given by $v_g = \frac{1}{\beta^{(1)}}$. Hence $A(z,t)$ should be written in terms of $A(z, T = t - \beta^{(1)} z)$. We can write equations for

---

[1] The derivation of this Kerr nonlinearity term is non-trivial and is discussed in detail in Ref. [56].

the transformation of variables as :

$$\frac{\partial A}{\partial z} = \frac{\partial A}{\partial T}\frac{\partial T}{\partial z} + \frac{\partial A}{\partial z}\frac{\partial z}{\partial z} = -\beta^{(1)}\frac{\partial A}{\partial T} + \frac{\partial A}{\partial z}, \tag{3.12}$$

$$\frac{\partial A}{\partial t} = \frac{\partial A}{\partial T}\frac{\partial T}{\partial t} + \frac{\partial A}{\partial z}\frac{\partial z}{\partial t} = \frac{\partial A}{\partial T}, \tag{3.13}$$

$$\frac{\partial^m A}{\partial t^m} = \frac{\partial^m A}{\partial T^m} \text{ for } m = 1,2,3... . \tag{3.14}$$

Thus with the transformed variables, Equation (3.11) can be written as :

$$\frac{\partial A}{\partial z} - \sum_{n=2}^{4} \frac{i^{n+1}\beta^{(n)}}{n!}\frac{\partial^n A}{\partial T^n} = i\gamma|A|^2 A. \tag{3.15}$$

We should note here that in the retarded time reference frame, the term with $\beta^{(1)}$ in Equation (3.11) gets dropped. Also, this transformation makes the NLSE easier to solve numerically as we are always looking at variations in the wave near the center of the wave envelope.

We also note that the initial conditions for both the frames of reference, i.e. t and T, are the same, i.e. at $z = 0$, we have $A(z = 0, t) = A(z = 0, t - 0 = T) = A(0, T)$. However, after solving the NLSE, we obtain $A(z = L, T = t - \beta^{(1)}L)$. Therefore to retrieve the solution of the field amplitude in the t-frame, we need to change the variable back to t from T. This means that for a given length L of the fiber, the solution of the complex amplitude A, in the t-frame is the same solution in the T-frame but retarded (for $\beta^{(1)} > 0$) or advanced (for $\beta^{(1)} < 0$) by an amount $\beta^{(1)}L$.

3.1.5 Attenuation of the Medium

So far we did not consider any fiber attenuation in the model. However, the fiber attenuation can be incorporated by just adding a term $\frac{\alpha}{2}A$ on the left hand side of Equation (3.15). α is the attenuation coefficient of the fiber. Thus we get :

$$\frac{\partial A}{\partial z} + \frac{i\beta^{(2)}}{2}\frac{\partial^2 A}{\partial T^2} - \frac{\beta^{(3)}}{6}\frac{\partial^3 A}{\partial T^3} - \frac{i\beta^{(4)}}{24}\frac{\partial^4 A}{\partial T^4} + \frac{\alpha}{2}A - i\gamma|A|^2 A = 0. \tag{3.16}$$

Equation (3.16) is the final form of NLSE that we solve numerically in the subsequent sections.

3.1.6 Calculation of Parameters

For a given fiber, the attenuation coefficient α and the nonlinear coefficient γ are provided by the manufacturer. Depending on the composition of the fiber, we also know the frequency dependence of the effective refractive index, i.e. $n(\omega)$ and the frequency dependence of the derivative of refractive index with respect to ω, i.e. $\frac{dn}{d\omega}(\omega)$ for the fiber. The $\beta^{(n)}$'s are given as follows :

- $\beta^{(1)}$:

  We know that $\beta(\omega)$ can be expressed as :

  $$\beta(\omega) = \frac{n(\omega)\omega}{c}. \tag{3.17}$$

  Now we can take the derivative of Equation (3.17) with respect to ω at $\omega = \omega_c$ and use Equation (3.5) to write :

  $$\beta^{(1)} = \frac{d\beta}{d\omega}\Big|_{\omega=\omega_c} = \frac{1}{c}\left[\left(\frac{dn}{d\omega}\right)_{\omega=\omega_c}\omega_c + n(\omega_c)\right], \tag{3.18}$$

  where $\frac{1}{\beta^{(1)}}$ represents the group velocity of the wave.

  In our case, we have seen that by changing the reference frame from t to T, the term with $\beta^{(1)}$ in the NLSE dropped out. Therefore for using a NLSE based model, we do not need to calculate $\beta^{(1)}$.

- $\beta^{(2)}$:

  The dispersion parameter $D(\lambda)$ of a fiber at a central wavelength λ_c is related to $\beta^{(1)}(\omega_c)$ as :

  $$D(\lambda_c) = \frac{d\beta^{(1)}(\omega_c)}{d\lambda_c} = \frac{d\beta^{(1)}}{d\omega_c}\frac{d\omega_c}{d\lambda_c} = \beta^{(2)}\frac{d\omega_c}{d\lambda_c} = -\frac{2\pi c\beta^{(2)}}{{\lambda_c}^2}, \tag{3.19}$$

  where λ_c is the wavelength corresponding to the central angular frequency ω_c. Thus we get :

  $$\beta^{(2)} = -\frac{{\lambda_c}^2 D(\lambda_c)}{2\pi c}. \tag{3.20}$$

  For most practical scenarios, we can approximate a linear relation between D and λ as (see Fig. 3.1) :

  $$D(\lambda) = D'(\lambda - \lambda_{ZDW}), \tag{3.21}$$

  where D' is the slope of the dispersion parameter of the fiber with respect to wavelength λ. λ_{ZDW} is the wavelength corresponding to zero dispersion ($D = 0$). Both D' and λ_{ZDW} are provided by the manufacturer of the fiber. Hence we can write $\beta^{(2)}$ as :

  $$\beta^{(2)} = -\frac{{\lambda_c}^2 D'(\lambda_c - \lambda_{ZDW})}{2\pi c}. \tag{3.22}$$

- $\beta^{(3)}$:

  Similarly, with subsequent derivatives of $\beta^{(2)}$ with respect to ω_c, we can find $\beta^{(3)}$ and $\beta^{(4)}$. $\beta^{(3)}$ is given by the derivative of $\beta^{(2)}$ with respect to ω_c. Thus we

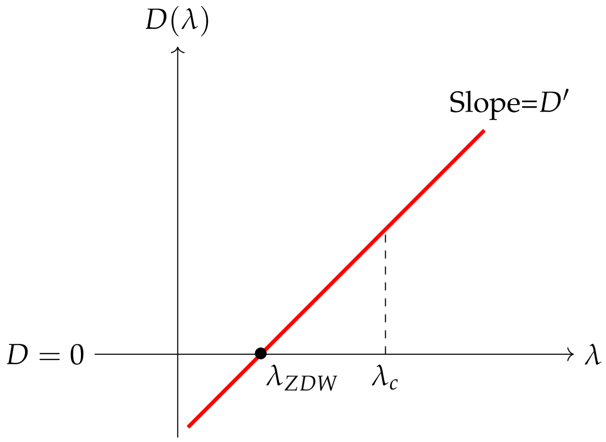

Figure 3.1. Dependence of dispersion parameter D on wavelength λ in an optical fiber. For a given wavelength λ_c, we can find D if we know D' and λ_{ZDW}.

can write :

$$\begin{aligned}\beta^{(3)} &= \frac{d\beta^{(2)}}{d\omega_c} = \frac{d\beta^{(2)}}{d\lambda_c}\frac{d\lambda_c}{d\omega_c} = \frac{d\beta^{(2)}}{d\lambda_c}\frac{d}{d\omega_c}\left(\frac{2\pi c}{\omega_c}\right) \\ &= \frac{-2\pi c}{{\omega_c}^2}\frac{d}{d\lambda_c}\left(-\frac{{\lambda_c}^2 D'(\lambda_c-\lambda_{ZDW})}{2\pi c}\right) \\ &= \frac{{\lambda_c}^3 D'(3\lambda_c-2\lambda_{ZDW})}{4\pi^2c^2}.\end{aligned} \tag{3.23}$$

To derive this we have used the relation $\lambda_c = \frac{2\pi c}{\omega_c}$.

- $\beta^{(4)}$:

  Similarly, we can calculate $\beta^{(4)}$ as :

$$\begin{aligned}\beta^{(4)} &= \frac{d\beta^{(3)}}{d\omega_c} = \frac{d\beta^{(3)}}{d\lambda_c}\frac{d\lambda_c}{d\omega_c} \\ &= \frac{-2\pi c}{{\omega_c}^2}\frac{d}{d\lambda_c}\left(\frac{{\lambda_c}^3 D'(3\lambda_c-2\lambda_{ZDW})}{4\pi^2c^2}\right) \\ &= \frac{-6{\lambda_c}^4 D'(2\lambda_c-\lambda_{ZDW})}{8\pi^3c^3}.\end{aligned} \tag{3.24}$$

Here we have considered D' to be a constant i.e. $D''=0$.

3.2 Numerical Model

The NLSE is a nonlinear partial differential equation. Due to the coupled existence of the linear and the nonlinear terms, it is difficult to find a general form of an analytical solution for the NLSE except for some special cases. These correspond to situations where the inverse scattering method can be employed [183]. Also, some particular classes of analytical solutions are obtainable from the Akhmediev breather theory

[184–188][2]. Moreover these solutions are mostly obtainable considering only a second order derivative term in T, whereas for nonlinear optics, it is often instructive to go up to fourth order derivatives in T (as in Equation (3.16)). Thus in our case, to solve the nonlinear partial differential equation, we resort to a numerical approach.

In the literature, there exist several schemes for solving a nonlinear partial differential equation like the NLSE [26, 56, 58, 190–216]. These methods can be broadly classified into two kinds : 1. finite difference methods and 2. pseudospectral methods. The pseudospectral methods are generally faster up to an order of magnitude than the finite difference methods [196]. Such computational advantage over finite difference methods can be primarily attributed to the use of finite Fourier transform algorithms [217] used in the pseudospectral methods.

In this section we introduce a pseudospectral algorithm, known as the split step Fourier method (SSFM) [26, 191, 192], which we use to solve the NLSE numerically. However there are other pseudospectral methods implementing other transforms, such as the wavelet transform [214] that can perform better than the SSFM method computationally, but at the cost of increased implementation complexity.

The basic idea behind the SSFM algorithm is to break down the NLSE into two simpler differential equations, one with the linear part and the other with the nonlinear part. These simpler equations can be tackled easily numerically. Thus the fiber is divided into small segments and the output field of each segment is numerically calculated based on the input field of that segment treating the linear and nonlinear part separately. In the case of NLSE the linear part corresponds to dispersion and the nonlinear part is the Kerr nonlinearity. The treatment of dispersion and nonlinearity of the medium separately is a reasonable approximation as long as the segment lengths are small. A detailed discussion on this algorithm is presented subsequently.

3.2.1 SSFM Algorithm

The SSFM algorithm is implemented as follows [56, 58, 193, 218]. First we divide the fiber of length L, into n small segments of length $\frac{L}{n} = dz$. Then starting from the first segment, using the input field $E_{in}(0, T)$ (where $T = t - \beta^{(1)} z$ is the retarded time), we calculate the field iteratively through each segment along the length of the fiber to get the output field $E_{out}(L, T)$ at the end of the last segment. In each segment, we treat the dispersion $\hat{D}$ and nonlinearity part $\hat{N}$ of the wave evolution separately. Note that $\hat{D}$ and $\hat{N}$ are considered as operators here. Thus $\hat{D}$ and $\hat{N}$ are given by :

$$\hat{D} = -\frac{i\beta^{(2)}}{2}\frac{\partial^2}{\partial T^2} + \frac{\beta^{(3)}}{6}\frac{\partial^3}{\partial T^3} + \frac{i\beta^{(4)}}{24}\frac{\partial^4}{\partial T^4} - \frac{\alpha}{2}, \tag{3.25}$$

$$\hat{N} = i\gamma|A|^2. \tag{3.26}$$

---

[2] There are other particular solutions to the NLSE, like the Kuznetsov-Ma breather and the Peregrine soliton [189], however such discussion is beyond the scope of this thesis.

Hence we can write Equation (3.16) or the NLSE as :

$$\frac{\partial A}{\partial z} = (\hat{D} + \hat{N})A. \tag{3.27}$$

Although we know that in reality, the dispersion and the nonlinearity of the medium act simultaneously during the evolution of the wave through a nonlinear fiber, nevertheless for sufficiently small segment lengths, we can approximate them to work one at a time. In order to get a numerical solution of the NLSE, we propagate the wave over a small segment dz where first we consider the propagation over a length $\frac{dz}{2}$ considering no nonlinearity. This is performed with the Fourier transformed field amplitude which is simpler to compute, because in the Fourier domain, this propagation only corresponds to addition of a phase. Next we revert back to the time domain and add the effect of nonlinearity for the whole segment in one go. Then finally for the next half of the segment of length $\frac{dz}{2}$, we again move to the Fourier domain and propagate the wave linearly neglecting nonlinearity (see Fig. 3.2). This algorithm is also known as the symmetrized SSFM algorithm [193].

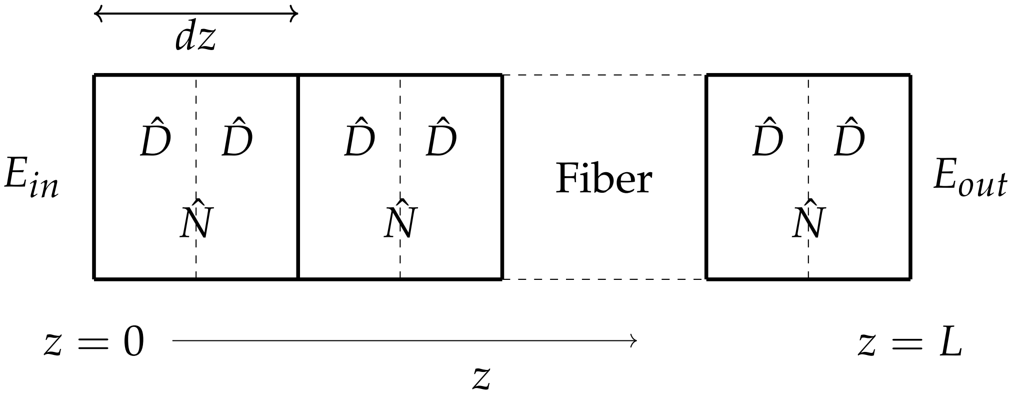

Figure 3.2. A schematic representation of the symmetrized SSFM algorithm to calculate the output field at the end of a nonlinear fiber. $\hat{D}$ represents the dispersion operator and $\hat{N}$ represents the nonlinearity operator.

3.2.1.1 Dispersion

In the case where we consider only dispersion $\hat{D}$, the equation for the evolution of $A(z, T)$ can be written as :

$$\frac{\partial A(z,T)}{\partial z} = \hat{D}A(z,T) = \Big[\sum_{k=2}^{4} \frac{i^{k+1}\beta^{(k)}}{k!}\frac{\partial^k}{\partial T^k} - \frac{\alpha}{2}\Big]A(z,T). \tag{3.28}$$

Now $A(z, T)$ and $B(z, \Omega)$ are related by the Fourier transform as :

$$A(z,T) = \frac{1}{\sqrt{2\pi}}\int_{\Omega=-\infty}^{\infty} B(z,\Omega)e^{-i\Omega T}d\Omega = I\hat{F}T(B(z,\Omega)), \tag{3.29}$$

$$B(z,\Omega) = \frac{1}{\sqrt{2\pi}} \int_{T=-\infty}^{\infty} A(z,T) e^{i\Omega T} dT = \hat{FT}(A(z,T)), \tag{3.30}$$

where $\hat{FT}$ is the Fourier transform operator and $I\hat{FT}$ is the inverse Fourier transform operator. Using Equation (3.29) in Equation (3.28), we get :

$$\begin{aligned}
\frac{\partial A(z,T)}{\partial z} &= \Big[\sum_{k=2}^{4} \frac{i^{k+1}\beta^{(k)}}{k!} \frac{\partial^k}{\partial T^k} - \frac{\alpha}{2} \Big] I\hat{FT}\Big(B(z,\Omega)\Big) \\
&= \Big[\sum_{k=2}^{4} \frac{i^{k+1}\beta^{(k)}}{k!} \frac{\partial^k}{\partial T^k} - \frac{\alpha}{2} \Big] \Big(\frac{1}{\sqrt{2\pi}} \int_{\Omega=-\infty}^{\infty} B(z,\Omega) e^{-i\Omega T} d\Omega \Big) \\
&= \frac{1}{\sqrt{2\pi}} \int_{\Omega=-\infty}^{\infty} \Big[\sum_{k=2}^{4} \frac{i^{k+1}\beta^{(k)}}{k!} (-i\Omega)^k B(z,\Omega) e^{i\Omega T} d\Omega - \frac{\alpha}{2} \Big] I\hat{FT}(B(z,\Omega)) \\
&= I\hat{FT}\Bigg(\Big[\sum_{k=2}^{4} \frac{i\beta^{(k)}}{k!} \Omega^k - \frac{\alpha}{2} \Big] B(z,\Omega) \Bigg) \\
&= I\hat{FT}\Bigg(\Big[\sum_{k=2}^{4} \frac{i\beta^{(k)}}{k!} \Omega^k - \frac{\alpha}{2} \Big] \hat{FT}(A(z,T)) \Bigg).
\end{aligned} \tag{3.31}$$

To derive this, we have used the distributive property of the Fourier transform operator. Also we considered the commutativity of the $\frac{\partial^k}{\partial T^k}$ operator and the $I\hat{FT}$ operator as one works on functions of T and the other on functions of Ω which are separate variables. Then when we take the Fourier transform on both sides of Equation (3.31), we get :

$$\frac{\partial B(z,\Omega)}{\partial z} = \Big[\sum_{k=2}^{4} \frac{i\beta^{(k)}}{k!} \Omega^k - \frac{\alpha}{2} \Big] B(z,\Omega). \tag{3.32}$$

The solution of this differential equation is given by :

$$B(z,\Omega) = B(0,\Omega) \exp\Bigg[\Big(\sum_{k=2}^{4} \frac{i\beta^{(k)}}{k!} \Omega^k - \frac{\alpha}{2} \Big) z \Bigg], \tag{3.33}$$

Thus $B\Big(z + \frac{dz}{2}, \Omega\Big)$ can be written as :

$$B\Big(z + \frac{dz}{2}, \Omega\Big) = B(z,\Omega) \exp\Bigg[\Big(\sum_{k=2}^{4} \frac{i\beta^{(k)}}{k!} \Omega^k - \frac{\alpha}{2} \Big) \frac{dz}{2} \Bigg]. \tag{3.34}$$

As we see here, in the Fourier domain, the evaluation of $B(z + dz/2, \Omega)$ is just a multiplication by an extra phase, and thus it is computationally straightforward, and due to this reason, the SSFM method can perform better than the finite difference methods in solving the NLSE [196].

3.2.1.2 Nonlinearity

In the case where we consider only nonlinearity $\hat{N}$, the equation for the evolution of $A(z,T)$ can be written as [56] :

$$\frac{\partial A(z,T)}{\partial z} = \hat{N}A(z,T) = i\gamma|A(z,T)|^2 A(z,T). \tag{3.35}$$

The solution for this differential equation is given by :

$$A(z,T) = A(0,T)e^{i\gamma|A(z,T)|^2 z}. \tag{3.36}$$

In this case we have considered $|A(z,T)|^2$ is almost constant over z since we are looking at evolution of the wave over small segments of length dz. Thus, we can write :

$$A(z+dz,T) = A(z,T)e^{i\gamma|A(z,T)|^2 dz}. \tag{3.37}$$

3.2.1.3 Final Form of Algorithm

Putting everything together, we write down the final form of the symmetrized SSFM algorithm that we use for solving the NLSE. For each segment of length dz, at a position z, we know the input electric field characterized by the envelope of the field $A(z,T)$. Our aim is to find $A(z+dz,T)$ using the SSFM method.

In the first half of the segment we are only considering dispersion. Thus $A_{D1}(z+\frac{dz}{2},T)$, or the envelope of the field in the first half of the segment can be written as :

$$A_{D1}\Big(z+\frac{dz}{2},T\Big) = I\hat{F}T\Big(\exp\Big[\Big(\sum_{k=2}^{4}\frac{i\beta^{(k)}}{k!}\Omega^k - \frac{\alpha}{2}\Big)\frac{dz}{2}\Big]\hat{FT}(A(z,T))\Big). \tag{3.38}$$

Then we add the nonlinearity and get $A_N\Big(z+\frac{dz}{2},T\Big)$ as :

$$A_N\Big(z+\frac{dz}{2},T\Big) = e^{i\gamma|A(z,T)|^2 dz}A_{D1}\Big(z+\frac{dz}{2},T\Big). \tag{3.39}$$

Note that here we have added the nonlinearity for the whole segment dz at once. Next we add the dispersion for the next half of the segment and we write the output envelope of the field $A_{D2}(z+dz,T) = A(z+dz,T)$ as :

$$A(z+dz,T) = I\hat{F}T\Bigg(\exp\Big[\Big(\sum_{k=2}^{4}\frac{i\beta^{(k)}}{k!}\Omega^k - \frac{\alpha}{2}\Big)\frac{dz}{2}\Big]\hat{FT}\Big(A_N\Big(z+\frac{dz}{2},T\Big)\Big)\Bigg). \tag{3.40}$$

3.2.2 Step Size

In most numerical simulations, the step size dz is an important factor to maintain the required accuracy of the computation [219–221]. For solving the NLSE, if we look at the simplest form of the SSFM algorithm, considering the dispersion $\hat{D}$ and nonlinearity $\hat{N}$ act independently in the segments of length dz, i.e. in the first half of the segment only dispersion is present and in the second half only nonlinearity[3], we can approximate the field amplitude A at $z+dz$ as :

$$A(z+dz,T) \approx e^{dz\hat{D}} e^{dz\hat{N}} A(z,T). \tag{3.41}$$

We should note here that, by assuming $\hat{D}$ and $\hat{N}$ act independently in the segments, we have ignored the non-commuting nature of the operators $\hat{D}$ and $\hat{N}$. This non-commutation is a source of error in our numerical model. This error can be computed using the Baker-Hausdorff formula [222] for two non-commuting operators $\hat{a}$ and $\hat{b}$:

$$e^{\hat{a}} e^{\hat{b}} = \exp\left(\hat{a} + \hat{b} + \frac{1}{2}[\hat{a},\hat{b}] + \frac{1}{12}[\hat{a} - \hat{b}, [\hat{a},\hat{b}]] + ...\right), \tag{3.42}$$

where $[\hat{a},\hat{b}] = \hat{a}\hat{b} - \hat{b}\hat{a}$ with $[\ ,\ ]$ being the commutator. Now considering $\hat{a} = dz\hat{D}$ and $\hat{b} = dz\hat{N}$ in Equation (3.42), we get the dominant error term for the SSFM method to be $\frac{1}{2}dz^2[\hat{D},\hat{N}]$. Thus we can say that the simplest form of SSFM algorithm is accurate to the order of dz^2.

Consequently, for the symmetrized SSFM algorithm that we use in our case, the field envelope A at $z+dz$ is approximated as :

$$A(z+dz,T) \approx \exp\left(\frac{dz}{2}\hat{D}\right) \exp\left(\int_z^{z+dz} \hat{N}(z')dz'\right) \exp\left(\frac{dz}{2}\hat{D}\right) A(z,T). \tag{3.43}$$

In this case, the effect of nonlinearity is provided at the middle of the segment rather than at the boundary in contrast to the previous case. For a small dz, this can be approximated to :

$$A(z+dz,T) \approx \exp\left(\frac{dz}{2}\hat{D}\right) \exp\left(dz\hat{N}\right) \exp\left(\frac{dz}{2}\hat{D}\right) A(z,T). \tag{3.44}$$

Now we use Equation (3.42) and write :

$$\begin{aligned}
&\exp\left(\frac{dz}{2}\hat{D}\right) \exp\left(dz\hat{N}\right) \exp\left(\frac{dz}{2}\hat{D}\right) = \exp\left(\frac{dz}{2}\hat{D} + dz\hat{N} + \frac{dz^2}{4}[\hat{D},\hat{N}] + ...\right) \exp\left(\frac{dz}{2}\hat{D}\right) \\
&\approx \exp\left(\frac{dz}{2}\hat{D} + dz\hat{N} + \frac{dz^2}{4}[\hat{D},\hat{N}]\right) \exp\left(\frac{dz}{2}\hat{D}\right) \\
&\approx \exp\left(\frac{dz}{2}\hat{D} + dz\hat{N} + \frac{dz^2}{4}[\hat{D},\hat{N}] + \frac{dz}{2}\hat{D} + \frac{1}{2}(\frac{dz}{2}\hat{D} + dz\hat{N} + \frac{dz^2}{4}[\hat{D},\hat{N}])\frac{dz}{2}\hat{D} \right. \\
&\left. - \frac{1}{2}\frac{dz}{2}\hat{D}(\frac{dz}{2}\hat{D} + dz\hat{N} + \frac{dz^2}{4}[\hat{D},\hat{N}])\right) \\
&= \exp\left(\frac{dz}{2}\hat{D} + dz\hat{N} + \frac{dz}{2}\hat{D} + \frac{dz^2}{4}[\hat{D},\hat{N}] - \frac{dz^2}{4}[\hat{D},\hat{N}] + \frac{dz^3}{16}[[\hat{D},\hat{N}],\hat{D}]\right) \\
&= \exp\left(\frac{dz}{2}\hat{D} + dz\hat{N} + \frac{dz}{2}\hat{D} + \frac{dz^3}{16}[[\hat{D},\hat{N}],\hat{D}]\right),
\end{aligned} \tag{3.45}$$

---

[3] This approach is different from the symmetrized SSFM algorithm where we added the nonlinearity for the whole segment at the middle of the segment.

where we have used $[\hat{D}, \hat{D}] = 0$. Thus we see that the leading error term for the symmetrized SSFM algorithm is of the order of dz^3 [58, 193, 221], which is an order of magnitude improvement over the general SSFM algorithm. The simulation accuracy can be further improved by considering a variable step size along the length of the fiber [221], however for our analysis, a constant step size approach suffices.

3.2.3 Spectral Leakage

When we work with digital signals, we often come across errors arising due to spectral leakage or windowing effect. These errors predominantly arise due to performing a discrete Fourier transform (DFT) [223, 224] while considering an improper window size. To explain this effect, we take the example of a discretized sine wave of frequency f in the time domain with N data points each separated by a time interval of Δt :

$$y(m) = \sin(2\pi f m \Delta t) \text{ where } m = 0, 1, 2, ..., N-1. \tag{3.46}$$

Let k be the number of cycles completed by this sine wave over the total time $t_{tot} = (N-1)\Delta t$. k is given by :

$$k = (N-1)\Delta t f. \tag{3.47}$$

The amplitude spectrum of the DFT of Equation (3.46), given by $\Gamma(m)$ can be approximated by a sinc function as [224] :

$$\Gamma(m) = \frac{N}{2} \frac{\sin(\pi(k-m))}{\pi(k-m)} \text{ where } m = 0, 1, 2, ..., N-1. \tag{3.48}$$

Now we can consider two cases, i.e. k is an integer and k is a fraction.

- k is an integer :

  If k is an integer between 0 and $N-1$, then we have :

  $$\Gamma(m) = \begin{cases} \frac{N}{2} & \text{if } m = k \\ 0 & \text{if } m \neq k \end{cases} \tag{3.49}$$

  Thus we see that $\Gamma(m)$ is non-zero only for a frequency $\frac{k}{N\Delta t}$. For all other frequencies, i.e. $\frac{m}{N\Delta t}$ for $m = 0, 1, 2, ..., N-1$ and $m \neq k$, $\Gamma(m)$ is zero. Hence in this case we have a correct Fourier representation of the discrete time domain signal as expected for the continuous case (see Fig. 3.3).

- k is a fraction :

  When k is a fraction, we no longer have the sinc function going to zero at all m except $m = k$. The discrete signal of Equation (3.46) with one frequency f in the time domain leaks to other nearby frequencies when represented in the Fourier domain (see Fig. 3.4).

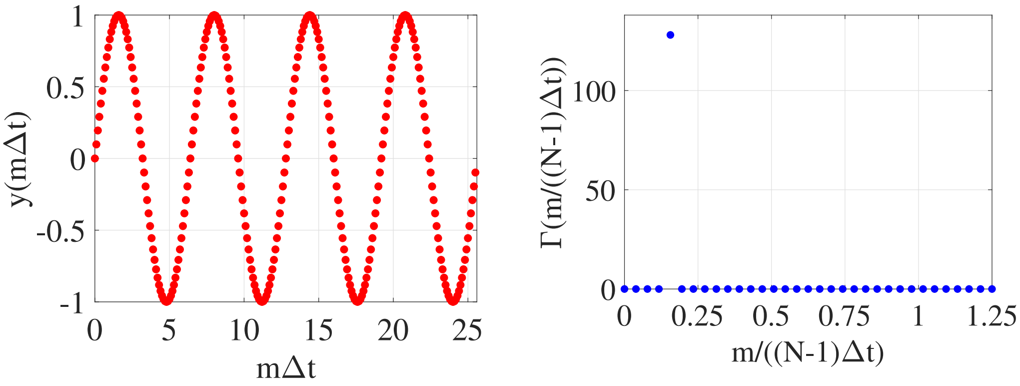

(a) Discretized time domain signal.

(b) Discretized Fourier domain signal.

Figure 3.3. Figure (a) shows a discrete time domain signal with a single frequency such that an integer number of cycles ($k = 4$) are completed. Figure (b) shows the corresponding discrete frequency domain signal where all except one frequency has an amplitude zero. $N = 256$, $\Delta t = 0.1$ and $k = 4$.

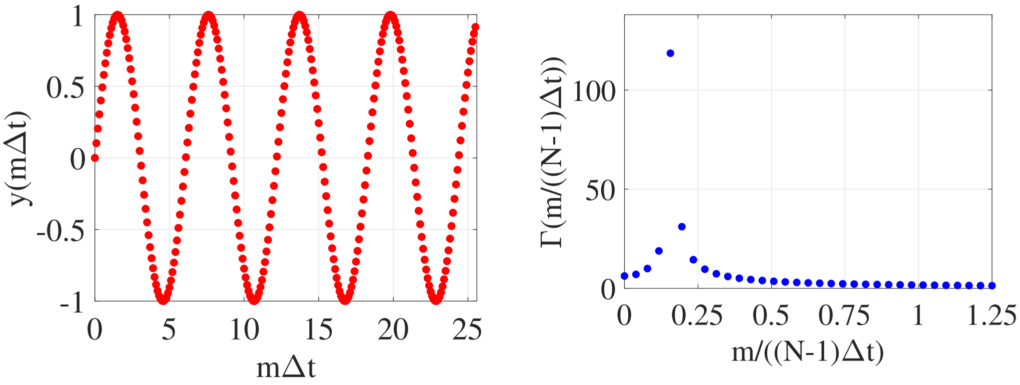

(a) Discretized time domain signal.

(b) Discretized Fourier domain signal.

Figure 3.4. Figure (a) shows a discrete time domain signal with a single frequency such that a non-integer number of cycles ($k = 4.2$) are completed. Figure (b) shows the corresponding discrete frequency domain signal. $N = 256$, $\Delta t = 0.1$ and $k = 4.2$.

From the above discussion we conclude that while performing our simulation, we need to ensure that the choice of N and Δt should be such that in Equation (3.47), k becomes an integer for all the different frequencies that we are using.

3.3 Verification of Numerical Model

In order to check the effectiveness of our developed numerical model based on the SSFM algorithm, we produce some sample runs numerically and compare the results with experimental data. In the first part of this section we introduce the parameters used for the simulations and experiments. Next we consider the PIA configuration of a FOPA and finally we look at the PSA configuration.

3.3.1 Parameters

Here we list the different parameters that we use in our theoretical calculations, simulations and experiments for light propagation in a FOPA. In the different tables we provide the set of parameters for different cases that are utilized subsequently.

3.3.1.1 Numerical parameters

The numerical parameters considered in our simulation is listed in Table 3.1 :

Numerical Parameter List		
Parameter	**Value**	**Unit**
Sampling number: N	$2^{17} = 131072$	
Total time considered: t_{tot}	2.18	μs
Time resolution: $dt = \frac{t_{tot}}{N}$	16	ps

Table 3.1. Table for the numerical parameters used in simulations.

3.3.1.2 System parameters

The system parameters used for the simulations and the experiments are listed in the following tables. Case 1 and Case 2 refer to the parameters corresponding to those used in Ref. [155] and Case 3 refers to the experiment performed. :

System Parameter List : Case 1			
HNLF	**Parameter**	**Value**	**Unit**
Standard	Input signal power : P_{-1}	-13	dBm
	Input pump power : P	20	dBm
	Pump wavelength : λ_0	1547	nm
	Pump-signal frequency separation : Δf_{Ps}	20	GHz
	Length of the fiber : L	200	m
	Zero dispersion wavelength of HNLF : λ_{ZDW}	1547	nm
	Nonlinear coefficient of HNLF : γ	11.3	$(\text{W.km})^{-1}$
	Dispersion slope of HNLF : $D^{'}$	0.017	$\text{ps.nm}^{-2}.\text{km}^{-1}$

Table 3.2. Table of system parameters in the case of a standard HNLF.

System Parameter List : Case 2			
HNLF	**Parameter**	**Value**	**Unit**
SPINE	Input signal power : P_{-1}	-3.5	dBm
	Input pump power : P	24	dBm
	Pump wavelength : λ_0	1547	nm
	Pump-signal frequency separation : Δf_{Ps}	20	GHz
	Length of the fiber : L	500	m
	Zero dispersion wavelength of HNLF : λ_{ZDW}	1566	nm
	Nonlinear coefficient of HNLF : γ	8.7	$(\text{W.km})^{-1}$
	Dispersion slope of HNLF : $D^{'}$	0.083	$\text{ps.nm}^{-2}.\text{km}^{-1}$

Table 3.3. Table of system parameters in the case of a SPINE HNLF.

System Parameter List : Case 3			
HNLF	**Parameter**	**Value**	**Unit**
Standard	Input signal power : P_{-1}	-1	dBm
	Input pump power : P	20	dBm
	Pump wavelength : λ_0	1552.5	nm
	Pump-signal frequency separation : Δf_{Ps}	562	GHz
	Length of the fiber : L	200	m
	Zero dispersion wavelength of HNLF : λ_{ZDW}	1547	nm
	Nonlinear coefficient of HNLF : γ	11.3	$(\text{W.km})^{-1}$
	Dispersion slope of HNLF : $D^{'}$	0.017	$\text{ps.nm}^{-2}.\text{km}^{-1}$

Table 3.4. Table of system parameters in the case of a standard HNLF.

3.3.2 PIA

For a PIA configuration of a FOPA, at the input of the fiber, we have the pump and the signal wave only. Note that here we use a 3-wave model and use only one pump wave. Thus the real input field $E_{in}(z=0,T)$ can be written as :

$$\begin{aligned} E_{in}(0,T) &= |A_{-1}(0)|e^{-i(\omega_c+\Omega_{-1})T}e^{-i\phi_{-1}} + |A_0(0)|e^{-i(\omega_c+\Omega_0)T}e^{-i\phi_0} + c.c. \\ &= \left[|A_{-1}(0)|e^{-i\Omega_{-1}T}e^{-i\phi_{-1}} + |A_0(0)|e^{-i\Omega_0 T}e^{-i\phi_0}\right]e^{-i\omega_c T} + c.c.\ , \end{aligned} \tag{3.50}$$

where A_{-1}, A_0 are the complex amplitudes of the signal and pump respectively that depend only on z. $\omega_c+\Omega_{-1}$, $\omega_c+\Omega_0$ are the frequencies of the signal and pump respectively expressed with respect to the central frequency ω_c. ϕ_{-1}, ϕ_0 are the initial phases of the signal and pump respectively. $T=t-\beta^{(1)}z$ denotes the retarded time. We should note here that since we are considering a PIA case, we can use ϕ_{-1} and ϕ_0 to be 0 as the result does not depend on ϕ_{-1} or ϕ_0. Also, we can overlook the $e^{i\omega_c T}$ term and only solve for how the complex envelope A evolves along the fiber, where A is given by :

$$A = A_{-1}e^{-i\Omega_{-1}T} + A_0 e^{-i\Omega_0 T}\ . \tag{3.51}$$

Considering the pump frequency to be the central frequency, we have $\Omega_0 = 0$. Thus A becomes :

$$A = A_0 + A_{-1}e^{-i\Omega_{-1}T} \,. \tag{3.52}$$

Considering the above definition of A, in Fig. 3.5 we show a sample input and output power spectrum of the FOPA, for PIA configuration. In Appendix E we provide a MATLAB code to generate this spectrum. The parameters of this simulation correspond to the Case 3 mentioned in Table 3.4 except that we changed the length of the fiber to 2000 m to better visualize the nonlinear effects. We can see from Fig. 3.5 that apart from the signal getting amplified by the FOPA, four wave mixing processes inside the fiber lead to the generation of sidebands at frequencies other than that of the pump and the signal.

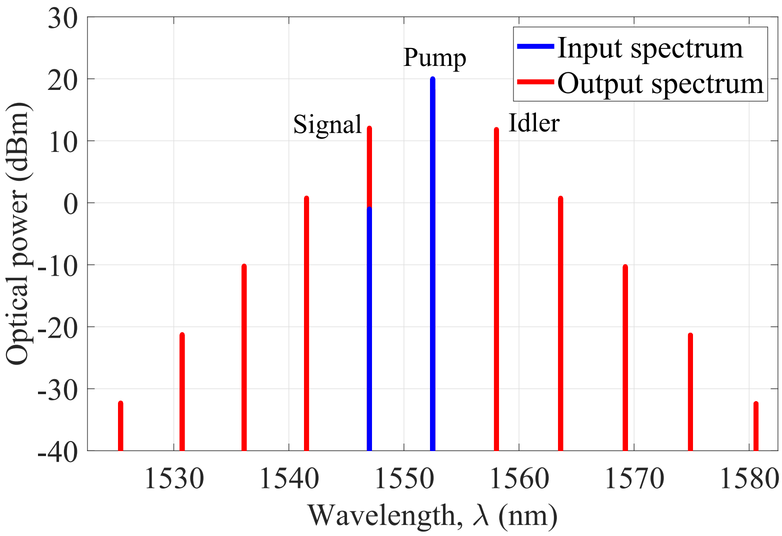

Figure 3.5. A sample input (blue) and output (red) spectrum of a FOPA in PIA configuration with parameters of Case 3 (Table 3.4) except $L = 2000$ m.

3.3.2.1 Experiment

In order to validate our numerical approach, we perform a simple experiment of light propagation through a FOPA considering the PIA configuration. Figure 3.6 shows a schematic representation of the experiment.

In the experiment we used two tunable wavelength lasers to generate a signal and a pump wave at frequencies 1548nm (Pure Photonics PPCL550 laser) and 1552.5nm (Yenista Tunics laser) respectively. The output of the laser at 1552.5nm was fed into an EDFA (Keopsys) to generate a much stronger output than the signal. The outputs of the EDFA and the Pure Photonics laser were combined with a 90%/10% fiber coupler and launched inside a standard HNLF of length 200 m which acted as the FOPA in our case. The zero dispersion wavelength λ_{ZDW} of the HNLF was 1547nm, nonlinear coefficient γ was 11.3 (W.km)$^{-1}$, and the dispersion slope D' was 0.017 ps.nm^{-2}.km^{-1}. We also recorded the total power at the input of the

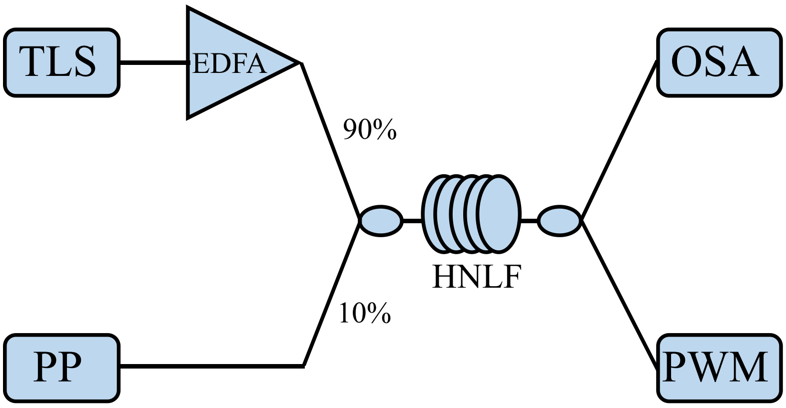

Figure 3.6. Experimental scheme to measure the signal gain of a FOPA in PIA configuration. TLS : Tunable Laser Source (Yenista Tunics) at wavelength 1552.5 nm. PP : Pure Photonics laser at wavelength 1548 nm. EDFA : Erbium doped fiber amplifier. HNLF : Highly nonlinear fiber. OSA : Optical spectrum analyzer.

HNLF using a power meter (PWM). The output of the HNLF was fed into an optical spectrum analyzer (OSA) and the spectrum of the idler was recorded for different values of power at the input of the HNLF. For each case the spectrum of the input of the HNLF was also recorded using the OSA.

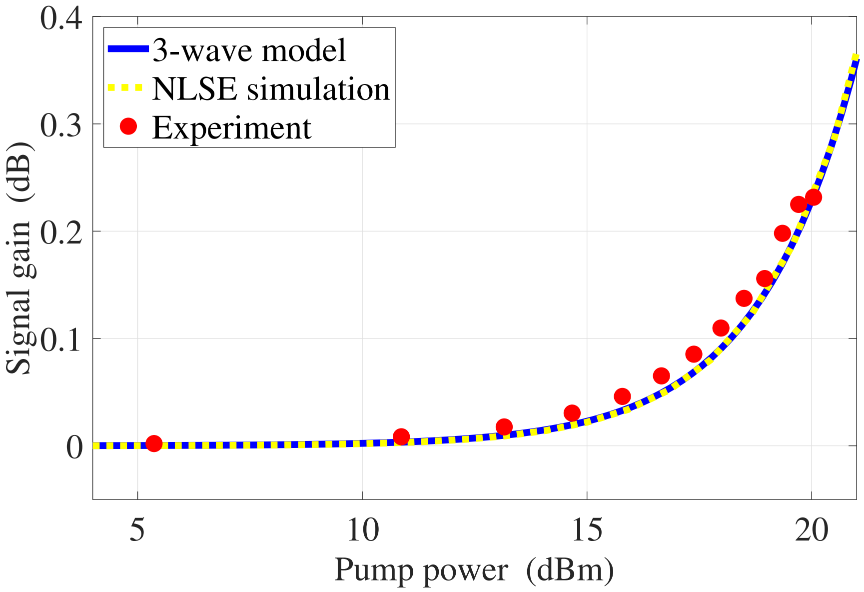

Figure 3.7. Dependence of signal gain in PIA on input pump power. Blue solid line : analytical result from the 3-wave model; yellow dotted line : numerical solution of NLSE; red full circles : experiment. $L = 204$ m, $\gamma = 11.3$ (W.km)$^{-1}$, $\lambda_{ZDW} = 1547$ nm, $P_{-1} = -1$ dBm, $\lambda_0 = 1552.5$ nm and $\lambda_{-1} = 1548$ nm.

3.3.2.2 Results

In the case of PIA configuration, we plot the gain of the signal G_{-1} as a function of the input pump power P in Fig. 3.7. We compare three different approaches: (a) analytical result from the 3-wave model as given by Equation (2.14) (blue solid line), (b) numerically simulated result solving the NLSE (yellow dotted line) and (c) result from the experiment (red full circles) using the scheme shown in Fig. 3.6. The parameters used correspond to the Case 3 as given in Table 3.4. From Fig. 3.7 we see that the theoretical calculation, the numerical model and the experimental data agree considerably. This validates our numerical model for the PIA configuration of a FOPA.

3.3.3 PSA

In the case of PSA, for the numerical model we proceed similarly as for PIA, the only differences with PIA being, now we have to consider an idler at the input of the fiber and the phases of the input waves must be optimized to maximize the signal gain. Thus in this case we consider an input field $E_{in}(0,T)$ of the form :

$$\begin{aligned} E_{in}(0,T) &= |A_{-1}(0)|e^{-i(\omega_c+\Omega_{-1})T}e^{-i\phi_{-1}} + |A_0(0)|e^{-i(\omega_c+\Omega_0)T}e^{-i\phi_0} + |A_1(0)|e^{-i(\omega_c+\Omega_1)T}e^{-i\phi_1}c.c. \\ &= \left[|A_{-1}(0)|e^{-i\Omega_{-1}T}e^{-i\phi_{-1}} + |A_0(0)|e^{-i\Omega_0 T}e^{-i\phi_0} + |A_1(0)|e^{-i\Omega_1 T}e^{-i\phi_1}\right]e^{-i\omega_c T} + c.c.\,, \end{aligned} \tag{3.53}$$

where A_{-1}, A_0 and A_1 are the complex amplitudes, $\omega_c + \Omega_{-1}$, $\omega_c + \Omega_0$ and $\omega_c + \Omega_1$ are the frequencies expressed with respect to the central frequency ω_c and ϕ_{-1}, ϕ_0 and ϕ_1 are the initial phases of the signal, pump and idler respectively. Note that for our case $\Omega_{-1} = -\Omega_1$. For the sake of simplicity we set $|A_{-1}(0)| = |A_1(0)|$. As we know that for PSA, the signal gain G_{-1} depends on the relative phase $\Theta = \phi_{-1} + \phi_1 - 2\phi_0$ (see Equation (2.15)) and not the absolute phases of the waves, we set $\phi_0 = 0$ and $\phi_{-1} = \phi_1$ in the simulation. Thus we just scan ϕ_{-1} to get the dependence of signal gain on Θ. An experimental analogue of such an approach to scan the signal gain with respect to relative phase Θ is discussed in Ref. [155].

Next in Fig. 3.8 we plot the dependence of signal gain on the relative phase Θ, both for the analytical 3-wave model (blue solid line) calculated using Equation (2.15) and the NLSE simulation (red full circles). We also plot the analytical result for the PIA configuration from the 3-wave model (green solid line) using Equation (2.14) with the same set of parameters for comparison. In Fig. 3.8 (a) we considered parameters from Case 1 or Table 3.2, while for Fig. 3.8 (b) Case 2 or Table 3.3 was considered.

From Fig. 3.8 we see that the numerical NLSE simulation correctly reproduces the dependence of signal gain on the relative phase Θ as predicted by the 3-wave model for two different HNLF's. An experimental validation of this is shown in [155]. We also see that as expected, the signal gain in PIA configuration is insensitive to the relative phase Θ and the maximum PSA gain is larger than the PIA gain.

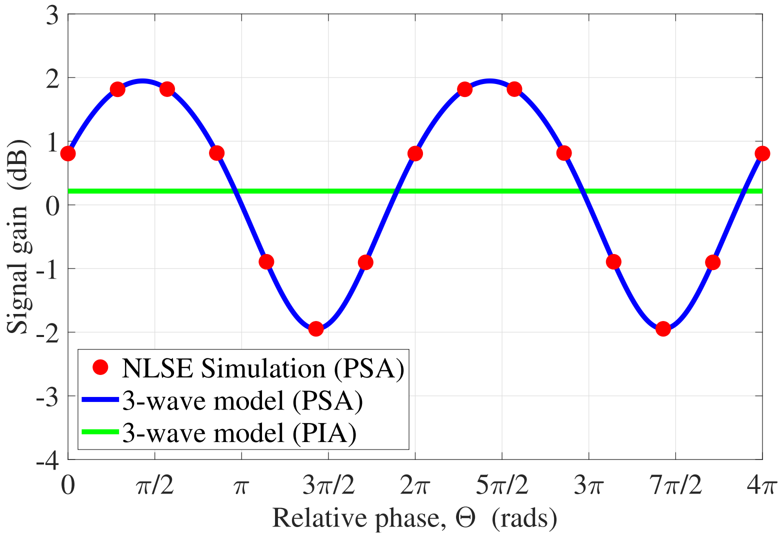

(a) Standard HNLF.

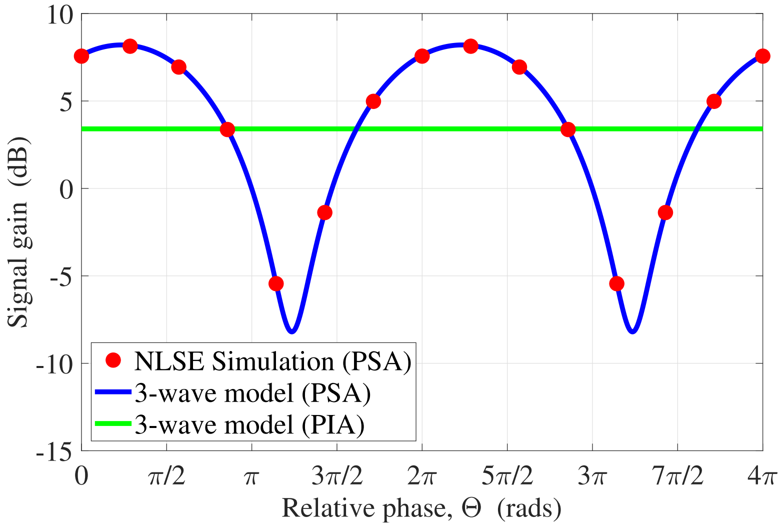

(b) SPINE HNLF.

Figure 3.8. Dependence of signal gain in PSA and PIA configuration of a FOPA on the relative phase Θ between the signal, pump and the idler. The blue solid line is the analytical result for PSA from the 3-wave model. The red full circles are obtained from the numerical solution of NLSE for PSA. The green solid line is the analytical solution of PIA from the 3-wave model. Parameters of (a) : Case 1 (Standard fiber) given in Table 3.2. Parameters of (b) : Case 2 given in Table 3.3 (SPINE fiber). Degenerate pump configuration is considered.

3.4 Discussion and Conclusion

3.4.1 Comparison of Models

In this subsection we will provide a qualitative comparison of the different models that we described in this thesis so far. They are, analytical 3-wave model, analytical 7-wave model, numerical 7-wave model and the numerical NLSE model.

We have seen in Chapter 2 that when the nonlinearity of the fiber is not very

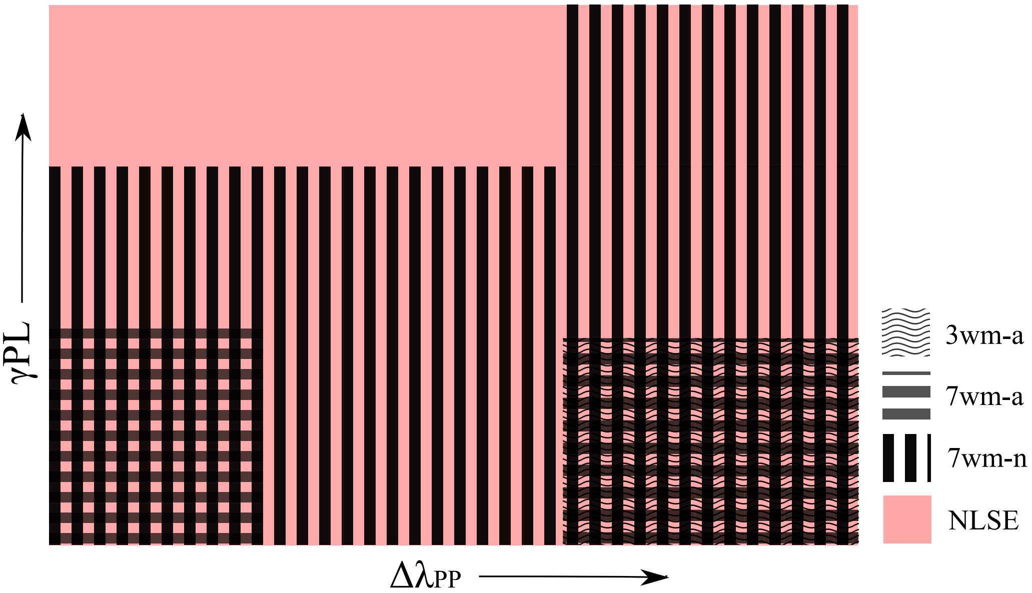

Figure 3.9. An illustration of validity regions for different models to describe CW light propagation through a FOPA with respect to the nonlinearity parameter γPL and pump-pump wavelength separation $\Delta\lambda_{PP}$, considering a dual pump configuration. 3wm-a : analytical 3-wave model; 7wm-a : analytical 7-wave model; 7wm-n : numerical 7-wave model; NLSE : numerical NLSE model. (not to scale)

strong (or $\gamma PL < 0.2$), and the pump-pump wavelength separation is large, the analytical 3-wave model can effectively describe the propagation of signal and/or idler through the FOPA. When the pump-pump wavelength separation is small ($<$ 10 nm) however, still with a weakly nonlinear condition, the analytical 7-wave model remains valid whereas the analytical 3-wave model becomes invalid. This is because, for small pump-pump wavelength separation, some FWM processes become efficient that are not accounted for in the 3-wave model.

The analytical 7-wave model breaks down when the non-pump depletion approximation cannot be applied which corresponds to the fiber nonlinearity being large (or $\gamma PL > 0.5$). The analytical 7-wave model also becomes inapplicable for pump-pump wavelength separations typically between 10 nm and 40 nm, as in such cases different FWM processes involving higher order waves needs to be considered and are not addressed in the 7-wave analytical model. In such cases, the numerical 7-wave model describes the dynamics of a FOPA accurately as it considers all the involved FWM processes.

Apart from these, there can be scenarios where due to cascaded FWM processes, a large number of waves are generated in the FOPA and hence influence the signal gain. This is typically observed in a strongly nonlinear regime ($\gamma PL > 1$). In such cases, the implementation of the n-wave model becomes complicated due to the large number of FWM terms involved. Hence in such cases the numerical NLSE model needs to be invoked. The validity of these different models is summarized in

Fig. 3.9.

The above discussion provides us an overview of the different validity regimes of the models described. The numerical NLSE model is the most robust one spanning all the situations and therefore will become our model of choice in the later parts of this thesis.

3.4.2 Conclusion

In this chapter we described a NLSE based model for the propagation of multiple CW waves through a nonlinear fiber. In particular, we discussed about the symmetrized SSFM algorithm to solve the NLSE numerically. The key advantage of the SSFM algorithm is that it treats the dispersive and nonlinear effects of the fiber separately in a small fiber segment. This leads to a decoupled set of equations that can be easily solved for that segment (see Equations (3.34) and (3.37)). Thus solving the evolution of the fields for each segment iteratively, we can find the field at the output of the fiber.

Consequently we applied this numerical technique to simulate simple cases of wave propagation through a nonlinear fiber. We considered a FOPA in a PIA configuration and obtained agreement of the simulation results with the analytical 3-wave model and experimental data. We also validated the simulation results for a PSA configuration which agreed with the analytical 3-wave model and with the experimental data used in Ref. [155].

Chapter Highlights

- **Nonlinear Schrödinger Equation (NLSE) :** We introduced the nonlinear Schrödinger equation to describe propagation of a continuous distribution of frequencies through a nonlinear fiber. In particular, we considered the case of an arbitrary number of CW waves.
- **Numerical Model to Solve NLSE :** We described an efficient algorithm known as the split step Fourier method (SSFM) to solve the NLSE for an arbitrary number of CW waves. We verified the numerical model with available experimental data.
- **Qualitative Comparison of Models :** We compared qualitatively the numerical NLSE approach with analytical n-wave model approaches developed in the previous chapter to describe CW wave propagation though a nonlinear fiber. While the numerical NLSE approach is the most accurate one, the analytical n-wave models suffice when the number of waves is small and the pump-signal wavelength separation is not too large (<10nm).

Chapter 4

PSA in a Microwave Photonics Link

Contents

4.1 Scheme . . . 106
- 4.1.1 Electro-Optic Conversion : Phase Modulator . . . 107
- 4.1.2 Electro-Optic Conversion : Mach-Zehnder Modulator . . . 109
- 4.1.3 Opto-RF Conversion . . . 111

4.2 Two-Tone Test . . . 113
- 4.2.1 MZM Output Power . . . 114
- 4.2.2 Part of Total Optical Power at Fundamental Frequency . . . 118
- 4.2.3 Part of Total Optical Power at IMD3 Frequency . . . 120
- 4.2.4 SFDR . . . 122

4.3 Numerical Model . . . 124
- 4.3.1 Model Outline . . . 124
- 4.3.2 Experimental Setup . . . 124
- 4.3.3 Experimental Validation . . . 126

4.4 AM vs PM . . . 127
- 4.4.1 AM . . . 127
- 4.4.2 PM . . . 129
- 4.4.3 Simulation Results . . . 130

4.5 Saturation Behaviour : Standard Intensity Modulator . . . 131
- 4.5.1 Scan of Input RF Power . . . 132
- 4.5.2 Scan of Input Signal Power . . . 134
- 4.5.3 Scan of Input Pump Power . . . 136
- 4.5.4 Scan of Input Signal Phase . . . 137
- 4.5.5 SFDR . . . 138
- 4.5.6 Discussion . . . 140

4.6 Saturation Behaviour : Linear Intensity Modulator . . . 141

4.7 Physical Interpretation . . . 142

4.8 Conclusion . . . 148

Microwave photonics plays a crucial role in the development of modern-day analog RF systems. Its applications range from antenna remoting [225], radio-over-fiber systems [226], phased array antennas [227], etc to name a few. The inclusion of photonic links for the transfer of analog RF signals can be advantageous in several ways compared to traditional electrical distribution lines such as coaxial cables or waveguides. For example, a photonic link for RF signal distribution leads to an increase in processing bandwidth, decrease in signal loss, enhancement of immunity to electromagnetic interference, etc. [98, 102, 228, 229].

In order to further improve the performance of such links, research efforts in this field have focused on reducing link loss, noise figure and distortion and thereby increasing the available dynamic range of the link [99, 230, 231]. However, for achieving links with a longer range, optical amplifiers are necessary to boost the signal periodically. The gain of traditional optical amplifiers, such as Erbium Doped Fiber Amplifiers (EDFA) is independent of the phase of the signal. The noise figure of such phase insensitive amplifiers (PIA) cannot be smaller than 3 dB [47, 232]. On the other hand, in some fiber optic parametric amplifiers (FOPA), the signal gain depends on the relative phase between the different waves injected in the amplifier. Such phase sensitive amplifiers (PSA) can have a noise figure as low as 0 dB [47, 87, 155].

In the context of microwave photonic links, utilization of a PSA can offer the possibility of realizing other functionalities such as optical filtering through phase sensitive amplification and de-amplification [233], wideband photonic assisted radio over fiber systems [119] and microwave photonic frequency measurement [120]. Such a possibility of noiseless amplification in PSAs has been extensively studied in the context of digital optical communication links [54, 55, 57, 62, 121, 234]. Nowadays digital links are widely used across communication platforms, but such links are limited by the bandwidth of analog-to-digital converters (ADC). Although efforts to overcome such limitations were made using photonics based ADCs [235], fully analog microwave photonic links are still promising. Preliminary studies on performance of analog links with respect to modulation formats [122], signal multicasting [123] and PSA inclusion in a link [118, 124–126] were performed. However, the possibility of incorporating a PSA within an analog microwave photonic link needs further exploration with respect to its distortion characteristics and its dependence on various parameters of modulation and PSA processes.

An important factor for the performance of a microwave photonic link is the signal fidelity across the link. In a traditional microwave photonic link without PSA, the E/O (Electric to Optic) conversion process is achieved with a Mach-Zehnder modulator (MZM). This MZM, due to its nonlinear transfer function, is a source of distortion in the link. Moreover, when a PSA is added in such a link, further distortions might be generated due to nonlinear processes in the optical amplification. Generation and mitigation of nonlinearities by a PSA has been comprehensively studied for digital links [84, 128–133]. But, in the case of analog links, it is still a topic of ongoing research [134].

An important question in this context is to investigate the nonlinearities coming from the PSA process only. While it is well known that such distortions are negligible in the case of an EDFA [41], the question still deserves to be investigated in the case of a PSA. In this chapter, we use numerical modelling to find nonlinearities that are generated solely due to the addition of a PSA and not from the nonlinear MZM of the link. Since PSAs based on two pumps and degenerate signal and idler exhibit cascaded four-wave mixing phenomena that make them difficult to model [90, 91], we focus here on a PSA scheme with degenerate pumps and nondegenerate signal and idler. The strength of the distortions induced on the signal is characterized using the so-called two-tone test in which the carrier is modulated by two nearby frequencies from which the system nonlinearities generate third order intermodulation products (IMD3). The amplitudes of these IMD3's are used as a measure of the nonlinearity of the PSA. Moreover, under certain circumstances, like high optical power of the signal or larger nonlinear coefficient of the fiber or longer length of the fiber optic amplifier[1], the PSA gain can attain saturation and hence can change several properties of the link [236–238]. We thus also investigate the distortion performance of the link when the PSA gain reaches saturation.

This chapter is organized as follows. In Section 4.1 we introduce the scheme of a microwave photonic link with a PSA and describe its different components. In Section 4.2 we discuss about the concepts of the two-tone test and the spurious free dynamic range (SFDR) which will be later used to evaluate the distortion performance of our system. Then in Section 4.3 we introduce the numerical model that we use to simulate our system i.e. a microwave photonic link with a PSA. We also describe the experimental setup corresponding to our model and validate our numerical approach with corresponding experimental data. Thereafter in Section 4.4 we compare the performance of two modulation formats : 1. Amplitude modulation (AM) and 2. Phase modulation (PM) with respect to the PSA-based microwave photonic link. Then in Section 4.5 we consider a standard intensity modulator and study the dependence of the system nonlinearities on several parameters like the input RF power, input signal power and input pump power. In this section we also explore situations when the PSA attains gain saturation. Next in Section 4.6 we show a similar analysis as in Section 4.5 but for a linearized intensity modulator. Then in Section 4.7 we propose a physical interpretation of the optical amplification of the different waves in the PSA. Finally in Section 4.8 we discuss the conclusions and project some perspectives of this investigation.

---

[1] This is equivalent to using a nonlinear fiber with a higher value of γPL.

4.1 Scheme

As we have seen in Chapter 1, a microwave photonics link consists of three main components : 1. Electro-optic converter, 2. Photonic link and 3. Opto-electric converter. As the name suggests, the electro-optic converter converts an analog RF signal into an optical signal. Then this optical signal is transmitted to a different location through the photonic link. Finally, at the receiver end, the optical signal is converted back to the RF electrical signal. However, when the distance between the remote antenna (where the RF signal is produced) and the receiver station is large, the requirement of an optical amplifier becomes unavoidable. An example of such a situation can be a radar antenna located on a mountain top with a receiver base station at the foot of the mountain (see Fig. 4.1). As we have discussed before, in such a scenario a FOPA with a low-noise (PSA configuration) and high-gain profile can be installed in the photonic link connecting the remote antenna and the receiver station. The different parts of such a microwave photonic link are explained in the following.

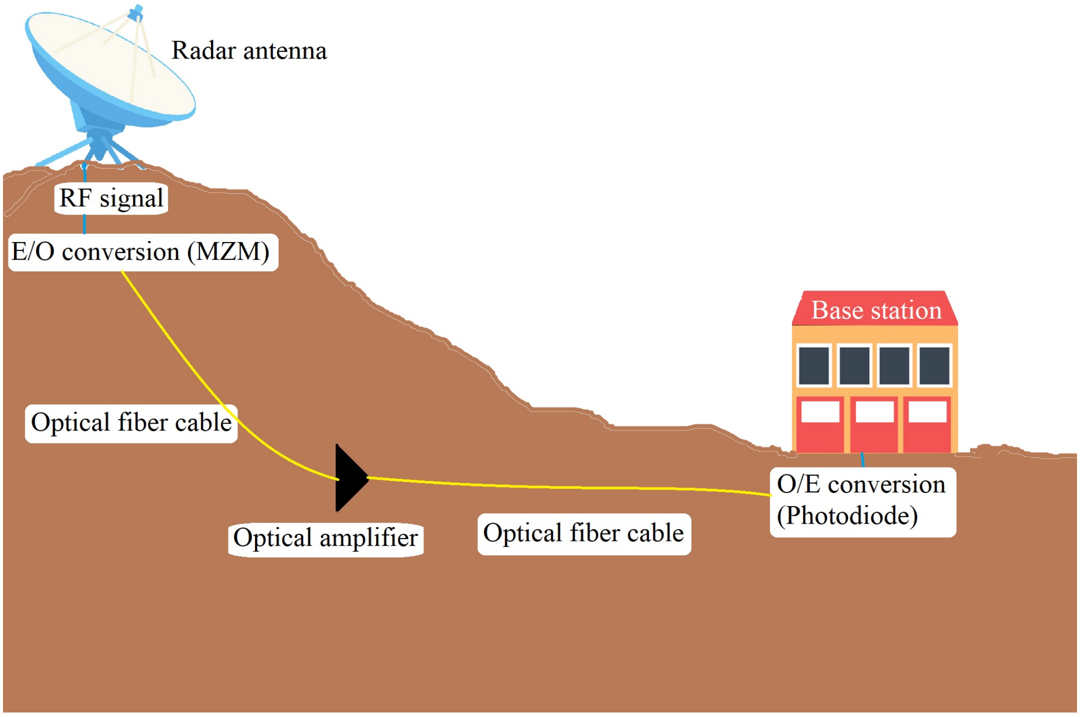

Figure 4.1. An illustration of a microwave photonic link with a remote antenna connected to a base station via a photonic link with an optical amplifier.

4.1.1 Electro-Optic Conversion : Phase Modulator

In a microwave photonic link, the input signal carrying information is a microwave or RF signal[2]. Before it can be transmitted via optical fibers, it needs to be converted into an optical signal. This conversion of the signal from the eletric to the optical domain is mostly done using electro-optic modulation techniques [99].

4.1.1.1 Pockels Effect

Most electro-optic converters are based on the principle of Pockel's effect. It is a linear electro-optic effect which states that the refractive index of a medium undergoes a change on application of an external electric field. This change is proportional to the strength of the applied electric field [239]. Non-centrosymmetric crystal materials such as lithium niobate ($LiNbO_3$), lithium tantalate ($LiTaO_3$), potassium di-deuterium phosphate (KD*P), β-barium borate (BBO), potassium titanium oxide phosphate (KTP), and compound semiconductors such as gallium arsenide (GaAs) and indium phosphide (InP) are known to show this effect [240].

4.1.1.2 Phase Modulator

An optical phase modulator is fabricated by embedding an optical waveguide in an electro-optic substrate. By utilizing the Pockel's effect, one can change the effective refractive index n_{eff} of the waveguide, by applying an external voltage via a coated electrode, and thus the electrical field of the incoming optical carrier can be modulated in phase (see Fig 4.2). Thus if we apply an external voltage of $V_m(t)$ across an waveguide carrying a wave at wavelength λ, with electrodes of length l, then the modulation of the phase $\phi(t)$ of the wave and the change in the effective refractive index $\Delta n_{eff}(t)$ follows [241] :

$$\phi(t) = \frac{2\pi \Delta n_{eff}(t) l}{\lambda} \propto V_m(t). \tag{4.1}$$

4.1.1.3 Input Field

The electric field of the optical carrier signal $E_{in}(t)$ going inside the modulator can be written as :

$$E_{in} = \mathcal{E} e^{-i\omega t} + c.c. \,, \tag{4.2}$$

where $\mathcal{E}$ is the complex amplitude of the optical field and ω is the angular frequency.

---

[2] RF waves have frequencies roughly between 30 KHz and 300 GHz, whereas microwaves have frequencies roughly between 300 MHz and 300 GHz. Thus we can say microwaves form a subset of RF waves.

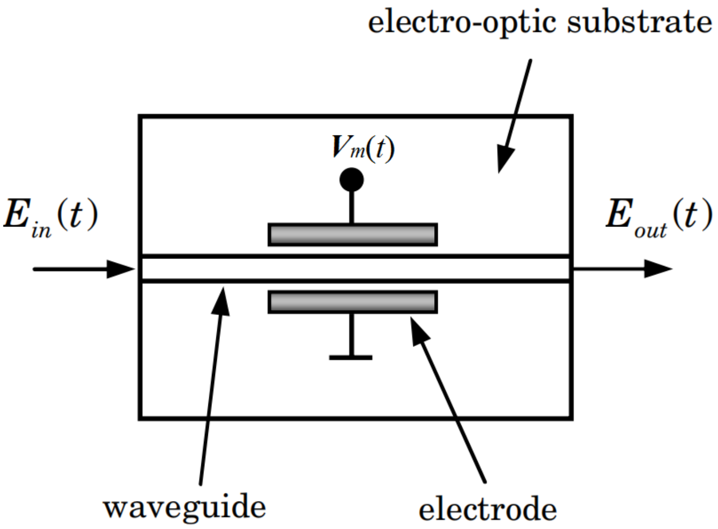

Figure 4.2. Scheme of a phase modulator. (courtesy : Ref. [241])

4.1.1.4 Modulator Voltage

The time varying driving voltage $V_m(t)$ across the waveguide is of the form :

$$V_m(t) = V_{DC} + V_{RF}(t), \tag{4.3}$$

where V_{DC} is the constant DC part of the signal, $V_{RF}(t)$ is the time varying voltage determined by the RF frequencies. When the number of modulation frequencies is one and two, the modulating voltages $V_{RF}(t)$ are given by :

$$V_{RF}(t) = \begin{cases} V_{AC}\Big(\cos(\Omega t)\Big) & \text{for one modulation frequency } \Omega, \\ V_{AC}\Big(\cos(\Omega_1 t) + \cos(\Omega_2 t)\Big) & \text{for two modulation frequencies } \Omega_1 \text{ and } \Omega_2. \end{cases} \tag{4.4}$$

where V_{AC} is the amplitude of the sinusoids. The requirement of two modulation frequencies will be clear when we discuss the two-tone test in Section 4.2.

4.1.1.5 Input RF Power

In the case of a single frequency modulation, the average input RF power $\langle P_{RF,in}\rangle$ can be written as :

$$\begin{aligned} \langle P_{RF,in}\rangle &= \frac{\langle V_{RF}(t)^2\rangle}{R_m} \\ &= \frac{\Big\langle {V_{AC}}^2\big(\cos^2(\Omega t)\big)\Big\rangle}{R_m} = \frac{{V_{AC}}^2}{2R_m}, \end{aligned} \tag{4.5}$$

where R_m is the load of the modulator and we have considered that the average value of $\cos^2(\Omega t)$ is $\frac{1}{2}$ over large number of cycles. Similarly, when we have two modulating frequencies Ω_1 and Ω_2, $\langle P_{RF,in} \rangle$ can be written as :

$$\begin{aligned} \langle P_{RF,in} \rangle &= \frac{\langle V_{RF}(t)^2 \rangle}{R_m} \\ &= \frac{\Big\langle {V_{AC}}^2 \big(\cos^2(\Omega_1 t) + \cos^2(\Omega_2 t) + 2\cos(\Omega_1 t)\cos(\Omega_2 t) \big) \Big\rangle}{R_m} \\ &= \frac{{V_{AC}}^2(\frac{1}{2} + \frac{1}{2} + 0)}{R_m} = \frac{{V_{AC}}^2}{R_m}, \end{aligned} \tag{4.6}$$

where we have considered that the beat-note frequency $(\Omega_1 - \Omega_2)$ is much larger than the detection bandwidth.

4.1.1.6 Half Wave Voltage V_π

The voltage across the waveguide that leads to a π rad phase shift for the light is known as the half wave voltage or V_π for the phase modulator. This parameter is generally provided by the manufacturer.

4.1.1.7 Output Field

Following the definitions of the input field and the half wave voltage, the output field $E_{out}(t)$ can be written as [241] :

$$\begin{aligned} E_{out}(t) &= \mathcal{E} e^{-i\omega t} e^{i\phi(t)} + c.c. = \mathcal{E} e^{-i\omega t} e^{i\frac{V_m(t)\pi}{V_\pi}} + c.c. = \mathcal{E} e^{-i\omega t} e^{i\frac{(V_{DC}+V_{RF}(t))\pi}{V_\pi}} + c.c. \\ &= \mathcal{E} e^{-i\omega t} e^{i(\phi_{DC}+\phi_{AC}(t))} + c.c. \, , \end{aligned} \tag{4.7}$$

where $\phi_{DC} = \frac{V_{DC}\pi}{V_\pi}$ and $\phi_{AC}(t) = \frac{V_{RF}(t)\pi}{V_\pi}$. Here we can see from Equation (4.7) that the output field acquires a constant phase ϕ_{DC} and a time varying phase $\phi_{AC}(t)$ that depends on the time dependent part of the modulator voltage $V_{RF}(t)$.

4.1.2 Electro-Optic Conversion : Mach-Zehnder Modulator

A Mach-Zehnder modulator (MZM) is a device often used in RF-optical communication systems for the electro-optic conversion. At the input of the MZM, an optical signal is provided and then divided into two arms. Both the arms are provided with a phase modulator that modulates the phases of the respective arms by an amount $\phi_1(t)$ and $\phi_2(t)$. At the end, the two arms are united leading to an interference between the two waves. This is depicted in Fig. 4.3. Depending on the relative phase shifts between the two arms, the interference can vary from constructive to destructive leading to an amplitude modulated output.

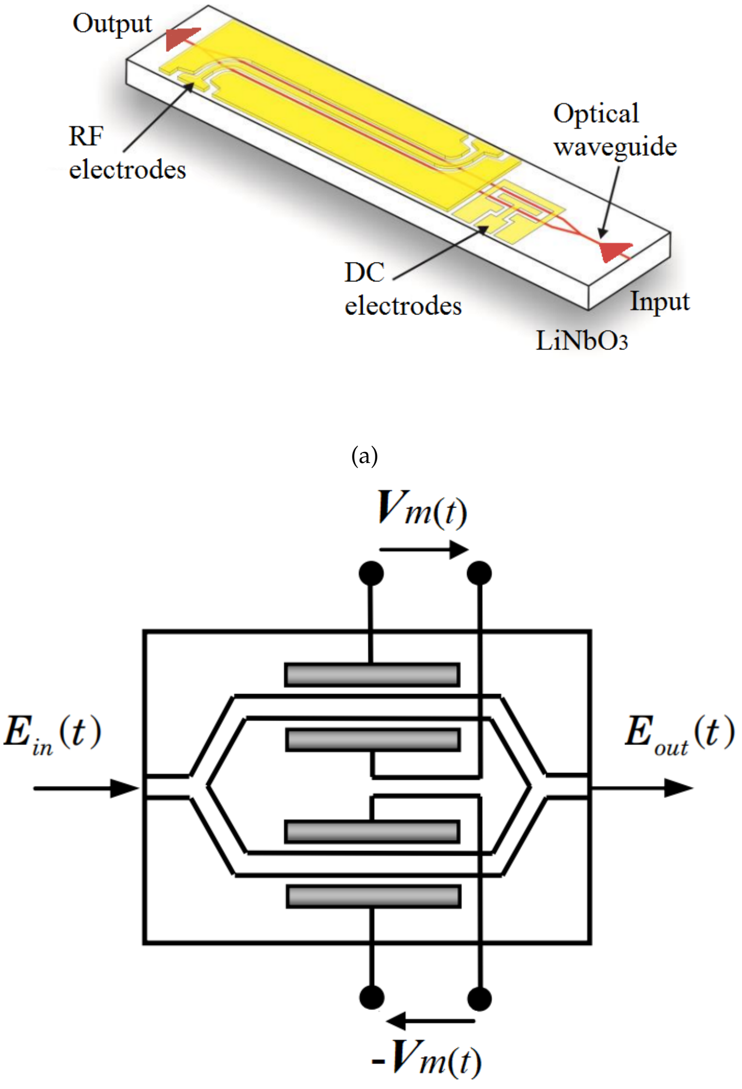

Figure 4.3. (a)Illustration of Mach-Zehnder modulator on an electro-optic (LiNBO$_3$) substrate. (courtesy : iXblue Photonics Inc.) (b) Scheme of a Mach-Zehnder modulator operating in a push-pull configuration. (courtesy : Ref. [241])

4.1.2.1 Output Field

For a standard MZM, with an input field as in Equation (4.2) and a phase modulation of $\phi_1(t)$ and $\phi_2(t)$ in the respective arms, the output field E_{out} is given by [241] :

$$E_{out} = \mathcal{E} e^{-i\omega t} \left(\frac{e^{i\phi_1(t)} + e^{i\phi_2(t)}}{2} \right) + c.c. \, , \tag{4.8}$$

where $\phi_1(t)$ and $\phi_2(t)$ are given by :

$$\phi_1(t) = \frac{V_{m1}(t)\pi}{V_{\pi 1}}, \tag{4.9}$$

$$\phi_2(t) = \frac{V_{m2}(t)\pi}{V_{\pi 2}}, \tag{4.10}$$

where $V_{m1}(t)$ and $V_{m2}(t)$ are the voltages applied across the respective arms and $V_{\pi 1}$ and $V_{\pi 2}$ are their half wave voltages. We can see from Equation (4.8) that when $\phi_1(t) = \phi_2(t) = \phi(t)$, we have a phase modulated output signal as given by Equation (4.7). In such a case, the MZM is said to operate in a push-push configuration.

4.1.2.2 Amplitude Modulation

In the special case when we have $\phi_1(t) = \phi(t) = -\phi_2(t)$, the output field is given by :

$$E_{out} = \cos(\phi(t))E_{in}. \tag{4.11}$$

Considering $V_{\pi 1} = V_{\pi 2}$, we have $V_{m1}(t) = V_m(t) = -V_{m2}(t)$ and in such a case the MZM is said to operate in a push-pull configuration. We can see from the above equation that the amplitude of E_{in} is modulated by the function $\phi(t)$. Hence we can write :

$$\begin{aligned} E_{out} &= \cos\left(\frac{\pi V_m(t)}{2V_\pi}\right)\mathcal{E}e^{-i\omega t} + c.c. \\ &= \cos\left(\frac{\pi V_{DC}}{2V_\pi} + \frac{\pi V_{RF}(t)}{2V_\pi}\right)\mathcal{E}e^{-i\omega t} + c.c. \end{aligned} \tag{4.12}$$

Thus the power transfer function $\frac{P_{out}}{P_{in}}$ is given as :

$$\frac{P_{out}}{P_{in}} = \frac{1}{2}\left(1 + \cos\left(\frac{V_m(t)\pi}{V_\pi}\right)\right). \tag{4.13}$$

Also we note here that in this case we define $V_m(t)$ such that $V_m(t) = V_\pi$ induces a phase shift of π in the power transfer function of the MZM. A MZM is often operated with a DC bias of $V_\pi/2$ and a peak-to-peak modulation voltage of V_π as shown in Fig. 4.4. This type of operation is also known as quadrature point operation.

4.1.3 Opto-RF Conversion

The conversion of an optical signal into an electrical one is often done using a (some) photodetector(s) (PD). Depending on the nature of the modulation, different schemes of detection can be employed. For example, an amplitude modulated signal can be detected with a direct detection scheme, whereas for phase modulated signals a more complex coherent detection scheme is required [99]. In this chapter, we will only focus on the simpler direct detection scheme for the down-conversion of an amplitude modulated optical signal.

In the direct detection scheme, only a single PD is used to down-convert the modulated signal coming from the MZM to an electrical signal. If the part of the total optical power incident on the PD corresponding that is oscillating at a RF frequency

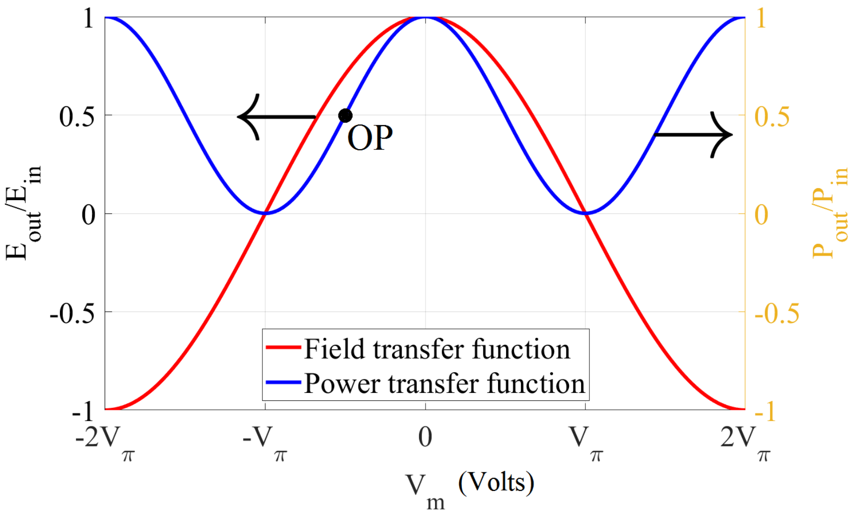

Figure 4.4. Plot of field (red) and power (blue) transfer functions of a Mach-Zehnder modulator working in push-pull configuration. OP : operation point for quadrature point operation.

Ω is P_Ω, then the current generated $I_{det,\Omega}$ by the PD is given by :

$$I_{det,\Omega} = sP_\Omega. \tag{4.14}$$

where s is the sensitivity of the detector. s depends on the kind of PD used and the wavelength of the incident light. Typically at telecom wavelengths ($\sim$ 1.5 μm), s has a value around 0.9 A/W. s can be expressed in terms of quantum efficiency η i.e. the ratio between the number of incident photons and the number of electron-hole pairs generated in the PD. Thus s can be written as :

$$s = \frac{\eta e}{h\nu}, \tag{4.15}$$

where e is the electronic charge constant, h is the Planck's constant and ν is the frequency of the incident light. For an ideal photodetection ($\eta = 1$), at a wavelength of 1550 nm, s is found to be 1.25 A/W.

The total output RF power $P_{det,\Omega}$ generated in the detector circuit corresponding to frequency Ω is then given by :

$$P_{det,\Omega} = I^2_{det,\Omega}R_{det} = s^2P^2_\Omega R_{det}. \tag{4.16}$$

where R_{det} is the load resistance of the detector.

We should note here that, a PD cannot detect optical frequencies (which oscillate typically at few hundreds of THz frequency) due to its limited response time [242]. However it can detect the beating between several optical frequencies which are often of the order of a few GHz. Thus when we have multiple optical frequencies that beat at the same RF frequency (say Ω), the situation becomes quite complicated to analyze, as the optical power corresponding to RF frequency Ω incident on the detector can have multiple beating sources with their individual phases. An example of such a case is shown in Appendix F, where three input optical frequencies ω_1 (sideband 1), ω_2 (signal) and ω_3 (sideband 2) with optical powers P_{ω_1}, P_{ω_2} and P_{ω_3} respectively are incident on a PD. We also have $|\omega_1 - \omega_2| = |\omega_3 - \omega_2| = \Omega$ (see Fig. 4.5). In such a case, the optical power at a frequency Ω detected by PD i.e. P_Ω is given by (see Appendix F) :

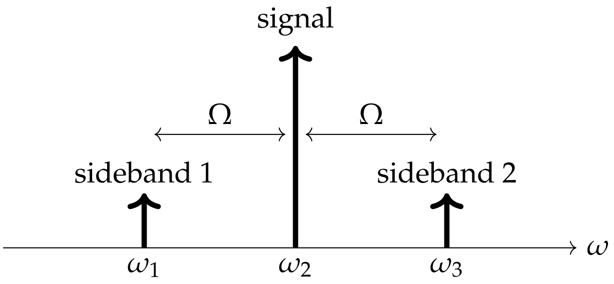

Figure 4.5. The three optical frequencies incident on the photodetector (PD) are denoted by ω_1, ω_2 and ω_3 which correspond to the signal and two sidebands. The difference between the consecutive frequencies are Ω. (not to scale)

$$P_\Omega = 2\sqrt{P_{\omega_1} P_{\omega_2}}\,\cos(\Omega t + \Phi_{12}) + 2\sqrt{P_{\omega_2} P_{\omega_3}}\,\cos(\Omega t + \Phi_{23})\,, \tag{4.17}$$

where Φ_{ij} represent the relative phase difference between the waves at frequencies ω_i and ω_j.

4.2 Two-Tone Test

To understand the two-tone test, first let us look at an example. Let us consider a microwave photonic link in a radar system. The microwave photonic link connects the remotely located radar antenna to a base station. Let us suppose that the radar operates at a RF frequency Ω_1. Now we consider an enemy aircraft entering into the airspace monitored by this radar. Suppose the enemy aircraft tries jamming the radar with an emission of a wave at a RF frequency Ω_2 (which is close to Ω_1). So now, the radar will start picking up both the frequencies Ω_1 (reflected from the aircraft) and Ω_2 (emitted by the aircraft for jamming). When these two signals will be fed to an E/O converter (like a MZM), due to the nonlinearity of the E/O conversion process, higher order inter-modulation products will be created in the optical domain. For example optical third order inter-modulation frequencies (optical IMD3's) will be generated at frequencies like $\omega_s \pm (2\Omega_1 - \Omega_2)$ and $\omega_s \pm (2\Omega_2 - \Omega_1)$ where ω_s is the optical carrier frequency. Then after transmission through an optical link, at the end an O/E conversion will down-convert these optical frequencies and will produce RF waves at frequencies $2\Omega_1 - \Omega_2$ and $2\Omega_2 - \Omega_1$ (apart from the waves at other linear combinations of Ω_1 and Ω_2). Note, that when Ω_1 is close to Ω_2, $(2\Omega_1 - \Omega_2)$ and $(2\Omega_2 - \Omega_1)$ will also be close to Ω_1 and Ω_2. This means that it will be quite difficult to filter out the RF IMD3 waves from the operating frequency Ω_1. Thus when the powers of the RF IMD3 waves are high, it will cause severe distortions in the radar system rendering the link highly ineffective.

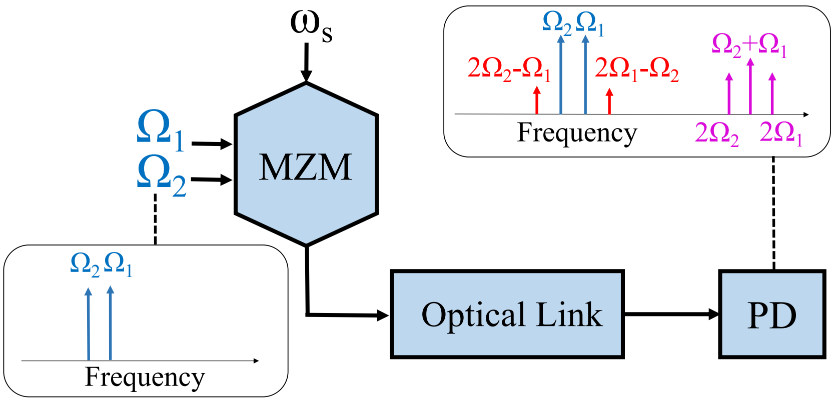

Figure 4.6. Illustration of a nonlinear microwave photonic link. The different RF frequencies (fundamentals : blue, IMD3's : red, others : magenta) at the input and the output are shown with arrows in boxes. MZM : Mach-Zehnder modulator, PD : photodetector, Ω_1, Ω_2 : fundamental RF frequencies, ω_s : optical carrier frequency. (not to scale)

From the above discussed example, we can develop a scheme to characterize the strength of distortions in a microwave photonic link, which is also known as the two-tone test [99, 243]. In the two-tone test, first we need to launch two closely spaced RF modulation frequencies Ω_1 and Ω_2 (known as fundamental RF frequencies) with equal amplitudes via a MZM[3] (often used for E/O conversion for an amplitude modulation format) for modulating an optical carrier signal at a frequency ω_s. The nonlinearity of the MZM will lead to production of third-order inter-modulation products (optical IMD3's) at optical frequencies $\omega_s \pm (2\Omega_1 - \Omega_2)$ and $\omega_s \pm (2\Omega_2 - \Omega_1)$. Then after propagation through the optical link[4], all the optical frequencies are down-converted into RF frequencies by a PD (see Fig. 4.6). The output RF powers of the fundamental and the IMD3's are monitored as a function of the input RF power of the fundamental RF frequencies. The RF powers of the output IMD3 waves can be treated as a quantifier of the distortion of the link. This means a link with high fidelity will have a lower output IMD3 RF power and vice versa.

4.2.1 MZM Output Power

When we use a MZM for amplitude modulation of an optical signal at frequency ω_s with RF frequencies Ω_1 and Ω_2, ideally we expect to see waves generated at frequencies $\omega_s \pm \Omega_1$ and $\omega_s \pm \Omega_2$. However in reality, the modulation process is nonlinear and leads to generation of more sidebands. To understand this process in

---

[3] For a phase modulation format just a phase modulator can be used.

[4] In this subsection we consider an optical link that does not add extra nonlinearities apart from that produced by the MZM. Later in this chapter however, we will look at optical links that add nonlinearities of their own. Introducing a FOPA in the optical link leads to such a scenario.

more detail, let us write down the x-polarized output field $\vec{E}_{out}$ of a MZM with a carrier frequency ω_s and modulation frequencies Ω_1 and Ω_2 :

$$\begin{aligned}\vec{E}_{out} &= \frac{\mathcal{E}}{2} e^{-i\omega_s t}\left(e^{i\phi} e^{iA\cos(\Omega_1 t)} e^{iA\cos(\Omega_2 t)} + e^{-i\phi} e^{-iA\cos(\Omega_1 t)} e^{-iA\cos(\Omega_2 t)}\right)\vec{e_x} + c.c.\\ &= \frac{\mathcal{E}}{2} e^{-i\omega_s t}\left(e^{i\phi}\Big(\sum_{m=-\infty}^{\infty} i^m J_m(A) e^{im\Omega_1 t}\Big)\Big(\sum_{n=-\infty}^{\infty} i^n J_n(A) e^{in\Omega_2 t}\Big)\right.\\ &\left. + e^{-i\phi}\Big(\sum_{p=-\infty}^{\infty} i^p J_p(-A) e^{ip\Omega_1 t}\Big)\Big(\sum_{q=-\infty}^{\infty} i^q J_q(-A) e^{iq\Omega_2 t}\Big)\right)\vec{e_x} + c.c.\,,\end{aligned} \tag{4.18}$$

where $\vec{e_x}$ represent the unit vector in the x-direction. The input field of the MZM is of the form of Equation (4.2) with $\omega = \omega_s$, the modulation voltage is of the form of Equations (4.3) and (4.4). Thus $\phi = \frac{V_{DC}\pi}{V_\pi}$ and $A = \frac{V_{AC}\pi}{V_\pi}$. For a better understanding, we have shown the terms at the optical frequencies in red and those at RF frequencies in blue. J_n represents the Bessel function of the first kind of order n. To arrive here we have used the Jacobi-Anger expansion which is given as :

$$e^{iA\cos(\Omega t)} = \sum_{n=-\infty}^{\infty} i^n J_n(A) e^{in\Omega t}. \tag{4.19}$$

Thus the amplitude of the component of the output electric field oscillating at a frequency $\omega_s - m\Omega_1 - n\Omega_2$ is given by :

$$\begin{aligned}\mathcal{E}_{mn} &= \frac{\mathcal{E}}{2} J_m(A) J_n(A) e^{i\frac{\pi}{2}(m+n)}\left(e^{i\phi} + (-1)^{(m+n)} e^{-i\phi}\right)\\ &= \frac{\mathcal{E}}{2} J_m(A) J_n(A) i^{(m+n)} P_{m,n},\end{aligned} \tag{4.20}$$

where $P_{m,n}$ is given by :

$$P_{m,n} = \begin{cases} 2\cos(\phi) & \text{for } m+n \text{ even,}\\ 2i\sin(\phi) & \text{for } m+n \text{ odd.}\end{cases} \tag{4.21}$$

To arrive here we have used a property of the Bessel function of the first kind, given as (see Appendix G) :

$$J_n(-A) = (-1)^n J_n(A). \tag{4.22}$$

Thus the total output electric field $\vec{E}_{out}$ can be rewritten as :

$$\vec{E}_{out} = \sum_{m=-\infty}^{\infty}\sum_{n=-\infty}^{\infty} \mathcal{E}_{mn} e^{-i(\omega_s - m\Omega_1 - n\Omega_2)t}\,\vec{e_x} + c.c.\,. \tag{4.23}$$

Similarly the total output magnetic field $\vec{H}_{out}$ polarized in the y-direction is given by :

$$\begin{aligned}\vec{H}_{out} &= \sum_{m=-\infty}^{\infty}\sum_{n=-\infty}^{\infty} \mathcal{H}_{mn} e^{-i(\omega_s - m\Omega_1 - n\Omega_2)t}\ \vec{e_y} + c.c. \\ &= \sum_{m=-\infty}^{\infty}\sum_{n=-\infty}^{\infty} c\epsilon_0 \mathcal{E}_{mn} e^{-i(\omega_s - m\Omega_1 - n\Omega_2)t}\ \vec{e_y} + c.c.\ ,\end{aligned} \tag{4.24}$$

where $\vec{e_y}$ is the unit vector in the y-direction. Thus the output Poynting vector $\vec{S}_{out}$ is given by :

$$\begin{aligned}\vec{S}_{out} &= \vec{E}_{out} \times \vec{H}_{out} \\ &= c\epsilon_0 \left(\sum_{m=-\infty}^{\infty}\sum_{n=-\infty}^{\infty} \mathcal{E}_{mn} e^{-i(\omega_s - m\Omega_1 - n\Omega_2)t}\ \vec{e_x} + c.c. \right) \\ &\times \left(\sum_{p=-\infty}^{\infty}\sum_{q=-\infty}^{\infty} \mathcal{E}_{pq} e^{-i(\omega_s - p\Omega_1 - q\Omega_2)t}\ \vec{e_y} + c.c. \right) .\end{aligned} \tag{4.25}$$

Rearranging the terms, we get :

$$\begin{aligned}\vec{S}_{out} = c\epsilon_0 &\left(\sum_{m,n,p,q=-\infty}^{\infty} \mathcal{E}_{mn}\mathcal{E}_{pq} e^{-i(2\omega_s - (m+p)\Omega_1 - (n+q)\Omega_2)t}\ \vec{e_z} + c.c. \right) \\ + c\epsilon_0 &\left(\sum_{m,n,p,q=-\infty}^{\infty} \mathcal{E}_{mn}\mathcal{E}^*_{pq} e^{i((m-p)\Omega_1 + (n-q)\Omega_2)t}\ \hat{k} + c.c. \right) ,\end{aligned} \tag{4.26}$$

where $\vec{e_z}$ is the unit vector in the z-direction. Since the first group of terms oscillate at the order of the optical frequency ω_s, the detector cannot detect its variation. Thus on time averaging, all the high frequency terms are neglected (see Appendix F), and we get the time-averaged Poynting vector $\langle \vec{S}_{out} \rangle$ as :

$$\langle \vec{S}_{out} \rangle = c\epsilon_0 \left(\sum_{m,n,p,q=-\infty}^{\infty} \mathcal{E}_{mn}\mathcal{E}^*_{pq} e^{i((m-p)\Omega_1 + (n-q)\Omega_2)t}\ \vec{e_z} + c.c. \right) . \tag{4.27}$$

Thus the total detected optical power, i.e. $P_{opt,tot} = a||\langle \vec{S}_{out} \rangle||$ (where a is the area of the beam cross section) (see Appendix F) can be written using Equation (4.20) as :

$$\begin{aligned}P_{opt,tot} = a||\langle \vec{S}_{out} \rangle|| = \frac{2a\epsilon_0\mathcal{E}^2}{8} \Bigg| &\sum_{m,n,p,q=-\infty}^{\infty} J_m(A)J_n(A)J_p(A)J_q(A) \\ e^{i\frac{\pi}{2}(m+n-p-q)} &\left(e^{i\phi} + (-1)^{(m+n)} e^{-i\phi} \right) \left(e^{-i\phi} + (-1)^{(p+q)} e^{i\phi} \right) e^{i((m-p)\Omega_1 + (n-q)\Omega_2)t} + c.c. \Bigg| \\ = \frac{P_s}{8} \Bigg| &\sum_{m,n,p,q=-\infty}^{\infty} J_m(A)J_n(A)J_p(A)J_q(A) e^{i\frac{\pi}{2}(m+n-p-q)} P_{mnpq} e^{i((m-p)\Omega_1 + (n-q)\Omega_2)t} + c.c. \Bigg| .\end{aligned} \tag{4.28}$$

where P_s is the input carrier signal power (before the MZM). We have defined the quantity P_{mnpq} as :

$$P_{mnpq} = 1 + (-1)^{(p+q)} e^{i2\phi} + (-1)^{(m+n)} e^{-i2\phi} + (-1)^{(m+n+p+q)} . \tag{4.29}$$

We note here that P_{mnpq} can be evaluated depending on whether $m+n$ and $p+q$ are even or odd. Thus it can be rewritten as follows :

$$P_{mnpq} = \begin{cases} 4\cos^2(\phi) & \text{for } \ m+n \text{ even}, \ p+q \text{ even}, \\ -2i\sin(2\phi) & \text{for } \ m+n \text{ even}, \ p+q \text{ odd}, \\ 2i\sin(2\phi) & \text{for } \ m+n \text{ odd}, \ p+q \text{ even}, \\ 4\sin^2(\phi) & \text{for } \ m+n \text{ odd}, \ p+q \text{ odd}. \end{cases} \tag{4.30}$$

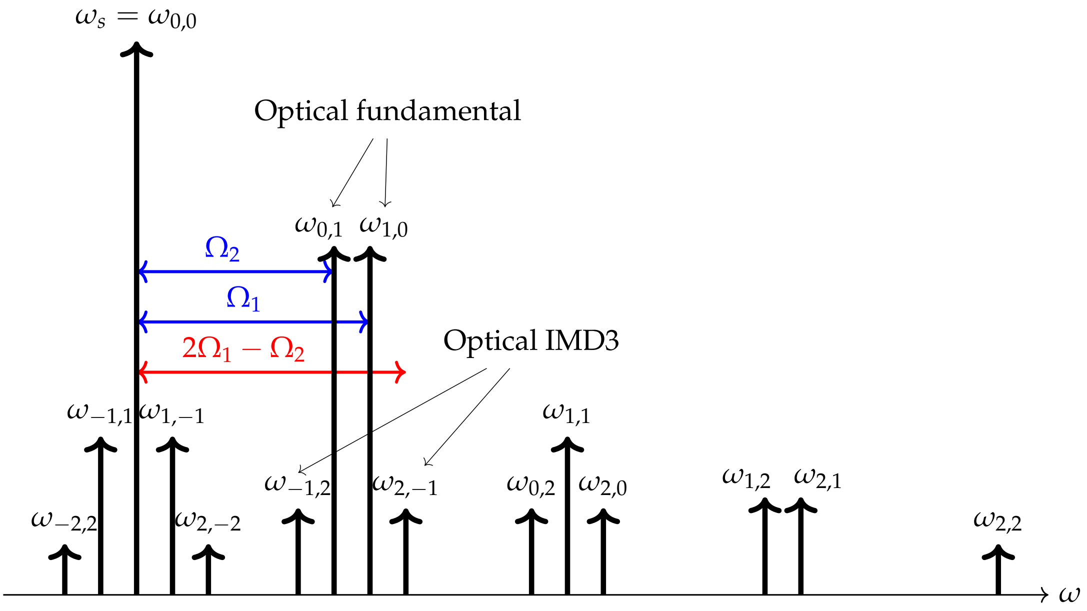

Figure 4.7. An illustration of some of the different frequencies generated when a signal with optical frequency $\omega_s = \omega_{0,0}$ is modulated in a MZM with two RF frequencies Ω_1 and Ω_2 in a push-pull configuration. $2\Omega_1 - \Omega_2$ is the RF frequency corresponding to the third order inter-modulation product. In the figure each wave is labelled with its frequency $\omega_{i,j}$ where $\omega_{i,j} = \omega_s + i\Omega_1 + j\Omega_2$. $0 \leq i, j \leq 2$ for this figure. (not to scale)

Form Equation (4.28) we can see that due to the modulation with two RF frequencies Ω_1 and Ω_2, in the optical domain, a large number of different frequencies of the form $\omega_s + m\Omega_1 + n\Omega_2$ are produced, where m and n are arbitrary integers. Some of these different frequencies are shown in Fig. 4.7. Although we have not shown both sides of the spectrum, we should note that this spectrum is symmetric with respect to the signal frequency ω_s.

4.2.2 Part of Total Optical Power at Fundamental Frequency

As defined before, Ω_1 and Ω_2 are the fundamental RF frequencies. When these RF frequencies are used to modulate an optical signal at ω_s, sidebands are produced at $\omega \pm \Omega_1$ and $\omega \pm \Omega_2$ frequencies. We refer to these frequencies as optical fundamental frequencies. So if we want to find the part of the total optical power that oscillates at a frequency Ω_1[5] i.e. P_{opt,Ω_1}, at the end of the link, we have to pick only those terms in Equation (4.28) where the oscillating part gives $e^{i\Omega_1 t}$. This can be achieved by setting m, n, p and q as : (a) m, n, $(m-1)$ and n and (b) $(m-1)$, n, m and n in Equation (4.28) respectively. Both the cases will lead to the same set of terms and combining them we get :

$$P_{opt,\Omega_1} = \frac{P_s}{8}\left| 2\sum_{m,n=-\infty}^{\infty} J_m J_n J_{(m-1)} J_n i P_{mn(m-1)n} e^{i\Omega_1 t} + c.c.\right| . \tag{4.31}$$

Here we have changed the notation $J_n(A)$ to J_n for brevity. We note, that when $m+n$ is even, $(m-1)+n$ is odd and vice versa. Thus using Equation (4.30), $P_{mn(m-1)n}$ can be expressed as :

$$P_{mn(m-1)n} = (-1)^{(m+n+1)} 2i \sin(2\phi). \tag{4.32}$$

Thus when $m+n$ is even, $(-1)^{(m+n+1)} = -1$ and when $m+n$ is odd, $(-1)^{(m+n+1)} = 1$. We can regroup the terms and write P_{opt,Ω_1} as :

$$\begin{aligned}
P_{opt,\Omega_1} &= \frac{P_s}{2}\left| \sin(2\phi) e^{i\Omega_1 t} \sum_{m,n=-\infty}^{\infty} J_m J_{(m-1)} {J_n}^2 (-1)^{(m+n)} + c.c.\right| \\
&= \frac{P_s}{2}\left| \sin(2\phi) e^{i\Omega_1 t} \left(\sum_{m=-\infty}^{0} \sum_{n=-\infty}^{\infty} J_m J_{m-1} {J_n}^2 (-1)^{(m+n)} \right.\right. \\
&\quad \left.\left. + \sum_{m=1}^{\infty} \sum_{n=-\infty}^{\infty} J_m J_{m-1} {J_n}^2 (-1)^{(m+n)} \right) + c.c. \right| .
\end{aligned} \tag{4.33}$$

We know that for the Bessel functions of the first kind, the negative orders satisfy (see Appendix G) :

$$J_{-n}(A) = (-1)^n J_n(A), \tag{4.34}$$

where n is non negative. Using this relation we can write :

$$\begin{aligned}
P_{opt,\Omega_1} &= \frac{P_s}{2}\left| \sin(2\phi) e^{i\Omega_1 t} \left(\sum_{m=1}^{\infty} \sum_{n=-\infty}^{\infty} (-1)^{2m-1} J_m J_{m-1} {J_n}^2 (-1)^{(-m+1+n)} \right.\right. \\
&\quad \left.\left. + \sum_{m=1}^{\infty} \sum_{n=-\infty}^{\infty} J_m J_{m-1} {J_n}^2 (-1)^{(m+n)} \right) + c.c. \right| \\
&= P_s \left| \sin(2\phi) e^{i\Omega_1 t} \left(\sum_{m=1}^{\infty} \sum_{n=-\infty}^{\infty} J_m J_{m-1} {J_n}^2 (-1)^{(m+n)} \right) + c.c. \right| .
\end{aligned} \tag{4.35}$$

---

[5] Note that here we refer to the optical power that is incident on the PD and not the electrical power generated in the detection circuit.

Although the right hand side of the above equation is an infinite series, we can approximate it to a few leading terms. Thus restricting the infinite series to $m = 2$ and $|n| = 2$[6], we get :

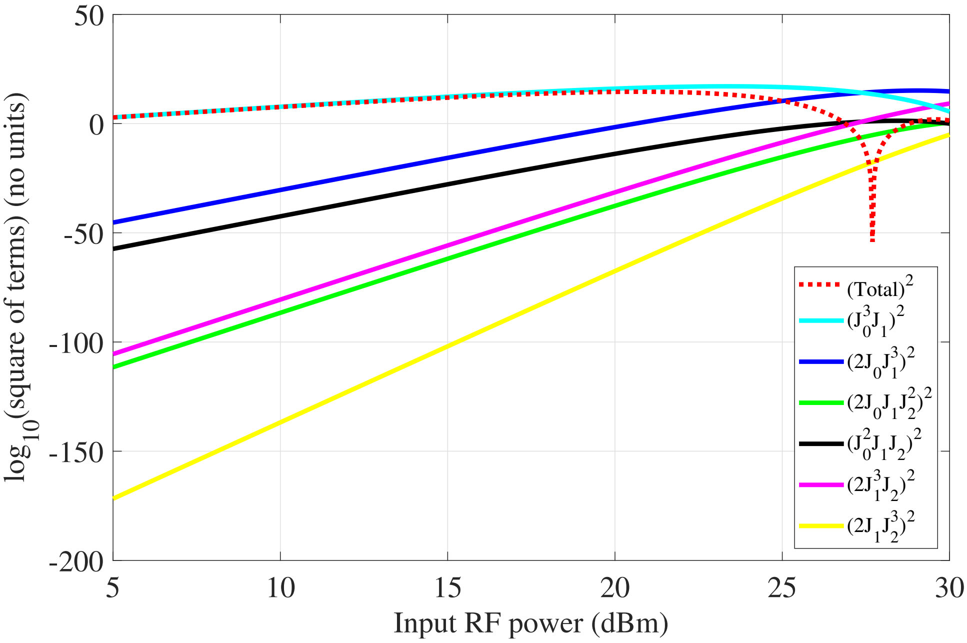

Figure 4.8. Comparison of individual Bessel function terms ($({J_0}^3 J_1)^2$: cyan, $(2J_0 {J_1}^3)^2$: blue, $(2J_0 J_1 {J_2}^2)^2$: green, $({J_0}^2 J_1 J_2)^2$: black, $(2{J_1}^3 J_2)^2$: magenta and $(2J_1 {J_2}^3)^2$: yellow) with the total combination of terms ($(-{J_0}^3 J_1 + 2J_0 {J_1}^3 - 2J_0 J_1 {J_2}^2 + {J_0}^2 J_1 J_2 - 2{J_1}^3 J_2 + 2J_1 {J_2}^3)^2$: red dashed) in the expression of power of part of the total optical power oscillating at the fundamental frequency (see Equation (4.36)). Arbitrary units are considered in the y-axis. $V_\pi = 5$ V and $V_{DC} = 2.5$ V.

$$\begin{aligned}
P_{opt,\Omega_1} &= 2P_s \left| \sin(2\phi)\cos(\Omega_1 t) \left(\sum_{m=1,2} J_m J_{m-1} \sum_{n=-2}^{2} (-1)^{m+n} {J_n}^2 \right) \right| \\
&= 2P_s \left| \sin(2\phi)\cos(\Omega_1 t) \left(J_1 J_0 \sum_{n=-2}^{2} (-1)^{1+n} {J_n}^2 + J_2 J_1 \sum_{n=-2}^{2} (-1)^{2+n} {J_n}^2 \right) \right| \\
&= 2P_s \left| \sin(2\phi)\cos(\Omega_1 t) \left(-{J_0}^3 J_1 + 2J_0 {J_1}^3 - 2J_0 J_1 {J_2}^2 + {J_0}^2 J_1 J_2 - 2{J_1}^3 J_2 + 2J_1 {J_2}^3 \right) \right| .
\end{aligned} \tag{4.36}$$

In the above equation, the dominant term is ${J_0}^3 J_1$ (leaving the pre-factor). This can also be seen from Fig. 4.8 (see cyan solid curve) where we plot the square of all the terms in Equation (4.36) (leaving the pre-factors) in the logarithmic scale, as a function of the input RF power. In Fig. 4.8 we also plot the square of the sum of all the terms (dashed red curve) : $(-{J_0}^3 J_1 + 2J_0 {J_1}^3 - 2J_0 J_1 {J_2}^2 + {J_0}^2 J_1 J_2 - 2{J_1}^3 J_2 + 2J_1 {J_2}^3)^2$. The parameters of the MZM used for the plot are : $V_\pi = 5$ V and $V_{DC} = 2.5$ V. From Fig. 4.8, we see that when the input RF power is more than about 22 dBm, the higher

---

[6] This choice of indices ensures that we generate terms that only contain J_0, J_1 and J_2 and not higher order terms like J_3.

order terms in Equation (4.36) become important as the MZM starts showing more and more nonlinearity. For lower input RF powers, ${J_0}^3 J_1$ is the most significant term.

4.2.3 Part of Total Optical Power at IMD3 Frequency

As calculated for the fundamental frequency Ω_1, now we will look at the part of the total optical power generated at the output of the MZM, oscillating at a frequency $2\Omega_1 - \Omega_2$. To achieve this we use Equation (4.28) and set m, n, p and q as : (a) $m, n, m-2$ and $n+1$ and (b) $m-2, n+1, m$ and n. Thus we can write the power of the part of the total optical power oscillating at IMD3 frequency, i.e. $P_{opt,2\Omega_1-\Omega_2}$ as :

$$P_{opt,2\Omega_1-\Omega_2} = \frac{P_s}{8}\left| 2 \sum_{m,n=-\infty}^{\infty} J_m J_n J_{m-2} J_{n+1} i P_{mn(m-2)(n+1)} e^{i(2\Omega_1-\Omega_2)t} + c.c. \right| . \tag{4.37}$$

We note here that when $m+n$ is even, $(m-2)+(n+1) = m+n-1$ is odd and vice versa. Thus we can evaluate $P_{mn(m-2)(n+1)}$ and write :

$$\begin{aligned}
P_{opt,2\Omega_1-\Omega_2} &= \frac{P_s}{2}\left| \sin(2\phi) e^{i(2\Omega_1-\Omega_2)t} \sum_{m,n=-\infty}^{\infty} J_m J_n J_{m-2} J_{n+1} (-1)^{m+n} + c.c. \right| \\
&= \frac{P_s}{2}\Bigg| \sin(2\phi) e^{i(2\Omega_1-\Omega_2)t} \Bigg(\sum_{m=-\infty}^{0} J_m J_{m-2} \sum_{n=-\infty}^{\infty} J_n J_{n+1} (-1)^{m+n} \\
&+ J_1 J_{-1} \sum_{n=-\infty}^{\infty} J_n J_{n+1} (-1)^{1+n} + \sum_{m=2}^{\infty} J_m J_{m-2} \sum_{n=-\infty}^{\infty} J_n J_{n+1} (-1)^{m+n} \Bigg) + c.c. \Bigg| \\
&= P_s \Bigg| \sin(2\phi) \cos((2\Omega_1-\Omega_2)t) \Bigg(2 \sum_{m=2}^{\infty} J_m J_{m-2} \sum_{n=-\infty}^{\infty} J_n J_{n+1} (-1)^{m+n} \\
&- {J_1}^2 \sum_{n=-\infty}^{\infty} J_n J_{n+1} (-1)^{1+n} \Bigg) \Bigg| .
\end{aligned} \tag{4.38}$$

When we truncate the series at $m=2$ and $n=-2$ to $n=1$[7], we have :

$$\begin{aligned}
P_{opt,2\Omega_1-\Omega_2} = P_s \Bigg| &\sin(2\phi) \cos((2\Omega_1-\Omega_2)t) \Bigg(2J_2 J_0 \Big(J_{-2}J_{-1} - J_{-1}J_0 + J_0 J_1 - J_1 J_2 \Big) \\
&- {J_1}^2 \Big(- J_{-2}J_{-1} + J_{-1}J_0 - J_0 J_1 + J_1 J_2 \Big) \Bigg) \Bigg| .
\end{aligned} \tag{4.39}$$

---

[7] This choice of indices are to ensure that we generate terms that only contain J_0, J_1 and J_2 and not higher order terms like J_3.

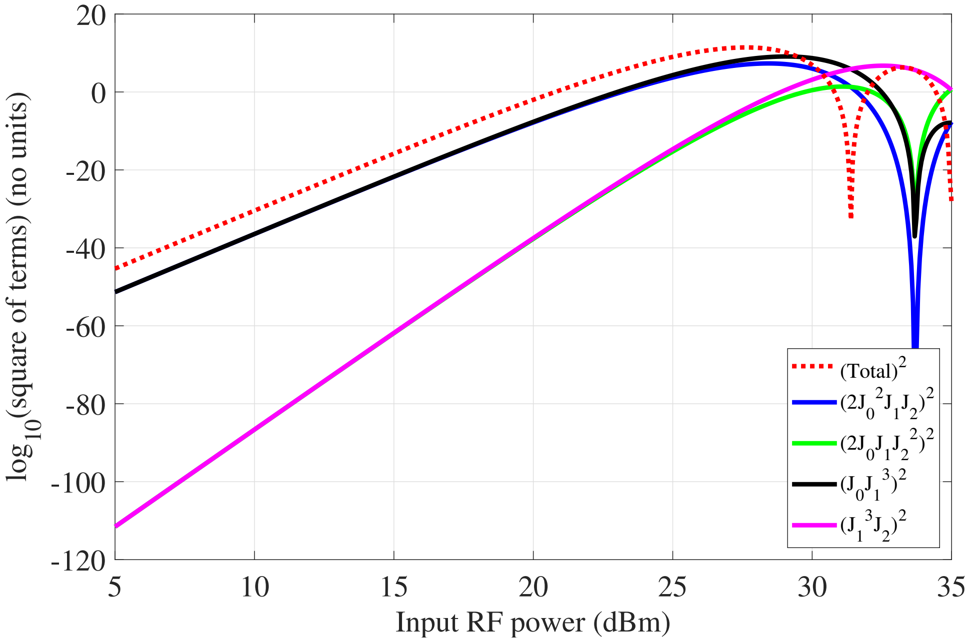

Figure 4.9. Comparison of individual Bessel function terms ($(2{J_0}^2 J_1 J_2)^2$: blue, $(2 J_0 J_1 {J_2}^2)^2$: green, $(J_0 {J_1}^3)^2$: black and $({J_1}^3 J_2)^2$: magenta) with the total combination of terms ($(-{J_0}^3 J_1 + 2 J_0 {J_1}^3 - 2 J_0 J_1 {J_2}^2 + {J_0}^2 J_1 J_2 - 2 {J_1}^3 J_2 + 2 J_1 {J_2}^3)^2$: red dashed) in the expression of part of total power oscillating at IMD3 frequency (see Equation (4.40)). Arbitrary units are considered in the y-axis. $V_\pi = 5$ V and $V_{DC} = 2.5$ V.

Using the second property of Bessel functions of the first kind (see Appendix G) we get :

$$\begin{aligned}
P_{opt,2\Omega_1-\Omega_2} &= P_s \Bigg| \sin(2\phi)\cos((2\Omega_1-\Omega_2)t)\Bigg(2J_2J_0\Big(-J_2J_1+J_1J_0+J_0J_1-J_1J_2\Big) \\
&\quad -{J_1}^2\Big(J_2J_1-J_1J_0-J_0J_1+J_1J_2\Big)\Bigg)\Bigg| \\
&= 2P_s\Big|\sin(2\phi)\cos((2\Omega_1-\Omega_2)t)\Big(2J_0J_2+J_1^2\Big)\Big(J_0J_1-J_1J_2\Big)\Big| \\
&= 2P_s\Big|\sin(2\phi)\cos((2\Omega_1-\Omega_2)t)\Big(2{J_0}^2J_1J_2-2J_0J_1{J_2}^2+J_0{J_1}^3-{J_1}^3J_2\Big)\Big|.
\end{aligned} \tag{4.40}$$

In Fig. 4.9 we plot the square of all the terms in Equation (4.40) (leaving the prefactors) in the logarithmic scale, as a function of the input RF power. In Fig. 4.9 we also plot the square of the sum of all the terms (dashed red curve) : $(2{J_0}^2 J_1 J_2 - 2 J_0 J_1 {J_2}^2 + J_0 {J_1}^3 - {J_1}^3 J_2)^2$. The parameters of the MZM used for the plot are : $V_\pi = 5$ V and $V_{DC} = 2.5$ V. From Fig. 4.9, we see that till 27 dBm of input RF power, the IMD3 power shows a linear relationship with input RF power (in the log scale). For larger input RF powers it deviates from the linear relationship.

4.2.4 SFDR

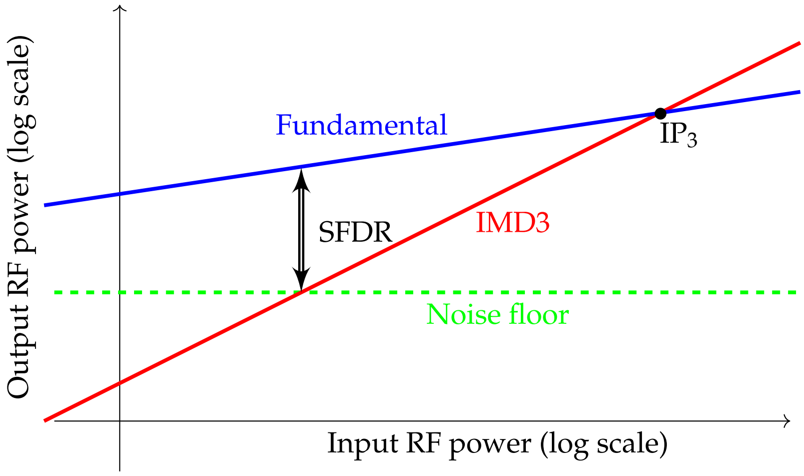

Figure 4.10. An illustration of dependence of output RF power of fundamental (blue solid line) and that of IMD3 (red solid line) in a microwave photonic link as a function of the corresponding input RF powers. The noise floor is shown in green dashed line The SFDR and IP$_3$ are shown in double sided arrow and black point respectively. (not to scale)

We have seen in Figs. 4.8 and 4.9 that the parts of the output optical powers at fundamental and IMD3 frequencies grow linearly (in a log scale) with slopes 1 and 3 respectively with the input RF power of modulation. This linear growth persists up to a certain limit of input RF power. Beyond this limit, we see a saturation. In the context of microwave photonic links, this relationship between the input and output RF powers of the fundamental and IMD3 waves leads to the determination of the dynamic range of the link. The spurious free dynamic range (SFDR) is often used to gauge the linearity of a link. The SFDR of a link is calculated by finding the input RF power where the output RF power of the IMD3 is equal to the noise floor level. The difference of the output RF power of the fundamental and the noise floor (considering a log scale) at that input RF power gives the SFDR. For example, in Fig. 4.10 we show the noise floor (green dashed line) along with the input-output dependence of IMD3 (red solid line) and the fundamental (blue solid line) RF powers of a microwave photonic link. The corresponding SFDR is shown in double sided black arrow.[8]

Another widely used quantifier of link quality is the third-order intercept point (IP$_3$). IP$_3$ is the point where the linear extrapolation of the fundamental and IMD3 curves intersect (in the log-log scale) as shown in Fig. 4.10.

---

[8] Note that in Fig. 4.10 we have considered the fundamental and IMD3 curves to be linear throughout the whole range of input RF powers for simplicity. In reality the linearity breaks down for higher values of input RF powers as shown in Figs. 4.8 and 4.9.

In the linear regime of the curve (as in Fig. 4.10) from Equation (4.36) we can approximate P_{opt,Ω_1} as :

$$P_{opt,\Omega_1} \approx 2P_s|\sin(2\phi)\cos(\Omega_1 t)(-{J_0}^3 J_1)|. \tag{4.41}$$

Also from Equation (4.40), $P_{opt,2\Omega_1-\Omega_2}$ can be approximated as :

$$P_{opt,2\Omega_1-\Omega_2} \approx 2P_s|\sin(2\phi)\cos((2\Omega_1-\Omega_2)t)(2{J_0}^2 J_1 J_2 + J_0 {J_1}^3)|. \tag{4.42}$$

We remind here that J_0, J_1 and J_2 are functions of $A = \frac{V_{AC}\pi}{V_\pi}$. From the definition of the Bessel function of the first kind, of order n, we have (see Appendix G) :

$$J_n(A) = \sum_{m=0}^{\infty} K_{mn} A^{2m+n}, \tag{4.43}$$

where K_{mn} is a constant independent on A. For small values of A, the series can be approximated by terminating after finite number of terms. If we only consider terms till A^2, then $J_0(A)$, $J_1(A)$ and $J_2(A)$ can be approximated as :

$$J_0(A) \approx 1, \tag{4.44}$$

$$J_1(A) \approx \frac{A}{2}, \tag{4.45}$$

$$J_2(A) \approx \frac{A^2}{8}. \tag{4.46}$$

Hence we can write :

$$P_{opt,\Omega_1} \propto {J_0(A)}^3 J_1(A) \propto A \propto V_{AC} \propto \langle P_{RF,in}\rangle^{\frac{1}{2}}, \tag{4.47}$$

$$P_{opt,2\Omega_1-\Omega_2} \propto (2{J_0}^2 J_1 J_2 + J_0 {J_1}^3) \propto A^3 \propto {V_{AC}}^3 \propto \langle P_{RF,in}\rangle^{\frac{3}{2}}, \tag{4.48}$$

where $\langle P_{RF,in}\rangle$ is the average input RF power. From Equation (4.16) we know that the detected power at Ω, i.e. $P_{det,\Omega} \propto P^2_{opt,\Omega}$. Thus we can write the detected powers at Ω_1 and $2\Omega_1 - \Omega_2$ are proportional to :

$$P_{det,\Omega_1} \propto \langle P_{RF,in}\rangle, \tag{4.49}$$

$$P_{det,2\Omega_1-\Omega_2} \propto \langle P_{RF,in}\rangle^3. \tag{4.50}$$

Hence in the log-log plot of outpur RF power detected by the PD versus the input RF power, the curve of fundamental RF should have a slope of one while the IMD3 RF curve should have a slope of three.

4.3 Numerical Model

In the previous sections we discussed about a microwave photonic link that converts an input RF signal to an optical signal with an electro-optic modulation and transmits the modulated signal through an optical link that is down-converted to an electrical signal at the end of the link. In this process we talked about the nonlinearities generated by a MZM used for the E/O conversion. However we did not say anything about the nonlinearities (if any) that might have originated in the optical link. In this section we will focus on the nonlinearities that originate from the optical link. Thus we describe an experimental scheme (developed previously in our group [244]) and a corresponding numerical model to probe the effect of nonlinearities from an optical link on the performance of the microwave photonic link.

4.3.1 Model Outline

As we discussed at the beginning of this chapter, in a microwave photonic link, the optical link might be quite long to connect the remote antenna with the base station. In such cases incorporation of an optical amplifier within the optical link is solicited. A traditional phase insensitive amplifier (like an EDFA) is limited by a quantum noise figure of 3 dB [47]. However fiber phase sensitive amplifiers have the potential to outperform such phase insensitive amplifiers by reaching noise figure values as low as 0 dB theoretically [87]. But in the context of a microwave photonic link, the optical amplification process can induce extra nonlinearities into the link. Hence it is worth investigating the impact of introduction of a PSA in a microwave photonic link on the global performance of the link.

To numerically model a microwave photonic link with a PSA, we consider the following scheme (shown in Fig. 4.11 [125, 127]). In this scheme, a signal and an idler are fed into a MZM that operates in an amplitude modulation mode (push-pull configuration) and modulates the input signal and idler with two RF frequencies Ω_1 and Ω_2. The modulated signal and idler are then coupled with a strong pump beam and injected in a HNLF for optical phase sensitive amplification. After the amplification the waves are incident on a PD and subsequently fed to an electronic spectrum analyzer (ESA) to monitor the powers of the fundamental and IMD3 RF waves.

4.3.2 Experimental Setup

A test setup was previously developed by Ihsan Fsaifes and Tarek Labidi in our group mimicking a microwave photonic link including a PSA following the scheme in Fig. 4.11. A detailed scheme of the setup is shown in Fig. 4.12. The output of a tunable laser source (TLS) is divided into two branches. On one branch, the light is modulated by a RF signal at frequency $(\omega_s - \omega_p)/2\pi = 20\,\text{GHz}$ to create the signal and idler from the laser source tuned at a central frequency of 1547 nm. It is then amplified with an EDFA and filtered with two bandpass filters (BPF) tuned at

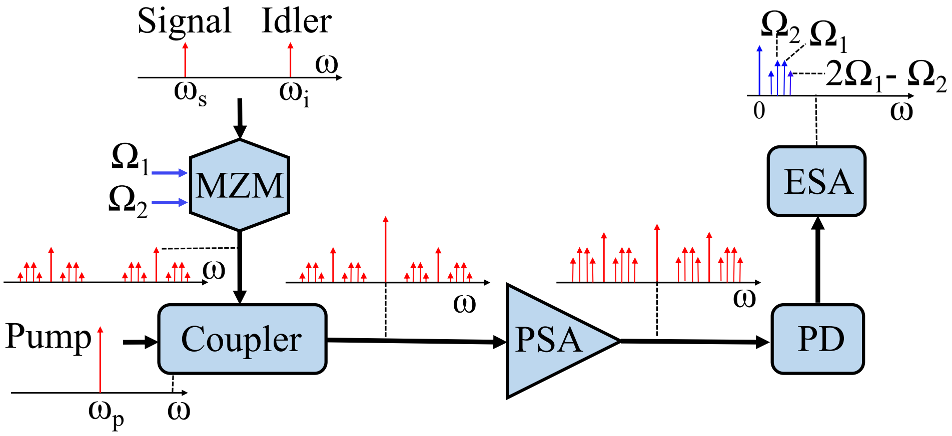

Figure 4.11. Principle of two-tone test of a microwave photonic link including a PSA. The signal (ω_s) and idler (ω_i) waves are modulated at two frequencies Ω_1 and Ω_2 and combined with a pump (ω_p) wave and launched in a HNLF (working as PSA). The spectra shown in red (blue) correspond to optical (RF) frequencies. MZM : Mach-Zehnder modulator; PD : Photodetector; ESA : Electrical spectrum analyzer.

the signal and idler frequencies to get rid of the central frequency. Then the signal and idler are modulated with two RF tones (Ω_1 and Ω_2) using a MZM in push-pull configuration. The other branch of the TLS is fed with several RF tones to suppress stimulatted Brillouin scattering (SBS). Then it is amplified with an EDFA. A fiber Bragg grating (FBG) with 0.2 nm optical bandwidth at 1547 nm along with a circulator (C) are used to filter out the amplified spontaneous emission (ASE) pedestal on the pump spectrum coming from the EDFA. A piezo-electric transducer (PZT) is used to control the phase of the pump. Then the two branches are coupled and fed into a HNLF which acts as a PSA. An isolator is used at the entry of the HNLF to eliminate any unwanted back reflection. As the PSA gain depends on the relative phase between the pump, signal, and idler, the relative phase is servo-locked such that the PSA gain of the signal is maximized. At the exit of the HNLF, the pump and the idler are removed using a notch filter. One part of this signal is detected by a photodiode and fed back using a PI servo loop to the PZT to control the phase of the pump. The other part is detected by a photodiode and is fed into an electrical spectrum analyzer (ESA) for retrieving the power of the RF fundamental and IMD3 waves for different input modulation powers.

The different parameters used in the experiment are the following. The pump wavelength is 1547 nm. The pump-signal frequency separation is $(\omega_s - \omega_p)/2\pi =$ 20 GHz. The modulation frequencies $\Omega_1/2\pi$ and $\Omega_2/2\pi$ are 1 GHz and 0.998 GHz, respectively. The half-wave voltage V_π of the modulator is 5 V and the DC bias V_{DC} is adjusted at 2.5 V. The pump power at the entry of HNLF is 22 dBm and the input signal and idler powers, including their sidebands, are equal to -16 dBm. The 1000-m-long HNLF has a nonlinear coefficient $\gamma = 11.3\,(\mathrm{W.km})^{-1}$, a zero-dispersion wavelength $\lambda_{ZDW} = 1547\,\mathrm{nm}$, an attenuation coefficient α corresponding to 0.9 dB/km, and a dispersion slope equal to $0.017\,\mathrm{ps.nm^{-2}.km^{-1}}$.

In the experiment, the output fundamental and IMD3 RF powers are recorded as a function of the input RF power applied to the modulator. The parameters used in the simulations are extracted from the experiment. We only changed the RF frequencies $\Omega_1/2\pi$ and $\Omega_2/2\pi$ to 1.567 GHz and 1.564 GHz, respectively, in order to avoid spectral leakage errors and computational complexities (see Subsection 3.2.3).

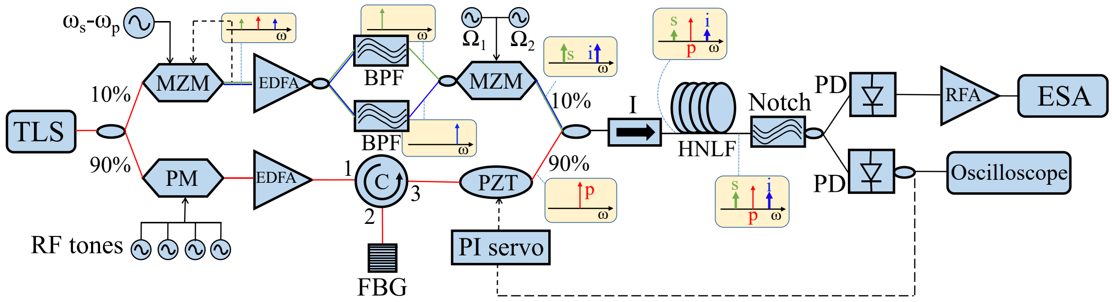

Figure 4.12. Experimental setup for the two tone test in a microwave photonic link with PSA. The spectrum at different positions of the setup are shown in yellow boxes (not to scale) where s, i and p represent signal, idler and pump waves. The feedback loops are shown in dashed arrows. TLS : Tunable laser source; MZM : Mach-Zehnder modulator; PM : Phase modulator; EDFA : Erbium doped fiber amplifier; C : Circulator; BPF : Bandpass filter; FBG : Fiber Bragg grating; PZT : Piezo-electric transducer; I : Isolator; HNLF : Highly nonlinear fiber; Notch : Notch filter; PD : Photodetector; RFA : RF amplifier; ESA : Electrical spectrum analyzer.

4.3.3 Experimental Validation

In order to validate our numerical model, we compare our numerical results with experimental data. Figure 4.13 compares the results obtained from the NLSE simulation (as we developed in the previous chapter) with the experimental results. The output fundamental RF powers are reproduced as blue symbols while the IMD3 RF powers are plotted in red. The numerical results correspond to the circles and the measurements to the stars. Finally, the open symbols correspond to the situation where the PSA is off (no injected pump) while the filled symbols hold for results obtained when the PSA is on (22 dBm input pump power) and provides an optical gain of 10 dB.

First of all, the open symbols in this figure illustrate the well known fact that the nonlinearity of a standard MZM induces strong IMD3's, as already discussed in Section 4.2. Second, by comparing the blue symbols with the red symbols, one can see that all the RF tones, both fundamental and IMD3's, experience a 20 dB gain, i.e. twice the optical gain, when the PSA is on. This shows that the PSA does not add any RF signal nonlinearity to the ones that were already created by the MZM; it just amplifies them with the same gain as the fundamentals.

Finally, the most important feature of Fig. 4.13 is that the agreement between theory and experiments is very good. This means that the model developed with the NLSE simulation is valid and that we can use it to predict the behavior of a PSA in more exotic configurations.

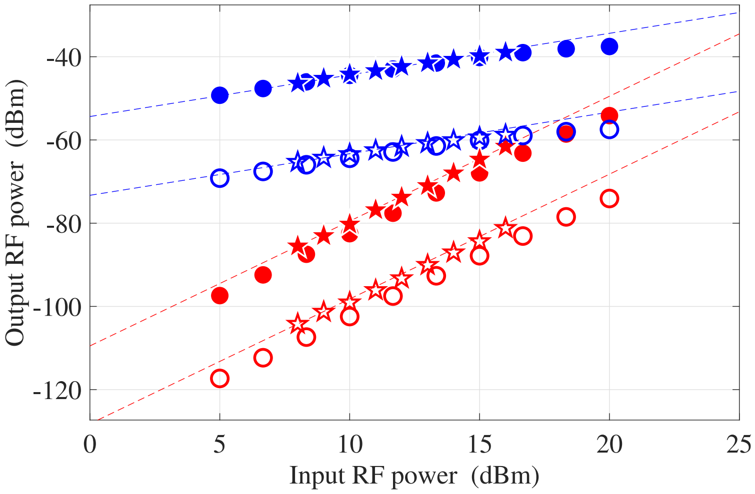

Figure 4.13. Output fundamental (blue symbols) and IMD3 (red symbols) RF powers vs. input RF power using a standard MZM. Stars: measurements; circles: simulations. Open symbols: PSA off; filled symbols: PSA on. Only the signal is detected. Blue (red) dashed lines: slope 1 (3). Parameters : input pump power: 22 dBm; input signal and idler power: -16 dBm; HNLF length: 1000 m.

4.4 AM vs PM

The electro-optic conversion of RF signals in a microwave photonic link is performed by a modulator. As discussed at the beginning of this chapter, the most common modulation formats are amplitude modulation (AM), which is most often performed by a Mach-Zehnder modulator (MZM), and phase modulation (PM), generally achieved using a single waveguide created in an electro-optic material. However the optical gain (from a PSA) of the different waves in the optical link depends on the relative phases between the different waves. AM and PM formats of modulation lead to different relative phases between the different optical waves launched into a PSA. Thus in this Section we investigate how the PSA gain is influenced by these two formats of operation.

4.4.1 AM

For AM, the output field of a MZM operating in push-pull configuration contains several oscillating frequencies as shown in Equation (4.18). For convenience we rewrite the output real electric field E_{out} here in a scalar form :

$$\begin{aligned} E_{out}(t) = \frac{\mathcal{E}}{2} e^{-i(\omega_j t+\theta)} \Bigg(& e^{i\phi} \Big(\sum_{m=-\infty}^{\infty} i^m J_m(A) e^{im\Omega_1 t}\Big)\Big(\sum_{n=-\infty}^{\infty} i^n J_n(A) e^{in\Omega_2 t}\Big) \\ & + e^{-i\phi}\Big(\sum_{p=-\infty}^{\infty} i^p J_p(-A) e^{ip\Omega_1 t}\Big)\Big(\sum_{q=-\infty}^{\infty} i^q J_q(-A)e^{iq\Omega_2 t}\Big)\Bigg) + c.c. \,, \end{aligned} \tag{4.51}$$

where all the symbols have their usual meanings. $j = s$ while considering the signal as the central wave and $j = i$ while considering the idler as the central wave. The terms oscillating at optical frequencies are shown in red and those at RF frequencies in blue. The component of the complex amplitude oscillating at a frequency $\omega_j - m\Omega_1 - n\Omega_2$ is consequently given in Equation (4.20) and is restated as :

$$\mathcal{E}_{mn} = \frac{\mathcal{E}}{2} J_m(A) J_n(A) e^{i\theta} i^{(m+n)} P_{m,n}, \tag{4.52}$$

where $P_{m,n}$ is given by :

$$P_{m,n} = \begin{cases} 2\cos(\phi) & \text{for } \ m+n \ \text{ even,} \\ 2i\sin(\phi) & \text{for } \ m+n \ \text{ odd.} \end{cases} \tag{4.53}$$

From the above equations it is easy to verify[9] that $\mathcal{E}_{mn} = \mathcal{E}_{|m||n|}$ for all integer m and n. That means the phases of the waves are symmetric with respect to the carrier or signal frequency. Thus the phase $\theta_{j,mn}$ of the complex amplitude $\mathcal{E}_{mn}$ is given by :

$$\theta_{j,mn} = \begin{cases} (|m| + |n|)\frac{\pi}{2} + \theta & \text{for } \ m+n \ \text{ even,} \\ (|m| + |n| + 1)\frac{\pi}{2} + \theta & \text{for } \ m+n \ \text{ odd,} \end{cases} \tag{4.54}$$

where $j = s$ for the signal branch waves and $j = i$ for the idler branch waves.

Let us consider the amplification of a wave at the fundamental optical frequency $\omega_s - \Omega_1$ i.e. $m = 1$ and $n = 0$. The gain of the phase sensitive amplification of this wave will depend on the relative phase $\Theta_{f,AM}$ between the pump, the wave at $\omega_i + \Omega_1$ and itself (considering a 3-wave model) [58][10]. Thus $\Theta_{f,AM}$ is given by :

$$\begin{aligned} \Theta_{f,AM} &= \theta_{s,10} + \theta_{i,-10} - 2\theta_p \\ &= \theta_{s,00} - \pi + \theta_{i,00} - \pi - 2\theta_p \\ &= \Theta_{s,AM}, \end{aligned} \tag{4.55}$$

where θ_p is the phase of the pump and $\Theta_{s,AM}$ is the relative phase of the PSA process involving the pump signal and idler waves. In the above equation we have used the fact that the phase of the optical fundamental wave ($m = 1$, $n = 0$) is same as the carrier wave ($m = n = 0$) following Equation (4.54) (see Fig. 4.14). The above equation implies that the optimization of the signal phase for a maximum PSA gain of the signal will also lead to a maximum PSA gain of the optical fundamental[11]. In fact from Equation (4.54) we can further see that all the modulation sidebands will have the same phase as the signal (or idler). Therefore under maximum PSA

---

[9] For negative values of m and n we can use the properties of Bessel functions of the first kind (see Appendix G) to verify this.

[10] Note that there can be many PSA processes that can influence the gain of the waves, however the ones containing the pump are the dominant ones in unsaturated PSA regime. Thus here we restrict ourselves to only one process.

[11] In this analysis we have not considered any initial phase of the modulation voltage. However this analysis holds true even if the MZM modulation voltage owns an initial phase [127].

gain condition for the signal (or idler), all its sidebands (including the optical IMD3 waves) will also undergo a maximum PSA gain as long as the sidebands are close to the signal (or idler) and the PSA is not gain saturated.

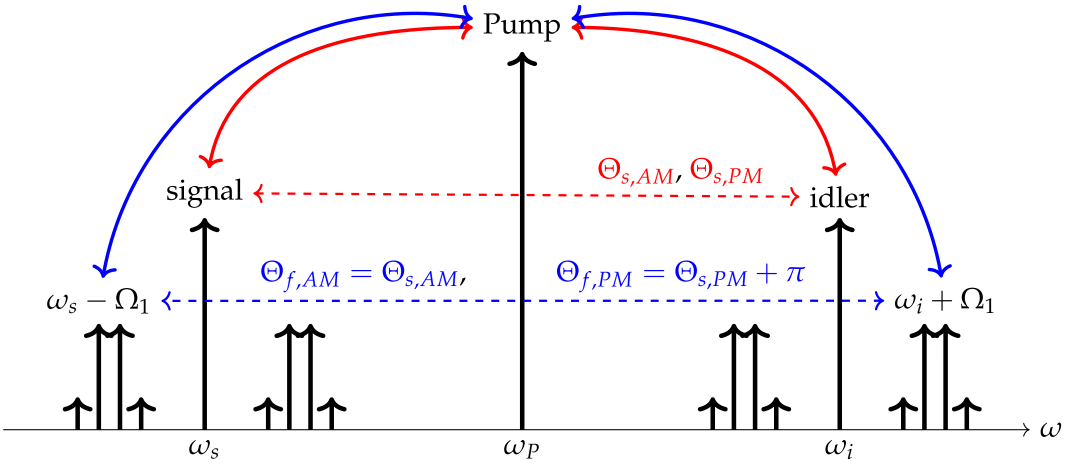

Figure 4.14. An illustration of PSA processes that lead to the amplification (or deamplification) of the signal (process with the pump, signal and idler; shown in red double sided arrows) and the optical fundamental wave (process with the pump, optical fundamental in the signal branch and its mirror image in the idler branch; shown in blue double sided arrows) under a non-pump depletion approximation. The corresponding relative phases $\Theta_{s,AM}$ (or $\Theta_{s,PM}$) and $\Theta_{f,AM}$ (or $\Theta_{f,PM}$) for the two processes are also indicated. Subscripts AM and PM refer to amplitude modulation and phase modulation formats respectively. (not to scale)

4.4.2 PM

Similar to the case of AM, the real output electric field E_{out} of a phase modulator is given by :

$$\begin{aligned} E_{out}(t) &= \mathcal{E}e^{-(i\omega_j t+\theta)}e^{iA\cos(\Omega_1 t)}e^{iA\cos(\Omega_2 t)} + c.c. \\ &= \mathcal{E}e^{-(i\omega_j t+\theta)}\Big(\sum_{m=-\infty}^{\infty} i^m J_m(A)e^{im\Omega_1 t}\Big)\Big(\sum_{n=-\infty}^{\infty} i^n J_n(A)e^{in\Omega_2 t}\Big) + c.c. \ , \end{aligned} \tag{4.56}$$

where $j = s$ for the signal wave and $j = i$ for the idler wave. All other symbols have their usual meanings. The terms oscillating at optical frequencies are shown in red and those at RF frequencies in blue. The complex electric field amplitude $\mathcal{E}_{mn}$ of a wave at a frequency $\omega_j - m\Omega_1 - n\Omega_2$ is thus given by :

$$\mathcal{E}_{m,n} = \mathcal{E}e^{i\theta}i^{(m+n)}J_m(A)J_n(A). \tag{4.57}$$

Note that unlike the AM case, in PM, $\mathcal{E}_{mn} = \mathcal{E}_{-m-n}$ when $m+n$ is even and $\mathcal{E}_{mn} = -\mathcal{E}_{-m-n}$ when $m+n$ is odd. The phase $\theta_{j,mn}$ of the complex amplitude $\mathcal{E}_{mn}$ is given by :

$$\theta_{j,mn} = (m+n)\frac{\pi}{2} + \theta. \tag{4.58}$$

Now similar to previous case of AM, we consider the amplification of the optical fundamental and signal waves that depend on relative phases $\Theta_{f,PM}$ and $\Theta_{s,PM}$ respectively. $\Theta_{f,PM}$ is given by :

$$\begin{aligned} \Theta_{f,PM} &= \theta_{s,10} + \theta_{i,-10} - 2\theta_p \\ &= (\theta_{s,00} + \frac{\pi}{2}) + (\theta_{i,00} + \frac{\pi}{2}) - 2\theta_p \\ &= \Theta_{s,PM} + \pi. \end{aligned} \tag{4.59}$$

All symbols have their usual meanings and to arrive here we have used Equation (4.58). In contrast to the AM case, the above equation tells us that when the relative phase $\Theta_{s,PM}$ is optimized such that the signal attains a maximum PSA gain, the relative phase $\Theta_{f,PM}$ for the PSA process with the optical fundamental is π radians shifted leading to minimum PSA gain (de-amplification) for the optical fundamental wave (see Fig. 4.14). In general we can say that when the signal attains a maximum PSA gain, all odd order waves (waves at frequencies $\omega_j - m\Omega_1 - n\Omega_2$ where $m + n$ is odd) will experience a minimum PSA gain or will be de-amplified. On the other hand, the even order waves (waves at frequencies $\omega_j - m\Omega_1 - n\Omega_2$ where $m + n$ is even), will undergo maximum PSA gain as the signal.

4.4.3 Simulation Results

Our analysis on the PM and AM formats show that for PM format, a maximum PSA gain for the signal and idler carriers leads to de-amplification of the first order sidebands (optical fundamental waves), and vice-versa. On the other hand, for AM format, a maximum PSA gain for the signal and idler leads to amplification of the first order sidebands. This is also reinforced by our simulation results. In Fig. 4.15 we plot the evolution of optical powers of different waves (pump : red, signal : blue, optical fundamental : green and optical IMD3 : magenta) along the length of the HNLF obtained from the simulation. An AM format was considered in Fig. 4.15 (a) and PM format was considered in Fig. 4.15 (b). The input pump power was 22 dBm, input signal and idler powers were -15 dBm and input RF power was 10 dBm. The phases of the signal and the idler waves were optimized to reach the maximum PSA gain. A standard HNLF was used as in Subsection 4.3.3 expect the attenuation loss was neglected in this case. From Fig. 4.15 we see that for AM, the signal, optical fundamental and optical IMD3 waves attain a PSA gain of about 11.6 dB, however for the PM format, while the signal attained a positive PSA gain of 11.5 dB, the optical fundamental and optical IMD3 waves were de-amplified with PSA gains of -10.6 dB and -10.9 dB respectively. Since at the output of the HNLF, the strength of the output fundamental RF signal mainly originates from the beating between the optical carrier and the optical fundamental wave, one can see that a PSA is a good choice to amplify AM signals but not PM signals. It should also be noted here that the above analysis only holds true for a PSA that is unsaturated. A comparison between PM

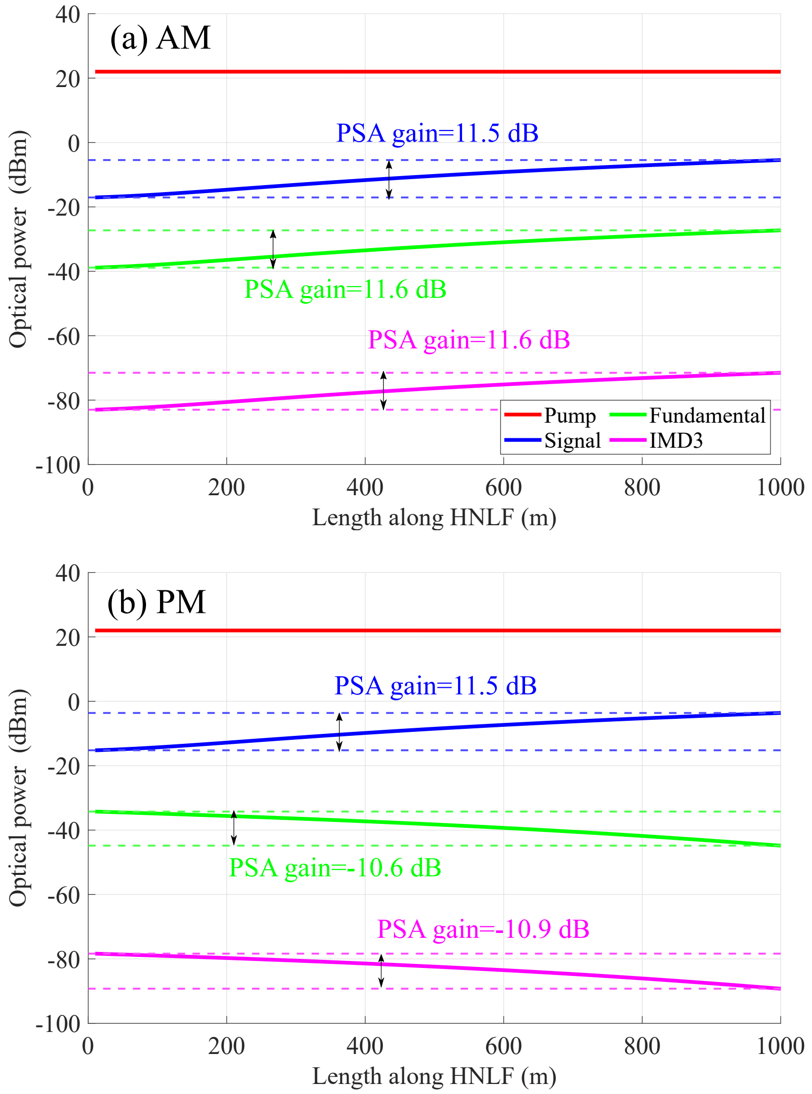

Figure 4.15. Simulation results for evolution of optical powers of different waves (pump : red, signal : blue, optical fundamental : green and optical IMD3 : magenta) along the length of the HNLF for a AM format : (a) and PM format : (b). Dashed lines are provided to indicate the PSA gains. Fiber attenuation is ignored. Input signal and idler powers : -15 dBm, input pump power : 22 dBm and input RF power : 10 dBm. All other parameters are same as used in the simulation of Fig. 4.13.

and AM under gain saturation conditions demands a more sophisticated mathematical treatment.

4.5 Saturation Behaviour : Standard Intensity Modulator

Previously in Subsection 4.3.3, the input signal and idler powers (-16 dBm each) were small enough so that, even after having propagated through the HNLF and experiences the PSA gain (10 dB), their output power would remain much smaller than the pump power (22 dBm). Then, in these conditions, one can neglect the depletion of the pump, i.e. saturation of the PSA. On the contrary, in the present section, we use our numerical model to gauge the situations where saturation of the PSA gain occurs, in order to explore whether the RF nonlinearity of the PSA increases in the presence of gain saturation. To this aim, we first observe the PSA behavior by scanning the input RF power for several input signal and idler powers (Subsection 4.5.1) when gain saturation occurs. Then in Subsection 4.5.2 we scan the input signal and idler powers with the same goal in mind. Subsequently in Subsection 4.5.3 we scan the input pump power of the PSA. After that in Subsection 4.5.4 we scan the phase of the input signal and idler going into the PSA to find if the RF nonlinearities can be counter balanced by the PSA nonlinearity. Finally in Subsection 4.5.5 we analyze the impact of the PSA on the SFDR of the link for different values of input signal powers.

4.5.1 Scan of Input RF Power

We can see from Equation (4.18) that, when the input RF power is increased, the powers of the higher order harmonics increase, making the modulator more and more nonlinear. We thus plot the output power of the RF fundamental (blue symbols) and IMD3 (red symbols) when the PSA is off (hollow symbols) and on (filled symbols) in Figs. 4.16 (a,b). In the simulations of Fig. 4.16 and all the following, we suppose that the detector is perfect, and that the signal undergoes 0.9 dB losses in the HNLF and 3 dB losses between the HNLF and the detector. Figure 4.16 (a) corresponds to a low (-14 dBm) signal and idler power, including all their sidebands, at the the input of the HNLF, while Fig. 4.16 (b) corresponds to a stronger (14 dBm) input signal and idler power. The corresponding RF gains for the fundamental (blue squares) and IMD3 (red triangles) tones, when the PSA is tuned at its maximum gain, are shown in Figs. 4.16 (c) and 4.16 (d), respectively. Finally, Figs. 4.16 (e) and 4.16 (f) show the corresponding PSA optical gains for the signal (magenta stars), the pump (black circles), the optical fundamental (blue squares), and the optical IMD3 (red triangles). For each case, the relative phase between the pump, signal and the idler is adjusted to maximize the PSA gain. The other parameters are the same as in Subsection 4.3.3.

From these results, we see that for a low input signal power (-14 dBm, left column in Fig. 4.16), the RF gain of fundamental and IMD3 tones is independent on the input RF power. This is due to the fact that the powers of the signal and idler and all their sidebands are too small to saturate the PSA gain, and thus experience the same optical gain. For higher RF powers ($>$ 15 dBm), the output RF powers of the RF fundamental and IMD3 shows some saturation due to the nonlinearity of the MZM.

On the contrary, in the case of a higher input signal power (14 dBm, right column in Fig. 4.16), gain saturation occurs, as can be seen by comparing the RF gains for the fundamentals and the IMD3's in Figs. 4.16 (c) and (d). For input RF powers typically larger than 16 dBm (as indicated by the dashed line in Figs. 4.16 (d,f), a large number of strong sidebands are generated by the MZM. Then, the numerous four-wave

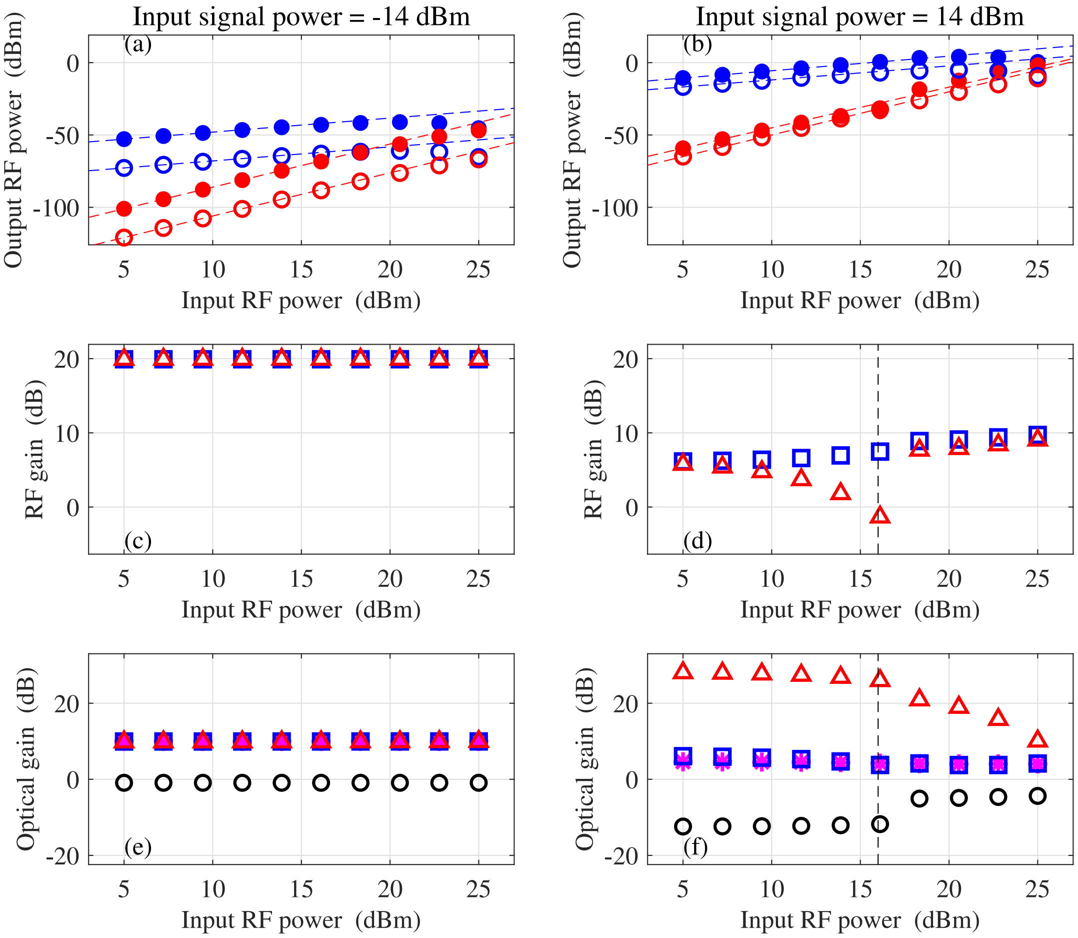

Figure 4.16. (a,b) : Output fundamental (blue) and IMD3 (red) RF powers versus input RF power with the PSA off (open symbols) and on (full symbols). Blue and red dashed lines: guides to the eye to stress gain saturation. (c,d) : Fundamental (blue squares) and IMD3 (red triangles) RF gains versus input RF power. (e,f) : Optical gain of the signal (magenta stars), pump (black circles), fundamental (blue squares) and IMD3 (red triangles) tones versus input RF power. A standard MZM is used and only the signal is detected. Signal power at the MZM input: -14 dBm (a,c,e) and 14 dBm (b,d,f); input pump power: 22 dBm; HNLF length: 1000 m.

mixing processes in the PSA modify the powers of all these frequencies in a complex manner. As an illustration, the optical spectra at the input and output of the PSA are shown in Figs. 4.17 (a) and (b) for relatively low (10 dBm) and high (20 dBm) RF powers, respectively. In Fig. 4.17 (b), the strong input RF power leads to the fact that the beatnote between many different optical waves contribute to a strong IMD3 RF tone. The dip in the IMD3 RF gain in Fig. 4.16 (d) can be attributed to the fact that the different beatnotes contributing to the RF IMD3 are out of phase. Moreover, we also checked in this case that this result does not critically depend on the values of the modulation frequencies Ω_1 and Ω_2.

Additionally, Fig. 4.16 (f) exhibits a decrease in the optical gain of the optical IMD3 above an input RF power of 16 dBm. This decrease is due to the presence of a higher number of strong optical sidebands at the input of the PSA, which deplete

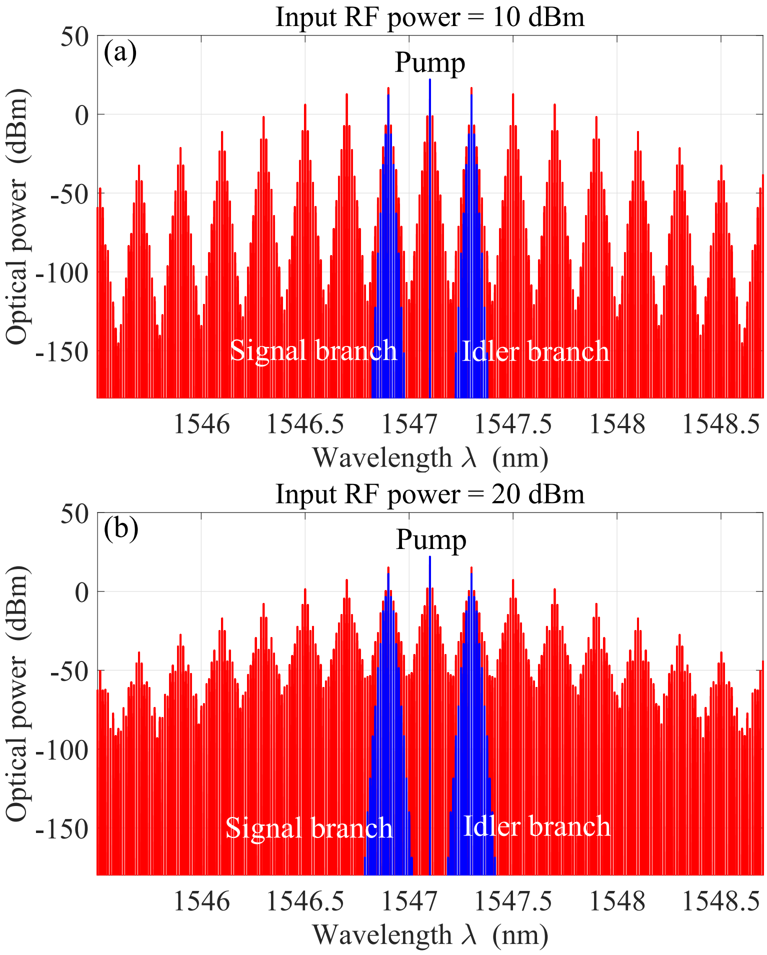

Figure 4.17. Optical spectra at the input (blue) and output (red) of the HNLF for (a) a low (10 dBm) input RF power and (b) a high (20 dBm) input RF power. Other parameters : input signal and idler power: 14 dBm; input pump power: 22 dBm; HNLF length: 1000 m. Optical losses : 3.9 dB. The detector is supposed to be ideal.

the available gain. Such a decrease of the IMD3 RF gain much below the RF gain of the fundamental tone opens interesting perspectives to use the PSA to decrease the nonlinearities of microwave photonics links, as also discussed in Refs. [134, 245].

4.5.2 Scan of Input Signal Power

As we have seen in Fig. 4.16, the increase of the input signal power leads to PSA gain saturation. We thus plot in Fig. 4.18 the evolution of the PSA behavior as a function of the signal and idler powers, in a manner similar to Fig. 4.16. The two columns of Fig. 4.18 correspond to two values of the input RF power: 10 dBm (left) and 20 dBm (right).

Figures 4.18 (e) and 4.18 (f) show that the pump depletion becomes significant, i. e., the pump gain becomes much smaller than 0 dB, for input signal powers larger than 0 dBm. This also corresponds to a decrease of the gain experienced by the signal and the optical fundamental tones. However, surprisingly, this corresponds to a strong increase, from 10 dB up to 25 dB, of the optical gain for the optical IMD3

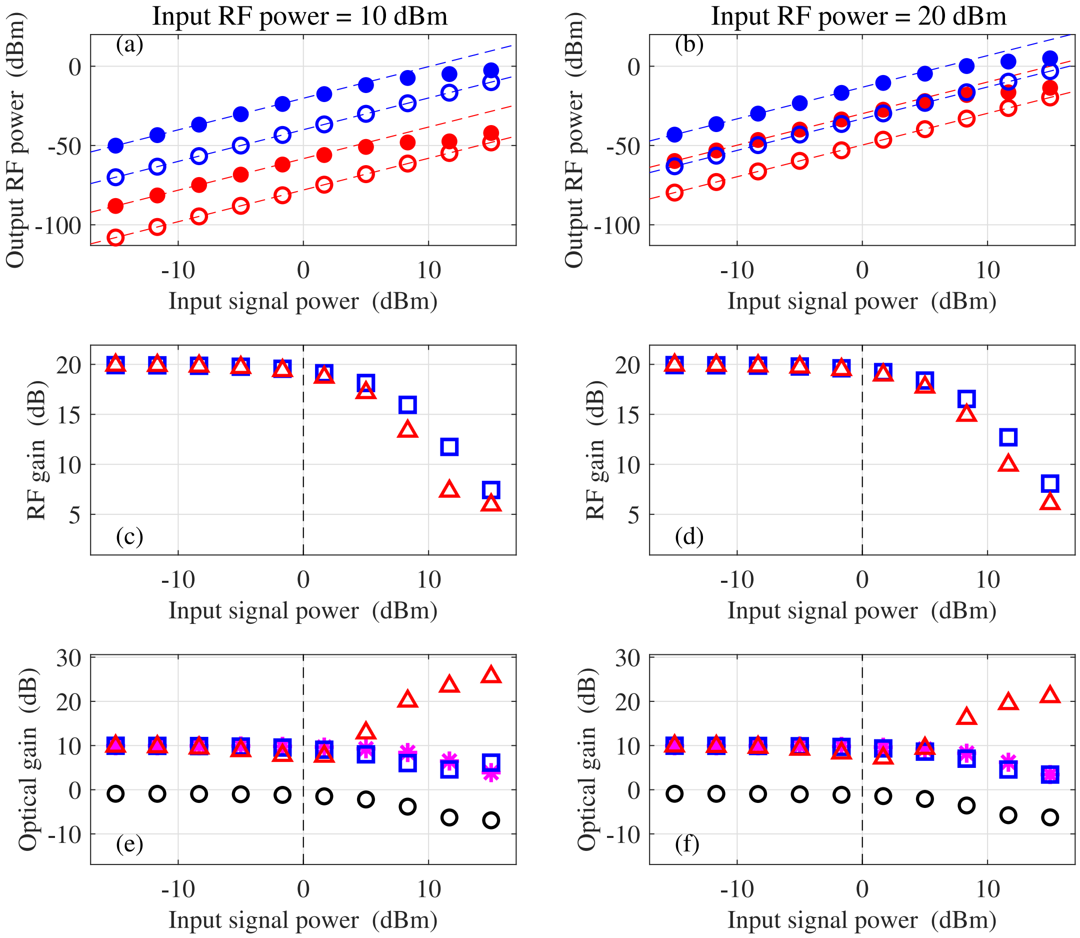

Figure 4.18. Same as Fig. 4.16 except the plots are shown as a function of the input signal and idler powers, for two values of the RF input power : 10 dBm (left column) and 20 dBm (right column).

frequencies. This can be explained by the fact that, for high enough input signal powers, the power of the optical fundamental wave entering the HNLF is also quite large. Moreover, these tones become even more powerful when they travel through the fiber. Consequently, the powers of the pump, signal, and optical fundamental become large enough to lead to a significant amplification of the optical IMD3 by four-wave mixing among these four waves, thus enhancing the optical IMD3 gain. However, as can be seen from Figs. 4.18 (c) and 4.18 (d), this gain enhancement for the optical IMD3 tones does not lead to an increase of the RF gain of the RF IMD3 tones, which actually strongly decreases for input signal powers larger than 0 dBm. This indicates that the increase of the power of the optical IMD3 wave is counterbalanced by the influence of other PSA-generated sidebands that beat at the IMD3 RF frequency and subtract from the contribution of the beating of the signal and the optical IMD3 in the output RF IMD3 power.

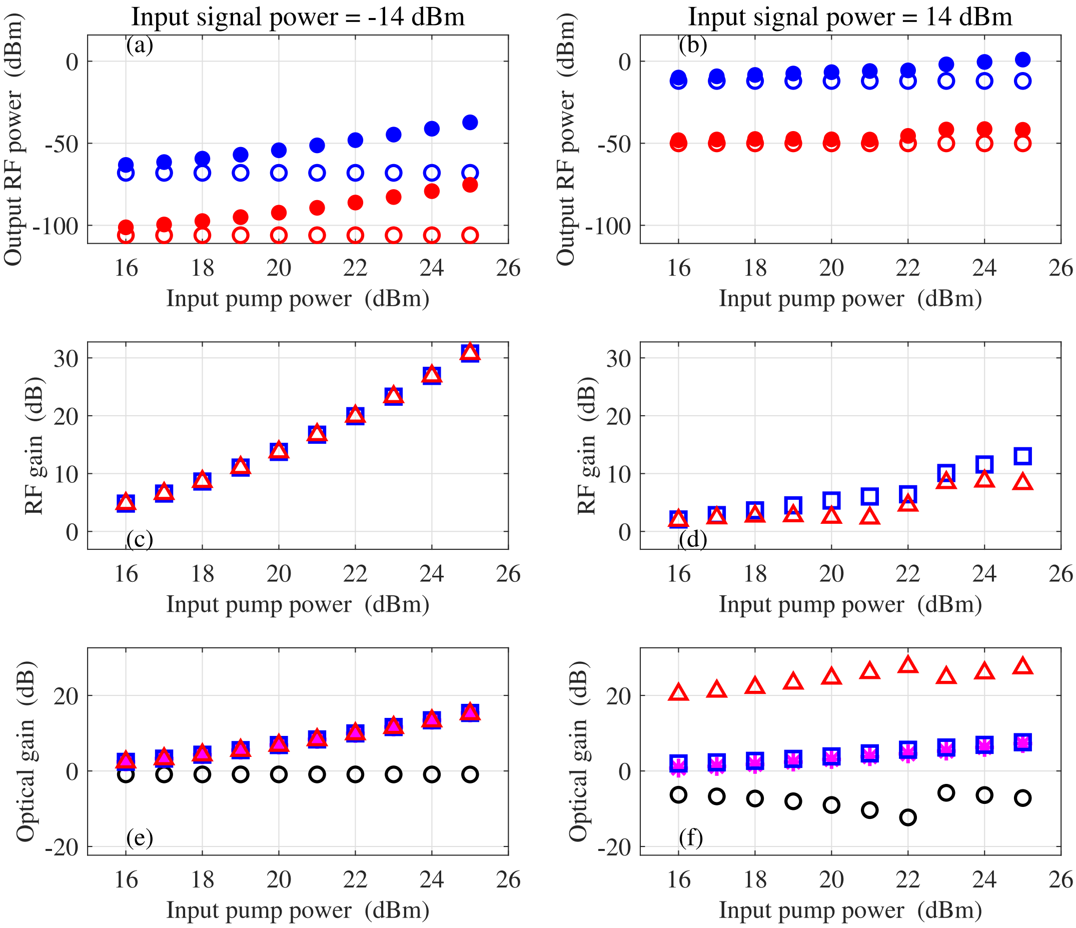

Figure 4.19. Same as Fig. 4.16 except the plots are shown as a function of the input pump power for two values of the input signal power : -14 dBm (left column) and 14 dBm (right column). Input RF power : 10 dBm.

4.5.3 Scan of Input Pump Power

Similar to Figs. 4.16 and 4.18, next we scan the input pump power of the PSA in Fig. 4.19 for two input signal powers : -14 dBm (left column) and 14 dBm (right column) with a 10 dBm input RF power. In the case of a low (-14 dBm) input signal power, the PSA gain is not saturated and hence an increase in the pump power leads to an increase in the PSA gain for the different optical waves (see Fig. 4.19 (e)) as predicted by the 3-wave model (see Equation (2.15) in Chapter 2). Consequently an increase in the PSA gain of all the optical waves leads to an increase in the RF gain of the fundamental and IMD3 RF waves as we see in Figs. 4.19 (a) and (c). On the contrary, the situation becomes more complex when the PSA gain is saturated. We see from Fig. 4.19 (f) that for a high input signal power, the pump undoubtedly gets depleted, the PSA gains of the signal and optical fundamental waves are slightly decreased compared to the unsaturated PSA case and the PSA gain for the optical IMD3 waves increase significantly. These observations can be explained as follows. The high input signal power at the input of the MZM implies a strong input optical fundamental at the input of the PSA. Furthermore, a large number of relatively stronger higher order sidebands enter the PSA. Therefore, now the pump acts as a PSA for not only the signal, optical fundamental and IMD3 waves, but also for the many MZM generated parasitic sidebands. So a large part of the pump energy is invested in amplifying the parasites. This is also confirmed from the fact that in Fig. 4.19 (d) we see a decrease in the IMD3 RF gain which is due to the generation of beatnotes from some of the parasitic modes at the IMD3 RF frequency that cancels out the beatnote arising from the beating of the signal and the optical IMD3 wave. The large PSA gain of the optical IMD3 waves can be explained as following. When the input signal power is large, the input fundamentals are also strong. In such a scenario, the two optical fundamentals at frequencies $\omega_s - \Omega_1$ and $\omega_s - \Omega_2$ respectively act as pumps for the two optical IMD3's at frequencies $\omega_s - (2\Omega_1 - \Omega_2)$ and $\omega_s - (2\Omega_2 - \Omega_1)$ respectively. This process is similar to that of a 4-wave model but with the speciality that the frequency separation between the optical fundamentals (pumps) is same as that between an optical fundamental and its closest optical IMD3. In Subsubsection 2.4.10 of Chapter 2 we had discussed the dynamics of such special four wave configurations and inferred that such processes are highly efficient due to the presence of an extra FWM term containing three pump terms. Therefore when we increase the input pump powers, the optical fundamentals get amplified more efficiently along the HNLF and can act as stronger pumps for the optical IMD3's leading to its increased PSA gain.

In fact the effect of the above mentioned efficient four wave mixing process between the two strong optical fundamental waves (acting as pumps) and the optical IMD3's (acting as signal and idler) can also be seen from Figs. 4.18 (e) and (f) when the input signal power is more than 0 dBm. We will revisit this phenomenon in Subsection 4.7.

4.5.4 Scan of Input Signal Phase

In all our previous analysis on the PSA dynamics under saturated gain condition, we noted an important feature : a high optical gain of the optical fundamental and IMD3 does not imply a high RF gain of the RF fundamental and IMD3. To explain this we argued that the RF fundamental and IMD3 waves are generated from the beatnotes between several optical frequencies. Thus often the different beatnotes do not add up constructively leading to a diminished RF gain. This leads us to the question : can we optimize our system such that we can have a large fundamental RF gain while a small IMD3 RF gain at the output of the link? The answer to this question lies in the choice of the input phase of the signal which we explain subsequently.

We know that the PSA gain depends on the input phase of the signal. In fact the input phase of the signal determines the phases of all the MZM generated sidebands at the input of the HNLF. Thus the effect of the PSA on all these waves depend on the input phase of the signal. So far we always considered the input phase of the signal that maximized the optical gain of the signal. However to achieve a link with low distortion, further optimization of the input signal phase could be interesting. Thus

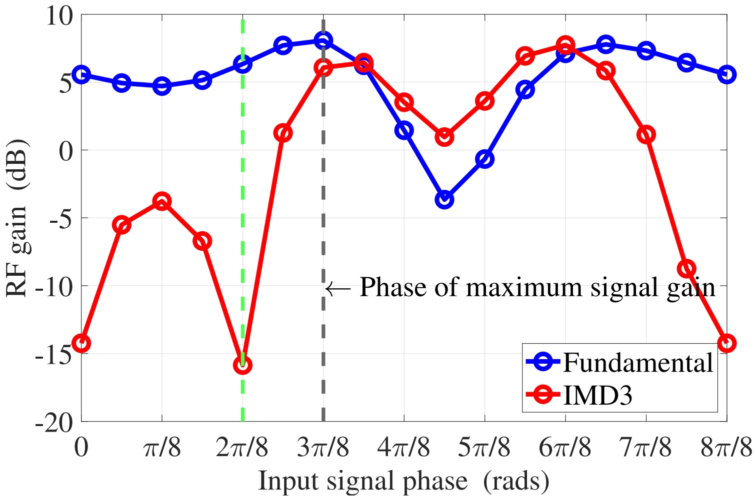

Figure 4.20. Plot of RF gain of fundamental RF (blue) and IMD3 RF (red) waves as a function of the input phase of the signal (and idler). Grey dashed line shows the signal phase that maximizes signal PSA gain. Green dashed line shows the phase corresponding to a low IMD3 RF gain. RF power at the MZM input : 20 dBm ; input signal power : 15 dBm ; input pump power : 22 dBm; HNLF length : 1000 m.

in Fig. 4.20 we scan the signal input phase for a saturated PSA (input signal power : 15 dBm) with 20 dBm of input RF power and 22 dBm input pump power. We see from Fig. 4.20 that a phase of $\frac{\pi}{4}$ rads lead to a very low (about -15 dB) IMD3 RF gain when the fundamental RF gain is about 6 dB (see green dashed line in Fig. 4.20). However, the PSA gain of the signal is maximized for a phase of about $\frac{3\pi}{8}$ rads (see grey dashed line in Fig. 4.20) where the IMD3 RF gain is about 6 dB which is much worse than the formar case. This provides interesting prospects for the design of a PSA-based microwave photonic link with ultra-low distortion.

4.5.5 SFDR

In Subsection 4.2.4 we discussed about the SFDR of a microwave photonic link without considering a PSA in the optical link. However when we include the PSA the SFDR is expected to change. To investigate this change of the SFDR on PSA inclusion, first we show in Fig. 4.21 an example of the SFDR's (brown double-sided arrows) when the PSA is off and on. A log-log scale is considered. The thick lines correspond to PSA on case and thin lines are for PSA off case. The color coding is same as in Fig. 4.10.

We see from Fig. 4.21 that when the PSA is on, the fundamental and IMD3 curves undergo a vertical shift of G_{dB} units from the PSA off case where G_{dB} is the RF gain in dB due to the presence of the PSA. For a shot-noise limited signal, the noise floor undergoes a vertical shift of $\frac{G_{dB}}{2}$ units (see Appendix H). Therefore the change in SFDR, i.e. $\Delta SFDR$ (between the PSA on and off cases) is given by (see Appendix H) :

$$\Delta SFDR = SFDR_{on} - SFDR_{off} = \frac{G_{dB}}{3} \tag{4.60}$$

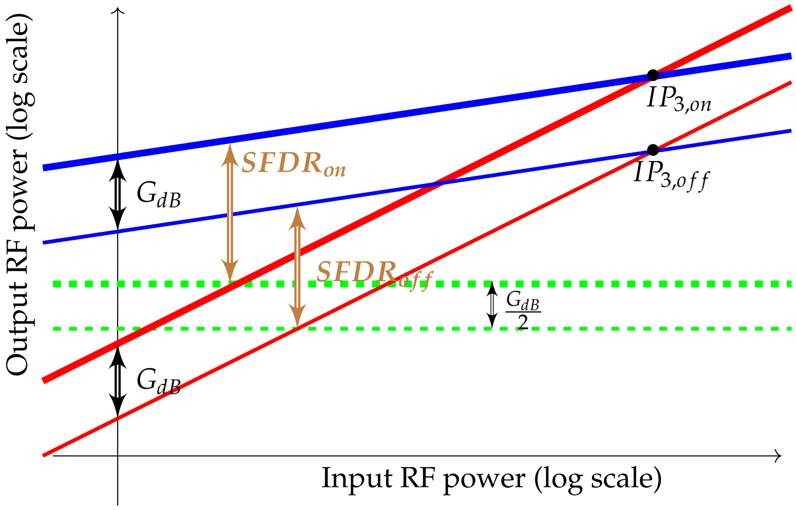

Figure 4.21. An illustration of output RF powers of fundamental (blue solid lines) and IMD3 (red solid lines) in a microwave photonic link with a PSA (with unsaturated gain) as a function of the input RF power considering a log-log scale. Two cases are considered : (a) PSA is off (thin lines) and (b) PSA is on (thick lines). The corresponding noise floors are shown in green dashed lines. The corresponding SFDR's and IP_3's for the PSA on and off cases are shown in brown double-sided arrows and black points respectively. G_{dB} : RF gain in dB due to the PSA. (not to scale)

We should note, that the above analysis only holds for a PSA that is unsaturated in gain.

In this subsection we use the results of Fig. 4.16 to predict the achievable SFDR of a link using a standard MZM and a PSA. All the parameters are the same as in Fig. 4.16. Figures 4.22 (a) and 4.22 (b) show the evolution the fundamental and IMD3 RF powers as a function of the input RF power in the conditions of Figs. 4.16 (a) and 4.16 (b), respectively, when the PSA is on and off. Moreover, these figures also show the noise floors, supposed to be limited by the shot noise corresponding to the photo-current generated by the detector. The vertical arrows in these plots permit to extract the SFDR of the link.

One can see from the plots in Fig. 4.22 that the link behaves differently, in terms of SFDR, depending on whether the PSA is saturated or not. Let us first focus on the case where the optical power incident on the PSA (-14 dBm) is weak enough to keep the gain unsaturated (Fig. 4.22 (a)). With the PSA off, taking into account the 0.9 dB losses of the fiber and the 3 dB losses supposed to exist between the fiber and the detector, the detected optical power is -17.9 dBm, leading to a shot noise level of -184.9 dBm/Hz. When the PSA is on, it amplifies all the tones by a 10 dB optical gain. The detected optical power is then -7.9 dBm, leading to a shot noise level equal to -174.9 dBm/Hz. Besides, the 10 dB optical gain results in a 20 dB RF gain for the fundamentals and the IMD3's. The SFDR of the link is then improved by about 7 dB by the PSA as expected from Equation (4.60). On the contrary, when the optical power incident on the PSA is equal to 14 dB, as in Fig. 4.22 (b), the saturated

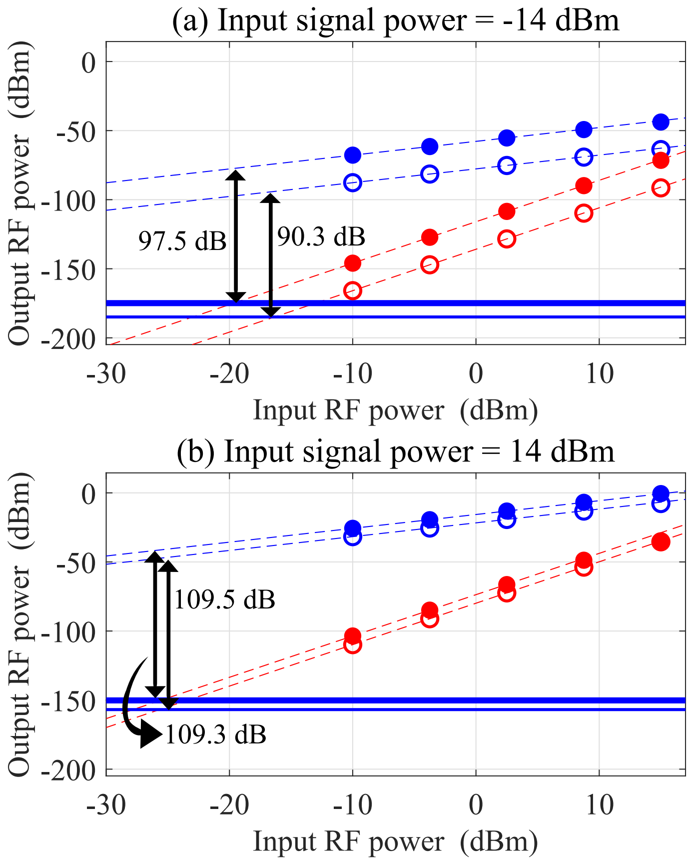

Figure 4.22. Characterization of the SFDR of the link. The parameters of the plots (a) and (b) are the same as in Figs. 4.16 (a) and (b), respectively. Noise floor: shot noise level for the PSA on (thick blue line) and off (thin blue line). The corresponding SFDR's are shown in black arrows.

optical gain of the signal is then only 6.7 dB, increasing the shot noise level from -156.9 dBm/Hz with the PSA off to -150.2 dB/Hz with the PSA on. As can be seen from Fig. 4.16 (d), the RF gain for the fundamental and the IMD3's are also of the order of 7 dB in this region. Consequently, as can be seen from Fig. 4.22 (b), the SFDR, which is equal to 109.3 dB with the PSA off, is neither improved nor degraded by the PSA.

4.5.6 Discussion

To summarize, we have seen in this section that, in the case of an AM RF signal applied to the signal and idler by a standard MZM, the PSA at its maximum gain is not at all detrimental to the linearity of the carried RF signal. On the one hand, in the absence of saturation, i.e. when the pump depletion is negligible, the RF IMD3's are just amplified by the PSA with the same gain as the RF fundamental tones. The contribution of the PSA to the RF nonlinearity of the link is thus completely negligible compared to the nonlinearity of the MZM. On the other hand, the saturation of the

PSA can lead to a lower gain for the RF IMD3's than for the RF fundamentals, thus leading to a mitigation of the RF nonlinearities of the MZM by the PSA.

4.6 Saturation Behaviour : Linear Intensity Modulator

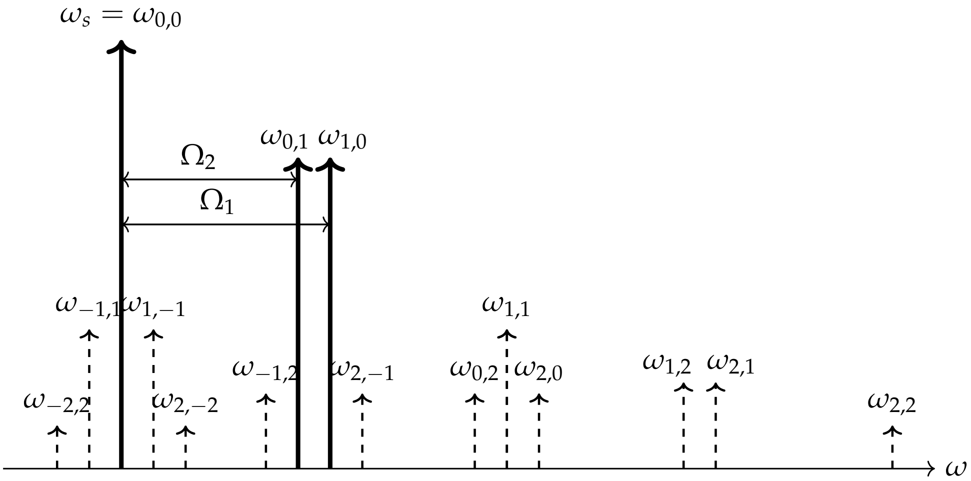

Figure 4.23. Solid arrows: optical spectrum at the output of a perfectly linear intensity modulator fed with two modulation frequencies Ω_1 and Ω_2. Dashed arrows: waves that would have been generated by a standard MZM (not to scale).

We have seen in the preceding sections that the nonlinearities created by a standard MZM largely exceed those which are induced by the nonlinearities of the PSA. Consequently, in order to determine the RF nonlinearities created by the PSA itself, we consider in the present section the case where the RF modulation is applied to the optical carriers using a perfectly linear intensity modulator. Such a modulator would generate no high order sidebands while modulating the signal. Hence, only the first order sidebands are supposed to be present, as shown in Fig. 4.23 in the case of modulation by the two frequencies Ω_1 and Ω_2. In such a case, the RF IMD3's detected at the output is solely due to the PSA.

Figure 4.24 shows the simulation results obtained in this case. In the case of a relatively low input signal and idler power (see Fig. 4.24 (a)), we can see that the RF IMD3's created by the PSA have an extremely small power level. For example, compared with the case of a standard MZM (see Fig. 4.16 (a)), the IMD3 power obtained in Fig. 4.24 (a) is reduced by about 58 dB when the input RF power is equal to 10 dBm.

However, when gain saturation enters the picture, the optical nonlinearity of the fiber becomes strong enough to create significant nonlinearities for the RF signal. This is particularly visible in Figs. 4.24 (b) and 4.24 (d), for relatively high input optical and RF powers. In such cases, one can see that the severe reduction by saturation of the gain of the fundamental RF tone is accompanied by an efficient generation of IMD3's. The powers of the created RF IMD3's can indeed become almost as large as those of the RF fundamentals.

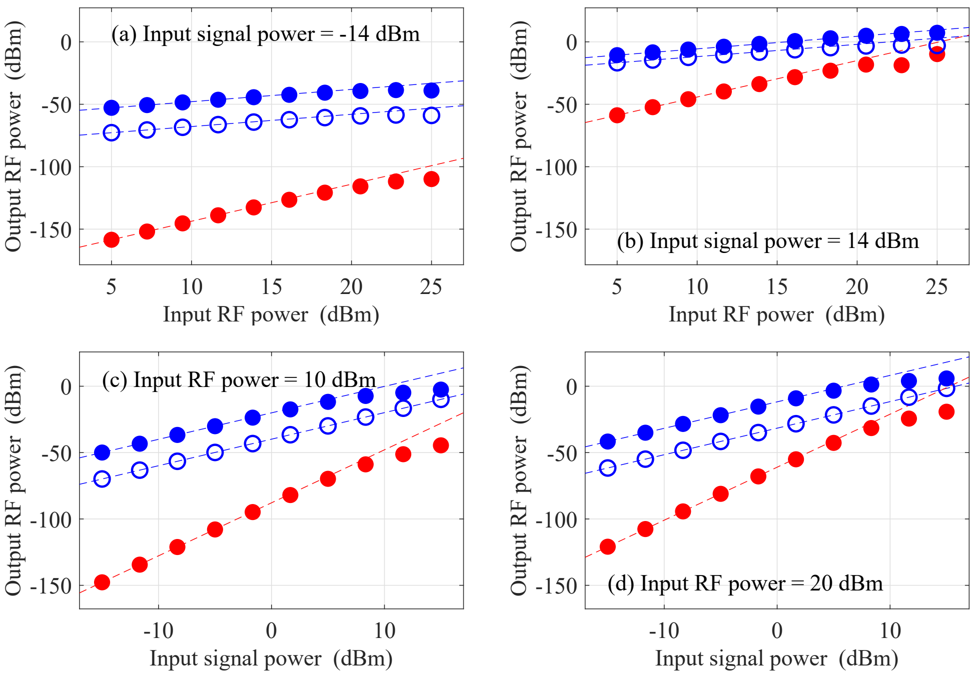

Figure 4.24. PSA nonlinearity with a linearized intensity modulator. (a,b) Output fundamental (blue circles) and IMD3 (red circles) RF powers when the PSA is off (open symbols) and on (filled symbols) versus input RF power. Input signal power: (a) -14 dBm), (b) 14 dBm. (c,d) Same as (a,b) versus input signal power. Input RF power: (c) 10 dBm), (d) 20 dBm. The dashed red and blue lines are guides to the eye.

It is clear from the plots of Fig. 4.24 that the most interesting situation from the point of view of applications is the one of Fig. 4.24 (a), where a linearized intensity modulator is used and the PSA gain is not saturated. Indeed, in these cases, the IMD3's at the output of the PSA are very small, much smaller than in the case where a standard modulator is used (see Fig. 4.16 (a)). We thus choose to investigate the SFDR of the link in the case of Fig. 4.24 (a). The result is reproduced in Fig. 4.25. With the PSA on, the -14 dBm signal power incident on the PSA is amplified by 10 dB. After the 0.9 dB losses of the fiber and 3 dB extra losses, -7.9 dBm optical power incident on the detector leads to a shot noise level of -174.9 dBm/Hz. The arrow in Fig. 4.25 then shows that the SFDR is then equal to 116.5 dB. By comparison with Fig. 4.22 (a), this corresponds to a 19 dB improvement. One interesting point here is that the SFDR achieved with the linearized modulator and the PSA with a relatively small input signal power (-14 dBm) is larger than the one obtained with a standard modulator with a much larger input signal power (14 dBm).

4.7 Physical Interpretation

From our previous discussions, we could relatively easily analyze the dynamics of wave propagation in a microwave photonics link with a PSA when the PSA was not saturated. On the contrary, when the PSA was saturated, the situation turned out

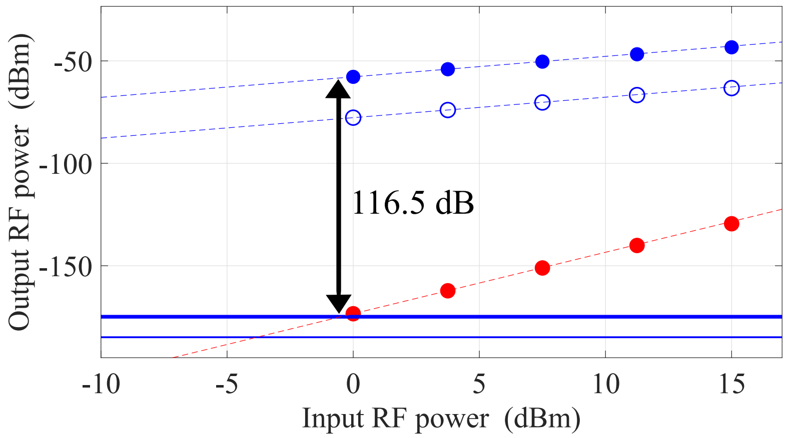

Figure 4.25. Same as Fig. 4.22 (a) with the parameters of Fig. 4.24 (a). The input signal power is -14 dBm.

to be more complex to deal with. This is because under saturated conditions the simple 3-wave model (with pump, modulated signal and modulated idler acting as the three waves) ceases to work. Thus in this section we propose a slightly different approach to capture the complex dynamics of the PSA carrying modulated signal and idler under gain saturated conditions.

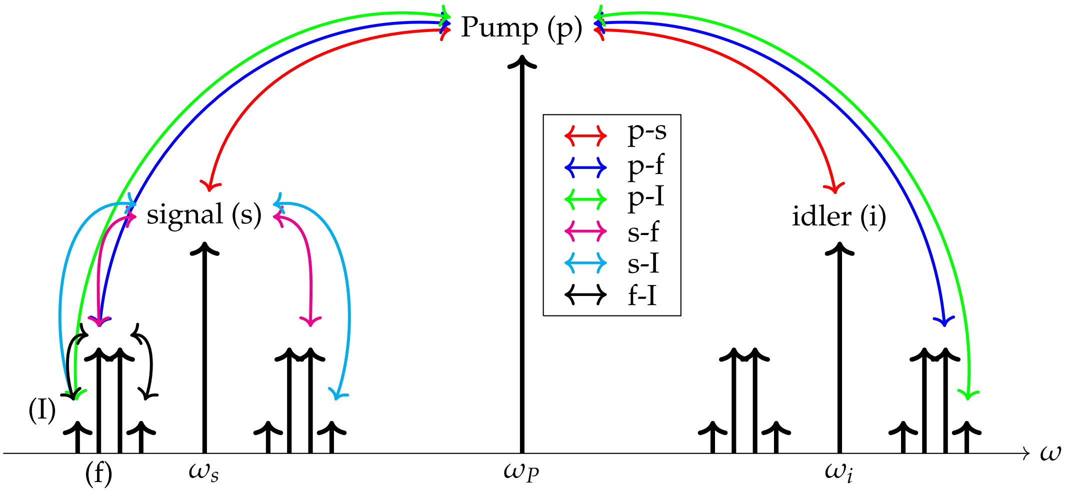

Figure 4.26. An illustration of some of the PSA processes occuring in a HNLF when fed with a pump and a modulated signal and idler with two modulation frequencies. Only the optical fundamental and IMD3's generated from the modulator are considered ignoring higher order sidebands. The different interactions corresponding to different PSA processes are shown in double-sided curved arrows. p-s : pump-signal interaction (red); p-f : pump-optical fundamental interaction (blue); p-I : pump-optical IMD3 interaction (green); s-f : signal-optical fundamental interaction (magenta); s-I : signal-optical IMD3 interaction (cyan); f-I : optical fundamental-optical IMD3 interaction (black). ω_s : signal frequency, ω_P : pump frequency, ω_i : idler frequency. (see Table 4.1 for more detaills on the PSA processes) (not to scale)

As explained previously, when the signal (or idler) power is much weaker than the pump, the pump amplifies all the waves (signal and idler with their sidebands) equivalently with the same PSA gain (see Fig. 4.18 (e)). However when the input signal power and/or the optical fundamental powers are large, they can act as secondary pumps amplifying the IMD3's. In fact the situation becomes equivalent to a 19-wave model (pump, signal, idler, eight optical fundamentals and eight optical IMD3's) (see Fig. 4.26) leading to a huge number of FWM terms making it quite complicated to deal with analytically. To overcome this hurdle, we break down the system into six different classes of PSA processes. These processes are labelled : p-s (pump-signal interaction); p-f (pump-optical fundamental interaction); p-I (pump-optical IMD3 interaction); s-f (signal-optical fundamental interaction); s-I (signal-optical IMD3 interaction); f-I (optical fundamental-optical IMD3 interaction), and the waves involved in these interactions are tabulated in Table 4.1 and illustrated in Fig. 4.26. We should note here that while the processes p-s, p-f, p-I, s-f and s-I are three wave interactions, the process f-I is a four wave interaction process. Moreover, f-I is a special kind of four wave interaction where the pump-pump wavelength separation is equal to the wavelength separation between the signal and its closest pump. In Subsubsection 2.4.10 of Chapter 2 we have already discussed about the dynamics of such processes in detail.

Table of PSA Processes				
PSA process	Role of signal	Role of pump	Role of idler	Colour coding
p-s	ω_s	ω_P	ω_i	red
p-f	$\omega_s - \Omega_1$	ω_P	$\omega_i + \Omega_1$	blue
p-I	$\omega_s - (2\Omega_1 - \Omega_2)$	ω_P	$\omega_i + (2\Omega_1 - \Omega_2)$	green
s-f	$\omega_s - \Omega_1$	ω_s	$\omega_s + \Omega_1$	magenta
s-I	$\omega_s - (2\Omega_1 - \Omega_2)$	ω_s	$\omega_i + (2\Omega_1 - \Omega_2)$	cyan
f-I	$\omega_s - (2\Omega_1 - \Omega_2)$	$\omega_s - \Omega_1$ and $\omega_s - \Omega_2$	$\omega_s - (\Omega_1 - 2\Omega_2)$	black

Table 4.1. Table of different PSA processes occuring in a HNLF when fed with a pump (ω_P) with a signal (ω_s) and idler (ω_i) modulated with two RF frequencies Ω_1 and Ω_2. Also see Fig. 4.26 for a visualization of the PSA processes.

Let us first focus on the three wave processes. From the 3-wave model with a degenerate pump configuration, the evolutions of the slowly varying envelope of the complex amplitudes of the signal (A_{-1}) and idler (A_1) waves are given by (see Appendix A) :

$$\frac{dA_1}{dz} = i\gamma\Big(|A_1|^2 A_1 + 2(|A_{-1}|^2 + |A_0|^2)A_1 + A_0^2 {A_{-1}}^* e^{i\Delta\beta_{001-1}z}\Big), \tag{4.61}$$

$$\frac{dA_{-1}}{dz} = i\gamma\Big(|A_{-1}|^2 A_{-1} + 2(|A_1|^2 + |A_0|^2)A_{-1} + A_0^2 {A_1}^* e^{i\Delta\beta_{001-1}z}\Big), \tag{4.62}$$

where γ is the nonlinear coefficient of the HNLF, A_0 is the amplitude of the pump and $\Delta\beta_{001-1}$ is the linear phase mismatch term as defined in Subsection 2.3.3 of Chapter 2. Now multiplying Equation (4.61) by ${A_1}^*$ and adding it with the conjugate of Equation (4.61) multiplied by A_1, we get :

$$\frac{dP_1}{dz} = 2\gamma(P_1 P_{-1} {P_0}^2)^{\frac{1}{2}} \sin(\Delta\beta_{1-100} z + \theta_1 + \theta_{-1} - 2\theta_0), \tag{4.63}$$

where $P_1 = |A_1|^2$ and θ_n is given by :

$$A_n = |A_n| e^{i\theta_n}, \tag{4.64}$$

for $n = 1, -1, 0$. In other words, θ_n represents the phase of the complex amplitude A_n. Similarly the evolution of $P_{-1} = |A_{-1}|^2$ is given by :

$$\frac{dP_{-1}}{dz} = 2\gamma(P_1 P_{-1} {P_0}^2)^{\frac{1}{2}} \sin(\Delta\beta_{1-100} z + \theta_1 + \theta_{-1} - 2\theta_0) = \frac{dP_1}{dz}. \tag{4.65}$$

Therefore we see from the above equation that the rate of change of power of the signal (or idler) at a particular length in the fiber depends on two factors : (a) $2\gamma(P_1(z) P_{-1}(z) P_0(z)^2)^{\frac{1}{2}}$, which we call the strength of growth rate and (b) $\sin(\Delta\beta_{1-100} z + \theta_1(z) + \theta_{-1}(z) - 2\theta_0(z))$, which we call the sine of growth rate phase. We should note here that the interaction strength is always a positive quantity whereas the sine of growth rate phase can have positive and negative values however bounded by -1 and 1. Depending on its sign, the local power of the signal (or idler) will either increase or decrease.

Next we turn our focus to the 4-wave model representing the optical fundamentals (as pumps) and the optical IMD3's (as signal and idler). We should keep in mind that the frequency separation between the optical fundamentals is the same as that between a fundamental and its nearest IMD3. We denote A_{-1}, A_1, A_{-2} and A_2 as the amplitudes of pump1, pump2, signal and idler respectively. Thus the equation of evolution of A_{-2} and A_2 are given by (see Equations (2.62) and (2.63)) :

$$\frac{dA_{-2}}{dz} = i\gamma\Big(2|A_{-1}|^2 A_{-2} + 2|A_1|^2 A_{-2} + {A_{-1}}^2 {A_1}^* e^{i\Delta\beta_{-1-11-2} z} + 2A_{-1} A_1 {A_2}^* e^{i\Delta\beta_{-112-2} z}\Big), \tag{4.66}$$

$$\frac{dA_2}{dz} = i\gamma\Big(2|A_{-1}|^2 A_2 + 2|A_1|^2 A_2 + {A_1}^2 {A_{-1}}^* e^{i\Delta\beta_{11-12} z} + 2A_{-1} A_1 {A_{-2}}^* e^{i\Delta\beta_{-11-22} z}\Big). \tag{4.67}$$

We note here that the terms $i\gamma {A_{-1}}^2 {A_1}^* e^{i\Delta\beta_{-1-11-2} z}$ in Equation (4.66) and $i\gamma {A_1}^2 {A_{-1}}^*$ $e^{i\Delta\beta_{11-12} z}$ in Equation (4.67) arise only when the frequency separation between the pumps are equal to the frequency separation of the pump and its closest sideband. Now proceeding as before, we multiply Equation (4.66) by ${A_{-2}}^*$ and add it to the conjugate of Equation (4.66) multiplied by A_{-2}. Thus we get :

$$\begin{aligned} \frac{dP_{-2}}{dz} &= 2\gamma({P_{-1}}^2 P_1 P_{-2})^{\frac{1}{2}} \sin(\Delta\beta_{1-2-1-1} z + \theta_1 + \theta_{-2} - 2\theta_{-1}) \\ &\quad + 4\gamma(P_{-1} P_1 P_{-2} P_2)^{\frac{1}{2}} \sin(\Delta\beta_{2-21-1} z + \theta_2 + \theta_{-2} - \theta_1 - \theta_{-1}). \end{aligned} \tag{4.68}$$

For most practical purposes we can assume that the pumps are much stronger than the signal and idler and ignore the second term in Equation (4.68). Thus we get :

$$\frac{dP_{-2}}{dz} = 2\gamma(P_{-1}{}^{2}P_1P_{-2})^{\frac{1}{2}}\sin(\Delta\beta_{1-2-1-1}z + \theta_1 + \theta_{-2} - 2\theta_{-1}). \tag{4.69}$$

In fact Equation (4.69) is the same as we would have got by considering a 3-wave model replacing the idler with a second pump. In this case the strength of the growth rate is given by $2\gamma(P_{-1}(z)^2P_1(z)P_{-2}(z))^{\frac{1}{2}}$ and the sine of phase of growth rate is given by $\sin(\Delta\beta_{1-2-1-1}z + \theta_1(z) + \theta_{-2}(z) - 2\theta_{-1}(z))$.

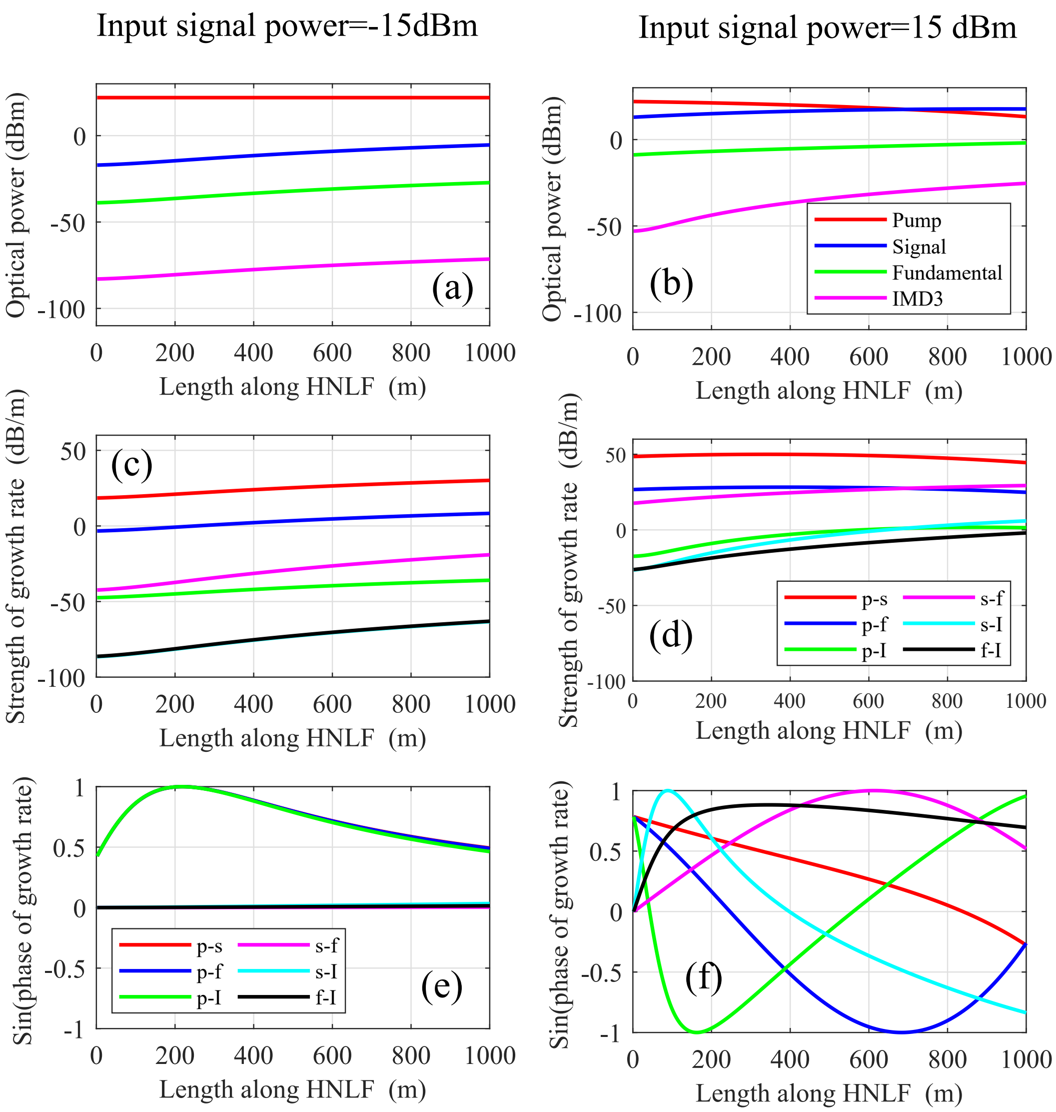

Figure 4.27. (a,b) Evolution of optical power of waves (Pump (red), signal (blue), optical fundamental (green) and optical IMD3 (magenta)) along the HNLF. (c,d) Evolution of strength of growth rate and (e,f) evolution of sine of phase of growth rate for different PSA processes (see Table 4.1 and Fig. 4.27 for details on the PSA processes) along the HNLF. Two input signal powers were used : -15 dBm (a,c,e) and 15 dBm (b,d,f). Input modulation power : 10 dBm. A standard HNLF was used as in Section 4.5 neglecting fiber attenuation.

Coming back to our model of the six different PSA processes (listed in Table 4.1), utilizing Equations (4.65) and (4.69) we can now monitor the strength and direction of energy transfer (pump to signal or signal to pump) for each of the processes along the length of the HNLF. To this aim, in Figs. 4.27 (c,d) we plot the strength of growth rates and in Figs. 4.27 (e,f) we plot the sine of growth rate phases for the different PSA processes (as listed in Table 4.1) as a function of the length along the HNLF considering two different input signal powers : -15 dBm (left column) and 15 dBm (right column). Also in Figs. 4.27 (a,b) we plot the power evolution of the pump (red), signal (blue), optical fundamental (green) and optical IMD3 (magenta) waves along the length of the HNLF. For the simulation, a standard HNLF was considered as in Section 4.5 neglecting fiber attenuation loss. An input modulation power of 10 dBm was used.

We first focus on the unsaturated PSA case (left column of Fig. 4.27). From Fig. 4.27 (c) we see that the dominant processes for the growth of the signal (red curve), optical fundamental (blue curve) and optical IMD3 (green curve) always involves the pump, *viz.* p-s, p-f and p-I respectively. Also from Fig. 4.27 (e) we find that the sine of the growth rate for processes s-f (magenta curve), s-I (cyan curve) and f-I (black curve) are almost 0 throughout the fiber length. This means processes s-f, s-I and f-I are inefficient. However the pump-involving processes (p-s, p-f and p-I) are non-zero and positive. This suggests that when the PSA is unsaturated, the gains of the different waves depend only on the pump.

Next we analyze the saturated PSA case (right column of Fig. 4.27). From Fig. 4.27 (b) we see that the IMD3 optical gain is greater than its counterpart (Fig. 4.27 (a)) from the unsaturated case[12]. From Fig. 4.27 (d) we see that the signal is chiefly amplified by the pump as the p-s process provides a much larger growth rate compared to all the other processes involving the signal (s-f and s-I). However for the fundamental, both the processes s-f and p-f contribute comparably towards the growth of the fundamental. From Fig. 4.27 (f) we see that s-f and p-f incur opposite signs for a large section inside the HNLF resulting in cancellation of each others effects. This explains the lower PSA gain of the optical fundamentals than optical IMD3's in Fig. 4.19 (f). Now coming to the optical IMD3's, we find from Fig. 4.27 (d) that all the three processes : p-I, s-I and f-I, have comparable strengths of growth rate for the IMD3. However Fig. 4.27 (f) shows that p-I and s-I often are of the opposite signs inside the HNLF counter-balancing each other. But the sine of growth rate for the f-I process attains a non-zero and positive value throughout the HNLF therefore leading to a large optical gain for the optical IMD3 wave.

To summarize, we find that for the unsaturated PSA, only the pump plays a role in amplifying the different waves. However when the PSA is saturated, the interplay of the different PSA processes between the waves lead to a diminished optical gain for the signal and the optical fundamental, whereas the optical IMD3 achieves a large gain. The dominant process leading to this large gain of the optical IMD3's originates from the strong pumping of the optical fundamentals.

---

[12] We already noted this feature in Figs. 4.19 (e) and (f).

4.8 Conclusion

In this chapter, we have discussed how the insertion of a PSA inside a microwave photonics link based on amplitude modulation alters the RF nonlinearities of the link. To this aim we used a numerical model to evaluate the powers of the fundamental and IMD3 RF waves at the output of the link. We validated the model by comparison with experimental results. We also developed a simplified theoretical model for analyzing complicated PSA-dynamics by breaking down the wave evolution process in terms of individual PSA processes.

In the context of nonlinearity analysis different situations were considered, based either on a standard MZM or a linearized modulator to transfer the RF signal to the optical carriers. We have also compared the cases of weak and strong optical powers, low and high RF powers applied to the modulator and weak and strong powers of the pump. The phase of the input carrier was also scanned to explore the possibility of optimization of the link SFDR. However, in this analysis we have not considered the random fluctuations of the ZDW of the fiber that can often degrade the noise and amplification performance of the link [59, 246].

One important conclusion of this chapter is that, in spite of its intrinsic optical nonlinearity, a PSA used at its maximum gain can behave in a surprisingly linear manner from the point of view of the carried RF signal. This linear behavior is observed when the input signal and idler powers are weak enough for the pump depletion to be negligible. Then, we have seen that, in the case of a standard MZM, the RF nonlinearity of the PSA is completely negligible compared to the one of the modulator. Even if one removes these latter nonlinearities by using a perfectly linear amplitude modulator, the nonlinearities induced by the PSA remain extremely small as long as the gain is not saturated.

In terms of SFDR, the conclusions of this work are the following. On the one hand, when one uses a standard MZM, the use of a PSA improves the SFDR when the gain is not saturated, while it neither improves nor degrades it when the gain is saturated. On the other hand, in case one uses a perfectly linear modulator, the RF nonlinearities created by the PSA itself are so small that the SFDR of the link can be significantly larger than in the case of a standard MZM. This can be useful to avoid the use of high signal powers or in the case the detector itself cannot handle such high powers before becoming nonlinear.

The picture becomes drastically different when the input signal power is strong enough to induce gain saturation via pump depletion. But, in this case, the PSA behavior is different in the case of a standard MZM and in the case of a linearized modulator. In the first case, we have shown that the strong signal nonlinearities created by the intrinsically nonlinear MZM can actually be strongly reduced by the PSA. The amplifier can thus be used to mitigate the link nonlinearities and improve its dynamic range. On the contrary, when one uses a linearized amplitude modulator, the saturated PSA can create signal nonlinearities that can become extremely detrimental to the linearity of the link. Indeed, we have seen that in some situations, extreme gain saturation can generate RF IMD3's with powers as large as those of the RF fundamentals.

Here we have considered only a direct detection scheme to detect the optical signal after amplification. However, a coherent detection scheme can be used to further improve the noise performance of the link [233]. Also, recent developments suggest the use of few mode fibers (FMF) in a microwave photonic link to increase the link's optical power handling capabilities [247]. One may wonder how incorporation of a PSA in a FMF based microwave photonic link could be achieved for further performance improvement. In particular, the problem of the control of the relative phases between the pump(s) and the different modes seems particularly tricky. Moreover, this work also opens new perspectives for the investigation of link nonlinearities using fibers exhibiting dispersion fluctuations [248–250] and dispersion oscillations [251].

Chapter Highlights

- **PSA in a Microwave Photonic Link :** Microwave photonic links are often used for analog signal distribution. However, does the introduction of a PSA in the optical link of a microwave photonic link generate extra distortions? To address this question, we performed numerical simulations to understand how a pump, a modulated signal and a modulated idler wave propagate through a nonlinear fiber. We investigated how the nonlinearities generated from the Mach-Zehnder modulator (MZM) used in the E/O conversion, are further amplified by the PSA.
- **Amplitude Modulation (AM) vs Phase Modulation (PM) :** The E/O conversion in a microwave photonic link can be done using an amplitude modulation (AM) or a phase modulation (PM) format. However, for a microwave photonic link with a PSA, the optical amplification only works for an AM format.
- **Unsaturated Gain PSA Operation :** When the PSA gain is not saturated, we show numerically, that the PSA does not add extra distortions into the link. The linearity of the link was evaluated by the so-called two-tone test. A linearized MZM was considered to investigate the distortions generated solely by the PSA and was found to be orders of magnitude smaller than those of the MZM.
- **Saturated Gain PSA Operation :** When the PSA gain attains saturation, interplay between the MZM-generated nonlinearities and the PSA-nonlinearities shows interesting properties. For example, although the optical IMD3 tones are often highly enhanced by the PSA in the link, the optimization of the phase of the optical carrier can lead to a suppressed RF IMD3 distortion at the link output, however at the cost of reduced RF gain.

Chapter 5

Perspectives and Conclusion

Contents

- **5.1 Perspectives** **152**
  - 5.1.1 Frequency Comb PSA 152
  - 5.1.2 Quantum Noise using a 7-Wave Model 153
- **5.2 Conclusion** **154**

5.1 Perspectives

Several perspectives were generated in the course of this research. In this subsection we note down a few of them.

5.1.1 Frequency Comb PSA

In the analytical 7-wave model developed in Chapter 2, we considered propagation of only seven waves through a nonlinear fiber. However, one can also ask the question : Is it possible to extend this approach to an arbitrary number of waves or in other words, to a PSA with a frequency comb? The answer to this question is tricky. From a practical point of view, when there are many ($n > 7$) waves propagating through the fiber, we expect the pumps to undergo a significant depletion after propagating a very short distance inside the fiber. Therefore finding an analytical solution for such a system would be quite challenging. A considerable effort has been made in Ref. [252]. Nevertheless, we can still deconstruct the system into two sets of subsystems : 1. odd order subsystem (see blue waves in Fig. 5.1) and 2. even order subsystem (see red waves in Fig. 5.1).

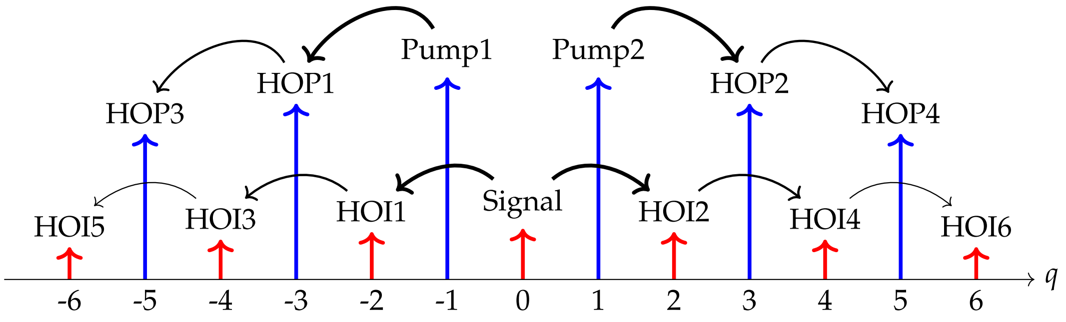

Figure 5.1. Illustration of a PSA configuration with generation of several higher order waves. Waves in blue (red) form the odd (even) order subsystem. The cascaded transfer of photons are shown in black curved arrows. HOI : higher order idler, HOP : higher order pump.

In the odd order subsystem, all the waves are located at odd values of q (like the pumps). The dynamics of this subsystem would be similar to that of the analytical 4-wave model with $q = 3$ (see Subsection 2.4.10 in Chapter 2). This means, the waves in this subsystem would be very efficiently generated due to the efficient pumping from the two pumps. However, their generation is supposed to be a cascaded process, meaning first HOP1 and HOP2 will be generated, then HOP3 and HOP4, and so on (see black arrows in Fig. 5.1). This efficient generation would make them act as secondary pumps for the weak even order subsystem waves.

The even order subsystem is similar to the odd order subsystem, but here the waves are located at even values of q (like the signal). The dynamics of this subsystem would be similar to that of coupled subsystems 1 and 2 described in the analytical 7-wave model (see Subsection 2.4.6 in Chapter 2). However, now instead of just two pumps, we would need to consider $2n$ pumps, where the $2(n-1)$ generated HOP's act as secondary pumps. We also expect to see a cascaded generation of HOI's with a cascaded generation of the HOP's similar to the PSFC phenomenon discussed in Chapter 2. Therefore, the first step in this approach would be to analyze how the waves in the even order subsystem are coupled with each other in the presence of a strong pump comb.

Analyzing the dynamics of such a system could provide further insights into the well-known modulation instability phenomenon in nonlinear optics. It might also lead to observation of a cascaded phase sensitive frequency conversion effect.

5.1.2 Quantum Noise using a 7-Wave Model

In Chapter 2 we have seen, that for the 3-wave model, the signal gain for a FOPA in a PIA configuration is independent of the relative phase between the pump(s), signal and/or idler. However for a PSA configuration, it depends on the relative phase (see Section 2.2 in Chapter 2). It turns out that this phase sensitivity has implications on the quantum noise properties of a FOPA [56]. Caves in 1982 showed that the quantum noise figure, which is the ratio of signal-to-noise ratio between the input and output of the FOPA, for a FOPA in PIA configuration is limited by 3 dB, whereas for PSA it can be as small as 0 dB [47]. This means a FOPA in a PSA configuration can act as a noiseless amplifier without degrading the signal-to-noise ratio after amplification [51].

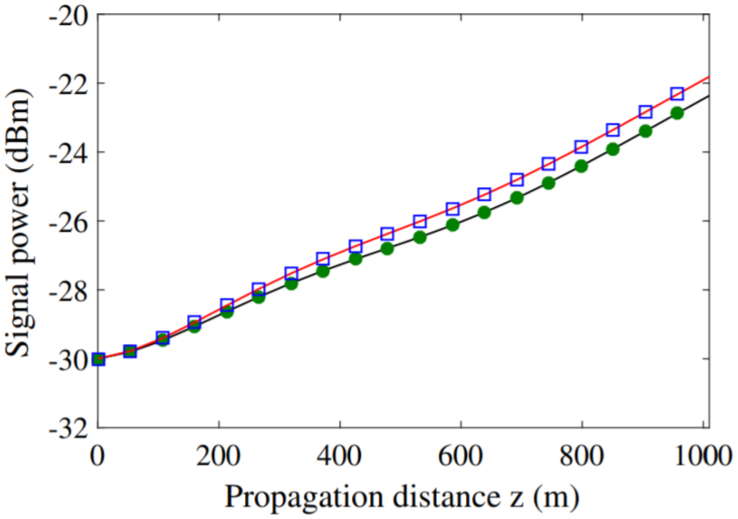

Figure 5.2. Signal power evolution versus fiber length z calculated using a numerical 7-wave model. Full black line : only signal is injected. Filled circles : signal, HOP1 and HOP2 injected. Full red line : signal, HOI1 and HOI2 injected. Open squares : signal, HOI1, HOI2, HOP1 and HOP2 injected. $P = 0.1$ W, $P_0 = 1\ \mu$W, $P_{\pm 2} = P_{\pm 3} = 1$ nW (when injected), fiber attenuation coefficient $\alpha = 0.9$ dB/km, $\gamma = 11.3$ W^{-1}km^{-1}, $D' = 0.017$ ps km^{-2} nm^{-2}, $L = 1011$ m, $\delta\lambda_{ofs} = 0$ nm, $\Delta\lambda_{PP} = 0.32$ nm. Reproduced from Ref. [166].

Although initial investigations in this area was based on 3- or 4-wave models, future developments considered the cases with larger number of waves [76, 157]. McKinstrie *et al.* [76] and Marhic *et al.* [163] analyzed the 6-wave model analytically, however ignoring dispersive effects of the fiber. More recently Inoue developed a semi-analytical model to solve for the two pumps and higher order pumps (HOP's) numerically while incorporating their effects on the signal and higher order idlers (HOI's) analytically [157]. However, Inoue's approach does not incorporate all the important FWM processes that influence the signal propagation through a FOPA. In our group, Bouasria *et al.* computed the noise figure considering a 7-wave model but using a semi-quantum approach which predicts the role of the HOI's in impacting the signal evolution (see Fig. 5.2) and in turn the noise figure of the amplifier [166]. However unavailability of a full analytical solution of the n-wave model turns out to a difficult challenge to develop a fully quantum model for the noise figure calculation.

In our development of the analytical 7-wave model, we incorporated the effect of fiber dispersion and solved the classical system exactly in the presence of the HOI's. Although our model is valid when the system is weakly nonlinear ($\gamma PL < 0.5$), still the results can be used to calculate the quantum noise figure following the approach described in Ref. [76]. In fact this work is in progress currently.

5.2 Conclusion

Finally, here we provide a general conclusion of the research presented in this thesis. This thesis provides a broad overview of the mechanisms of CW wave propagation through a nonlinear fiber. An analytical model with seven CW waves propagating through a fiber was developed. The system was analyzed by breaking it down into smaller subsystems and studying their interactions. Key insights were obtained with respect to the role of higher order idlers in the parametric amplification process in such systems. Using the analytical model, we predicted the possibility of signal gain enhancement by injecting the higher order idlers at the input of the fiber in a phase sensitive amplification scheme. We also predicted the phase sensitive frequency conversion capability of a five wave system using the developed analytical model.

In the second part of the thesis, the possibility of using a fiber phase sensitive amplifier in a microwave photonic link for analog signal distribution was investigated. A SSFM based numerical model was used to solve the nonlinear Schrödinger equation describing propagation of multiple CW waves through a nonlinear fiber. The numerical model was validated with available experimental data. The system was studied with respect to amplitude and phase modulation formats and the the effective operation of a fiber phase sensitive amplifier was shown to be possible only under amplitude modulation operation. The numerical model was further utilized to investigate the link linearity using the two-tone test, under gain saturation of the

FOPA. The numerical simulation results indicated, that under gain saturation, mitigation of the RF nonlinearities by the fiber nonlinearities is possible.

These findings project interesting perspectives with respect to development of fiber phase sensitive amplifiers with superior capabilities. It also generates the possibility of realizing highly linearized long-range microwave photonic links for antenna remoting applications.

In a world with a rapidly growing connectivity, the demand for higher performance communication systems is omnipresent. We believe, our research would contribute positively in the global effort to meet such demands.

Appendix A

Solution of the Analytical 3-wave Model

Following the approximations listed in Subsection 2.2.2 (except for the non-pump depletion approximation), the equations governing the evolution of the slowly varying amplitudes A_i's ($i = 1, 0, -1$) of the three waves are given by (also given in Equations (2.5), (2.6) and (2.7)) :

$$\frac{dA_1}{dz} = i\gamma\left(|A_1|^2 A_1 + 2(|A_{-1}|^2 + |A_0|^2)A_1 + A_0^2 {A_{-1}}^* e^{i\Delta\beta_{00-11} z}\right), \tag{A.1}$$

$$\frac{dA_{-1}}{dz} = i\gamma\left(|A_{-1}|^2 A_{-1} + 2(|A_1|^2 + |A_0|^2)A_{-1} + A_0^2 {A_1}^* e^{i\Delta\beta_{001-1} z}\right), \tag{A.2}$$

$$\frac{dA_0}{dz} = i\gamma\left(|A_0|^2 A_0 + 2(|A_1|^2 + |A_{-1}|^2)A_0 + 2A_1 A_{-1} {A_0}^* e^{i\Delta\beta_{1-100} z}\right), \tag{A.3}$$

where the symbols have their usual meanings. We note here that, depending on the configuration of the FOPA (either degenerate pump or non-degenerate pump), the indices of A will have different meanings. More precisely, for a non-degenerate pump configuration, $A_{\pm 1}$ represent the amplitudes of the pumps and A_0 represents the amplitude of the degenerate signal and idler (See Fig. A.1 (b)). However for a degenerate pump configuration, A_1 and A_{-1} represent the amplitudes of the signal and idler, respectively, and A_0 represents the amplitude of the degenerate pump (See Fig. A.1 (a)).

A.1 Degenerate Pump Configuration

For the degenerate pump configuration, the index 0 is for the pump, -1 for the signal and 1 is for the idler. Invoking the approximation that the pump is much stronger

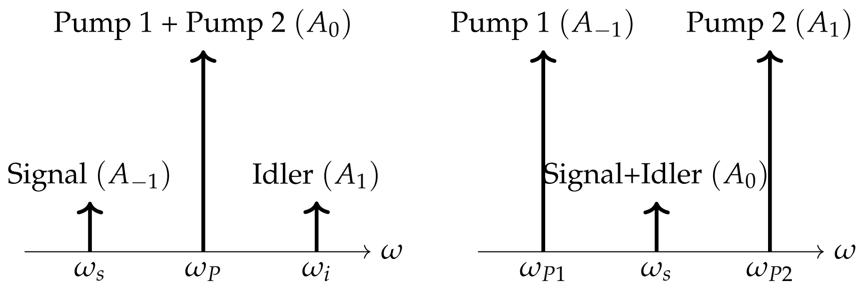

(a) (b)

Figure A.1. Configurations of a FOPA in a 3-wave model : (a) Degenerate pumps and non-degenerate signal and idler. (b) Degenerate signal and idler and non-degenerate pumps. We introduce a simplified notation A_0 and $A_{\pm1}$ for the different waves for convenience. ω is frequency and the height of the arrows represent intensity (not to scale).

than the signal and the idler, the equation for the pump is given as :

$$\frac{dA_0}{dz} = i\gamma|A_0|^2 A_0 = i\gamma P A_0, \tag{A.4}$$

where P is the undepleted pump power. Considering a zero phase of the pump at the input of the fiber, the solution for A_0 is given by :

$$A_0(z) = \sqrt{P} e^{i\gamma P z}. \tag{A.5}$$

Injecting A_0 into Equations (A.1) and (A.2) and also considering the pump power to be much stronger than the signal and idler, we write the equations for the signal and the idler as :

$$\frac{dA_1}{dz} = i\gamma P\left(2A_1 + A_{-1}{}^* e^{i(\Delta\beta_{00-11}+2\gamma P)z}\right), \tag{A.6}$$

$$\frac{dA_{-1}}{dz} = i\gamma P\left(2A_{-1} + A_1{}^* e^{i(\Delta\beta_{001-1}+2\gamma P)z}\right). \tag{A.7}$$

We know from Equation (2.23) that $\Delta\beta_{klmn}$ is given by :

$$\Delta\beta_{klmn} = \beta(\omega_k) + \beta(\omega_l) - \beta(\omega_m) - \beta(\omega_n). \tag{A.8}$$

Thus $\Delta\beta_{klmn} = \Delta\beta_{klnm}$ or $\Delta\beta_{00-11} = \Delta\beta_{001-1}$. From Equations (A.6) and (A.7) we see that the coefficient of the first term is $2i\gamma P$. Thus we make the following transformation of variables to eliminate the first terms as :

$$\begin{aligned} B_1 &= A_1 e^{-2i\gamma P z}, \\ B_{-1} &= A_{-1} e^{-2i\gamma P z}. \end{aligned} \tag{A.9}$$

Thus Equations (A.6) and (A.7) can be rewritten in terms of the transformed variables as :

$$\frac{dB_1}{dz} = i\gamma P B_{-1}{}^* e^{i\kappa z}, \tag{A.10}$$

$$\frac{dB_{-1}^{*}}{dz} = -i\gamma P B_1 e^{-i\kappa z}, \tag{A.11}$$

where κ is given by :

$$\kappa = \Delta\beta_{00-11} - 2\gamma P. \tag{A.12}$$

Taking the double derivative with respect to z, we arrive at :

$$\frac{d^2B_1}{dz^2} - i\kappa\frac{dB_1}{dz} - \gamma^2P^2B_1 = 0, \tag{A.13}$$

$$\frac{d^2B_{-1}^{*}}{dz^2} + i\kappa\frac{dB_{-1}^{*}}{dz} - \gamma^2P^2B_{-1}^{*} = 0. \tag{A.14}$$

The general solution to the above differential equations can be expressed in the form [135] :

$$B_1 = \left(a_1e^{gz} + a_2e^{-gz}\right)e^{i\frac{\kappa}{2}z}, \tag{A.15}$$

$$B_{-1}^{*} = \left(a_3e^{gz} + a_4e^{-gz}\right)e^{-i\frac{\kappa}{2}z}, \tag{A.16}$$

where g is given by :

$$g = \left(\gamma^2P^2 - \frac{\kappa^2}{4}\right)^{\frac{1}{2}}, \tag{A.17}$$

and a_1, a_2, a_3 and a_4 are arbitrary constants to be determined from the initial conditions. Imposing the initial condition, we have :

$$B_1(0) = a_1 + a_2, \tag{A.18}$$

$$B_{-1}^{*}(0) = a_3 + a_4. \tag{A.19}$$

Taking the derivative of Equation (A.15) with respect to z and imposing $z = 0$ and then equating it with Equation (A.10) at $z = 0$, we get :

$$i\gamma PB_{-1}^{*}(0) = (a_1g - a_2g) + (a_1 + a_2)\frac{i\kappa}{2} = (a_1g - (B_1(0) - a_1)g) + B_1(0)\frac{i\kappa}{2}. \tag{A.20}$$

Thus solving for a_1 and a_2, we get :

$$a_1 = \frac{B_1(0)(g - \frac{i\kappa}{2}) + i\gamma PB_{-1}^{*}(0)}{2g}, \tag{A.21}$$

$$a_2 = \frac{B_1(0)(g + \frac{i\kappa}{2}) - i\gamma PB_{-1}^{*}(0)}{2g}. \tag{A.22}$$

Let us say the input fields $B_1(0)$ and $B_{-1}(0)$ are given by :

$$B_1(0) = b_1e^{i\theta_1}, \tag{A.23}$$

$$B_{-1}(0) = b_{-1}e^{i\theta_{-1}}, \tag{A.24}$$

$$\vartheta = \frac{b_1}{b_{-1}}, \tag{A.25}$$

where b_i's and θ_i's are the amplitudes and phases of the respective waves at the input of the fiber with $i = 1, -1$. Using Equations (A.21) and (A.22) in Equation (A.15), we calculate the signal gain $G_1 = \frac{|B_1(L)|^2}{|B_1(0)|^2}$ as :

$$\begin{aligned} G_1 =& 1 + \left(1 + \frac{\kappa^2 + 4\gamma^2 P^2 \vartheta^2 - 4\kappa\gamma P\vartheta\cos(\Theta)}{4g^2}\right)\sinh^2(gL) \\ &+ \frac{\gamma P\vartheta\sin(\Theta)}{g}\sinh(2gL), \end{aligned} \tag{A.26}$$

where Θ is the relative phase $\Theta = 2\theta_0 - \theta_{-1} - \theta_1$. Here for simplicity we considered $\theta_0 = 0$.

A.2 Non-degenerate Pump Configuration

For the degenerate pump configuration, the index 0 is for the degenerate signal and idler, -1 and 1 are for the non-degenerate pumps. Invoking the approximation that the pump is much stronger than the signal and the idler, the equations for the pumps are given as :

$$\frac{dA_1}{dz} = i\gamma(|A_1|^2 A_1 + 2|A_{-1}|^2 A_1), \tag{A.27}$$

$$\frac{dA_{-1}}{dz} = i\gamma(|A_{-1}|^2 A_{-1} + 2|A_1|^2 A_{-1}). \tag{A.28}$$

Considering that the two pump waves have the same power $P = |A_1|^2 = |A_{-1}|^2$, we can write :

$$\frac{dA_j}{dz} = i\gamma(PA_j + 2PA_j) = i\gamma\, 3PA_j\,, \tag{A.29}$$

where $j = 1, -1$. Solving for A_j and considering that the pumps have zero phase at the input of the fiber, we get :

$$A_j(z) = A_j(0)e^{i\gamma 3Pz} = \sqrt{P}e^{i\gamma 3Pz}, \tag{A.30}$$

where $j = 1, -1$. Injecting A_1 and A_{-1} into Equation (A.3) and also considering the pump powers to be much stronger than the signal and idler, we write the equation for the signal as :

$$\frac{dA_0}{dz} = i\gamma P\left(4A_0 + 2{A_0}^* e^{i(\Delta\beta_{1-100} + 6\gamma P)z}\right) \tag{A.31}$$

To eliminate the first term of Equation (A.31), we perform a transformation of variable :

$$B_0 = A_0 e^{-4i\gamma Pz}. \tag{A.32}$$

Invoking this transformation in Equation (A.31) we get :

$$\frac{dB_0}{dz} = 2i\gamma P {B_0}^* e^{i\kappa z}, \tag{A.33}$$

where κ is given by :

$$\kappa = \Delta\beta_{1-100} - 2\gamma P. \tag{A.34}$$

The complex conjugate of Equation (A.33) is given by :

$$\frac{d{B_0}^*}{dz} = -2i\gamma P B_0 e^{-i\kappa z}. \tag{A.35}$$

Differentiating Equation (A.33) with respect to z and using Equation (A.35) we get :

$$\frac{d^2 B_0}{dz^2} - i\kappa \frac{dB_0}{dz} - 4\gamma^2 P^2 B_0 = 0. \tag{A.36}$$

The general solution to the above differential equation can be expressed in the form [135] :

$$B_0 = \left(a_1 e^{gz} + a_2 e^{-gz} \right) e^{i\frac{\kappa}{2}z}, \tag{A.37}$$

where g is given by :

$$g = \left(4\gamma^2 P^2 - \frac{\kappa^2}{4} \right)^{\frac{1}{2}}, \tag{A.38}$$

and a_1 and a_2 are arbitrary constants to be determined from the initial conditions. We note here that although the solutions have a similar functional form for the degenerate pump and non-degenerate pump cases, the definitions of κ and g differ for them. For $z = 0$ we have :

$$B_0(0) = a_1 + a_2. \tag{A.39}$$

Taking the derivative of Equation (A.37) with respect to z and imposing $z = 0$ and then equating it with Equation (A.33) at $z = 0$, we get :

$$2i\gamma P {B_0}^*(0) = (a_1 g - a_2 g) + (a_1 + a_2)\frac{i\kappa}{2} = (a_1 g - (B_0(0) - a_1)g) + B_0(0)\frac{i\kappa}{2}. \tag{A.40}$$

Thus solving for a_1 and a_2, we get :

$$a_1 = \frac{B_0(0)(g - \frac{i\kappa}{2}) + 2i\gamma P {B_0}^*(0)}{2g}, \tag{A.41}$$

$$a_2 = \frac{B_0(0)(g + \frac{i\kappa}{2}) - 2i\gamma P {B_0}^*(0)}{2g}. \tag{A.42}$$

Inserting the values of a_1 and a_2 in Equation (A.37) we calculate the signal gain $G_0 = \frac{|B_0(L)|^2}{|B_0(0)|^2}$ as :

$$\begin{aligned} G_0 =& 1 + \left(1 + \frac{\frac{\kappa^2}{4} + 4\gamma^2 P^2 - 2\kappa\gamma P\cos(\Theta)}{g^2}\right)\sinh^2(gL) \\ &+ \frac{2\gamma P\sin(\Theta)}{g}\sinh(2gL), \end{aligned} \tag{A.43}$$

where Θ is the relative phase $\Theta = 2\theta_0 - \theta_{-1} - \theta_1$. Here for simplicity we considered $\theta_{-1} = \theta_1 = 0$.

Appendix B

Coupled Equations for the 7-Wave Model

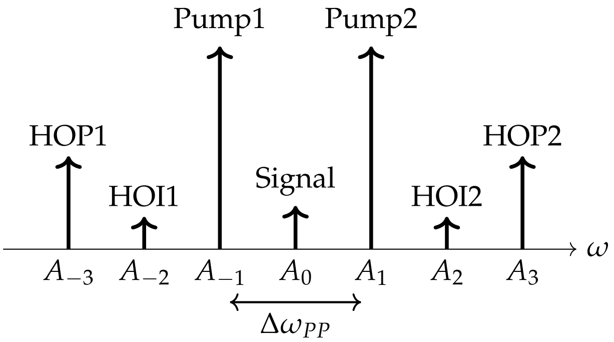

Figure B.1. Configuration of a dual-pump FOPA with degenerate signal and idler and non-degenerate pumps. ω is frequency. The two pumps are labelled A_1 and A_{-1}, the signal is labelled A_0, two higher order idlers (HOI) are labelled A_2 and A_{-2} and two higher order pumps (HOP) are labelled A_3 and A_{-3}. $\Delta\omega_{PP}$ is the frequency difference between the pumps. (not to scale)

The coupled differential equations governing the evolution of the slowly varying complex amplitudes A_j's of the $2k+1$ waves (see Fig. B.1) along the fiber can be derived from the general equation (see Equation (2.4))[56] :

$$\frac{dA_j}{dz} = i\gamma\Big[|A_j|^2 A_j + 2\sum_{l\neq j=-k}^{k} |A_l|^2 A_j + \sum_{\substack{m,n,p=-k,\\ \omega_m+\omega_n-\omega_p=\omega_j}}^{k} A_m A_n A_p^* e^{i\Delta\beta_{mnpj} z}\Big], \tag{B.1}$$

where $\Delta\beta_{mnpj} = \beta_m + \beta_n - \beta_p - \beta_j$ and γ is the nonlinear coefficient of the fiber. Here we have ignored the fiber attenuation.

When $k = 3$, we have seven waves, and the coupled equations considering all the FWM terms from Equation (B.1) are given by [89, 168] :

$$\begin{aligned}
\frac{dA_0}{dz} &= i\gamma\Big\{\big[|A_0|^2A_0 + 2\sum_{j=-3,j\neq 0}^{3}|A_j|^2\big]A_0 + A_{-1}^2A_{-2}^*e^{i\Delta\beta_{-1-1-20}} + A_1^2A_2^*e^{i\Delta\beta_{1120}} \\
&+ 2A_{-1}A_1A_0^*e^{i\Delta\beta_{-1100}} + 2A_{-1}A_3A_2^*e^{i\Delta\beta_{-1320}} + 2A_{-1}A_{-2}A_{-3}^*e^{i\Delta\beta_{-1-2-30}} + 2A_{-1}A_2A_1^*e^{i\Delta\beta_{-1210}} \\
&+ 2A_1A_{-3}A_{-2}^*e^{i\Delta\beta_{1-3-20}} + 2A_1A_{-2}A_{-1}^*e^{i\Delta\beta_{1-2-10}} + 2A_1A_2A_3^*e^{i\Delta\beta_{1230}} + 2A_{-3}A_2A_{-1}^*e^{i\Delta\beta_{-32-10}} \\
&+ 2A_{-3}A_3A_0^*e^{i\Delta\beta_{-3300}} + 2A_{-2}A_2A_0^*e^{i\Delta\beta_{-2200}} + 2A_3A_{-2}A_1^*e^{i\Delta\beta_{3-210}}\Big\}.
\end{aligned} \tag{B.2}$$

$$\begin{aligned}
\frac{dA_{-1}}{dz} &= i\gamma\Big\{\big[|A_{-1}|^2A_{-1} + 2\sum_{j=-3,j\neq -1}^{3}|A_j|^2\big]A_{-1} + A_1^2A_3^*e^{i\Delta\beta_{113-1}} + A_0^2A_1^*e^{i\Delta\beta_{001-1}} \\
&+ A_{-2}^2A_3^*e^{i\Delta\beta_{-2-2-3-1}} + 2A_0A_1A_2^*e^{i\Delta\beta_{012-1}} + 2A_1A_{-3}A_{-1}^*e^{i\Delta\beta_{1-3-1-1}} + 2A_{-3}A_3A_1^*e^{i\Delta\beta_{-331-1}} \\
&+ 2A_0A_{-3}A_{-2}^*e^{i\Delta\beta_{0-3-2-1}} + 2A_2A_{-3}A_0^*e^{i\Delta\beta_{2-30-1}} + 2A_0A_2A_3^*e^{i\Delta\beta_{023-1}} + 2A_1A_{-2}A_0^*e^{i\Delta\beta_{1-20-1}} \\
&+ 2A_0A_{-2}A_{-1}^*e^{i\Delta\beta_{0-2-1-1}} + 2A_{-2}A_3A_2^*e^{i\Delta\beta_{-232-1}} + 2A_{-2}A_2A_1^*e^{i\Delta\beta_{-221-1}}\Big\}.
\end{aligned} \tag{B.3}$$

$$\begin{aligned}
\frac{dA_1}{dz} &= i\gamma\Big\{\big[|A_1|^2A_1 + 2\sum_{j=-3,j\neq 1}^{3}|A_j|^2\big]A_1 + A_{-1}^2A_{-3}^*e^{i\Delta\beta_{-1-1-31}} + A_0^2A_{-1}^*e^{i\Delta\beta_{00-11}} \\
&+ A_2^2A_3^*e^{i\Delta\beta_{2231}} + 2A_0A_{-1}A_{-2}^*e^{i\Delta\beta_{0-1-21}} + 2A_{-1}A_3A_1^*e^{i\Delta\beta_{-1311}} + 2A_{-1}A_2A_0^*e^{i\Delta\beta_{-1201}} \\
&+ 2A_0A_3A_2^*e^{i\Delta\beta_{0321}} + 2A_0A_{-2}A_{-3}^*e^{i\Delta\beta_{0-2-31}} + 2A_0A_2A_1^*e^{i\Delta\beta_{0211}} + 2A_{-2}A_3A_0^*e^{i\Delta\beta_{-2301}} \\
&+ 2A_{-3}A_3A_{-1}^*e^{i\Delta\beta_{-33-11}} + 2A_2A_{-3}A_{-2}^*e^{i\Delta\beta_{2-3-21}} + 2A_{-2}A_2A_{-1}^*e^{i\Delta\beta_{-22-11}}\Big\}.
\end{aligned} \tag{B.4}$$

$$\begin{aligned}
\frac{dA_{-2}}{dz} &= i\gamma\Big\{\big[|A_{-2}|^2A_{-2} + 2\sum_{j=-3,j\neq -2}^{3}|A_j|^2\big]A_{-2} + A_{-1}^2A_0^*e^{i\Delta\beta_{-1-10-2}} + A_0^2A_2^*e^{i\Delta\beta_{002-2}} \\
&+ 2A_{-1}A_1A_2^*e^{i\Delta\beta_{-112-2}} + 2A_0A_{-1}A_1^*e^{i\Delta\beta_{0-11-2}} + 2A_{-1}A_{-3}A_{-2}^*e^{i\Delta\beta_{-1-3-2-2}} + 2A_{-1}A_2A_3^*e^{i\Delta\beta_{-123-2}} \\
&+ 2A_2A_{-3}A_1^*e^{i\Delta\beta_{2-31-2}} + 2A_{-3}A_3A_2^*e^{i\Delta\beta_{-332-2}} + 2A_0A_{-3}A_{-1}^*e^{i\Delta\beta_{0-3-1-2}} + 2A_1A_{-3}A_0^*e^{i\Delta\beta_{1-30-2}} \\
&+ 2A_0A_1A_3^*e^{i\Delta\beta_{013-2}}\Big\}.
\end{aligned} \tag{B.5}$$

$$\begin{aligned}
\frac{dA_2}{dz} &= i\gamma\Big\{\big[|A_2|^2A_2 + 2\sum_{j=-3,j\neq 2}^{3}|A_j|^2\big]A_2 + A_0^2A_{-2}^*e^{i\Delta\beta_{00-22}} + A_1^2A_0^*e^{i\Delta\beta_{1102}} \\
&+ 2A_{-1}A_1A_{-2}^*e^{i\Delta\beta_{-11-22}} + 2A_0A_{-1}A_{-3}^*e^{i\Delta\beta_{0-1-32}} + 2A_{-1}A_3A_0^*e^{i\Delta\beta_{-1302}} + 2A_0A_1A_{-1}^*e^{i\Delta\beta_{01-12}} \\
&+ 2A_1A_3A_2^*e^{i\Delta\beta_{1322}} + 2A_1A_{-2}A_{-3}^*e^{i\Delta\beta_{1-2-32}} + 2A_0A_3A_1^*e^{i\Delta\beta_{0312}} + 2A_{-3}A_3A_{-2}^*e^{i\Delta\beta_{-33-22}} \\
&+ 2A_{-2}A_3A_{-1}^*e^{i\Delta\beta_{-23-12}}\Big\}.
\end{aligned} \tag{B.6}$$

$$
\begin{aligned}
\frac{dA_{-3}}{dz} &= i\gamma\Big\{ \big[|A_{-3}|^2 A_{-3} + 2\sum_{j=-2}^{3} |A_j|^2\big] A_{-3} + A_{-1}^2 A_1^* e^{i\Delta\beta_{-1-11-3}} + A_0^2 A_3^* e^{i\Delta\beta_{003-3}} \\
&+ A_{-2}^2 A_{-1}^* e^{i\Delta\beta_{-2-2-1-3}} + 2A_{-1}A_1A_3^* e^{i\Delta\beta_{-113-3}} + 2A_0A_{-1}A_2^* e^{i\Delta\beta_{0-12-3}} + 2A_{-1}A_{-2}A_0^* e^{i\Delta\beta_{-1-20-3}} \\
&+ 2A_0A_{-2}A_1^* e^{i\Delta\beta_{0-21-3}} + 2A_1A_{-2}A_2^* e^{i\Delta\beta_{1-22-3}} + 2A_{-2}A_2A_3^* e^{i\Delta\beta_{-223-3}} \Big\}. \qquad \text{(B.7)}
\end{aligned}
$$

$$
\begin{aligned}
\frac{dA_3}{dz} &= i\gamma\Big\{ \big[|A_3|^2 A_3 + 2\sum_{j=-3}^{2} |A_j|^2\big] A_3 + A_1^2 A_{-1}^* e^{i\Delta\beta_{11-13}} + A_0^2 A_{-3}^* e^{i\Delta\beta_{00-33}} \\
&+ A_2^2 A_1^* e^{i\Delta\beta_{2213}} + 2A_{-1}A_1A_{-3}^* e^{i\Delta\beta_{-11-33}} + 2A_{-1}A_2A_{-2}^* e^{i\Delta\beta_{-12-23}} + 2A_0A_1A_{-2}^* e^{i\Delta\beta_{01-23}} \\
&+ 2A_{-2}A_2A_{-3}^* e^{i\Delta\beta_{-22-33}} + 2A_1A_2A_0^* e^{i\Delta\beta_{1203}} + 2A_0A_2A_{-1}^* e^{i\Delta\beta_{02-13}} \Big\}. \qquad \text{(B.8)}
\end{aligned}
$$

Appendix C

Signal and HOI Evolution in Analytical 7-wave Model

Considering the analytical 7-wave model, in the case of arbitrary initial conditions for the waves A_0, A_2 and A_{-2}, the input and output waves can be related as (as given in Equation (2.101)) :

$$\frac{d}{dz}\begin{bmatrix} A_0 \\ {A_0}^* \\ A_{-2} \\ {A_{-2}}^* \end{bmatrix} = i\gamma P \begin{bmatrix} 4 & 2e^{i(2\xi+2C)z} & 4e^{i4Cz} & 2e^{i(2\xi-2C)z} \\ -2e^{-i(2\xi+2C)z} & -4 & -2e^{-i(2\xi-2C)z} & -4e^{-i4Cz} \\ 2e^{-i4Cz} & e^{i(2\xi-2C)z} & 4 & 2e^{i(2\xi-6C)z} \\ -e^{-i(2\xi-2C)z} & -2e^{i4Cz} & -2e^{-i(2\xi-6C)z} & -4 \end{bmatrix} \begin{bmatrix} A_0 \\ {A_0}^* \\ A_{-2} \\ {A_{-2}}^* \end{bmatrix} + i\gamma P \begin{bmatrix} -2e^{i4Cz}\delta_2 - e^{i(2\xi-2C)z}\delta_2^* \\ 2e^{-i4Cz}\delta_2^* + e^{-i(2\xi-2C)z}\delta_2 \\ -2e^{i(2\xi-6C)z}\delta_2^* \\ 2e^{-i(2\xi-6C)z}\delta_2 \end{bmatrix}, \tag{C.1}$$

where P is the undepleted pump power, γ is the nonlinear coefficient of the fiber. ξ, C and δ_2 are given by :

$$\begin{aligned} \xi &= 3\gamma P, \\ C &= \frac{\beta^{(2)}(\omega_c)\Delta{\omega_{PP}}^2}{8} \\ \delta_2 &= A_{-2} - A_2. \end{aligned} \tag{C.2}$$

In order to remove the exponential terms from the Equation (C.1), we perform the following transformation of variables (as given in Equation (2.102)) :

$$\begin{aligned} A_0 &= B_0 e^{i(\xi+C)z}, \\ A_{-2} &= B_{-2} e^{i(\xi-3C)z}, \\ A_2 &= B_2 e^{i(\xi-3C)z}, \\ \tilde{\delta}_2 &= B_{-2} - B_2 = e^{-i(\xi-3C)z}\delta_2. \end{aligned} \tag{C.3}$$

Invoking these transformations we get :

$$\frac{d}{dz}\begin{bmatrix} B_0 \\ {B_0}^* \\ B_{-2} \\ {B_{-2}}^* \end{bmatrix} = i\gamma P \begin{bmatrix} 1-F_0 & 2 & 4 & 2 \\ -2 & -(1-F_0) & -2 & -4 \\ 2 & 1 & 1-F_2 & 2 \\ -1 & -2 & -2 & -(1-F_2) \end{bmatrix} \begin{bmatrix} B_0 \\ {B_0}^* \\ B_{-2} \\ {B_{-2}}^* \end{bmatrix} + i\gamma P \begin{bmatrix} -2\tilde{\delta_2} - \tilde{\delta_2}^* \\ 2\tilde{\delta_2}^* + \tilde{\delta_2} \\ -2\tilde{\delta_2}^* \\ 2\tilde{\delta_2} \end{bmatrix}, \tag{C.4}$$

where F_q is given by :

$$F_q = \frac{C(1-q^2)}{\gamma P}, \tag{C.5}$$

where $|q| = 0, 2$. Equation (C.4) is a coupled linear inhomogenious differential equation of the form :

$$\frac{d\mathbf{B}}{dz} = \mathbf{M}^{'}\mathbf{B} + \mathbf{N},$$

where $\mathbf{M}^{'}$ is the transfer matrix and $\mathbf{N}$ is the inhomogenity term. The eigenvalues (λ_1, λ_2, λ_3 and λ_4) and eigenvectors ($\mathbf{V_1}$, $\mathbf{V_2}$, $\mathbf{V_3}$ and $\mathbf{V_4}$,) of $\mathbf{M}^{'}$ are given as (also given in Equations (2.84) and (2.85) respectively) :

$$\lambda_1 = -i\gamma P\,\nu_0, \quad \lambda_2 = i\gamma P\,\nu_0, \quad \lambda_3 = -i\gamma P\,\nu_2, \quad \lambda_4 = i\gamma P\,\nu_2, \tag{C.6}$$

$$\mathbf{V_1} = \begin{bmatrix} \eta - \nu_0 \\ \eta + \nu_0 \\ 1 \\ 1 \end{bmatrix}, \quad \mathbf{V_2} = \begin{bmatrix} \eta + \nu_0 \\ \eta - \nu_0 \\ 1 \\ 1 \end{bmatrix}, \quad \mathbf{V_3} = \begin{bmatrix} \frac{-6}{\nu_2 - 3\eta} \\ \frac{6}{\nu_2 - 3\eta} \\ \frac{\nu_2 + 3\eta}{\nu_2 - 3\eta} \\ 1 \end{bmatrix}, \quad \mathbf{V_4} = \begin{bmatrix} \frac{6}{\nu_2 + 3\eta} \\ \frac{-6}{\nu_2 + 3\eta} \\ \frac{\nu_2 - 3\eta}{\nu_2 + 3\eta} \\ 1 \end{bmatrix}, \tag{C.7}$$

where η, ν_0 and ν_2 (as given by Equations (C.8)and (C.9)) are :

$$\eta = -1 - F_0\,, \tag{C.8}$$

$$\nu_q = \sqrt{3 - 2F_q + {F_q}^2}\,, \tag{C.9}$$

where $|q| = 0, 2$. Also using Equation (2.104) we can write $\tilde{\delta_2}(z)$ as :

$$\tilde{\delta_2}(z) = \left(\frac{-i\eta_2 \sin(\gamma P \mu_2 z)}{\mu_2} + \cos(\gamma P \mu_2 z)\right)\tilde{\delta_2}(0) - \left(\frac{2i\sin(\gamma P \mu_2 z)}{\mu_2}\right)\tilde{\delta_2}^*(0), \tag{C.10}$$

where η_2 and μ_2 are given by (see Equation (**??**)) :

$$\eta_2 = -1 + F_2 = -1 - 3F_0 = 2 + 3\eta, \tag{C.11}$$

$$\mu_2 = (-3 - 2F_2 + {F_2}^2)^{\frac{1}{2}} = (-3 + 6F_0 + 9{F_0}^2)^{\frac{1}{2}}. \tag{C.12}$$

We can also define the fundamental matrix $\mathbf{F}$ of $\mathbf{M}^{'}$ as :

$$\begin{aligned}\mathbf{F} &= \begin{bmatrix} e^{\lambda_1 z}\mathbf{V_1} & e^{\lambda_2 z}\mathbf{V_2} & e^{\lambda_3 z}\mathbf{V_3} & e^{\lambda_4 z}\mathbf{V_4} \end{bmatrix} \\ &= \begin{bmatrix} (\eta - \nu_0)e^{-i\gamma P\nu_0 z} & (\eta + \nu_0)e^{i\gamma P\nu_0 z} & \frac{-6}{\nu_2-3\eta}e^{-i\gamma P\nu_2 z} & \frac{6}{\nu_2+3\eta}e^{i\gamma P\nu_2 z} \\ (\eta + \nu_0)e^{-i\gamma P\nu_0 z} & (\eta - \nu_0)e^{i\gamma P\nu_0 z} & \frac{6}{\nu_2-3\eta}e^{-i\gamma P\nu_2 z} & \frac{-6}{\nu_2+3\eta}e^{i\gamma P\nu_2 z} \\ e^{-i\gamma P\nu_0 z} & e^{i\gamma P\nu_0 z} & \frac{\nu_2+3\eta}{\nu_2-3\eta}e^{-i\gamma P\nu_2 z} & \frac{\nu_2-3\eta}{\nu_2+3\eta}e^{i\gamma P\nu_2 z} \\ e^{-i\gamma P\nu_0 z} & e^{i\gamma P\nu_0 z} & e^{-i\gamma P\nu_2 z} & e^{i\gamma P\nu_2 z} \end{bmatrix},\end{aligned} \tag{C.13}$$

The solution to Equation (C.4) is given by :

$$\begin{aligned}\mathbf{B}(z) &= \mathbf{F}(z)\mathbf{F}(0)^{-1}\mathbf{B}(0) + \int_0^z \mathbf{F}(z)\mathbf{F}(s)^{-1}\mathbf{N}(s)ds \\ &= \bar{\mathbf{B}}(z)\mathbf{B}(0) + \Delta\mathbf{B}(z)\tilde{\mathbf{B}}(0) \\ &= \bar{\mathbf{B}}(z)\mathbf{B}(0) + \begin{bmatrix} b_{11} & b_{12} & b_{13} & b_{14} \\ b_{21} & b_{22} & b_{23} & b_{24} \\ b_{31} & b_{32} & b_{33} & b_{34} \\ b_{41} & b_{42} & b_{43} & b_{44} \end{bmatrix} \begin{bmatrix} B_{-2}(0) \\ B_{-2}{}^*(0) \\ B_2(0) \\ B_2{}^*(0) \end{bmatrix},\end{aligned} \tag{C.14}$$

where the first term on the right hand side of the above equation represents the solution when $\delta_2 = 0$ (or $\tilde{\delta_2} = 0$) (as $\mathbf{N} = \mathbf{0}$ when $\delta_2 = 0$) which is given by Equations (2.90) and (2.91). The second term arises due to the inhomogenity of the system. We should note here that the second term is independent of $B_0(0)$, which means any input fluctuations in the signal mode will not contaminate the mode produced by the beating between B_{-2} and B_2 modes. Using *Mathematica* [253], we find $\mathbf{F}(s)^{-1}$ as :

$$\mathbf{F}(s)^{-1} = \begin{bmatrix} \frac{\nu_0-\eta}{4\nu_0\eta}e^{i\gamma P\nu_0 s} & \frac{\nu_0+\eta}{4\nu_0\eta}e^{i\gamma P\nu_0 s} & \frac{-1}{2\nu_0\eta}e^{i\gamma P\nu_0 s} & \frac{1}{2\nu_0\eta}e^{i\gamma P\nu_0 s} \\ \frac{\nu_0+\eta}{4\nu_0\eta}e^{-i\gamma P\nu_0 s} & \frac{\nu_0-\eta}{4\nu_0\eta}e^{-i\gamma P\nu_0 s} & \frac{1}{2\nu_0\eta}e^{-i\gamma P\nu_0 s} & \frac{-1}{2\nu_0\eta}e^{-i\gamma P\nu_0 s} \\ \frac{-(\nu_2-3\eta)}{4\nu_2\eta}e^{i\gamma P\nu_2 s} & \frac{-(\nu_2-3\eta)}{4\nu_2\eta}e^{i\gamma P\nu_2 s} & \frac{(\nu_2+3\eta)(\nu_2-3\eta)}{12\nu_2\eta}e^{i\gamma P\nu_2 s} & \frac{-(\nu_2-3\eta)^2}{12\nu_2\eta}e^{i\gamma P\nu_2 s} \\ \frac{-(\nu_2+3\eta)}{4\nu_2\eta}e^{-i\gamma P\nu_2 s} & \frac{-(\nu_2+3\eta)}{4\nu_2\eta}e^{-i\gamma P\nu_2 s} & \frac{-(\nu_2+3\eta)(\nu_2-3\eta)}{12\nu_2\eta}e^{-i\gamma P\nu_2 s} & \frac{(\nu_2+3\eta)^2}{12\nu_2\eta}e^{-i\gamma P\nu_2 s} \end{bmatrix}. \tag{C.15}$$

In Equation (C.4), in the second term, we can pull $\mathbf{F}(z)$ out of the integral as the integral is on s. Thus we can write :

$$\int_0^z \mathbf{F}(z)\mathbf{F}(s)^{-1}\mathbf{N}(s)ds = \mathbf{F}(z)\int_0^z \mathbf{F}(s)^{-1}\mathbf{N}(s)ds. \tag{C.16}$$

We perform the computation in *Mathematica* [253] and first find the solutions for the b_{ij} coefficients in Equation (C.14) (see Appendix D)[1]. Note that we just need to find the elements in the first and third row of the b_{ij} matrix since the second and fourth rows are related to the first and third rows respectively. After that we find the final

---

[1] A different notation was used for the code : $\nu_0 \rightarrow \mu_0$, $\nu_2 \rightarrow \mu_2$, $\mu_2 \rightarrow \mu_2 o$, $\eta \rightarrow \eta_0$

solution for $B_0(z)$, $B_{-2}(z)$ and $B_2(z)$ as :

$$\begin{aligned}
B_0(z) = {} & B_0(0)\left(\cos(\gamma P\nu_0 z) + \frac{i(\eta^2+{\nu_0}^2)}{2\eta\nu_0}\sin(\gamma P\nu_0 z) - \frac{3i}{\eta\nu_2}\sin(\gamma P\nu_2 z)\right) \\
& + B_0^*(0)\left(\frac{i(-\eta^2+{\nu_0}^2)}{2\eta\nu_0}\sin(\gamma P\nu_0 z) - \frac{3i}{\eta\nu_2}\sin(\gamma P\nu_2 z)\right) \\
& + B_{-2}(0)\left(\frac{1}{2\eta}\cos(\gamma P\nu_0 z) - \frac{1}{2\eta}\cos(\gamma P\nu_2 z) + \frac{i}{2\nu_0}\sin(\gamma P\nu_0 z) + \frac{3i}{2\nu_2}\sin(\gamma P\nu_2 z)\right) \\
& + B_{-2}^*(0)\left(-\frac{1}{2\eta}\cos(\gamma P\nu_0 z) + \frac{1}{2\eta}\cos(\gamma P\nu_2 z) - \frac{i}{2\nu_0}\sin(\gamma P\nu_0 z) + \frac{3i}{2\nu_2}\sin(\gamma P\nu_2 z)\right) \\
& + B_2(0)\left(\frac{1}{2\eta}\cos(\gamma P\nu_0 z) - \frac{1}{2\eta}\cos(\gamma P\nu_2 z) + \frac{i}{2\nu_0}\sin(\gamma P\nu_0 z) + \frac{3i}{2\nu_2}\sin(\gamma P\nu_2 z)\right) \\
& + B_2^*(0)\left(-\frac{1}{2\eta}\cos(\gamma P\nu_0 z) + \frac{1}{2\eta}\cos(\gamma P\nu_2 z) - \frac{i}{2\nu_0}\sin(\gamma P\nu_0 z) + \frac{3i}{2\nu_2}\sin(\gamma P\nu_2 z)\right),
\end{aligned} \tag{C.17}$$

$$\begin{aligned}
B_{-2}(z) = {} & B_0(0)\left(\frac{1}{2\eta}\cos(\gamma P\nu_0 z) - \frac{1}{2\eta}\cos(\gamma P\nu_2 z) + \frac{i}{2\nu_0}\sin(\gamma P\nu_0 z) + \frac{3i}{2\nu_2}\sin(\gamma P\nu_2 z)\right) \\
& + B_0^*(0)\left(\frac{1}{2\eta}\cos(\gamma P\nu_0 z) - \frac{1}{2\eta}\cos(\gamma P\nu_2 z) - \frac{i}{2\nu_0}\sin(\gamma P\nu_0 z) + \frac{3i}{2\nu_2}\sin(\gamma P\nu_2 z)\right) \\
& + B_{-2}(0)\Bigg(\frac{1}{2}\cos(\gamma P\nu_2 z) + \frac{1}{2}\cos(\gamma P\mu_2 z) + \frac{i}{2\eta\nu_0}\sin(\gamma P\nu_0 z) \\
& - \frac{i(3\eta^2+2\eta+1)}{2\eta\nu_2}\sin(\gamma P\nu_2 z) - \frac{i(2+3\eta)}{2\mu_2}\sin(\gamma P\mu_2 z)\Bigg) \\
& + B_{-2}^*(0)\left(-\frac{i}{2\eta\nu_0}\sin(\gamma P\nu_0 z) + \frac{i(2\eta+1)}{2\eta\nu_2}\sin(\gamma P\nu_2 z) - \frac{i}{\mu_2}\sin(\gamma P\mu_2 z)\right) \\
& + B_2(0)\Bigg(\frac{1}{2}\cos(\gamma P\nu_2 z) - \frac{1}{2}\cos(\gamma P\mu_2 z) + \frac{i}{2\eta\nu_0}\sin(\gamma P\nu_0 z) \\
& - \frac{i(3\eta^2+2\eta+1)}{2\eta\nu_2}\sin(\gamma P\nu_2 z) + \frac{i(2+3\eta)}{2\mu_2}\sin(\gamma P\mu_2 z)\Bigg) \\
& + B_2^*(0)\left(-\frac{i}{2\eta\nu_0}\sin(\gamma P\nu_0 z) + \frac{i(2\eta+1)}{2\eta\nu_2}\sin(\gamma P\nu_2 z) + \frac{i}{\mu_2}\sin(\gamma P\mu_2 z)\right),
\end{aligned} \tag{C.18}$$

$$\begin{aligned}
B_2(z) = {} & B_0(0)\left(\frac{1}{2\eta}\cos(\gamma P\nu_0 z) - \frac{1}{2\eta}\cos(\gamma P\nu_2 z) + \frac{i}{2\nu_0}\sin(\gamma P\nu_0 z) + \frac{3i}{2\nu_2}\sin(\gamma P\nu_2 z)\right) \\
& + B_0^*(0)\left(\frac{1}{2\eta}\cos(\gamma P\nu_0 z) - \frac{1}{2\eta}\cos(\gamma P\nu_2 z) - \frac{i}{2\nu_0}\sin(\gamma P\nu_0 z) + \frac{3i}{2\nu_2}\sin(\gamma P\nu_2 z)\right) \\
& + B_{-2}(0)\Bigg(\frac{1}{2}\cos(\gamma P\nu_2 z) - \frac{1}{2}\cos(\gamma P\mu_2 z) + \frac{i}{2\eta\nu_0}\sin(\gamma P\nu_0 z) \\
& - \frac{i(3\eta^2+2\eta+1)}{2\eta\nu_2}\sin(\gamma P\nu_2 z) + \frac{i(2+3\eta)}{2\mu_2}\sin(\gamma P\mu_2 z)\Bigg) \\
& + B_{-2}^*(0)\left(-\frac{i}{2\eta\nu_0}\sin(\gamma P\nu_0 z) + \frac{i(2\eta+1)}{2\eta\nu_2}\sin(\gamma P\nu_2 z) + \frac{i}{\mu_2}\sin(\gamma P\mu_2 z)\right) \\
& + B_2(0)\Bigg(\frac{1}{2}\cos(\gamma P\nu_2 z) + \frac{1}{2}\cos(\gamma P\mu_2 z) + \frac{i}{2\eta\nu_0}\sin(\gamma P\nu_0 z) \\
& - \frac{i(3\eta^2+2\eta+1)}{2\eta\nu_2}\sin(\gamma P\nu_2 z) - \frac{i(2+3\eta)}{2\mu_2}\sin(\gamma P\mu_2 z)\Bigg) \\
& + B_2^*(0)\left(-\frac{i}{2\eta\nu_0}\sin(\gamma P\nu_0 z) + \frac{i(2\eta+1)}{2\eta\nu_2}\sin(\gamma P\nu_2 z) - \frac{i}{\mu_2}\sin(\gamma P\mu_2 z)\right),
\end{aligned} \tag{C.19}$$

Appendix D

Mathematica Code to Calculate b_{ij} Coefficients in Equation (C.14)

```
ClearAll["Global`*"]
Fz = {{Exp[-ⅈ*γ*P*μ0*z]*(η0-μ0), Exp[ⅈ*γ*P*μ0*z]*(η0+μ0),
    Exp[-ⅈ*γ*P*μ2*z]*(-6/(μ2-3*η0)), Exp[ⅈ*γ*P*μ2*z]*(6/(μ2+3*η0))},
   {Exp[-ⅈ*γ*P*μ0*z]*(η0+μ0), Exp[ⅈ*γ*P*μ0*z]*(η0-μ0),
    Exp[-ⅈ*γ*P*μ2*z]*(6/(μ2-3*η0)), Exp[ⅈ*γ*P*μ2*z]*(-6/(μ2+3*η0))},
   {Exp[-ⅈ*γ*P*μ0*z], Exp[ⅈ*γ*P*μ0*z], Exp[-ⅈ*γ*P*μ2*z]*
     (μ2+3*η0)/(μ2-3*η0), Exp[ⅈ*γ*P*μ2*z]*(μ2-3*η0)/(μ2+3*η0)},
   {Exp[-ⅈ*γ*P*μ0*z], Exp[ⅈ*γ*P*μ0*z], Exp[-ⅈ*γ*P*μ2*z],
    Exp[ⅈ*γ*P*μ2*z]}};(*F(z)*)
Fs = {{Exp[-ⅈ*γ*P*μ0*s]*(η0-μ0), Exp[ⅈ*γ*P*μ0*s]*(η0+μ0),
    Exp[-ⅈ*γ*P*μ2*s]*(-6/(μ2-3*η0)), Exp[ⅈ*γ*P*μ2*s]*(6/(μ2+3*η0))},
   {Exp[-ⅈ*γ*P*μ0*s]*(η0+μ0), Exp[ⅈ*γ*P*μ0*s]*(η0-μ0),
    Exp[-ⅈ*γ*P*μ2*s]*(6/(μ2-3*η0)), Exp[ⅈ*γ*P*μ2*s]*(-6/(μ2+3*η0))},
   {Exp[-ⅈ*γ*P*μ0*s], Exp[ⅈ*γ*P*μ0*s], Exp[-ⅈ*γ*P*μ2*s]*
     (μ2+3*η0)/(μ2-3*η0), Exp[ⅈ*γ*P*μ2*s]*(μ2-3*η0)/(μ2+3*η0)},
   {Exp[-ⅈ*γ*P*μ0*s], Exp[ⅈ*γ*P*μ0*s], Exp[-ⅈ*γ*P*μ2*s],
    Exp[ⅈ*γ*P*μ2*s]}};(*F(s)*)
MatrixForm[
 Fz]

FsI = FullSimplify[Inverse[Fs]];(*F(s)^(-1)*)
MatrixForm[FsI]

d2[s_] := d20*(Cos[γ*P*s*μ2o] - ⅈ*((-η2-2)/μ2o)*Sin[γ*P*s*μ2o]) -
   d2c0*2*ⅈ*Sin[γ*P*s*μ2o]/μ2o;(*δ₂(s)*)
d2c[s_] := d2c0*(Cos[γ*P*s*μ2o] + ⅈ*((-η2-2)/μ2o)*Sin[γ*P*s*μ2o]) +
   d20*2*ⅈ*Sin[γ*P*s*μ2o]/μ2o;(*Conjugate(δ₂(s))*)
Ns = ⅈ*γ*P*{{-2*d2[s] - d2c[s]}, {2*d2c[s] + d2[s]}, {-2*d2c[s]}, {2*d2[s]}};
(*N(s)*)
MatrixForm[Ns]

FsINs = FullSimplify[FsI.Ns];(*F(s)^(-1).N(s)*)
MatrixForm[FsINs]

IntFsINs = FullSimplify[Integrate[FsINs, {s, 0, z}]];
(*Integral(F(s)^(-1).N(s)ds) from s=0 to s=z*)
MatrixForm[IntFsINs]

B0inhomo = (Fz[[1, 1]]*IntFsINs[[1]]) + (Fz[[1, 2]]*IntFsINs[[2]]) +
     (Fz[[1, 3]]*IntFsINs[[3]]) + (Fz[[1, 4]]*IntFsINs[[4]]) /.
   {(4 + 3 η0 + η2) → 0, 11 + 6 η0 + 2 η2 → 3, μ2^2 - μ2o^2 → 6,
     (μ2 - μ2o) (μ2 + μ2o) → 6, η2 → -3 η0 - 4, d20 → bm2 - b2, d2c0 → bm2c - b2c};
 (*F(z).Integral(F(s)^(-1).N(s)ds) [[1]]*)

In[∘]:= B0inhomosort = Collect[B0inhomo, {b2, b2c, bm2, bm2c} ]
```

$$\text{B0inhomobm2c} = \text{FullSimplify}\Big[$$

$$\Bigg(\frac{3\,\mathrm{e}^{-\mathrm{i}\,P\,z\,\gamma\,\mu0}\,(4+3\,\eta0)\,(\eta0-\mu0)}{4\,\mu0\,(\mu0-\mu2o)\,(\mu0+\mu2o)} - \frac{\mathrm{e}^{-\mathrm{i}\,P\,z\,\gamma\,\mu0}\,(\eta0-\mu0)\,\mu0}{4\,\eta0\,(\mu0-\mu2o)\,(\mu0+\mu2o)} - \frac{3\,\mathrm{e}^{\mathrm{i}\,P\,z\,\gamma\,\mu0}\,(4+3\,\eta0)\,(\eta0+\mu0)}{4\,\mu0\,(\mu0-\mu2o)\,(\mu0+\mu2o)} +$$

$$\frac{\mathrm{e}^{\mathrm{i}\,P\,z\,\gamma\,\mu0}\,\mu0\,(\eta0+\mu0)}{4\,\eta0\,(\mu0-\mu2o)\,(\mu0+\mu2o)} - \frac{3\,\mathrm{e}^{-\mathrm{i}\,P\,z\,\gamma\,\mu2}}{2\,\eta0\,(\mu2-\mu2o)\,(\mu2+\mu2o)} -$$

$$\frac{3\,\mathrm{e}^{\mathrm{i}\,P\,z\,\gamma\,\mu2}}{2\,\eta0\,(\mu2-\mu2o)\,(\mu2+\mu2o)} - \frac{3\,\mathrm{e}^{-\mathrm{i}\,P\,z\,\gamma\,\mu2}\,(-4-3\,\eta0)\,(1+2\,\eta0)}{2\,\eta0\,\mu2\,(\mu2-\mu2o)\,(\mu2+\mu2o)} +$$

$$\frac{3\,\mathrm{e}^{\mathrm{i}\,P\,z\,\gamma\,\mu2}\,(-4-3\,\eta0)\,(1+2\,\eta0)}{2\,\eta0\,\mu2\,(\mu2-\mu2o)\,(\mu2+\mu2o)} - \frac{\mathrm{e}^{-\mathrm{i}\,P\,z\,\gamma\,\mu2}\,\mu2}{\eta0\,(\mu2-\mu2o)\,(\mu2+\mu2o)} +$$

$$\frac{\mathrm{e}^{\mathrm{i}\,P\,z\,\gamma\,\mu2}\,\mu2}{\eta0\,(\mu2-\mu2o)\,(\mu2+\mu2o)} - \frac{3\,(4+3\,\eta0)\,(\eta0-\mu0)\,\text{Cos}[P\,z\,\gamma\,\mu2o]}{4\,\mu0\,(\mu0-\mu2o)\,(\mu0+\mu2o)} +$$

$$\frac{(\eta0-\mu0)\,\mu0\,\text{Cos}[P\,z\,\gamma\,\mu2o]}{4\,\eta0\,(\mu0-\mu2o)\,(\mu0+\mu2o)} + \frac{3\,(4+3\,\eta0)\,(\eta0+\mu0)\,\text{Cos}[P\,z\,\gamma\,\mu2o]}{4\,\mu0\,(\mu0-\mu2o)\,(\mu0+\mu2o)} -$$

$$\frac{\mu0\,(\eta0+\mu0)\,\text{Cos}[P\,z\,\gamma\,\mu2o]}{4\,\eta0\,(\mu0-\mu2o)\,(\mu0+\mu2o)} + \frac{3\,\text{Cos}[P\,z\,\gamma\,\mu2o]}{\eta0\,(\mu2-\mu2o)\,(\mu2+\mu2o)} +$$

$$\frac{3\,\mathrm{i}\,(4+3\,\eta0)\,(\eta0-\mu0)\,\text{Sin}[P\,z\,\gamma\,\mu2o]}{4\,(\mu0-\mu2o)\,\mu2o\,(\mu0+\mu2o)} - \frac{\mathrm{i}\,(-4-3\,\eta0)\,(\eta0-\mu0)\,\mu0\,\text{Sin}[P\,z\,\gamma\,\mu2o]}{4\,\eta0\,(\mu0-\mu2o)\,\mu2o\,(\mu0+\mu2o)} +$$

$$\frac{3\,\mathrm{i}\,(4+3\,\eta0)\,(\eta0+\mu0)\,\text{Sin}[P\,z\,\gamma\,\mu2o]}{4\,(\mu0-\mu2o)\,\mu2o\,(\mu0+\mu2o)} + \frac{\mathrm{i}\,(-4-3\,\eta0)\,\mu0\,(\eta0+\mu0)\,\text{Sin}[P\,z\,\gamma\,\mu2o]}{4\,\eta0\,(\mu0-\mu2o)\,\mu2o\,(\mu0+\mu2o)} -$$

$$\frac{\mathrm{i}\,(\eta0-\mu0)\,\mu2o\,\text{Sin}[P\,z\,\gamma\,\mu2o]}{4\,\eta0\,(\mu0-\mu2o)\,(\mu0+\mu2o)} - \frac{\mathrm{i}\,(4+3\,\eta0)\,(\eta0-\mu0)\,\mu2o\,\text{Sin}[P\,z\,\gamma\,\mu2o]}{4\,\eta0\,\mu0\,(\mu0-\mu2o)\,(\mu0+\mu2o)} -$$

$$\frac{\mathrm{i}\,(\eta0+\mu0)\,\mu2o\,\text{Sin}[P\,z\,\gamma\,\mu2o]}{4\,\eta0\,(\mu0-\mu2o)\,(\mu0+\mu2o)} + \frac{\mathrm{i}\,(4+3\,\eta0)\,(\eta0+\mu0)\,\mu2o\,\text{Sin}[P\,z\,\gamma\,\mu2o]}{4\,\eta0\,\mu0\,(\mu0-\mu2o)\,(\mu0+\mu2o)} -$$

$$\frac{3\,\mathrm{i}\,(-4-3\,\eta0)\,(1+2\,\eta0)\,\text{Sin}[P\,z\,\gamma\,\mu2o]}{\eta0\,(\mu2-\mu2o)\,\mu2o\,(\mu2+\mu2o)} - \frac{2\,\mathrm{i}\,\mu2o\,\text{Sin}[P\,z\,\gamma\,\mu2o]}{\eta0\,(\mu2-\mu2o)\,(\mu2+\mu2o)}\Bigg) \,/.$$

$$\{\eta0 \to -1-\text{F0},\ \mu0 \to (3-2\,\text{F0}+\text{F0}\hat{}2)\hat{}(1/2),\ \mu2 \to (3+6\,\text{F0}+9\,\text{F0}\hat{}2)\hat{}(1/2),$$

$$\mu2o \to (-3+6\,\text{F0}+9\,\text{F0}\hat{}2)\hat{}(1/2)\}\Big]\ (*b_{12}*)$$

Out[ ]=

$$\frac{1}{2}\left(\frac{-\text{Cos}\left[\sqrt{3+(-2+\text{F0})\,\text{F0}}\;P\,z\,\gamma\right]+\text{Cos}\left[\sqrt{3+6\,\text{F0}+9\,\text{F0}^2}\;P\,z\,\gamma\right]}{1+\text{F0}}+\right.$$

$$\left.\mathrm{i}\left(\frac{\text{Sin}\left[\sqrt{3+(-2+\text{F0})\,\text{F0}}\;P\,z\,\gamma\right]}{\sqrt{3+(-2+\text{F0})\,\text{F0}}}-\frac{3\,\text{Sin}\left[\sqrt{3+6\,\text{F0}+9\,\text{F0}^2}\;P\,z\,\gamma\right]}{\sqrt{3+6\,\text{F0}+9\,\text{F0}^2}}\right)\right)$$

$$\text{B0inhomobm2} = \text{FullSimplify}\Bigg[\Bigg(-\frac{3\,\mathrm{e}^{-\mathrm{i}\,P\,z\,\gamma\,\mu0}\,(4+3\,\eta0)\,(\eta0-\mu0)}{4\,\mu0\,(\mu0-\mu2o)\,(\mu0+\mu2o)}+\frac{\mathrm{e}^{-\mathrm{i}\,P\,z\,\gamma\,\mu0}\,(\eta0-\mu0)\,\mu0}{4\,\eta0\,(\mu0-\mu2o)\,(\mu0+\mu2o)}+$$

$$\frac{3\,\mathrm{e}^{\mathrm{i}\,P\,z\,\gamma\,\mu0}\,(4+3\,\eta0)\,(\eta0+\mu0)}{4\,\mu0\,(\mu0-\mu2o)\,(\mu0+\mu2o)}-\frac{\mathrm{e}^{\mathrm{i}\,P\,z\,\gamma\,\mu0}\,\mu0\,(\eta0+\mu0)}{4\,\eta0\,(\mu0-\mu2o)\,(\mu0+\mu2o)}+\frac{3\,\mathrm{e}^{-\mathrm{i}\,P\,z\,\gamma\,\mu2}}{2\,\eta0\,(\mu2-\mu2o)\,(\mu2+\mu2o)}+$$

$$\frac{3\,\mathrm{e}^{\mathrm{i}\,P\,z\,\gamma\,\mu2}}{2\,\eta0\,(\mu2-\mu2o)\,(\mu2+\mu2o)}-\frac{3\,\mathrm{e}^{-\mathrm{i}\,P\,z\,\gamma\,\mu2}\,(-4-3\,\eta0)\,(1+2\,\eta0)}{2\,\eta0\,\mu2\,(\mu2-\mu2o)\,(\mu2+\mu2o)}+$$

$$\frac{3\,\mathrm{e}^{\mathrm{i}\,P\,z\,\gamma\,\mu2}\,(-4-3\,\eta0)\,(1+2\,\eta0)}{2\,\eta0\,\mu2\,(\mu2-\mu2o)\,(\mu2+\mu2o)}-\frac{\mathrm{e}^{-\mathrm{i}\,P\,z\,\gamma\,\mu2}\,\mu2}{\eta0\,(\mu2-\mu2o)\,(\mu2+\mu2o)}+$$

$$\frac{\mathrm{e}^{\mathrm{i}\,P\,z\,\gamma\,\mu2}\,\mu2}{\eta0\,(\mu2-\mu2o)\,(\mu2+\mu2o)}+\frac{3\,(4+3\,\eta0)\,(\eta0-\mu0)\,\text{Cos}[P\,z\,\gamma\,\mu2o]}{4\,\mu0\,(\mu0-\mu2o)\,(\mu0+\mu2o)}-$$

$$\frac{(\eta0-\mu0)\,\mu0\,\text{Cos}[P\,z\,\gamma\,\mu2o]}{4\,\eta0\,(\mu0-\mu2o)\,(\mu0+\mu2o)}-\frac{3\,(4+3\,\eta0)\,(\eta0+\mu0)\,\text{Cos}[P\,z\,\gamma\,\mu2o]}{4\,\mu0\,(\mu0-\mu2o)\,(\mu0+\mu2o)}+$$

$$\frac{\mu0\,(\eta0+\mu0)\,\text{Cos}[P\,z\,\gamma\,\mu2o]}{4\,\eta0\,(\mu0-\mu2o)\,(\mu0+\mu2o)}-\frac{3\,\text{Cos}[P\,z\,\gamma\,\mu2o]}{\eta0\,(\mu2-\mu2o)\,(\mu2+\mu2o)}-$$

$$\frac{3\,\mathrm{i}\,(4+3\,\eta0)\,(\eta0-\mu0)\,\text{Sin}[P\,z\,\gamma\,\mu2o]}{4\,(\mu0-\mu2o)\,\mu2o\,(\mu0+\mu2o)}-\frac{\mathrm{i}\,(-4-3\,\eta0)\,(\eta0-\mu0)\,\mu0\,\text{Sin}[P\,z\,\gamma\,\mu2o]}{4\,\eta0\,(\mu0-\mu2o)\,\mu2o\,(\mu0+\mu2o)}-$$

$$\frac{3\,\mathrm{i}\,(4+3\,\eta0)\,(\eta0+\mu0)\,\text{Sin}[P\,z\,\gamma\,\mu2o]}{4\,(\mu0-\mu2o)\,\mu2o\,(\mu0+\mu2o)}+\frac{\mathrm{i}\,(-4-3\,\eta0)\,\mu0\,(\eta0+\mu0)\,\text{Sin}[P\,z\,\gamma\,\mu2o]}{4\,\eta0\,(\mu0-\mu2o)\,\mu2o\,(\mu0+\mu2o)}+$$

$$\frac{\mathrm{i}\,(\eta0-\mu0)\,\mu2o\,\text{Sin}[P\,z\,\gamma\,\mu2o]}{4\,\eta0\,(\mu0-\mu2o)\,(\mu0+\mu2o)}-\frac{\mathrm{i}\,(4+3\,\eta0)\,(\eta0-\mu0)\,\mu2o\,\text{Sin}[P\,z\,\gamma\,\mu2o]}{4\,\eta0\,\mu0\,(\mu0-\mu2o)\,(\mu0+\mu2o)}+$$

$$\frac{\mathrm{i}\,(\eta0+\mu0)\,\mu2o\,\text{Sin}[P\,z\,\gamma\,\mu2o]}{4\,\eta0\,(\mu0-\mu2o)\,(\mu0+\mu2o)}+\frac{\mathrm{i}\,(4+3\,\eta0)\,(\eta0+\mu0)\,\mu2o\,\text{Sin}[P\,z\,\gamma\,\mu2o]}{4\,\eta0\,\mu0\,(\mu0-\mu2o)\,(\mu0+\mu2o)}-$$

$$\frac{3\,\mathrm{i}\,(-4-3\,\eta0)\,(1+2\,\eta0)\,\text{Sin}[P\,z\,\gamma\,\mu2o]}{\eta0\,(\mu2-\mu2o)\,\mu2o\,(\mu2+\mu2o)}-\frac{2\,\mathrm{i}\,\mu2o\,\text{Sin}[P\,z\,\gamma\,\mu2o]}{\eta0\,(\mu2-\mu2o)\,(\mu2+\mu2o)}\Bigg)\;/.$$

$$\{\eta0\to-1-\text{F0},\ \mu0\to(3-2\,\text{F0}+\text{F0}\wedge2)\wedge(1/2),\ \mu2\to(3+6\,\text{F0}+9\,\text{F0}\wedge2)\wedge(1/2),$$
$$\mu2o\to(-3+6\,\text{F0}+9\,\text{F0}\wedge2)\wedge(1/2)\}\Bigg]\ (*b_{11}*)$$

Out[∘]=
$$\frac{1}{2}\left(\frac{\text{Cos}\left[\sqrt{3+(-2+\text{F0})\,\text{F0}}\;P\,z\,\gamma\right]-\text{Cos}\left[\sqrt{3+6\,\text{F0}+9\,\text{F0}^2}\;P\,z\,\gamma\right]}{1+\text{F0}}-\right.$$
$$\left.\mathrm{i}\left(\frac{\text{Sin}\left[\sqrt{3+(-2+\text{F0})\,\text{F0}}\;P\,z\,\gamma\right]}{\sqrt{3+(-2+\text{F0})\,\text{F0}}}+\frac{3\,\text{Sin}\left[\sqrt{3+6\,\text{F0}+9\,\text{F0}^2}\;P\,z\,\gamma\right]}{\sqrt{3+6\,\text{F0}+9\,\text{F0}^2}}\right)\right)$$

B0inhomob2 = FullSimplify[

$$
\begin{aligned}
\Bigg(&\frac{3\,e^{-i\,P\,z\,\gamma\,\mu 0}\,(4+3\,\eta 0)\,(\eta 0-\mu 0)}{4\,\mu 0\,(\mu 0-\mu 2o)\,(\mu 0+\mu 2o)}-\frac{e^{-i\,P\,z\,\gamma\,\mu 0}\,(\eta 0-\mu 0)\,\mu 0}{4\,\eta 0\,(\mu 0-\mu 2o)\,(\mu 0+\mu 2o)}-\frac{3\,e^{i\,P\,z\,\gamma\,\mu 0}\,(4+3\,\eta 0)\,(\eta 0+\mu 0)}{4\,\mu 0\,(\mu 0-\mu 2o)\,(\mu 0+\mu 2o)}+\\
&\frac{e^{i\,P\,z\,\gamma\,\mu 0}\,\mu 0\,(\eta 0+\mu 0)}{4\,\eta 0\,(\mu 0-\mu 2o)\,(\mu 0+\mu 2o)}-\frac{3\,e^{-i\,P\,z\,\gamma\,\mu 2}}{2\,\eta 0\,(\mu 2-\mu 2o)\,(\mu 2+\mu 2o)}-\\
&\frac{3\,e^{i\,P\,z\,\gamma\,\mu 2}}{2\,\eta 0\,(\mu 2-\mu 2o)\,(\mu 2+\mu 2o)}+\frac{3\,e^{-i\,P\,z\,\gamma\,\mu 2}\,(-4-3\,\eta 0)\,(1+2\,\eta 0)}{2\,\eta 0\,\mu 2\,(\mu 2-\mu 2o)\,(\mu 2+\mu 2o)}-\\
&\frac{3\,e^{i\,P\,z\,\gamma\,\mu 2}\,(-4-3\,\eta 0)\,(1+2\,\eta 0)}{2\,\eta 0\,\mu 2\,(\mu 2-\mu 2o)\,(\mu 2+\mu 2o)}+\frac{e^{-i\,P\,z\,\gamma\,\mu 2}\,\mu 2}{\eta 0\,(\mu 2-\mu 2o)\,(\mu 2+\mu 2o)}-\\
&\frac{e^{i\,P\,z\,\gamma\,\mu 2}\,\mu 2}{\eta 0\,(\mu 2-\mu 2o)\,(\mu 2+\mu 2o)}-\frac{3\,(4+3\,\eta 0)\,(\eta 0-\mu 0)\,\mathrm{Cos}[P\,z\,\gamma\,\mu 2o]}{4\,\mu 0\,(\mu 0-\mu 2o)\,(\mu 0+\mu 2o)}+\\
&\frac{(\eta 0-\mu 0)\,\mu 0\,\mathrm{Cos}[P\,z\,\gamma\,\mu 2o]}{4\,\eta 0\,(\mu 0-\mu 2o)\,(\mu 0+\mu 2o)}+\frac{3\,(4+3\,\eta 0)\,(\eta 0+\mu 0)\,\mathrm{Cos}[P\,z\,\gamma\,\mu 2o]}{4\,\mu 0\,(\mu 0-\mu 2o)\,(\mu 0+\mu 2o)}-\\
&\frac{\mu 0\,(\eta 0+\mu 0)\,\mathrm{Cos}[P\,z\,\gamma\,\mu 2o]}{4\,\eta 0\,(\mu 0-\mu 2o)\,(\mu 0+\mu 2o)}+\frac{3\,\mathrm{Cos}[P\,z\,\gamma\,\mu 2o]}{\eta 0\,(\mu 2-\mu 2o)\,(\mu 2+\mu 2o)}+\\
&\frac{3\,i\,(4+3\,\eta 0)\,(\eta 0-\mu 0)\,\mathrm{Sin}[P\,z\,\gamma\,\mu 2o]}{4\,(\mu 0-\mu 2o)\,\mu 2o\,(\mu 0+\mu 2o)}+\frac{i\,(-4-3\,\eta 0)\,(\eta 0-\mu 0)\,\mu 0\,\mathrm{Sin}[P\,z\,\gamma\,\mu 2o]}{4\,\eta 0\,(\mu 0-\mu 2o)\,\mu 2o\,(\mu 0+\mu 2o)}+\\
&\frac{3\,i\,(4+3\,\eta 0)\,(\eta 0+\mu 0)\,\mathrm{Sin}[P\,z\,\gamma\,\mu 2o]}{4\,(\mu 0-\mu 2o)\,\mu 2o\,(\mu 0+\mu 2o)}-\frac{i\,(-4-3\,\eta 0)\,\mu 0\,(\eta 0+\mu 0)\,\mathrm{Sin}[P\,z\,\gamma\,\mu 2o]}{4\,\eta 0\,(\mu 0-\mu 2o)\,\mu 2o\,(\mu 0+\mu 2o)}-\\
&\frac{i\,(\eta 0-\mu 0)\,\mu 2o\,\mathrm{Sin}[P\,z\,\gamma\,\mu 2o]}{4\,\eta 0\,(\mu 0-\mu 2o)\,(\mu 0+\mu 2o)}+\frac{i\,(4+3\,\eta 0)\,(\eta 0-\mu 0)\,\mu 2o\,\mathrm{Sin}[P\,z\,\gamma\,\mu 2o]}{4\,\eta 0\,\mu 0\,(\mu 0-\mu 2o)\,(\mu 0+\mu 2o)}-\\
&\frac{i\,(\eta 0+\mu 0)\,\mu 2o\,\mathrm{Sin}[P\,z\,\gamma\,\mu 2o]}{4\,\eta 0\,(\mu 0-\mu 2o)\,(\mu 0+\mu 2o)}-\frac{i\,(4+3\,\eta 0)\,(\eta 0+\mu 0)\,\mu 2o\,\mathrm{Sin}[P\,z\,\gamma\,\mu 2o]}{4\,\eta 0\,\mu 0\,(\mu 0-\mu 2o)\,(\mu 0+\mu 2o)}+\\
&\frac{3\,i\,(-4-3\,\eta 0)\,(1+2\,\eta 0)\,\mathrm{Sin}[P\,z\,\gamma\,\mu 2o]}{\eta 0\,(\mu 2-\mu 2o)\,\mu 2o\,(\mu 2+\mu 2o)}+\frac{2\,i\,\mu 2o\,\mathrm{Sin}[P\,z\,\gamma\,\mu 2o]}{\eta 0\,(\mu 2-\mu 2o)\,(\mu 2+\mu 2o)}\Bigg)\ /.\\
&\{\eta 0\to -1-\mathrm{F0},\ \mu 0\to (3-2\,\mathrm{F0}+\mathrm{F0}\verb|^|2)\verb|^|(1/2),\ \mu 2\to (3+6\,\mathrm{F0}+9\,\mathrm{F0}\verb|^|2)\verb|^|(1/2),\\
&\mu 2o\to (-3+6\,\mathrm{F0}+9\,\mathrm{F0}\verb|^|2)\verb|^|(1/2)\}]\ (*b_{13}*)
\end{aligned}
$$

Out[ ]=

$$
\begin{aligned}
\frac{1}{2}\Bigg(&\frac{-\mathrm{Cos}\left[\sqrt{3+(-2+\mathrm{F0})\,\mathrm{F0}}\;P\,z\,\gamma\right]+\mathrm{Cos}\left[\sqrt{3+6\,\mathrm{F0}+9\,\mathrm{F0}^2}\;P\,z\,\gamma\right]}{1+\mathrm{F0}}+\\
&i\left(\frac{\mathrm{Sin}\left[\sqrt{3+(-2+\mathrm{F0})\,\mathrm{F0}}\;P\,z\,\gamma\right]}{\sqrt{3+(-2+\mathrm{F0})\,\mathrm{F0}}}+\frac{3\,\mathrm{Sin}\left[\sqrt{3+6\,\mathrm{F0}+9\,\mathrm{F0}^2}\;P\,z\,\gamma\right]}{\sqrt{3+6\,\mathrm{F0}+9\,\mathrm{F0}^2}}\right)\Bigg)
\end{aligned}
$$

$$
\begin{aligned}
&\text{B0inhomob2c} = \text{FullSimplify}\Bigg[\Bigg(-\frac{3\,e^{-i\,P\,z\,\gamma\,\mu 0}\,(4+3\,\eta 0)\,(\eta 0-\mu 0)}{4\,\mu 0\,(\mu 0-\mu 2o)\,(\mu 0+\mu 2o)}+\frac{e^{-i\,P\,z\,\gamma\,\mu 0}\,(\eta 0-\mu 0)\,\mu 0}{4\,\eta 0\,(\mu 0-\mu 2o)\,(\mu 0+\mu 2o)}+\\
&\frac{3\,e^{i\,P\,z\,\gamma\,\mu 0}\,(4+3\,\eta 0)\,(\eta 0+\mu 0)}{4\,\mu 0\,(\mu 0-\mu 2o)\,(\mu 0+\mu 2o)}-\frac{e^{i\,P\,z\,\gamma\,\mu 0}\,\mu 0\,(\eta 0+\mu 0)}{4\,\eta 0\,(\mu 0-\mu 2o)\,(\mu 0+\mu 2o)}+\frac{3\,e^{-i\,P\,z\,\gamma\,\mu 2}}{2\,\eta 0\,(\mu 2-\mu 2o)\,(\mu 2+\mu 2o)}+\\
&\frac{3\,e^{i\,P\,z\,\gamma\,\mu 2}}{2\,\eta 0\,(\mu 2-\mu 2o)\,(\mu 2+\mu 2o)}+\frac{3\,e^{-i\,P\,z\,\gamma\,\mu 2}\,(-4-3\,\eta 0)\,(1+2\,\eta 0)}{2\,\eta 0\,\mu 2\,(\mu 2-\mu 2o)\,(\mu 2+\mu 2o)}-\\
&\frac{3\,e^{i\,P\,z\,\gamma\,\mu 2}\,(-4-3\,\eta 0)\,(1+2\,\eta 0)}{2\,\eta 0\,\mu 2\,(\mu 2-\mu 2o)\,(\mu 2+\mu 2o)}+\frac{e^{-i\,P\,z\,\gamma\,\mu 2}\,\mu 2}{\eta 0\,(\mu 2-\mu 2o)\,(\mu 2+\mu 2o)}-\\
&\frac{e^{i\,P\,z\,\gamma\,\mu 2}\,\mu 2}{\eta 0\,(\mu 2-\mu 2o)\,(\mu 2+\mu 2o)}+\frac{3\,(4+3\,\eta 0)\,(\eta 0-\mu 0)\,\text{Cos}[P\,z\,\gamma\,\mu 2o]}{4\,\mu 0\,(\mu 0-\mu 2o)\,(\mu 0+\mu 2o)}-\\
&\frac{(\eta 0-\mu 0)\,\mu 0\,\text{Cos}[P\,z\,\gamma\,\mu 2o]}{4\,\eta 0\,(\mu 0-\mu 2o)\,(\mu 0+\mu 2o)}-\frac{3\,(4+3\,\eta 0)\,(\eta 0+\mu 0)\,\text{Cos}[P\,z\,\gamma\,\mu 2o]}{4\,\mu 0\,(\mu 0-\mu 2o)\,(\mu 0+\mu 2o)}+\\
&\frac{\mu 0\,(\eta 0+\mu 0)\,\text{Cos}[P\,z\,\gamma\,\mu 2o]}{4\,\eta 0\,(\mu 0-\mu 2o)\,(\mu 0+\mu 2o)}-\frac{3\,\text{Cos}[P\,z\,\gamma\,\mu 2o]}{\eta 0\,(\mu 2-\mu 2o)\,(\mu 2+\mu 2o)}-\\
&\frac{3\,i\,(4+3\,\eta 0)\,(\eta 0-\mu 0)\,\text{Sin}[P\,z\,\gamma\,\mu 2o]}{4\,(\mu 0-\mu 2o)\,\mu 2o\,(\mu 0+\mu 2o)}+\frac{i\,(-4-3\,\eta 0)\,(\eta 0-\mu 0)\,\mu 0\,\text{Sin}[P\,z\,\gamma\,\mu 2o]}{4\,\eta 0\,(\mu 0-\mu 2o)\,\mu 2o\,(\mu 0+\mu 2o)}-\\
&\frac{3\,i\,(4+3\,\eta 0)\,(\eta 0+\mu 0)\,\text{Sin}[P\,z\,\gamma\,\mu 2o]}{4\,(\mu 0-\mu 2o)\,\mu 2o\,(\mu 0+\mu 2o)}-\frac{i\,(-4-3\,\eta 0)\,\mu 0\,(\eta 0+\mu 0)\,\text{Sin}[P\,z\,\gamma\,\mu 2o]}{4\,\eta 0\,(\mu 0-\mu 2o)\,\mu 2o\,(\mu 0+\mu 2o)}+\\
&\frac{i\,(\eta 0-\mu 0)\,\mu 2o\,\text{Sin}[P\,z\,\gamma\,\mu 2o]}{4\,\eta 0\,(\mu 0-\mu 2o)\,(\mu 0+\mu 2o)}+\frac{i\,(4+3\,\eta 0)\,(\eta 0-\mu 0)\,\mu 2o\,\text{Sin}[P\,z\,\gamma\,\mu 2o]}{4\,\eta 0\,\mu 0\,(\mu 0-\mu 2o)\,(\mu 0+\mu 2o)}+\\
&\frac{i\,(\eta 0+\mu 0)\,\mu 2o\,\text{Sin}[P\,z\,\gamma\,\mu 2o]}{4\,\eta 0\,(\mu 0-\mu 2o)\,(\mu 0+\mu 2o)}-\frac{i\,(4+3\,\eta 0)\,(\eta 0+\mu 0)\,\mu 2o\,\text{Sin}[P\,z\,\gamma\,\mu 2o]}{4\,\eta 0\,\mu 0\,(\mu 0-\mu 2o)\,(\mu 0+\mu 2o)}+\\
&\frac{3\,i\,(-4-3\,\eta 0)\,(1+2\,\eta 0)\,\text{Sin}[P\,z\,\gamma\,\mu 2o]}{\eta 0\,(\mu 2-\mu 2o)\,\mu 2o\,(\mu 2+\mu 2o)}+\frac{2\,i\,\mu 2o\,\text{Sin}[P\,z\,\gamma\,\mu 2o]}{\eta 0\,(\mu 2-\mu 2o)\,(\mu 2+\mu 2o)}\Bigg)\ /.\\
&\quad\{\eta 0\to -1-\text{F0},\ \mu 0\to (3-2\,\text{F0}+\text{F0}^\wedge 2)^\wedge(1/2),\ \mu 2\to (3+6\,\text{F0}+9\,\text{F0}^\wedge 2)^\wedge(1/2),\\
&\quad\mu 2o\to (-3+6\,\text{F0}+9\,\text{F0}^\wedge 2)^\wedge(1/2)\}\Bigg]\ (*\text{b}_{14}*)
\end{aligned}
$$

Out[•]=

$$
\begin{aligned}
&\frac{1}{2}\Bigg(\frac{\text{Cos}\left[\sqrt{3+(-2+\text{F0})\,\text{F0}}\ P\,z\,\gamma\right]-\text{Cos}\left[\sqrt{3+6\,\text{F0}+9\,\text{F0}^2}\ P\,z\,\gamma\right]}{1+\text{F0}}-\\
&\frac{i\,\text{Sin}\left[\sqrt{3+(-2+\text{F0})\,\text{F0}}\ P\,z\,\gamma\right]}{\sqrt{3+(-2+\text{F0})\,\text{F0}}}+\frac{3\,i\,\text{Sin}\left[\sqrt{3+6\,\text{F0}+9\,\text{F0}^2}\ P\,z\,\gamma\right]}{\sqrt{3+6\,\text{F0}+9\,\text{F0}^2}}\Bigg)
\end{aligned}
$$

```
Bm2inhomo = (Fz[[3, 1]] * IntFsINs[[1]]) + (Fz[[3, 2]] * IntFsINs[[2]]) +
    (Fz[[3, 3]] * IntFsINs[[3]]) + (Fz[[3, 4]] * IntFsINs[[4]]) /.
   {(4 + 3 η0 + η2) → 0, 11 + 6 η0 + 2 η2 → 3, μ2^2 - μ2o^2 → 6,
    (μ2 - μ2o) (μ2 + μ2o) → 6, η2 → -3 η0 - 4, d20 → bm2 - b2, d2c0 → bm2c - b2c};
 (*F(z).Integral(F(s)^(-1).N(s)ds)  [[3]]*)

Bm2inhomosort = Collect[Bm2inhomo, {b2, b2c, bm2, bm2c} ];
```

Bm2inhomobm2c = FullSimplify[

$$\left(\frac{3\,e^{-i\,P\,z\,\gamma\,\mu 0}\,(4+3\,\eta 0)}{4\,\mu 0\,(\mu 0-\mu 2o)\,(\mu 0+\mu 2o)}-\frac{3\,e^{i\,P\,z\,\gamma\,\mu 0}\,(4+3\,\eta 0)}{4\,\mu 0\,(\mu 0-\mu 2o)\,(\mu 0+\mu 2o)}-\frac{e^{-i\,P\,z\,\gamma\,\mu 0}\,\mu 0}{4\,\eta 0\,(\mu 0-\mu 2o)\,(\mu 0+\mu 2o)}+\right.$$

$$\frac{e^{i\,P\,z\,\gamma\,\mu 0}\,\mu 0}{4\,\eta 0\,(\mu 0-\mu 2o)\,(\mu 0+\mu 2o)}-\frac{e^{i\,P\,z\,\gamma\,\mu 2}\,(-3\,\eta 0+\mu 2)}{4\,\eta 0\,(\mu 2-\mu 2o)\,(\mu 2+\mu 2o)}+$$

$$\frac{e^{i\,P\,z\,\gamma\,\mu 2}\,(-4-3\,\eta 0)\,(1+2\,\eta 0)\,(-3\,\eta 0+\mu 2)}{4\,\eta 0\,\mu 2\,(\mu 2-\mu 2o)\,(\mu 2+\mu 2o)}+\frac{e^{i\,P\,z\,\gamma\,\mu 2}\,\mu 2\,(-3\,\eta 0+\mu 2)}{6\,\eta 0\,(\mu 2-\mu 2o)\,(\mu 2+\mu 2o)}+$$

$$\frac{e^{-i\,P\,z\,\gamma\,\mu 2}\,(3\,\eta 0+\mu 2)}{4\,\eta 0\,(\mu 2-\mu 2o)\,(\mu 2+\mu 2o)}+\frac{e^{-i\,P\,z\,\gamma\,\mu 2}\,(-4-3\,\eta 0)\,(1+2\,\eta 0)\,(3\,\eta 0+\mu 2)}{4\,\eta 0\,\mu 2\,(\mu 2-\mu 2o)\,(\mu 2+\mu 2o)}+$$

$$\frac{e^{-i\,P\,z\,\gamma\,\mu 2}\,\mu 2\,(3\,\eta 0+\mu 2)}{6\,\eta 0\,(\mu 2-\mu 2o)\,(\mu 2+\mu 2o)}+\frac{(-3\,\eta 0+\mu 2)\,\mathrm{Cos}[P\,z\,\gamma\,\mu 2o]}{4\,\eta 0\,(\mu 2-\mu 2o)\,(\mu 2+\mu 2o)}+$$

$$\frac{(1+2\,\eta 0)\,(4+3\,\eta 0)\,(-3\,\eta 0+\mu 2)\,\mathrm{Cos}[P\,z\,\gamma\,\mu 2o]}{4\,\eta 0\,\mu 2\,(\mu 2-\mu 2o)\,(\mu 2+\mu 2o)}-\frac{\mu 2\,(-3\,\eta 0+\mu 2)\,\mathrm{Cos}[P\,z\,\gamma\,\mu 2o]}{6\,\eta 0\,(\mu 2-\mu 2o)\,(\mu 2+\mu 2o)}-$$

$$\frac{(3\,\eta 0+\mu 2)\,\mathrm{Cos}[P\,z\,\gamma\,\mu 2o]}{4\,\eta 0\,(\mu 2-\mu 2o)\,(\mu 2+\mu 2o)}+\frac{(1+2\,\eta 0)\,(4+3\,\eta 0)\,(3\,\eta 0+\mu 2)\,\mathrm{Cos}[P\,z\,\gamma\,\mu 2o]}{4\,\eta 0\,\mu 2\,(\mu 2-\mu 2o)\,(\mu 2+\mu 2o)}-$$

$$\frac{\mu 2\,(3\,\eta 0+\mu 2)\,\mathrm{Cos}[P\,z\,\gamma\,\mu 2o]}{6\,\eta 0\,(\mu 2-\mu 2o)\,(\mu 2+\mu 2o)}+\frac{3\,i\,(4+3\,\eta 0)\,\mathrm{Sin}[P\,z\,\gamma\,\mu 2o]}{2\,(\mu 0-\mu 2o)\,\mu 2o\,(\mu 0+\mu 2o)}-\frac{i\,\mu 2o\,\mathrm{Sin}[P\,z\,\gamma\,\mu 2o]}{2\,\eta 0\,(\mu 0-\mu 2o)\,(\mu 0+\mu 2o)}-$$

$$\frac{i\,(-4-3\,\eta 0)\,(1+2\,\eta 0)\,(-3\,\eta 0+\mu 2)\,\mathrm{Sin}[P\,z\,\gamma\,\mu 2o]}{4\,\eta 0\,(\mu 2-\mu 2o)\,\mu 2o\,(\mu 2+\mu 2o)}-\frac{i\,\mu 2\,(-3\,\eta 0+\mu 2)\,\mathrm{Sin}[P\,z\,\gamma\,\mu 2o]}{2\,(\mu 2-\mu 2o)\,\mu 2o\,(\mu 2+\mu 2o)}+$$

$$\frac{i\,(-4-3\,\eta 0)\,(1+2\,\eta 0)\,(3\,\eta 0+\mu 2)\,\mathrm{Sin}[P\,z\,\gamma\,\mu 2o]}{4\,\eta 0\,(\mu 2-\mu 2o)\,\mu 2o\,(\mu 2+\mu 2o)}-\frac{i\,\mu 2\,(3\,\eta 0+\mu 2)\,\mathrm{Sin}[P\,z\,\gamma\,\mu 2o]}{2\,(\mu 2-\mu 2o)\,\mu 2o\,(\mu 2+\mu 2o)}-$$

$$\frac{i\,(-3\,\eta 0+\mu 2)\,\mu 2o\,\mathrm{Sin}[P\,z\,\gamma\,\mu 2o]}{6\,\eta 0\,(\mu 2-\mu 2o)\,(\mu 2+\mu 2o)}+\frac{i\,(1+2\,\eta 0)\,(-3\,\eta 0+\mu 2)\,\mu 2o\,\mathrm{Sin}[P\,z\,\gamma\,\mu 2o]}{4\,\eta 0\,\mu 2\,(\mu 2-\mu 2o)\,(\mu 2+\mu 2o)}+$$

$$\left.\frac{i\,(3\,\eta 0+\mu 2)\,\mu 2o\,\mathrm{Sin}[P\,z\,\gamma\,\mu 2o]}{6\,\eta 0\,(\mu 2-\mu 2o)\,(\mu 2+\mu 2o)}+\frac{i\,(1+2\,\eta 0)\,(3\,\eta 0+\mu 2)\,\mu 2o\,\mathrm{Sin}[P\,z\,\gamma\,\mu 2o]}{4\,\eta 0\,\mu 2\,(\mu 2-\mu 2o)\,(\mu 2+\mu 2o)}\right)\;/.$$

$$\{\eta 0\to -1-F0,\ \mu 0\to (3-2\,F0+F0\hat{}2)\,\hat{}\,(1/2),\ \mu 2\to (3+6\,F0+9\,F0\hat{}2)\,\hat{}\,(1/2),$$

$$\mu 2o\to(-3+6\,F0+9\,F0\hat{}2)\,\hat{}\,(1/2)\}]\ (*b_{32}*)$$

Out[ ]=

$$-\frac{i\left(\frac{\mathrm{Sin}\left[\sqrt{3+(-2+F0)\,F0}\;P\,z\,\gamma\right]}{\sqrt{3+(-2+F0)\,F0}}+\frac{2\,(1+F0)\,\mathrm{Sin}\left[\sqrt{-3+6\,F0+9\,F0^2}\;P\,z\,\gamma\right]}{\sqrt{-3+6\,F0+9\,F0^2}}+\frac{(1+2\,F0)\,\mathrm{Sin}\left[\sqrt{3+6\,F0+9\,F0^2}\;P\,z\,\gamma\right]}{\sqrt{3+6\,F0+9\,F0^2}}\right)}{2\,(1+F0)}$$

$$
\begin{aligned}
&\textbf{Bm2inhomobm2 = FullSimplify}\Big[\\
&\Big(-\frac{3\,e^{-i P z \gamma \mu0}\left(4+3\,\eta0\right)}{4\,\mu0\left(\mu0-\mu2o\right)\left(\mu0+\mu2o\right)}+\frac{3\,e^{i P z \gamma \mu0}\left(4+3\,\eta0\right)}{4\,\mu0\left(\mu0-\mu2o\right)\left(\mu0+\mu2o\right)}+\frac{e^{-i P z \gamma \mu0}\,\mu0}{4\,\eta0\left(\mu0-\mu2o\right)\left(\mu0+\mu2o\right)}-\\
&\frac{e^{i P z \gamma \mu0}\,\mu0}{4\,\eta0\left(\mu0-\mu2o\right)\left(\mu0+\mu2o\right)}+\frac{e^{i P z \gamma \mu2}\left(-3\,\eta0+\mu2\right)}{4\,\eta0\left(\mu2-\mu2o\right)\left(\mu2+\mu2o\right)}+\\
&\frac{e^{i P z \gamma \mu2}\left(-4-3\,\eta0\right)\left(1+2\,\eta0\right)\left(-3\,\eta0+\mu2\right)}{4\,\eta0\,\mu2\left(\mu2-\mu2o\right)\left(\mu2+\mu2o\right)}+\frac{e^{i P z \gamma \mu2}\,\mu2\left(-3\,\eta0+\mu2\right)}{6\,\eta0\left(\mu2-\mu2o\right)\left(\mu2+\mu2o\right)}-\\
&\frac{e^{-i P z \gamma \mu2}\left(3\,\eta0+\mu2\right)}{4\,\eta0\left(\mu2-\mu2o\right)\left(\mu2+\mu2o\right)}+\frac{e^{-i P z \gamma \mu2}\left(-4-3\,\eta0\right)\left(1+2\,\eta0\right)\left(3\,\eta0+\mu2\right)}{4\,\eta0\,\mu2\left(\mu2-\mu2o\right)\left(\mu2+\mu2o\right)}+\\
&\frac{e^{-i P z \gamma \mu2}\,\mu2\left(3\,\eta0+\mu2\right)}{6\,\eta0\left(\mu2-\mu2o\right)\left(\mu2+\mu2o\right)}-\frac{\left(-3\,\eta0+\mu2\right)\text{Cos}[P\,z\,\gamma\,\mu2o]}{4\,\eta0\left(\mu2-\mu2o\right)\left(\mu2+\mu2o\right)}+\\
&\frac{\left(1+2\,\eta0\right)\left(4+3\,\eta0\right)\left(-3\,\eta0+\mu2\right)\text{Cos}[P\,z\,\gamma\,\mu2o]}{4\,\eta0\,\mu2\left(\mu2-\mu2o\right)\left(\mu2+\mu2o\right)}-\frac{\mu2\left(-3\,\eta0+\mu2\right)\text{Cos}[P\,z\,\gamma\,\mu2o]}{6\,\eta0\left(\mu2-\mu2o\right)\left(\mu2+\mu2o\right)}+\\
&\frac{\left(3\,\eta0+\mu2\right)\text{Cos}[P\,z\,\gamma\,\mu2o]}{4\,\eta0\left(\mu2-\mu2o\right)\left(\mu2+\mu2o\right)}+\frac{\left(1+2\,\eta0\right)\left(4+3\,\eta0\right)\left(3\,\eta0+\mu2\right)\text{Cos}[P\,z\,\gamma\,\mu2o]}{4\,\eta0\,\mu2\left(\mu2-\mu2o\right)\left(\mu2+\mu2o\right)}-\\
&\frac{\mu2\left(3\,\eta0+\mu2\right)\text{Cos}[P\,z\,\gamma\,\mu2o]}{6\,\eta0\left(\mu2-\mu2o\right)\left(\mu2+\mu2o\right)}-\frac{3\,i\left(4+3\,\eta0\right)\text{Sin}[P\,z\,\gamma\,\mu2o]}{2\left(\mu0-\mu2o\right)\mu2o\left(\mu0+\mu2o\right)}+\frac{i\,\mu2o\,\text{Sin}[P\,z\,\gamma\,\mu2o]}{2\,\eta0\left(\mu0-\mu2o\right)\left(\mu0+\mu2o\right)}-\\
&\frac{i\left(-4-3\,\eta0\right)\left(1+2\,\eta0\right)\left(-3\,\eta0+\mu2\right)\text{Sin}[P\,z\,\gamma\,\mu2o]}{4\,\eta0\left(\mu2-\mu2o\right)\mu2o\left(\mu2+\mu2o\right)}+\frac{i\,\mu2\left(-3\,\eta0+\mu2\right)\text{Sin}[P\,z\,\gamma\,\mu2o]}{2\left(\mu2-\mu2o\right)\mu2o\left(\mu2+\mu2o\right)}+\\
&\frac{i\left(-4-3\,\eta0\right)\left(1+2\,\eta0\right)\left(3\,\eta0+\mu2\right)\text{Sin}[P\,z\,\gamma\,\mu2o]}{4\,\eta0\left(\mu2-\mu2o\right)\mu2o\left(\mu2+\mu2o\right)}+\frac{i\,\mu2\left(3\,\eta0+\mu2\right)\text{Sin}[P\,z\,\gamma\,\mu2o]}{2\left(\mu2-\mu2o\right)\mu2o\left(\mu2+\mu2o\right)}-\\
&\frac{i\left(-3\,\eta0+\mu2\right)\mu2o\,\text{Sin}[P\,z\,\gamma\,\mu2o]}{6\,\eta0\left(\mu2-\mu2o\right)\left(\mu2+\mu2o\right)}-\frac{i\left(1+2\,\eta0\right)\left(-3\,\eta0+\mu2\right)\mu2o\,\text{Sin}[P\,z\,\gamma\,\mu2o]}{4\,\eta0\,\mu2\left(\mu2-\mu2o\right)\left(\mu2+\mu2o\right)}+\\
&\frac{i\left(3\,\eta0+\mu2\right)\mu2o\,\text{Sin}[P\,z\,\gamma\,\mu2o]}{6\,\eta0\left(\mu2-\mu2o\right)\left(\mu2+\mu2o\right)}-\frac{i\left(1+2\,\eta0\right)\left(3\,\eta0+\mu2\right)\mu2o\,\text{Sin}[P\,z\,\gamma\,\mu2o]}{4\,\eta0\,\mu2\left(\mu2-\mu2o\right)\left(\mu2+\mu2o\right)}\Big)\;/.\\
&\{\eta0\to-1-F0,\ \mu0\to\left(3-2\,F0+F0\text{^}2\right)\text{^}\left(1/2\right),\ \mu2\to\left(3+6\,F0+9\,F0\text{^}2\right)\text{^}\left(1/2\right),\\
&\mu2o\to\left(-3+6\,F0+9\,F0\text{^}2\right)\text{^}\left(1/2\right)\}\Big]\ (*b_{31}*)
\end{aligned}
$$

Out[ ]=

$$
\frac{1}{2}\left(\text{Cos}\left[\sqrt{-3+6\,F0+9\,F0^2}\;P\,z\,\gamma\right]-\text{Cos}\left[\sqrt{3+6\,F0+9\,F0^2}\;P\,z\,\gamma\right]+\frac{i\left(\frac{\text{Sin}\left[\sqrt{3+(-2+F0)\,F0}\;P\,z\,\gamma\right]}{\sqrt{3+(-2+F0)\,F0}}+\frac{(1+F0)\,(1+3\,F0)\,\text{Sin}\left[\sqrt{-3+6\,F0+9\,F0^2}\;P\,z\,\gamma\right]}{\sqrt{-3+6\,F0+9\,F0^2}}-\frac{(2+F0\,(4+3\,F0))\,\text{Sin}\left[\sqrt{3+6\,F0+9\,F0^2}\;P\,z\,\gamma\right]}{\sqrt{3+6\,F0+9\,F0^2}}\right)}{1+F0}\right)
$$

$$
\begin{aligned}
&\mathbf{Bm2inhomob2} = \mathbf{FullSimplify}\Big[\\
&\Big(\frac{3\,e^{-i\,P\,z\,\gamma\,\mu 0}\,(4+3\,\eta 0)}{4\,\mu 0\,(\mu 0-\mu 2o)\,(\mu 0+\mu 2o)}-\frac{3\,e^{i\,P\,z\,\gamma\,\mu 0}\,(4+3\,\eta 0)}{4\,\mu 0\,(\mu 0-\mu 2o)\,(\mu 0+\mu 2o)}-\frac{e^{-i\,P\,z\,\gamma\,\mu 0}\,\mu 0}{4\,\eta 0\,(\mu 0-\mu 2o)\,(\mu 0+\mu 2o)}+\\
&\frac{e^{i\,P\,z\,\gamma\,\mu 0}\,\mu 0}{4\,\eta 0\,(\mu 0-\mu 2o)\,(\mu 0+\mu 2o)}-\frac{e^{i\,P\,z\,\gamma\,\mu 2}\,(-3\,\eta 0+\mu 2)}{4\,\eta 0\,(\mu 2-\mu 2o)\,(\mu 2+\mu 2o)}-\\
&\frac{e^{i\,P\,z\,\gamma\,\mu 2}\,(-4-3\,\eta 0)\,(1+2\,\eta 0)\,(-3\,\eta 0+\mu 2)}{4\,\eta 0\,\mu 2\,(\mu 2-\mu 2o)\,(\mu 2+\mu 2o)}-\frac{e^{i\,P\,z\,\gamma\,\mu 2}\,\mu 2\,(-3\,\eta 0+\mu 2)}{6\,\eta 0\,(\mu 2-\mu 2o)\,(\mu 2+\mu 2o)}+\\
&\frac{e^{-i\,P\,z\,\gamma\,\mu 2}\,(3\,\eta 0+\mu 2)}{4\,\eta 0\,(\mu 2-\mu 2o)\,(\mu 2+\mu 2o)}-\frac{e^{-i\,P\,z\,\gamma\,\mu 2}\,(-4-3\,\eta 0)\,(1+2\,\eta 0)\,(3\,\eta 0+\mu 2)}{4\,\eta 0\,\mu 2\,(\mu 2-\mu 2o)\,(\mu 2+\mu 2o)}-\\
&\frac{e^{-i\,P\,z\,\gamma\,\mu 2}\,\mu 2\,(3\,\eta 0+\mu 2)}{6\,\eta 0\,(\mu 2-\mu 2o)\,(\mu 2+\mu 2o)}+\frac{(-3\,\eta 0+\mu 2)\,\mathrm{Cos}[P\,z\,\gamma\,\mu 2o]}{4\,\eta 0\,(\mu 2-\mu 2o)\,(\mu 2+\mu 2o)}+\\
&\frac{(-4-3\,\eta 0)\,(1+2\,\eta 0)\,(-3\,\eta 0+\mu 2)\,\mathrm{Cos}[P\,z\,\gamma\,\mu 2o]}{4\,\eta 0\,\mu 2\,(\mu 2-\mu 2o)\,(\mu 2+\mu 2o)}+\frac{\mu 2\,(-3\,\eta 0+\mu 2)\,\mathrm{Cos}[P\,z\,\gamma\,\mu 2o]}{6\,\eta 0\,(\mu 2-\mu 2o)\,(\mu 2+\mu 2o)}-\\
&\frac{(3\,\eta 0+\mu 2)\,\mathrm{Cos}[P\,z\,\gamma\,\mu 2o]}{4\,\eta 0\,(\mu 2-\mu 2o)\,(\mu 2+\mu 2o)}+\frac{(-4-3\,\eta 0)\,(1+2\,\eta 0)\,(3\,\eta 0+\mu 2)\,\mathrm{Cos}[P\,z\,\gamma\,\mu 2o]}{4\,\eta 0\,\mu 2\,(\mu 2-\mu 2o)\,(\mu 2+\mu 2o)}+\\
&\frac{\mu 2\,(3\,\eta 0+\mu 2)\,\mathrm{Cos}[P\,z\,\gamma\,\mu 2o]}{6\,\eta 0\,(\mu 2-\mu 2o)\,(\mu 2+\mu 2o)}+\frac{3\,i\,(4+3\,\eta 0)\,\mathrm{Sin}[P\,z\,\gamma\,\mu 2o]}{2\,(\mu 0-\mu 2o)\,\mu 2o\,(\mu 0+\mu 2o)}-\frac{i\,\mu 2o\,\mathrm{Sin}[P\,z\,\gamma\,\mu 2o]}{2\,\eta 0\,(\mu 0-\mu 2o)\,(\mu 0+\mu 2o)}+\\
&\frac{i\,(-4-3\,\eta 0)\,(1+2\,\eta 0)\,(-3\,\eta 0+\mu 2)\,\mathrm{Sin}[P\,z\,\gamma\,\mu 2o]}{4\,\eta 0\,(\mu 2-\mu 2o)\,\mu 2o\,(\mu 2+\mu 2o)}-\frac{i\,\mu 2\,(-3\,\eta 0+\mu 2)\,\mathrm{Sin}[P\,z\,\gamma\,\mu 2o]}{2\,(\mu 2-\mu 2o)\,\mu 2o\,(\mu 2+\mu 2o)}-\\
&\frac{i\,(-4-3\,\eta 0)\,(1+2\,\eta 0)\,(3\,\eta 0+\mu 2)\,\mathrm{Sin}[P\,z\,\gamma\,\mu 2o]}{4\,\eta 0\,(\mu 2-\mu 2o)\,\mu 2o\,(\mu 2+\mu 2o)}-\frac{i\,\mu 2\,(3\,\eta 0+\mu 2)\,\mathrm{Sin}[P\,z\,\gamma\,\mu 2o]}{2\,(\mu 2-\mu 2o)\,\mu 2o\,(\mu 2+\mu 2o)}+\\
&\frac{i\,(-3\,\eta 0+\mu 2)\,\mu 2o\,\mathrm{Sin}[P\,z\,\gamma\,\mu 2o]}{6\,\eta 0\,(\mu 2-\mu 2o)\,(\mu 2+\mu 2o)}+\frac{i\,(1+2\,\eta 0)\,(-3\,\eta 0+\mu 2)\,\mu 2o\,\mathrm{Sin}[P\,z\,\gamma\,\mu 2o]}{4\,\eta 0\,\mu 2\,(\mu 2-\mu 2o)\,(\mu 2+\mu 2o)}-\\
&\frac{i\,(3\,\eta 0+\mu 2)\,\mu 2o\,\mathrm{Sin}[P\,z\,\gamma\,\mu 2o]}{6\,\eta 0\,(\mu 2-\mu 2o)\,(\mu 2+\mu 2o)}+\frac{i\,(1+2\,\eta 0)\,(3\,\eta 0+\mu 2)\,\mu 2o\,\mathrm{Sin}[P\,z\,\gamma\,\mu 2o]}{4\,\eta 0\,\mu 2\,(\mu 2-\mu 2o)\,(\mu 2+\mu 2o)}\Big)\;/.\\
&\{\eta 0\to -1-\mathrm{F0},\ \mu 0\to (3-2\,\mathrm{F0}+\mathrm{F0}\hat{}2)\hat{}(1/2),\ \mu 2\to (3+6\,\mathrm{F0}+9\,\mathrm{F0}\hat{}2)\hat{}(1/2),\\
&\mu 2o\to (-3+6\,\mathrm{F0}+9\,\mathrm{F0}\hat{}2)\hat{}(1/2)\}\Big]\ (*b_{33}*)
\end{aligned}
$$

Out[∘]=

$$
\frac{1}{2}\left(-\mathrm{Cos}\Big[\sqrt{-3+6\,\mathrm{F0}+9\,\mathrm{F0}^2}\;P\,z\,\gamma\Big]+\mathrm{Cos}\Big[\sqrt{3+6\,\mathrm{F0}+9\,\mathrm{F0}^2}\;P\,z\,\gamma\Big]-\frac{i\left(\frac{\mathrm{Sin}\left[\sqrt{3+(-2+\mathrm{F0})\,\mathrm{F0}}\;P\,z\,\gamma\right]}{\sqrt{3+(-2+\mathrm{F0})\,\mathrm{F0}}}+\frac{(1+\mathrm{F0})\,(1+3\,\mathrm{F0})\,\mathrm{Sin}\left[\sqrt{-3+6\,\mathrm{F0}+9\,\mathrm{F0}^2}\;P\,z\,\gamma\right]}{\sqrt{-3+6\,\mathrm{F0}+9\,\mathrm{F0}^2}}-\frac{(2+\mathrm{F0}\,(4+3\,\mathrm{F0}))\,\mathrm{Sin}\left[\sqrt{3+6\,\mathrm{F0}+9\,\mathrm{F0}^2}\;P\,z\,\gamma\right]}{\sqrt{3+6\,\mathrm{F0}+9\,\mathrm{F0}^2}}\right)}{1+\mathrm{F0}}\right)
$$

$$
\begin{aligned}
&\mathbf{Bm2inhomob2c = FullSimplify}\Big[\\
&\Big(-\frac{3\, e^{-i P z \gamma \mu 0}\, (4+3\,\eta 0)}{4\,\mu 0\,(\mu 0-\mu 2o)\,(\mu 0+\mu 2o)}+\frac{3\, e^{i P z \gamma \mu 0}\, (4+3\,\eta 0)}{4\,\mu 0\,(\mu 0-\mu 2o)\,(\mu 0+\mu 2o)}+\frac{e^{-i P z \gamma \mu 0}\,\mu 0}{4\,\eta 0\,(\mu 0-\mu 2o)\,(\mu 0+\mu 2o)}-\\
&\frac{e^{i P z \gamma \mu 0}\,\mu 0}{4\,\eta 0\,(\mu 0-\mu 2o)\,(\mu 0+\mu 2o)}+\frac{e^{i P z \gamma \mu 2}\,(-3\,\eta 0+\mu 2)}{4\,\eta 0\,(\mu 2-\mu 2o)\,(\mu 2+\mu 2o)}-\\
&\frac{e^{i P z \gamma \mu 2}\,(-4-3\,\eta 0)\,(1+2\,\eta 0)\,(-3\,\eta 0+\mu 2)}{4\,\eta 0\,\mu 2\,(\mu 2-\mu 2o)\,(\mu 2+\mu 2o)}-\frac{e^{i P z \gamma \mu 2}\,\mu 2\,(-3\,\eta 0+\mu 2)}{6\,\eta 0\,(\mu 2-\mu 2o)\,(\mu 2+\mu 2o)}-\\
&\frac{e^{-i P z \gamma \mu 2}\,(3\,\eta 0+\mu 2)}{4\,\eta 0\,(\mu 2-\mu 2o)\,(\mu 2+\mu 2o)}-\frac{e^{-i P z \gamma \mu 2}\,(-4-3\,\eta 0)\,(1+2\,\eta 0)\,(3\,\eta 0+\mu 2)}{4\,\eta 0\,\mu 2\,(\mu 2-\mu 2o)\,(\mu 2+\mu 2o)}-\\
&\frac{e^{-i P z \gamma \mu 2}\,\mu 2\,(3\,\eta 0+\mu 2)}{6\,\eta 0\,(\mu 2-\mu 2o)\,(\mu 2+\mu 2o)}-\frac{(-3\,\eta 0+\mu 2)\,\mathrm{Cos}[P\,z\,\gamma\,\mu 2o]}{4\,\eta 0\,(\mu 2-\mu 2o)\,(\mu 2+\mu 2o)}+\\
&\frac{(-4-3\,\eta 0)\,(1+2\,\eta 0)\,(-3\,\eta 0+\mu 2)\,\mathrm{Cos}[P\,z\,\gamma\,\mu 2o]}{4\,\eta 0\,\mu 2\,(\mu 2-\mu 2o)\,(\mu 2+\mu 2o)}+\frac{\mu 2\,(-3\,\eta 0+\mu 2)\,\mathrm{Cos}[P\,z\,\gamma\,\mu 2o]}{6\,\eta 0\,(\mu 2-\mu 2o)\,(\mu 2+\mu 2o)}+\\
&\frac{(3\,\eta 0+\mu 2)\,\mathrm{Cos}[P\,z\,\gamma\,\mu 2o]}{4\,\eta 0\,(\mu 2-\mu 2o)\,(\mu 2+\mu 2o)}+\frac{(-4-3\,\eta 0)\,(1+2\,\eta 0)\,(3\,\eta 0+\mu 2)\,\mathrm{Cos}[P\,z\,\gamma\,\mu 2o]}{4\,\eta 0\,\mu 2\,(\mu 2-\mu 2o)\,(\mu 2+\mu 2o)}+\\
&\frac{\mu 2\,(3\,\eta 0+\mu 2)\,\mathrm{Cos}[P\,z\,\gamma\,\mu 2o]}{6\,\eta 0\,(\mu 2-\mu 2o)\,(\mu 2+\mu 2o)}-\frac{3\,i\,(4+3\,\eta 0)\,\mathrm{Sin}[P\,z\,\gamma\,\mu 2o]}{2\,(\mu 0-\mu 2o)\,\mu 2o\,(\mu 0+\mu 2o)}+\frac{i\,\mu 2o\,\mathrm{Sin}[P\,z\,\gamma\,\mu 2o]}{2\,\eta 0\,(\mu 0-\mu 2o)\,(\mu 0+\mu 2o)}+\\
&\frac{i\,(-4-3\,\eta 0)\,(1+2\,\eta 0)\,(-3\,\eta 0+\mu 2)\,\mathrm{Sin}[P\,z\,\gamma\,\mu 2o]}{4\,\eta 0\,(\mu 2-\mu 2o)\,\mu 2o\,(\mu 2+\mu 2o)}+\frac{i\,\mu 2\,(-3\,\eta 0+\mu 2)\,\mathrm{Sin}[P\,z\,\gamma\,\mu 2o]}{2\,(\mu 2-\mu 2o)\,\mu 2o\,(\mu 2+\mu 2o)}-\\
&\frac{i\,(-4-3\,\eta 0)\,(1+2\,\eta 0)\,(3\,\eta 0+\mu 2)\,\mathrm{Sin}[P\,z\,\gamma\,\mu 2o]}{4\,\eta 0\,(\mu 2-\mu 2o)\,\mu 2o\,(\mu 2+\mu 2o)}+\frac{i\,\mu 2\,(3\,\eta 0+\mu 2)\,\mathrm{Sin}[P\,z\,\gamma\,\mu 2o]}{2\,(\mu 2-\mu 2o)\,\mu 2o\,(\mu 2+\mu 2o)}+\\
&\frac{i\,(-3\,\eta 0+\mu 2)\,\mu 2o\,\mathrm{Sin}[P\,z\,\gamma\,\mu 2o]}{6\,\eta 0\,(\mu 2-\mu 2o)\,(\mu 2+\mu 2o)}-\frac{i\,(1+2\,\eta 0)\,(-3\,\eta 0+\mu 2)\,\mu 2o\,\mathrm{Sin}[P\,z\,\gamma\,\mu 2o]}{4\,\eta 0\,\mu 2\,(\mu 2-\mu 2o)\,(\mu 2+\mu 2o)}-\\
&\frac{i\,(3\,\eta 0+\mu 2)\,\mu 2o\,\mathrm{Sin}[P\,z\,\gamma\,\mu 2o]}{6\,\eta 0\,(\mu 2-\mu 2o)\,(\mu 2+\mu 2o)}-\frac{i\,(1+2\,\eta 0)\,(3\,\eta 0+\mu 2)\,\mu 2o\,\mathrm{Sin}[P\,z\,\gamma\,\mu 2o]}{4\,\eta 0\,\mu 2\,(\mu 2-\mu 2o)\,(\mu 2+\mu 2o)}\Big)\ /.\\
&\{\eta 0\to -1-F0,\ \mu 0\to (3-2\,F0+F0\,\hat{}\,2)\,\hat{}\,(1/2),\ \mu 2\to (3+6\,F0+9\,F0\,\hat{}\,2)\,\hat{}\,(1/2),\\
&\mu 2o\to (-3+6\,F0+9\,F0\,\hat{}\,2)\,\hat{}\,(1/2)\}\Big]\ (*b_{34}*)
\end{aligned}
$$

Out[∘]=

$$
\frac{i\left(\frac{\mathrm{Sin}\left[\sqrt{3+(-2+F0)\,F0}\;P\,z\,\gamma\right]}{\sqrt{3+(-2+F0)\,F0}}+\frac{2\,(1+F0)\,\mathrm{Sin}\left[\sqrt{-3+6\,F0+9\,F0^{2}}\;P\,z\,\gamma\right]}{\sqrt{-3+6\,F0+9\,F0^{2}}}+\frac{(1+2\,F0)\,\mathrm{Sin}\left[\sqrt{3+6\,F0+9\,F0^{2}}\;P\,z\,\gamma\right]}{\sqrt{3+6\,F0+9\,F0^{2}}}\right)}{2\,(1+F0)}
$$

Appendix E

MATLAB Code to Simulate Input and Output Spectrum of a HNLF

[1]

```
clc
close all
clear all

%% Propagation of a PIA input through a nonlinear fiber considering upto
%second order dispersive effects. The equations are solved in the group
%velocity reference frame of the pulse

%% parameters (default values)

c=299792458;                %(299792458)speed of light in vacuum(m/s)
n=2^17;                     %(2^17)number of sampling points
lsig=1547.0e-9;             %(1547.0e-9)wavelength of signal(m)
lpump=1552.5e-9;            %(1552.5e-9)wavelength of pump(m)
fsig=c/lsig;                %frequency of signal(Hz)
fpump=c/lpump;              %frequency of pump(Hz)
ps_frq_sep=abs(fsig-fpump);%pump-signal frequency separation(Hz)
fspan=6;                    %varies span of Fourier domain
dt=1/(2^fspan*ps_frq_sep);%spacing in time domain(s)
T_tot=n*dt;                 %total time in the time domain(s)
t=(-(n/2):1:(n/2)-1)*dt;%vector of time points
f=(-(n/2):1:(n/2)-1)/T_tot;%vector of frequency points
om=(-(n/2):1:(n/2)-1)*2*pi/T_tot;%vector of angular frequency points
P_s_dbm=-1;                 %(-1)input power of signal(dBm)
P_s=1.0e-3*10^(P_s_dbm/10);%input power of signal(W)
As=sqrt(P_s);               %input amplitude of signal(W^0.5)
P_p_dbm=20;                 %(20)input power of pump(dBm)
P_p=1.0e-3*10^(P_p_dbm/10);%input power of pump(W)
Ap=sqrt(P_p);               %input amplitude of pump(V/m)
```

---

[1] MATLAB Version 2015a was used for this code.

```
lc=lpump;                 %we consider the pump wavelength as central
lzdw=1547.0e-9;           %(1547.0e-9)zero dispersion wavelength(m)
z=2*1.e3;                 %(1.0e3)length of the fiber(m)
dz=1.0e1;                 %(10)step size along the fiber(m)
gamma=11.3e-3;            %(11.3e-3)nonlinear coefficient of fiber(1/(W.km))
loff=lc-lzdw;          %offset of the central wavelength(m)
D1=17.0;                  %(17)dispersion slope of the fiber(s/m^3)
D=D1*loff;                %dispersion of the fiber(s/m^2)
beta2=-lc^2*D/(2*pi*c);   %second order dispersion parameter(s^2/m)
proplen=0;                %initialization of propagation length

%% definition of input electric field without the carrier

Ein=Ap+As*exp(1i*2*pi*ps_frq_sep*t);

%% Inversion of vectors for DFT

Ein_inv(1:n/2)=Ein((n/2)+1:n);  %shift of vector for DFT
Ein_inv((n/2)+1:n)=Ein(1:n/2);  %shift of vector for DFT

om_inv_sq(1:n/2)=om((n/2)+1:n).^2;%shift of vector for DFT
om_inv_sq((n/2)+1:n)=om(1:n/2).^2;%shift of vector for DFT

freal=(-1)*f+fpump;       %real frequency vector adding the carrier
lamvec=c./freal;          %real wavelength vector

%% Propagation of field

Einput=(fftshift(abs(ifft(Ein_inv))));%input field in Fourier domain
Edisp1=(ifft(Ein_inv)); %initial fourier domain field

while proplen<z           %loop on z to propagate field
    Edisp1=Edisp1.*exp(1i*(beta2/2)*om_inv_sq*dz/2);%linear propagation
    Enonl=fft(Edisp1);    %moving to time domain
    Enonl=Enonl.*exp(1i*gamma*abs(Enonl).^2*dz);%nonlinear propagation
    Edisp2=ifft(Enonl);   %moving to Fourier domain
    Edisp2=Edisp2.*exp(1i*(beta2/2)*om_inv_sq*dz/2);%linear propagation
    Edisp1=Edisp2;
    proplen=proplen+dz;   %length increment
end

%% Plotting of field

Einplot=10.*log10(1000*Einput.^2);%Watts to dBm of input field
Eoutplot=10.*log10(1000*(fftshift(abs(Edisp1))).^2);
                          %Watts to dBm of output field

f1=figure('name','Input and output power spectrum');
```

```
hold on

fig1(1)=plot(lamvec*1.0e9,Eoutplot,'r','LineWidth',1.5);%plot of output field
fig1(2)=plot(lamvec*1.0e9,Einplot,'b','LineWidth',1.5);%plot of input field

set(gca,'yLim',[-25, 25],...
'FontName','Times New Roman',...
'FontSize',12.0,'FontWeight','normal');
grid on;
xlabel(['Wavelength, \lambda',' (m)'],...
'FontName','Times New Roman','FontSize',18.0,'FontWeight','Normal');
ylabel(['Optical power',' (dBm)'],...
'FontName','Times New Roman','FontSize',18.0,'FontWeight','Normal');
title('Input and output optical power spectrum for PIA (simulation)', ...
'FontName','Times New Roman','FontSize',18.0,'FontWeight','Normal');
legend([fig1(1),fig1(2)],{'Input spectrum';...
'Output spectrum'},'FontName','Times New Roman',...
'FontSize',16,'FontWeight','Normal',...
'Location','Northeast');
saveas(f1,'iospectrum.png');%saves the figure
hold off
```

Appendix F

Optical Power in an Electromagnetic Field

In this appendix we calculate the optical power in an electromagnetic field consisting of (a) one frequency (Subsection F.1) and (b) three frequencies (Subsection F.2). In both the cases we will also find out the power detected by a photodetector (PD) when these waves are incident on it. Note that a PD cannot detect frequencies of the order of few hundreds of THz, which correspond to typical optical frequencies [242].

F.1 One Erequency

- **Field** :

  Let us consider the general case of an electromagnetic field of angular frequency ω and wave-vector $\vec{k}$. We can write the electric $\vec{E}$ and magnetic $\vec{H}$ fields in such an electromagnetic wave as :

  $$\vec{E} = \vec{\mathcal{E}}\, e^{-i(\omega t - \vec{k}.\vec{r})} + c.c.\ , \tag{F.1}$$

  $$\vec{H} = \vec{\mathcal{H}}\, e^{-i(\omega t - \vec{k}.\vec{r})} + c.c.\ , \tag{F.2}$$

  where $\vec{\mathcal{E}}$ and $\vec{\mathcal{H}}$ are the complex electric and magnetic field amplitudes and *c.c.* means complex conjugate.

- **Poynting Vector** :

  In order to find the optical power, first we need to calculate the Poynting vector

$\vec{S}$ of the field, which represents the directional energy flux of an electromagnetic wave. In vacuum, it is given by :

$$\begin{aligned}\vec{S} =&\vec{E} \times \vec{H} \\ =&(\vec{\mathcal{E}}\ e^{-i(\omega t-\vec{k}.\vec{r})} + c.c.) \times (\vec{\mathcal{H}}\ e^{-i(\omega t-\vec{k}.\vec{r})} + c.c.) \\ =&(\vec{\mathcal{E}} \times \vec{\mathcal{H}}\ e^{-2i(\omega t-\vec{k}.\vec{r})} + c.c.) + (\vec{\mathcal{E}} \times \vec{\mathcal{H}}^* + c.c.)\ .\end{aligned} \tag{F.3}$$

Since in a real experiment we are limited by the response time of the detector, thus we need to take the time average of $\vec{S}$ to account for the terms that oscillate with high frequencies and hence are not detected by the detector. Thus we get $\langle\vec{S}\rangle$ as :

$$\begin{aligned}\langle\vec{S}\rangle =&\langle\vec{\mathcal{E}} \times \vec{\mathcal{H}}\ e^{-2i(\omega t-\vec{k}.\vec{r})} + c.c.\rangle + \langle\vec{\mathcal{E}} \times \vec{\mathcal{H}}^* + c.c.\rangle \\ =&\ \vec{\mathcal{E}} \times \vec{\mathcal{H}}\ .0 + (\vec{\mathcal{E}} \times \vec{\mathcal{H}}^* + c.c.) \\ =&\ \vec{\mathcal{E}} \times \vec{\mathcal{H}}^* + c.c.\ .\end{aligned} \tag{F.4}$$

Here we have used the fact that the time average of a cosine function over large number of cycles is 0. We also know from electromagnetism that $\vec{k} \times \vec{\mathcal{E}} = \omega\mu_0\vec{\mathcal{H}}$, where μ_0 is the magnetic permeability of vacuum. Thus we can rewrite the time-averaged Poynting vector $\langle\vec{S}\rangle$ as :

$$\begin{aligned}\langle\vec{S}\rangle =&\vec{\mathcal{E}} \times \left(\frac{1}{\omega\mu_0}\vec{k} \times \vec{\mathcal{E}}\right)^* + c.c. \\ =&\frac{1}{\omega\mu_0}\vec{\mathcal{E}} \times (\vec{k} \times \vec{\mathcal{E}}^*) + c.c. \\ =&\frac{1}{\omega\mu_0}\left(\vec{k}(\vec{\mathcal{E}}.\vec{\mathcal{E}}^* - \vec{\mathcal{E}}^*(\vec{k}.\vec{\mathcal{E}}))\right) + c.c. \\ =&\frac{\vec{k}(\vec{\mathcal{E}}.\vec{\mathcal{E}}^*)}{\omega\mu_0} + c.c.\ ,\end{aligned} \tag{F.5}$$

where we have used the fact that $\vec{k}$ is a vector with real components and thus $\vec{k} = \vec{k}^*$. Also, since we know $\vec{k}$, $\vec{\mathcal{E}}$ and $\vec{\mathcal{H}}$ are mutually perpendicular to each other, thus $\vec{k}.\vec{\mathcal{E}} = 0$. Without loss of generality, we consider $\vec{k} = k\hat{z}$ and $\vec{\mathcal{E}} = \mathcal{E}\hat{x}$. Then we can write :

$$\langle\vec{S}\rangle =\frac{2k|\mathcal{E}|^2}{\omega\mu_0}\hat{z} = \frac{2|\mathcal{E}|^2}{c\mu_0}\hat{z} = 2c\epsilon_0|\mathcal{E}|^2\hat{z}\ , \tag{F.6}$$

where ϵ_0 is the dielectric permittivity of vacuum. c is the speed of light in vacuum. Here we have also used, $c = \frac{\omega}{k} = \frac{1}{\sqrt{\epsilon_0\mu_0}}$.

- **Detected Optical Power** :

The detected optical power P_{opt} is the average energy that is incident on the PD per unit time. We know, that the norm of the time-averaged Poynting vector

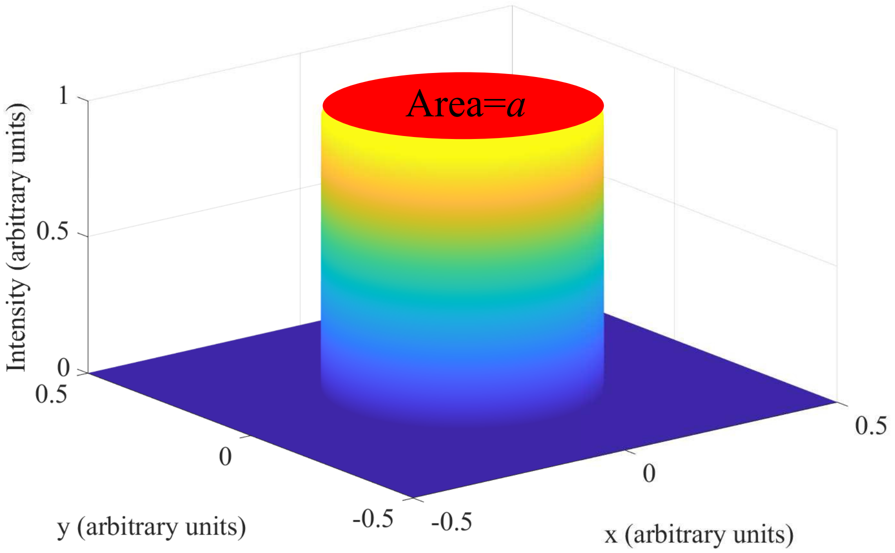

Figure F.1. Illustration of a beam profile of a so-called top-hat beam, with arbitrary units. The beam is propagating in the z-direction. a is shown as the beam cross-section. (not to scale)

$||\langle\vec{S}\rangle||$ is the total energy that is incident per unit time, per unit area of the detector. Thus to compute the total optical power, we just need to integrate $||\langle\vec{S}\rangle||$ over the beam cross-section. For the sake of simplicity, we considered a beam profile which is a box-function i.e. constant over the beam cross-section and 0 everywhere else (see Fig. F.1). Thus P_{opt} is expressed as :

$$P_{opt} = \int\limits_{x,y=-\infty}^{\infty} ||\langle\vec{S}\rangle||dxdy = a2\epsilon_0 c|\mathcal{E}|^2 \,, \tag{F.7}$$

where a is the total beam cross-section.

F.2 Three Frequencies

- **Field** :

  When we have a field with three different optical frequencies ω_1, ω_2 and ω_3, propagating along the direction of $\vec{r}$, as the previous case, we can write our electric and magnetic fields as :

$$\vec{E} = \vec{\mathcal{E}}_1\, e^{-i(\omega_1 t - \vec{k}_1.\vec{r})} + \vec{\mathcal{E}}_2\, e^{-i(\omega_2 t - \vec{k}_2.\vec{r})} + \vec{\mathcal{E}}_3\, e^{-i(\omega_3 t - \vec{k}_3.\vec{r})} + c.c.\,, \tag{F.8}$$

$$\vec{H} = \vec{\mathcal{H}}_1\, e^{-i(\omega_1 t - \vec{k}_1.\vec{r})} + \vec{\mathcal{H}}_2\, e^{-i(\omega_2 t - \vec{k}_2.\vec{r})} + \vec{\mathcal{H}}_3\, e^{-i(\omega_3 t - \vec{k}_3.\vec{r})} + c.c.\,, \tag{F.9}$$

where the indices correspond to the respective frequencies (see Fig. F.2). Without loss of generality, we consider the z-direction as the propagation direction

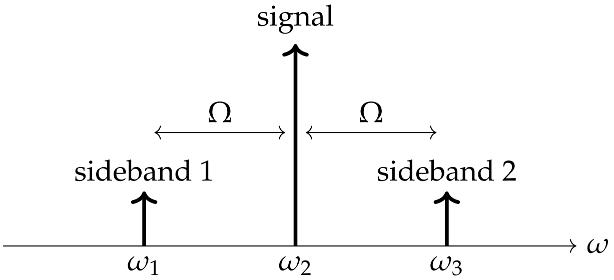

Figure F.2. The three optical frequencies are denoted by ω_1, ω_2 and ω_3 which correspond to the signal and two sidebands. The difference between the consecutive frequencies are Ω. (not to scale)

of the beam. Thus we have :

$$\vec{k}.\vec{r} = (k\hat{z}).(z\hat{z}) = kz \ . \tag{F.10}$$

- **Poynting Vector** :

  As discussed in the previous case, the Poynting vector $\vec{S}$ can be written as :

$$\begin{aligned}
\vec{S} &= \vec{E} \times \vec{H} \\
&= (\vec{\mathcal{E}}_1 \times \vec{\mathcal{H}}_1^{\,*} + c.c.) + (\vec{\mathcal{E}}_2 \times \vec{\mathcal{H}}_2^{\,*} + c.c.) + (\vec{\mathcal{E}}_3 \times \vec{\mathcal{H}}_3^{\,*} + c.c.) \\
&+ (\vec{\mathcal{E}}_1 \times \vec{\mathcal{H}}_2^{\,*}\ e^{-i(\omega_1 t - k_1 z)+i(\omega_2 t - k_2 z)} + c.c.) + (\vec{\mathcal{E}}_1 \times \vec{\mathcal{H}}_3^{\,*}\ e^{-i(\omega_1 t - k_1 z)+i(\omega_3 t - k_3 z)} + c.c.) \\
&+ (\vec{\mathcal{E}}_2 \times \vec{\mathcal{H}}_1^{\,*}\ e^{-i(\omega_2 t - k_2 z)+i(\omega_1 t - k_1 z)} + c.c.) + (\vec{\mathcal{E}}_2 \times \vec{\mathcal{H}}_3^{\,*}\ e^{-i(\omega_2 t - k_2 z)+i(\omega_3 t - k_3 z)} + c.c.) \\
&+ (\vec{\mathcal{E}}_3 \times \vec{\mathcal{H}}_1^{\,*}\ e^{-i(\omega_3 t - k_3 z)+i(\omega_1 t - k_1 z)} + c.c.) + (\vec{\mathcal{E}}_3 \times \vec{\mathcal{H}}_2^{\,*}\ e^{-i(\omega_3 t - k_3 z)+i(\omega_2 t - k_2 z)} + c.c.) \\
&+ (\vec{\mathcal{E}}_1 \times \vec{\mathcal{H}}_1\ e^{-2i(\omega_1 t - k_1 z)} + c.c.) + (\vec{\mathcal{E}}_2 \times \vec{\mathcal{H}}_2\ e^{-2i(\omega_2 t - k_2 z)} + c.c.) + (\vec{\mathcal{E}}_3 \times \vec{\mathcal{H}}_3\ e^{-2i(\omega_3 t - k_3 z)} + c.c.) \\
&+ (\vec{\mathcal{E}}_1 \times \vec{\mathcal{H}}_2\ e^{-i(\omega_1 t - k_1 z)-i(\omega_2 t - k_2 z)} + c.c.) + (\vec{\mathcal{E}}_1 \times \vec{\mathcal{H}}_3\ e^{-i(\omega_1 t - k_1 z)-i(\omega_3 t - k_3 z)} + c.c.) \\
&+ (\vec{\mathcal{E}}_2 \times \vec{\mathcal{H}}_1\ e^{-i(\omega_2 t - k_2 z)-i(\omega_1 t - k_1 z)} + c.c.) + (\vec{\mathcal{E}}_2 \times \vec{\mathcal{H}}_3\ e^{-i(\omega_2 t - k_2 z)-i(\omega_3 t - k_3 z)} + c.c.) \\
&+ (\vec{\mathcal{E}}_3 \times \vec{\mathcal{H}}_1\ e^{-i(\omega_3 t - k_3 z)-i(\omega_1 t - k_1 z)} + c.c.) + (\vec{\mathcal{E}}_3 \times \vec{\mathcal{H}}_2\ e^{-i(\omega_3 t - k_3 z)-i(\omega_2 t - k_2 z)} + c.c.) \ .
\end{aligned} \tag{F.11}$$

  As we have seen before, if we do a time averaging, then all the terms with frequencies that are of the order of ω_1, ω_2, ω_3 or higher can be approximated to 0 as they oscillate too fast to be detected by the detector. Thus we have :

$$\begin{aligned}
\langle\vec{S}\rangle &= (\vec{\mathcal{E}}_1 \times \vec{\mathcal{H}}_1^{\,*} + c.c.) + (\vec{\mathcal{E}}_2 \times \vec{\mathcal{H}}_2^{\,*} + c.c.) + (\vec{\mathcal{E}}_3 \times \vec{\mathcal{H}}_3^{\,*} + c.c.) \\
&+ (\vec{\mathcal{E}}_1 \times \vec{\mathcal{H}}_2^{\,*}\ e^{-i(\omega_1 t - k_1 z)+i(\omega_2 t - k_2 z)} + c.c.) + (\vec{\mathcal{E}}_1 \times \vec{\mathcal{H}}_3^{\,*}\ e^{-i(\omega_1 t - k_1 z)+i(\omega_3 t - k_3 z)} + c.c.) \\
&+ (\vec{\mathcal{E}}_2 \times \vec{\mathcal{H}}_1^{\,*}\ e^{-i(\omega_2 t - k_2 z)+i(\omega_1 t - k_1 z)} + c.c.) + (\vec{\mathcal{E}}_2 \times \vec{\mathcal{H}}_3^{\,*}\ e^{-i(\omega_2 t - k_2 z)+i(\omega_3 t - k_3 z)} + c.c.) \\
&+ (\vec{\mathcal{E}}_3 \times \vec{\mathcal{H}}_1^{\,*}\ e^{-i(\omega_3 t - k_3 z)+i(\omega_1 t - k_1 z)} + c.c.) + (\vec{\mathcal{E}}_3 \times \vec{\mathcal{H}}_2^{\,*}\ e^{-i(\omega_3 t - k_3 z)+i(\omega_2 t - k_2 z)} + c.c.) \ .
\end{aligned} \tag{F.12}$$

  To simplify this expression, we can evaluate $\vec{\mathcal{E}}_i \times \vec{\mathcal{H}}_j^{\,*}$ (where $i,j = 1,2,3$) as we did in the last section as :

$$\vec{\mathcal{E}}_i \times \vec{\mathcal{H}}_j^{\,*} = \frac{1}{\omega_j\mu_0}\vec{\mathcal{E}}_i \times (\vec{k}_j \times \vec{\mathcal{E}}_j)^* = \frac{\vec{k}_j(\vec{\mathcal{E}}_i.\vec{\mathcal{E}}_j^{\,*}) - \vec{\mathcal{E}}_j^{\,*}(\vec{\mathcal{E}}_i.\vec{k}_j)}{\omega_j\mu_0} = \frac{\vec{k}_j(\vec{\mathcal{E}}_i.\vec{\mathcal{E}}_j^{\,*})}{\omega_j\mu_0} \ . \tag{F.13}$$

Without loss of generality, we consider $\vec{k_j} = k_j\hat{z}$. We can replace $\frac{k_j}{\omega_j\mu_0}$ by $c\epsilon_0$. We also consider all the electric fields are polarized in the x-direction, i.e. $\vec{\mathcal{E}_i} = \mathcal{E}_i\hat{x}$ for $i = 1, 2, 3$. Thus, if $i = j$ we can use the expression of optical power derived in the previous section as :

$$\vec{\mathcal{E}_i} \times \vec{\mathcal{H}_i}^* + c.c. = 2c\epsilon_0|\mathcal{E}_i|^2\hat{z} = \frac{P_{\omega_i}}{a}\hat{z}\,. \tag{F.14}$$

where P_{ω_i} is the part of the optical power of the field that oscillates at a frequency ω_i. a is the beam cross-section. If we have $i \neq j$, then we can write :

$$\begin{aligned}&\vec{\mathcal{E}_i} \times \vec{\mathcal{H}_j}^*\ e^{-i(\omega_i t - k_i z) + i(\omega_j t - k_j z)} + c.c. = c\epsilon_0\ \vec{\mathcal{E}_i}.\vec{\mathcal{E}_j}^*\ e^{-i(\omega_i t - k_i z) + i(\omega_j t - k_j z)}\hat{z} + c.c.\\ &= c\epsilon_0\ \mathcal{E}_i\mathcal{E}_j^*\ e^{-i(\omega_i t - k_i z) + i(\omega_j t - k_j z)}\hat{z} + c.c.\,.\end{aligned} \tag{F.15}$$

Writing $\mathcal{E}_i$ as $\mathcal{E}_i = |\mathcal{E}_i|\ e^{-i\phi_i}$ we have :

$$\begin{aligned}\vec{\mathcal{E}_i} \times \vec{\mathcal{H}_j}^*\ e^{-i(\omega_i t - k_i z) + i(\omega_j t - k_j z)} + c.c. &= c\epsilon_0\ |\mathcal{E}_i||\mathcal{E}_j^*|\ e^{-i(\omega_i t - k_i z) + i(\omega_j t - k_j z) - i(\phi_i - \phi_j)}\hat{z} + c.c.\\ &= 2c\epsilon_0\ |\mathcal{E}_i||\mathcal{E}_j|\ \cos\big(-(\omega_i t - k_i z) + (\omega_j t - k_j z) - (\phi_i - \phi_j)\big)\hat{z}\\ &= \sqrt{P_{\omega_i}P_{\omega_j}}\ \cos\big((\omega_j - \omega_i)t + (k_i - k_j)z + (\phi_j - \phi_i)\big)\\ &= \sqrt{P_{\omega_i}P_{\omega_j}}\ \cos\big(\Omega_{ji}t + \Phi_{ij}(z)\big)\ ,\end{aligned} \tag{F.16}$$

where $\Omega_{ji} = \omega_j - \omega_i$ and $\Phi_{ij}(z) = (k_i - k_j)z + (\phi_j - \phi_i)$. In our case, $\Omega_{21} = \Omega_{32} = \Omega$ and $\Omega_{31} = 2\Omega$. Also note, $\Omega_{ji}t + \Phi_{ij} = -(\Omega_{ij}t + \Phi_{ji})$. Using Equations (F.14) and (F.16), we can write the time-averaged Poynting vector $\langle\vec{S}\rangle$ as :

$$\begin{aligned}\langle\vec{S}\rangle &= \frac{1}{a}(P_{\omega_1} + P_{\omega_2} + P_{\omega_3} + \sqrt{P_{\omega_1}P_{\omega_2}}\ \cos(\Omega_{21}t + \Phi_{12})\\ &+ \sqrt{P_{\omega_1}P_{\omega_3}}\ \cos(\Omega_{31}t + \Phi_{13}) + \sqrt{P_{\omega_2}P_{\omega_1}}\ \cos(\Omega_{12}t + \Phi_{21})\\ &+ \sqrt{P_{\omega_2}P_{\omega_3}}\ \cos(\Omega_{32}t + \Phi_{23}) + \sqrt{P_{\omega_3}P_{\omega_1}}\ \cos(\Omega_{13}t + \Phi_{31})\\ &+ \sqrt{P_{\omega_3}P_{\omega_2}}\ \cos(\Omega_{23}t + \Phi_{32}))\hat{z}\\ &= (P_{\omega_1} + P_{\omega_2} + P_{\omega_3} + 2\sqrt{P_{\omega_1}P_{\omega_2}}\ \cos(\Omega t + \Phi_{12})\\ &+ 2\sqrt{P_{\omega_2}P_{\omega_3}}\ \cos(\Omega t + \Phi_{23}) + 2\sqrt{P_{\omega_1}P_{\omega_3}}\ \cos(2\Omega t + \Phi_{13}))\hat{z}\,.\end{aligned} \tag{F.17}$$

- **Detected Optical Power** :

  The total optical power P_{tot} can be written as :

$$\begin{aligned}P_{tot} = a||\langle\vec{S}\rangle|| &= P_{\omega_1} + P_{\omega_2} + P_{\omega_3} + 2\sqrt{P_{\omega_1}P_{\omega_2}}\ \cos(\Omega t + \Phi_{12})\\ &+ 2\sqrt{P_{\omega_2}P_{\omega_3}}\ \cos(\Omega t + \Phi_{23}) + 2\sqrt{P_{\omega_1}P_{\omega_3}}\ \cos(2\Omega t + \Phi_{13})\,.\end{aligned} \tag{F.18}$$

Here we can see that the part of the detected optical power oscillating at a frequency Ω, i.e. P_Ω is :

$$P_\Omega = 2\sqrt{P_{\omega_1} P_{\omega_2}}\ \cos(\Omega t + \Phi_{12}) + 2\sqrt{P_{\omega_2} P_{\omega_3}}\ \cos(\Omega t + \Phi_{23})\ . \tag{F.19}$$

Appendix G

Properties of Bessel Functions of the First Kind

The Bessel function of the first kind $J_n(x)$ (of order n), is defined as :

$$J_n(x) = \sum_{m=0}^{\infty} \frac{(-1)^m}{m!\Gamma(m+n+1)} \left(\frac{x}{2}\right)^{2m+n}, \tag{G.1}$$

where $\Gamma()$ represents the standard Gamma function defined as :

$$\Gamma(z) = \int_0^{\infty} x^{z-1} e^{-x} dx. \tag{G.2}$$

- **Property 1** :

  We want to evaluate $J_n(-x)$. If we replace x with $-x$ in Equation (G.1), we get :

$$\begin{aligned} J_n(-x) &= \sum_{m=0}^{\infty} \frac{(-1)^m}{m!\Gamma(m+n+1)} \left(\frac{-x}{2}\right)^{2m+n} \\ &= \sum_{m=0}^{\infty} (-1)^{2m+n} \frac{(-1)^m}{m!\Gamma(m+n+1)} \left(\frac{x}{2}\right)^{2m+n} \\ &= (-1)^n J_n(x). \end{aligned} \tag{G.3}$$

- **Property 2** :

  Let us consider n to be a positive integer. Now we want to evaluate $J_{-n}(x)$ in terms of $J_n(x)$. Thus replacing n by $-n$ in Equation (G.1), we get :

$$\begin{aligned} J_{-n}(x) &= \sum_{m=0}^{\infty} \frac{(-1)^m}{m!\Gamma(m-n+1)} \left(\frac{x}{2}\right)^{2m-n} \\ &= \sum_{m=0}^{\infty} \frac{(-1)^m}{m!(m-n)!} \left(\frac{x}{2}\right)^{2m-n}, \end{aligned} \tag{G.4}$$

where we have used the property of the Gamma function :

$$\Gamma(n) = (n-1)!, \tag{G.5}$$

where n is a positive integer. Now, let us make a change of variable as :

$$m' = m - n. \tag{G.6}$$

Thus substituting it in Equation (G.4) we get :

$$\begin{aligned} J_{-n}(x) &= \sum_{m'+n=0}^{\infty} \frac{(-1)^{(m'+n)}}{(m'+n)!m'!}\left(\frac{x}{2}\right)^{2m'+n} \\ &= \sum_{m'=-n}^{-1} \frac{(-1)^{(m'+n)}}{(m'+n)!m'!}\left(\frac{x}{2}\right)^{2m'+n} + \sum_{m'=0}^{\infty} \frac{(-1)^{(m'+n)}}{(m'+n)!m'!}\left(\frac{x}{2}\right)^{2m'+n}. \end{aligned} \tag{G.7}$$

But $m'! = \infty$ for $m' = -n, ..., -1$, so the denominator is infinite for the first set of terms and thus all these terms are zero. We therefore have :

$$\begin{aligned} J_{-n}(x) &= \sum_{m'=0}^{\infty} \frac{(-1)^{(m'+n)}}{(m'+n)!m'!}\left(\frac{x}{2}\right)^{2m'+n} \\ &= \sum_{m'=0}^{\infty} \frac{(-1)^{(m'+n)}}{m'!\Gamma(m'+n+1)}\left(\frac{x}{2}\right)^{2m'+n} \\ &= (-1)^n \sum_{m'=0}^{\infty} \frac{(-1)^{m'}}{m'!\Gamma(m'+n+1)!}\left(\frac{x}{2}\right)^{2m'+n} \\ &= (-1)^n J_n(x). \end{aligned} \tag{G.8}$$

Appendix H

SFDR of a Microwave Photonic Link with PSA

In this appendix we calculate the SFDR's of a microwave photonic link with and without a PSA operating in the unsaturated gain regime. For a better understanding, in Fig. H.1 we show an example of the output power (denoted as y) relationship of the fundamental (blue) and IMD3 (red) RF waves with the input RF power (denoted as x) when the PSA is on (thick solid line) and off (thin solid line) considering a log-log scale. The noise floors for the PSA on (thick dashed line) and off (thin dashed line) cases are shown in green dashed lines. When the PSA is on, the fundamental and IMD3 curves undergo a vertical shift of G_{dB} units from the PSA off case. G_{dB} is the RF gain due to the PSA in dB's. Similarly the noise floor undergoes a vertical shift of aG_{dB} units, where a is a scaling factor used to express the noise floor shift in terms of G_{dB}. The SFDR's for the PSA on and off cases are shown in brown double-sided arrows. The fundamental and IMD3 curves are supposed to have slopes of 1 and 3 following Equations (4.49) and (4.50). The corresponding geometric equations for the different curves are shown in their respective colors.

Let us first consider the case when the PSA is off. The equations for the input and output powers of the fundamentals, IMD3's and the noise floor are given by (in the same order) (see Fig. H.1) :

$$y = x + C_{f,off}, \tag{H.1}$$

$$y = 3x + C_{I,off}, \tag{H.2}$$

$$y = N_{off}, \tag{H.3}$$

where $C_{f,off}$, $C_{I,off}$ and N_{off} are the intercepts for the fundamental, IMD3 and noise floor curves. When the PSA is on, we can write down the equations for the fundamentals, IMD3's and the noise floor as before just adding the extra gain as (in the

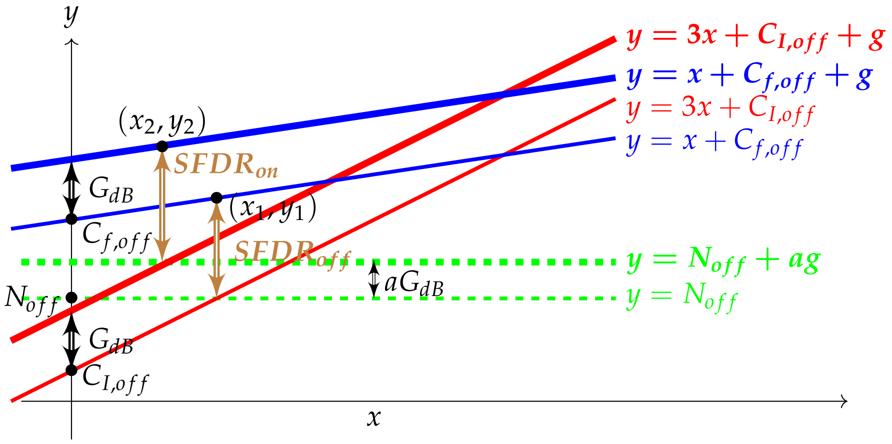

Figure H.1. An illustration of output RF powers (denoted as y in figure) of fundamental (blue solid lines) and IMD3 (red solid lines) in a microwave photonic link with a PSA (with unsaturated gain) as a function of the corresponding input RF powers (denoted as x in figure). A log-log scale is considered. The noise floors are shown in green dashed lines. Two cases are considered : (a) PSA is off (thin lines) and (b) PSA is on (thick lines). The corresponding SFDR's for the PSA on and off cases are shown in brown double sided arrows. The geometric equations of the lines for the fundamentals (slope=1), IMD3's (slope=3) and noise floors (slope=0) are also shown in their corresponding colours. N_{off} : noise floor for PSA off, $C_{I,off}$: intercept of IMD3 for PSA off, $C_{f,off}$: intercept of fundamental for PSA off, G_{dB} : RF gain due to PSA in dB and aG_{dB} : gain of the noise floor in dB's. (not to scale)

same order) (see Fig. H.1) :

$$y = x + C_{f,off} + G_{dB}, \tag{H.4}$$

$$y = 3x + C_{I,off} + G_{dB}, \tag{H.5}$$

$$y = N_{off} + aG_{dB}. \tag{H.6}$$

Let us consider the point (x_1, N_{off}) which is the intersection of the IMD3 curve (see Equation (H.2)) and the noise floor when the PSA is off. Using Equations (H.2) and (H.3) we find :

$$x_1 = \frac{N_{off} - C_{I,off}}{3}. \tag{H.7}$$

Now let us suppose (x_1, y_1) is the point where the line $x = x_1$ intersects the fundamental curve (see Equation (H.1)) for PSA off. Thus using Equation (H.1) we get :

$$y_1 = \frac{N_{off} - C_{I,off}}{3} + C_{f,off}. \tag{H.8}$$

The SFDR for the PSA off case i.e. $SFDR_{off}$ is nothing but the distance between the points (x_1, N_{off}) and (x_1, y_1) and is given by :

$$SFDR_{off} = -\frac{2}{3}N_{off} - \frac{C_{I,off}}{3} + C_{f,off}. \tag{H.9}$$

For the PSA on case, we proceed as before and first consider the point $(x_2, N_{off} + aG_{dB})$ which is the intersection of the IMD3 curve (see Equation (H.5)) with the noise floor (see Equation (H.6)). Thus we get x_2 as :

$$x_2 = \frac{N_{off} - C_{I,off} - aG_{dB}}{3}. \tag{H.10}$$

Now let (x_2, y_2) be the point where the line $x = x_2$ intersects the fundamental curve (see Equation (H.4)) for PSA on. Thus using Equation (H.4) we get :

$$y_2 = \frac{N_{off} - C_{I,off} - aG_{dB}}{3} + C_{f,off} + G_{dB}. \tag{H.11}$$

The SFDR for the PSA on case i.e. $SFDR_{on}$ is nothing but the distance between the points $(x_2, N_{off} + aG_{dB})$ and (x_2, y_2) and is given by :

$$SFDR_{on} = -\frac{2}{3}N_{off} - \frac{C_{I,off}}{3} + C_{f,off} + G_{dB}\left(1 - \frac{4a}{3}\right). \tag{H.12}$$

Therefore we see from Equations (H.9) and (H.12) that the change in the SFDR i.e. $\Delta SFDR$ between the PSA on and off conditions is given by :

$$\Delta SFDR = SFDR_{on} - SFDR_{off} = G_{dB}\left(1 - \frac{4a}{3}\right). \tag{H.13}$$

Thus when a is less than $\frac{3}{4}$, the PSA should increase the SFDR of the link.

In the case of a shot-noise limited signal, the noise floor N_{sh} is given by :

$$N_{sh} = 2ResP_{opt}, \tag{H.14}$$

where R is the impedance of the detection circuit, e is the electronic charge constant, s is the sensitivity of the PD and P_{opt} is the total optical power incident on the PD. We considered 1 Hz bandwidth of detection. Form Equation (4.16) we know that the gain of the optical waves is half the RF gain G_{dB}. Thus when the PSA is off or on, the shot noise levels $N_{sh,off}$ and $N_{sh,on}$ are respectively given by :

$$N_{sh,off} = 2ResP_{opt,off}, \tag{H.15}$$

$$N_{sh,on} = 2Res\frac{G_{dB}}{2}P_{opt,off}, \tag{H.16}$$

where $P_{opt,off}$ is the optical power incident on the detector when the PSA is off. Therefore in the log scale, the noise floor will have a shift of $\frac{G_{dB}}{2}$ units upon turning on the PSA. This means for a shot-noise limited signal, $a = \frac{1}{2}$. Therefore $\Delta SFDR$ is given by :

$$\Delta SFDR = \frac{G_{dB}}{3}. \tag{H.17}$$

Bibliography

[1] Jeff Hecht. *City of light: the story of fiber optics*. Oxford University Press on Demand, 2004.

[2] Jeff Hecht. Illuminating the origin of light guiding. *Optics and Photonics News*, 10(10):26, 1999.

[3] Daniel Colladon. The colladon fountain. *Scientific American*, 51(23):359–359, 1884.

[4] Jacques Babinet. Note on the transmission of light by sinuous canals. *Comptes Rendus*, 15:802, 1842.

[5] Abraham CS van Heel. A new method of transporting optical images without aberrations. *Nature*, 173(4392):39–39, 1954.

[6] HH Hopkins and NS Kapany. Transparent fibres for the transmission of optical images. *Optica Acta: International Journal of Optics*, 1(4):164–170, 1955.

[7] Narinder S Kapany. Fiber optics. *Scientific American*, 203(5):72–81, 1960.

[8] N Kapany. Fiber optics. principles and applications. *fopa*, 1967.

[9] FP Kapron, Donald B Keck, and Robert D Maurer. Radiation losses in glass optical waveguides. *Applied Physics Letters*, 17(10):423–425, 1970.

[10] P Kaiser, EAJ Marcatili, and SE Miller. A new optical fiber. *Bell System Technical Journal*, 52(2):265–269, 1973.

[11] William G French, John B MacChesney, PB O'connor, and GW Tasker. Bstj brief: Optical waveguides with very low losses. *The Bell System Technical Journal*, 53(5):951–954, 1974.

[12] M Horiguchi and H Osanai. Spectral losses of low-oh-content optical fibres. *Electronics Letters*, 12(12):310–312, 1976.

[13] M Kawachi, A Kawana, and T Miyashita. Low-loss single-mode fibre at the material-dispersion-free wavelength of 1.27 μm. *Electronics Letters*, 13(15):442–443, 1977.

[14] H Murata and N Inagaki. Low-loss single-mode fiber development and splicing research in japan. *IEEE Journal of Quantum Electronics*, 17(6):835–849, 1981.

[15] Vincent Jude Urick, Keith J Williams, and Jason D McKinney. *Fundamentals of microwave photonics*. John Wiley & Sons, 2015.

[16] KC Kao and George A Hockham. Dielectric-fibre surface waveguides for optical frequencies. In *Proceedings of the Institution of Electrical Engineers*, volume 113, pages 1151–1158. IET, 1966.

[17] Terenuma Miya, Y Terunuma, Tatsuya Hosaka, and Tadakazu Miyashita. Ultimate low-loss single-mode fibre at 1.55 μm. *Electronics Letters*, 15(4):106–108, 1979.

[18] R H_ Stolen, EP Ippen, and AR Tynes. Raman oscillation in glass optical waveguide. *Applied Physics Letters*, 20(2):62–64, 1972.

[19] EP Ippen and RH Stolen. Stimulated brillouin scattering in optical fibers. *Applied Physics Letters*, 21(11):539–541, 1972.

[20] Richard G Smith. Optical power handling capacity of low loss optical fibers as determined by stimulated raman and brillouin scattering. *Applied optics*, 11(11):2489–2494, 1972.

[21] RH Stolen and A Ashkin. Optical kerr effect in glass waveguide. *Applied Physics Letters*, 22(6):294–296, 1973.

[22] RH Stolen, JE Bjorkholm, and A Ashkin. Phase-matched three-wave mixing in silica fiber optical waveguides. *Applied Physics Letters*, 24(7):308–310, 1974.

[23] KO Hill, DC Johnson, BS Kawasaki, and RI MacDonald. cw three-wave mixing in single-mode optical fibers. *Journal of Applied Physics*, 49(10):5098–5106, 1978.

[24] R Stolen. Phase-matched-stimulated four-photon mixing in silica-fiber waveguides. *IEEE Journal of Quantum Electronics*, 11(3):100–103, 1975.

[25] RH Stolen and Chinlon Lin. Self-phase-modulation in silica optical fibers. *Physical Review A*, 17(4):1448, 1978.

[26] Akira Hasegawa and Frederick Tappert. Transmission of stationary nonlinear optical pulses in dispersive dielectric fibers. i. anomalous dispersion. *Applied Physics Letters*, 23(3):142–144, 1973.

[27] Linn F Mollenauer, Roger H Stolen, and James P Gordon. Experimental observation of picosecond pulse narrowing and solitons in optical fibers. *Physical Review Letters*, 45(13):1095, 1980.

[28] Mohammed N Islam, Linn F Mollenauer, Roger H Stolen, Jay R Simpson, and Hen-Tai Shang. Amplifier/compressor fiber raman lasers. *Optics letters*, 12(10):814–816, 1987.

[29] JD Kafka and T Baer. Fiber raman soliton laser pumped by a nd: Yag laser. *Optics letters*, 12(3):181–183, 1987.

[30] Hiroki Nakatsuka, D Grischkowsky, and AC Balant. Nonlinear picosecond-pulse propagation through optical fibers with positive group velocity dispersion. *Physical Review Letters*, 47(13):910, 1981.

[31] CV Shank, RL Fork, R Yen, RH Stolen, and W Jack Tomlinson. Compression of femtosecond optical pulses. *Applied Physics Letters*, 40(9):761–763, 1982.

[32] JD Kafka, BH Kolner, T Baer, and DM Bloom. Compression of pulses from a continuous-wave mode-locked nd: Yag laser. *Optics letters*, 9(11):505–506, 1984.

[33] ASL Gomes, AS Gouveia-Neto, and JR Taylor. Optical fibre-grating pulse compressors. *Optical and quantum electronics*, 20(2):95–112, 1988.

[34] MC Farries and DN Payne. Optical fiber switch employing a sagnac interferometer. *Applied physics letters*, 55(1):25–26, 1989.

[35] KJ Blow, NJ Doran, and Bimal Kumar Nayar. Experimental demonstration of optical soliton switching in an all-fiber nonlinear sagnac interferometer. *Optics letters*, 14(14):754–756, 1989.

[36] Mohammed N Islam, ER Sunderman, Roger H Stolen, William Pleibel, and Jay R Simpson. Soliton switching in a fiber nonlinear loop mirror. *Optics letters*, 14(15):811–813, 1989.

[37] SA Akhmanov, Victor A Vysloukh, and Anatolii S Chirkin. Self-action of wave packets in a nonlinear medium and femtosecond laser pulse generation. *Soviet Physics Uspekhi*, 29(7):642, 1986.

[38] KJ Blow and NJ Doran. Nonlinear effects in optical fibres and fibre devices. *IEE Proceedings J (Optoelectronics)*, 134(3):138–144, 1987.

[39] Robert J Mears, L Reekie, IM Jauncey, and David N Payne. Low-noise erbium-doped fibre amplifier operating at 1.54 μm. *Electronics Letters*, 23(19):1026–1028, 1987.

[40] Emmanuel Desurvire, Jay R Simpson, and PC Becker. High-gain erbium-doped traveling-wave fiber amplifier. *Optics letters*, 12(11):888–890, 1987.

[41] Emmanuel Desurvire. *Erbium-Doped Fiber Amplifiers. Principles and Applications*. Wiley-Interscience, 2002.

[42] K Washio, K Inoue, and T Tanigawa. Efficient generation of near-ir stimulated light scattering in optical fibres pumped in low-dispersion region at 1.3 spl mu/m. *Electronics Letters*, 16(9):331–333, 1980.

[43] JP Pocholle, J Raffy, M Papuchon, and E Desurvire. Raman and four photon mixing amplification in single mode fibers. *Optical engineering*, 24(4):244600, 1985.

[44] I Bar-Joseph, AA Friesem, RG Waarts, and HH Yaffe. Parametric interaction of a modulated wave in a single-mode fiber. *Optics letters*, 11(8):534–536, 1986.

[45] Peter A Andrekson and Magnus Karlsson. Fiber-based phase-sensitive optical amplifiers and their applications. *Advances in Optics and Photonics*, 12(2):367–428, 2020.

[46] Rodney Loudon. *The quantum theory of light*. OUP Oxford, 2000.

[47] Carlton M Caves. Quantum limits on noise in linear amplifiers. *Physical Review D*, 26(8):1817, 1982.

[48] James Power Gordon. Quantum effects in communications systems. *Proceedings of the IRE*, 50(9):1898–1908, 1962.

[49] Y Yamamoto and HA Haus. Preparation, measurement and information capacity of optical quantum states. *Reviews of Modern Physics*, 58(4):1001, 1986.

[50] N Anders Olsson. Lightwave systems with optical amplifiers. *Journal of Lightwave Technology*, 7(7):1071–1082, 1989.

[51] Juan-Ariel Levenson, Izo Abram, Th Rivera, Ph Fayolle, JC Garreau, and Philippe Grangier. Quantum optical cloning amplifier. *Physical Review Letters*, 70(3):267, 1993.

[52] ME Marhic, CH Hsia, and J-M Jeong. Optical amplification in a nonlinear fibre interferometer. *Electronics letters*, 27(3):210–211, 1991.

[53] W Imajuku, A Takada, and Y Yamabayashi. Low-noise amplification under the 3 db noise figure in high-gain phase-sensitive fibre amplifier. *Electronics Letters*, 35(22):1954–1955, 1999.

[54] Zhi Tong and Stojan Radic. Low-noise optical amplification and signal processing in parametric devices. *Advances in Optics and Photonics*, 5(3):318–384, 2013.

[55] Magnus Karlsson. Transmission systems with low noise phase-sensitive parametric amplifiers. *Journal of Lightwave Technology*, 34(5):1411–1423, 2015.

[56] Michel E Marhic. *Fiber optical parametric amplifiers, oscillators and related devices*. Cambridge university press, 2008.

[57] Michel E Marhic, Peter A Andrekson, Periklis Petropoulos, Stojan Radic, Christophe Peucheret, and Mahmoud Jazayerifar. Fiber optical parametric amplifiers in optical communication systems. *Laser & Photonics Reviews*, 9(1):50–74, 2015.

[58] Govind Agrawal. *Nonlinear Fiber Optics Fifth Edition*. Elsevier, 2013.

[59] Magnus Karlsson. Four-wave mixing in fibers with randomly varying zero-dispersion wavelength. *JOSA B*, 15(8):2269–2275, 1998.

[60] Masaaki Hirano, Tetsuya Nakanishi, Toshiaki Okuno, and Masashi Onishi. Silica-based highly nonlinear fibers and their application. *IEEE Journal of Selected Topics in Quantum Electronics*, 15(1):103–113, 2009.

[61] Jonas Hansryd and Peter A Andrekson. Broad-band continuous-wave-pumped fiber optical parametric amplifier with 49-db gain and wavelength-conversion efficiency. *IEEE Photonics Technology Letters*, 13(3):194–196, 2001.

[62] Jonas Hansryd, Peter A Andrekson, Mathias Westlund, Jie Li, and P-O Hedekvist. Fiber-based optical parametric amplifiers and their applications. *IEEE Journal of Selected Topics in Quantum Electronics*, 8(3):506–520, 2002.

[63] D Cotter. Transient stimulated brillouin scattering in long single-mode fibres. *Electronics Letters*, 18(12):504–506, 1982.

[64] Justin L Blows and Sylvia E French. Low-noise-figure optical parametric amplifier with a continuous-wave frequency-modulated pump. *Optics Letters*, 27(7):491–493, 2002.

[65] Andrey Kobyakov, Shiva Kumar, Dipak Q Chowdhury, A Boh Ruffin, Michael Sauer, Scott R Bickham, and Raj Mishra. Design concept for optical fibers with enhanced sbs threshold. *Optics Express*, 13(14):5338–5346, 2005.

[66] James B Coles, BP-P Kuo, Nikola Alic, Slaven Moro, C-S Bres, JM Chavez Boggio, PA Andrekson, Magnus Karlsson, and S Radic. Bandwidth-efficient phase modulation techniques for stimulated brillouin scattering suppression in fiber optic parametric amplifiers. *Optics Express*, 18(17):18138–18150, 2010.

[67] WA Gambling, H Matsumura, and CM Ragdale. Mode dispersion, material dispersion and profile dispersion in graded-index single-mode fibres. *IEE Journal on Microwaves, Optics and Acoustics*, 3(6):239–246, 1979.

[68] Thomas Torounidis, Peter A Andrekson, and B-E Olsson. Fiber-optical parametric amplifier with 70-db gain. *IEEE Photonics Technology Letters*, 18(10):1194–1196, 2006.

[69] Thomas Torounidis and Peter Andrekson. Broadband single-pumped fiber-optic parametric amplifiers. *IEEE Photonics Technology Letters*, 19(9):650–652, 2007.

[70] Per Kylemark, Per Olof Hedekvist, Henrik Sunnerud, Magnus Karlsson, and Peter A Andrekson. Noise characteristics of fiber optical parametric amplifiers. *Journal of Lightwave Technology*, 22(2):409–416, 2004.

[71] Per Kylemark, Per Olof Hedekvist, Henrik Sunnerud, Magnus Karlsson, and Peter A Andrekson. Correction to "noise characteristics of fiber optical parametric amplifiers". *Journal of Lightwave Technology*, 23(6):2192–2192, 2005.

[72] Zhi Tong, Adonis Bogris, Magnus Karlsson, and Peter A Andrekson. Full characterization of the signal and idler noise figure spectra in single-pumped fiber optical parametric amplifiers. *Optics express*, 18(3):2884–2893, 2010.

[73] Michel E Marhic, KK-Y Wong, and Leonid G Kazovsky. Wide-band tuning of the gain spectra of one-pump fiber optical parametric amplifiers. *IEEE Journal of Selected Topics in Quantum Electronics*, 10(5):1133–1141, 2004.

[74] Colin J McKinstrie, Stojan Radic, and Andrew R Chraplyvy. Parametric amplifiers driven by two pump waves. *IEEE Journal of Selected Topics in Quantum Electronics*, 8(3):538–547, 2002.

[75] S Radic and CJ McKinstrie. Two-pump fiber parametric amplifiers. *Optical Fiber Technology*, 9(1):7–23, 2003.

[76] Colin J McKinstrie, S Radic, and MG Raymer. Quantum noise properties of parametric amplifiers driven by two pump waves. *Optics Express*, 12(21):5037–5066, 2004.

[77] CJ McKinstrie, M Yu, MG Raymer, and S Radic. Quantum noise properties of parametric processes. *Optics express*, 13(13):4986–5012, 2005.

[78] CJ McKinstrie, MG Raymer, S Radic, and MV Vasilyev. Quantum mechanics of phase-sensitive amplification in a fiber. *Optics communications*, 257(1):146–163, 2006.

[79] CJ McKinstrie and S Radic. Phase-sensitive amplification in a fiber. *Optics express*, 12(20):4973–4979, 2004.

[80] Michael Vasilyev. Distributed phase-sensitive amplification. *Optics Express*, 13(19):7563–7571, 2005.

[81] Kevin Croussore, Cheolhwan Kim, and Guifang Li. All-optical regeneration of differential phase-shift keying signals based on phase-sensitive amplification. *Optics letters*, 29(20):2357–2359, 2004.

[82] Kevin Croussore, Inwoong Kim, Yan Han, Cheolhwan Kim, Guifang Li, and Stojan Radic. Demonstration of phase-regeneration of dpsk signals based on phase-sensitive amplification. *Optics Express*, 13(11):3945–3950, 2005.

[83] Kevin Croussore and Guifang Li. Phase and amplitude regeneration of differential phase-shift keyed signals using phase-sensitive amplification. *IEEE Journal of Selected Topics in Quantum Electronics*, 14(3):648–658, 2008.

[84] Radan Slavík, Francesca Parmigiani, Joseph Kakande, Carl Lundström, Martin Sjödin, Peter A Andrekson, Ruwan Weerasuriya, Stylianos Sygletos, Andrew D Ellis, Lars Grüner-Nielsen, et al. All-optical phase and amplitude regenerator for next-generation telecommunications systems. *Nature Photonics*, 4(10):690–695, 2010.

[85] Radan Slavík, Adonis Bogris, Francesca Parmigiani, Joseph Kakande, Mathias Westlund, Mats Sköld, Lars Grüner-Nielsen, Richard Phelan, Dimitris Syvridis, Periklis Petropoulos, et al. Coherent all-optical phase and amplitude regenerator of binary phase-encoded signals. *IEEE Journal of Selected Topics in Quantum Electronics*, 18(2):859–869, 2011.

[86] Renyong Tang, Jacob Lasri, Preetpaul S Devgan, Vladimir Grigoryan, Prem Kumar, and Michael Vasilyev. Gain characteristics of a frequency nondegenerate phase-sensitive fiber-optic parametric amplifier with phase self-stabilized input. *Optics Express*, 13(26):10483–10493, 2005.

[87] Zhi Tong, Carl Lundström, PA Andrekson, CJ McKinstrie, Magnus Karlsson, DJ Blessing, Ekawit Tipsuwannakul, BJ Puttnam, Hiroyuki Toda, and L Grüner-Nielsen. Towards ultrasensitive optical links enabled by low-noise phase-sensitive amplifiers. *Nature Photonics*, 5(7):430, 2011.

[88] Zhi Tong, Carl Lundström, Peter A Andrekson, Magnus Karlsson, and Adonis Bogris. Ultralow noise, broadband phase-sensitive optical amplifiers, and their applications. *IEEE Journal of Selected Topics in Quantum Electronics*, 18(2):1016–1032, 2011.

[89] Weilin Xie. *Nonlinear properties of phase-sensitive fiber-optic parametric amplifiers for signal processing*. PhD thesis, Paris Saclay, 2018.

[90] Maxime Baillot, Thierry Chartier, and Michel Joindot. Multiple four-wave mixing in optical fibres. In *2014 The European Conference on Optical Communication (ECOC)*, pages 1–3. IEEE, 2014.

[91] Weilin Xie, Ihsan Fsaifes, Tarek Labidi, and Fabien Bretenaker. Investigation of degenerate dual-pump phase sensitive amplifier using multi-wave model. *Optics Express*, 23(25):31896–31907, 2015.

[92] Jiaqin Qian, Mingyi Gao, Lian Xiang, and Gangxiang Shen. Investigation of high gain dual-pump phase sensitive amplifiers. *Optik*, 135:210–218, 2017.

[93] Michael J Adams. *An introduction to optical waveguides*, volume 14. Wiley New York, 1981.

[94] Tingye Li. *Optical fiber communications: fiber fabrication*. Elsevier, 2012.

[95] LG Cohen, WL Mammel, and SJ Jang. Low-loss quadruple-clad single-mode lightguides with dispersion below 2 ps/km nm over the 1.28 μm-1.65 μm wavelength range. *Electronics Letters*, 18(24):1023–1024, 1982.

[96] JH Marburger. Self-focusing: theory. *Progress in quantum electronics*, 4:35–110, 1975.

[97] AJ Seeds, CH Lee, EE Funk, and M Naganuma. Microwave photonics. *Journal of Lightwave Technology*, 21(12):2959–2960, 2003.

[98] José Capmany and Dalma Novak. Microwave photonics combines two worlds. *Nature photonics*, 1(6):319, 2007.

[99] Charles Howard Cox. *Analog optical links: theory and practice*. Cambridge University Press, 2006.

[100] Kenneth M Johnson. Microwave light modulation by the pockel effect. *Microwave J*, 7:51–56, 1964.

[101] Tibor Berceli and Peter R Herczfeld. Microwave photonics—a historical perspective. *IEEE transactions on microwave theory and techniques*, 58(11):2992–3000, 2010.

[102] Alwyn J Seeds and Keith J Williams. Microwave photonics. *Journal of Lightwave Technology*, 24(12):4628–4641, 2006.

[103] Ralph H Blumenthal. Design of a microwave-frequency light modulator. *Proceedings of the IRE*, 50(4):452–456, 1962.

[104] RD Standley and GDt Mandeville. Performance of an 11-ghz optical modulator using litao 3. *Applied optics*, 10(5):1022–1023, 1971.

[105] Charlses H Cox, Gary E Betts, and Leonard M Johnson. An analytic and experimental comparison of direct and external modulation in analog fiber-optic links. *IEEE Transactions on microwave theory and techniques*, 38(5):501–509, 1990.

[106] RG Walker. Electro-optic modulation at mm-wave frequencies in gaas/algaas guided wave devices. In *LEOS'95. IEEE Lasers and Electro-Optics Society 1995 Annual Meeting. 8th Annual Meeting. Conference Proceedings*, volume 1, pages 118–119. IEEE, 1995.

[107] SR Sakamoto, R Spickermann, and N Dagli. Narrow gap coplanar slow wave electrode for travelling wave electro-optic modulators. *Electronics Letters*, 31(14):1183–1185, 1995.

[108] Kazuto Noguchi, Osamu Mitomi, and Hiroshi Miyazawa. Millimeter-wave ti: Linbo/sub 3/optical modulators. *Journal of Lightwave Technology*, 16(4):615–619, 1998.

[109] RP Riesz. High speed semiconductor photodiodes. *Review of Scientific Instruments*, 33(9):994–998, 1962.

[110] Kenneth M Johnson. High-speed photodiode signal enhancement at avalanche breakdown voltage. *IEEE Transactions on Electron Devices*, 12(2):55–63, 1965.

[111] K Berchtold, Oskar Krumpholz, and J Suri. Avalanche photodiodes with a gain-bandwidth product of more than 200 ghz. *Applied Physics Letters*, 26(10):585–587, 1975.

[112] JE Bowers, CA Burrus, and RJ McCoy. Ingaas pin photodetectors with modulation response to millimetre wavelengths. *Electronics Letters*, 21(18):812–814, 1985.

[113] Donald Toman. Towed decoy with fiber optic link, February 28 1989. US Patent 4,808,999.

[114] Felix J Lockman. Green bank telescope: an overview. In *Advanced Technology MMW, Radio, and Terahertz Telescopes*, volume 3357, pages 656–665. International Society for Optics and Photonics, 1998.

[115] Richard M Prestage, Kim T Constantikes, Todd R Hunter, Lee J King, Richard J Lacasse, Felix J Lockman, and Roger D Norrod. The green bank telescope. *Proceedings of the IEEE*, 97(8):1382–1390, 2009.

[116] Steven D White. Implementation of a photonic automatic gain control system for correcting gain variations in the green bank telescope fiber optic system. *Review of Scientific Instruments*, 71(8):3196–3199, 2000.

[117] John M Payne and WP Shillue. Photonic techniques for local oscillator generation and distribution in millimeter-wave radio astronomy. In *Proc. MWP*, pages 9–12, 2002.

[118] Anjali Agarwal, Thomas Banwell, and Ted K Woodward. Rf photonic link employing optical phase sensitive amplification. In *Optical Fiber Communication Conference*, pages OM3B–5. Optical Society of America, 2012.

[119] Arismar Cerqueira Sodré, Natalia Cañas-Estrada, Dionisio F Noque, Ramon M Borges, Suzanne AS Melo, Neil G González, and Julio CRF Oliveira. Photonic-assisted microwave amplification using four-wave mixing. *IET Optoelectronics*, 10(5):163–168, 2016.

[120] Hossein Emami and Mohsen Ashourian. Improved dynamic range microwave photonic instantaneous frequency measurement based on four-wave mixing. *IEEE Transactions on Microwave Theory and Techniques*, 62(10):2462–2470, 2014.

[121] André AC Albuquerque, Benjamin J Puttnam, José MD Mendinueta, Miguel V Drummond, Satoshi Shinada, Rogério N Nogueira, and Naoya Wada. Experimental investigation of phase-sensitive amplification of data signals in a four-mode fiber-based psa. *Optics letters*, 40(2):288–291, 2015.

[122] RF Kalman, JC Fan, and LG Kazovsky. Dynamic range of coherent analog fiber-optic links. *Journal of Lightwave Technology*, 12(7):1263–1277, 1994.

[123] Camille-Sophie Bres, Andreas OJ Wiberg, Bill P-P Kuo, Evgeny Myslivets, Nikola Alic, Bryan Stossel, and Stojan Radic. Low distortion multicasting of an analog signal by self-seeded parametric mixer. *IEEE Photonics Technology Letters*, 22(5):332–334, 2010.

[124] Oo-Kaw Lim, Vladimir Grigoryan, Matthew Shin, and Prem Kumar. Ultra-low-noise inline fiber-optic phase-sensitive amplifier for analog optical signals. In *Optical Fiber Communication Conference*, page OML3. Optical Society of America, 2008.

[125] Ihsan Fsaifes, Tarek Labidi, Fabienne Goldfarb, and Fabien Bretenaker. Intermodulation distortion analysis of an analog photonic link employing parametric phase sensitive amplification. In *2014 The European Conference on Optical Communication (ECOC)*, pages 1–3. IEEE, 2014.

[126] Ping Zhao, Ravikiran Kakarla, Magnus Karlsson, and Peter A Andrekson. Enhanced analog-optical link performance with noiseless phase-sensitive fiber optical parametric amplifiers. *Optics Express*, 28(16):23534–23544, 2020.

[127] Debanuj Chatterjee, Yousra Bouasria, Weilin Xie, Tarek Labidi, Fabienne Goldfarb, Ihsan Fsaifes, and Fabien Bretenaker. Investigation of analog signal distortion introduced by a fiber phase sensitive amplifier. *JOSA B*, 37(8):2405–2415, 2020.

[128] Lan Liu, Eduardo Temprana, Vahid Ataie, Andreas OJ Wiberg, Bill P-P Kuo, Evgeny Myslivets, Nikola Alic, and Stojan Radic. All optical wavelength multicaster and regenerator based on four-mode phase-sensitive parametric mixer. *Optics express*, 23(24):30956–30969, 2015.

[129] Samuel LI Olsson, Magnus Karlsson, and Peter A Andrekson. Nonlinear phase noise mitigation in phase-sensitive amplified transmission systems. *Optics express*, 23(9):11724–11740, 2015.

[130] A Perentos, S Fabbri, M Sorokina, ID Phillips, SK Turitsyn, AD Ellis, and S Sygletos. Qpsk 3r regenerator using a phase sensitive amplifier. *Optics express*, 24(15):16649–16658, 2016.

[131] Henrik Eliasson, Samuel LI Olsson, Magnus Karlsson, and Peter A Andrekson. Mitigation of nonlinear distortion in hybrid raman/phase-sensitive amplifier links. *Optics Express*, 24(2):888–900, 2016.

[132] Egon Astra, Samuel LI Olsson, Henrik Eliasson, and Peter A Andrekson. Dispersion management for nonlinearity mitigation in two-span 28 gbaud qpsk phase-sensitive amplifier links. *Optics Express*, 25(12):13163–13173, 2017.

[133] KRH Bottrill, Graham Hesketh, Liam Jones, Francesca Parmigiani, DJ Richardson, and Periklis Petropoulos. Full quadrature regeneration of qpsk signals using sequential phase sensitive amplification and parametric saturation. *Optics express*, 25(2):696–705, 2017.

[134] Amit Bhatia, Hong-Fu Ting, and Mark A Foster. Linearization of phase-modulated analog optical links using a four-wave mixing comb source. *Optics express*, 22(25):30899–30909, 2014.

[135] R Stolen and J Bjorkholm. Parametric amplification and frequency conversion in optical fibers. *IEEE Journal of Quantum Electronics*, 18(7):1062–1072, 1982.

[136] H Pakarzadeh and A Zakery. Numerical modelling of the pump-to-signal relative intensity noise transfer in two-pump fibre optical parametric amplifiers. *Pramana*, 77(4):655–667, 2011.

[137] Mingyi Gao, Takashi Inoue, Takayuki Kurosu, and Shu Namiki. Evolution of the gain extinction ratio in dual-pump phase sensitive amplification. *Optics Letters*, 37(9):1439–1441, 2012.

[138] Maxime Baillot, Mathilde Gay, Christophe Peucheret, Joindot Michel, and Thierry Chartier. Phase quadrature discrimination based on three-pump four-wave mixing in nonlinear optical fibers. *Optics Express*, 24(23):26930–26941, 2016.

[139] Kyo Inoue. Polarization independent wavelength conversion using fiber four-wave mixing with two orthogonal pump lights of different frequencies. *Journal of Lightwave Technology*, 12(11):1916–1920, 1994.

[140] ME Marhic, N Kagi, T-K Chiang, and LG Kazovsky. Broadband fiber optical parametric amplifiers. *Optics Letters*, 21(8):573–575, 1996.

[141] Min-Chen Ho, Katsumi Uesaka, Michel Marhic, and Youichi Akasaka. 200-nm-bandwidth fiber optical amplifier combining parametric and raman gain. *Journal of Lightwave Technology*, 19(7):977, 2001.

[142] K Inoue and T Mukai. Signal wavelength dependence of gain saturation in a fiber optical parametric amplifier. *Optics Letters*, 26(1):10–12, 2001.

[143] David A Chestnut, Christiano JS de Matos, and J Roy Taylor. Raman-assisted fiber optical parametric amplifier and wavelength converter in highly nonlinear fiber. *JOSA B*, 19(8):1901–1904, 2002.

[144] Herbert B Callen. A note on the manley-rowe energy relations for parametric amplifiers. *Journal of the Franklin Institute*, 269(2):93–96, 1960.

[145] Robert W Boyd. *Nonlinear optics*. Academic press, 2019.

[146] S Radic, CJ McKinstrie, AR Chraplyvy, G Raybon, JC Centanni, CG Jorgensen, K Brar, and C Headley. Continuous-wave parametric gain synthesis using nondegenerate pump four-wave mixing. *IEEE Photonics Technology Letters*, 14(10):1406–1408, 2002.

[147] Jose M Chavez Boggio, Slaven Moro, Evgeny Myslivets, Joshua R Windmiller, Nikola Alic, and Stojan Radic. 155-nm continuous-wave two-pump parametric amplification. *IEEE Photonics Technology Letters*, 21(10):612–614, 2009.

[148] Kwok Shien Yeo, Faisal Rafiq Mahamd Adikan, Makhfudzah Mokhtar, Salasiah Hitam, and Mohd Adzir Mahdi. Fiber optical parametric amplifier with double-pass pump configuration. *Optics Express*, 21(25):31623–31631, 2013.

[149] H Pakarzadeh and A Zakery. Investigation of two-pump fiber optical parametric amplifiers for a broadband and flat gain with a low pump-to-signal noise transfer. *Journal of Nonlinear Optical Physics & Materials*, 24(03):1550038, 2015.

[150] V Gordienko, MFC Stephens, and NJ Doran. Broadband gain-spectrum measurement for fiber optical parametric and raman amplifiers. *IEEE Photonics Technology Letters*, 29(16):1399–1402, 2017.

[151] Thomas Torounidis, Henrik Sunnerud, Per Olof Hedekvist, and Peter A Andrekson. Amplification of wdm signals in fiber-based optical parametric amplifiers. *IEEE Photonics Technology Letters*, 15(8):1061–1063, 2003.

[152] Kyo Inoue. Tunable and selective wavelength conversion using fiber four-wave mixing with two pump lights. *IEEE Photonics Technology Letters*, 6(12):1451–1453, 1994.

[153] Claudio Floridia, ML Sundheimer, L de S Menezes, and ASL Gomes. Optimization of spectrally flat and broadband single-pump fiber optic parametric amplifiers. *Optics Communications*, 223(4-6):381–388, 2003.

[154] Yue Tian, Yue-Kai Huang, Shaoliang Zhang, Paul R Prucnal, and Ting Wang. Demonstration of digital phase-sensitive boosting to extend signal reach for long-haul wdm systems using optical phase-conjugated copy. *Optics Express*, 21(4):5099–5106, 2013.

[155] Tarek Labidi, Ihsan Fsaifes, Weilin Xie, Debanuj Chatterjee, Fabienne Goldfarb, and Fabien Bretenaker. Phase evolution of the direct detection noise figure of a nondegenerate fiber phase-sensitive amplifier. *Optics Letters*, 43(18):4546–4549, 2018.

[156] Zhi Tong, Adonis Bogris, Carl Lundström, CJ McKinstrie, Michael Vasilyev, Magnus Karlsson, and Peter A Andrekson. Modeling and measurement of

the noise figure of a cascaded non-degenerate phase-sensitive parametric amplifier. *Optics Express*, 18(14):14820–14835, 2010.

[157] Kyo Inoue. Influence of multiple four-wave-mixing processes on quantum noise of dual-pump phase-sensitive amplification in a fiber. *JOSA B*, 36(6):1436–1446, 2019.

[158] MV Berry. Pumping a swing revisited: minimal model for parametric resonance via matrix products. *European Journal of Physics*, 39(5):055007, 2018.

[159] VI Arnold. *Mathematical methods of classical mechanics*. Springer-Verlag, 1978.

[160] Takuo Tanemura and Kazuro Kikuchi. Unified analysis of modulational instability induced by cross-phase modulation in optical fibers. *JOSA B*, 20(12):2502–2514, 2003.

[161] Yijiang Chen and Allan W Snyder. Four-photon parametric mixing in optical fibers: effect of pump depletion. *Optics Letters*, 14(1):87–89, 1989.

[162] Yijiang Chen. Combined processes of stimulated raman scattering and four-wave mixing in optical fibers. *JOSA B*, 7(1):43–52, 1990.

[163] ME Marhic, AA Rieznik, and HL Fragnito. Investigation of the gain spectrum near the pumps of two-pump fiber-optic parametric amplifiers. *JOSA B*, 25(1):22–30, 2008.

[164] Armand Vedadi, Michel E Marhic, Eric Lantz, Hervé Maillotte, and Thibaut Sylvestre. Investigation of gain ripple in two-pump fiber optical parametric amplifiers. *Optics Letters*, 33(19):2203–2205, 2008.

[165] Hassan Pakarzadeh, Raziye Golabi, and Christophe Peucheret. Two-pump fiber optical parametric amplifiers: Beyond the 6-wave model. *Optical Fiber Technology*, 45:223–230, 2018.

[166] Yousra Bouasria, Debanuj Chatterjee, Weilin Xie, Ihsan Fsaifes, Fabienne Goldfarb, Yassine Hassouni, and Fabien Bretenaker. Investigation of the noise figure in a degenerate dual-pump phase-sensitive amplifier using a multi-wave model. *JOSA B*, 37(9):2745–2754, 2020.

[167] X-M Liu. Theory and experiments for multiple four-wave-mixing processes with multifrequency pumps in optical fibers. *Physical Review A*, 77(4):043818, 2008.

[168] Maxime Baillot. *Mélange à quatre ondes multiple pour le traitement tout-optique du signal dans les fibres optiques non linéaires*. PhD thesis, Rennes 1, 2017.

[169] Niels Henrik Abel. Demonstration of the impossibility of the algebraic resolution of the general equations which pass the fourth degree. *Journal für die Reine und Angewandte Mathematik*, 1:65–96, 1826.

[170] George B Arfken and Hans J Weber. *Mathematical methods for physicists*. American Association of Physics Teachers, 1999.

[171] Tarek Labidi, Ihsan Fsaifes, Fabienne Goldfarb, and Fabien Bretenaker. Distortionless analog photonic link employing optical phase sensitive amplification. In *Optical Sensors*, pages JM5A–39. Optical Society of America, 2014.

[172] Joseph Kakande, Radan Slavík, Francesca Parmigiani, Adonis Bogris, Dimitris Syvridis, Lars Grüner-Nielsen, Richard Phelan, Periklis Petropoulos, and David J Richardson. Multilevel quantization of optical phase in a novel coherent parametric mixer architecture. *Nature Photonics*, 5(12):748, 2011.

[173] Francesco Da Ros, Kjeld Dalgaard, Lei Lei, Jing Xu, and Christophe Peucheret. Qpsk-to-2× bpsk wavelength and modulation format conversion through phase-sensitive four-wave mixing in a highly nonlinear optical fiber. *Optics express*, 21(23):28743–28750, 2013.

[174] G Millot. Multiple four-wave mixing–induced modulational instability in highly birefringent fibers. *Optics letters*, 26(18):1391–1393, 2001.

[175] Stefano Trillo, Stefan Wabnitz, and TAB Kennedy. Nonlinear dynamics of dual-frequency-pumped multiwave mixing in optical fibers. *Physical Review A*, 50(2):1732, 1994.

[176] Zhanchang Liu, Zhirong Chen, Xiaojie Guo, Jiangbing Du, and Zhaohui Li. Noise evolution with the phase-sensitive gain in a hybrid fiber phase-sensitive amplifier. *Optics Letters*, 45(11):3075–3078, 2020.

[177] Dmitry Levandovsky, Michael Vasilyev, and Prem Kumar. Near-noiseless amplification of light by a phase-sensitive fibre amplifier. *Pramana*, 56(2-3):281–285, 2001.

[178] Yuri S Kivshar and Govind P Agrawal. *Optical solitons: from fibers to photonic crystals*. Academic press, 2003.

[179] Jerome V Moloney and Alan C Newell. *Nonlinear optics*. Westview Press, 2004.

[180] Mario F Ferreira. *Nonlinear effects in optical fibers*, volume 2. John Wiley & Sons, 2011.

[181] Jing Huang. Nonlinear schrödinger equation. In *Nonlinear Optics-Novel Results in Theory and Applications*. IntechOpen, 2018.

[182] Hideki Ishio, Junichiro Minowa, and Kiyoshi Nosu. Review and status of wavelength-division-multiplexing technology and its application. *Journal of Lightwave Technology*, 2(4):448–463, 1984.

[183] A Shabat and V Zakharov. Exact theory of two-dimensional self-focusing and one-dimensional self-modulation of waves in nonlinear media. *Soviet Physics JETP*, 34(1):62, 1972.

[184] NN Akhmediev and VI Korneev. Modulation instability and periodic solutions of the nonlinear schrödinger equation. *Theoretical and Mathematical Physics*, 69(2):1089–1093, 1986.

[185] Bertrand Kibler, Julien Fatome, Christophe Finot, Guy Millot, Frédéric Dias, Goëry Genty, Nail Akhmediev, and John M Dudley. The peregrine soliton in nonlinear fibre optics. *Nature Physics*, 6(10):790–795, 2010.

[186] Kamal Hammani, Benjamin Wetzel, Bertrand Kibler, Julien Fatome, Christophe Finot, Guy Millot, Nail Akhmediev, and John M Dudley. Spectral dynamics of modulation instability described using akhmediev breather theory. *Optics Letters*, 36(11):2140–2142, 2011.

[187] John M Dudley, Frédéric Dias, Miro Erkintalo, and Goëry Genty. Instabilities, breathers and rogue waves in optics. *Nature Photonics*, 8(10):755–764, 2014.

[188] A Chowdury, DJ Kedziora, A Ankiewicz, and N Akhmediev. Breather solutions of the integrable quintic nonlinear schrödinger equation and their interactions. *Physical Review E*, 91(2):022919, 2015.

[189] N Karjanto. Peregrine soliton as a limiting behavior of the kuznetsov-ma and akhmediev breathers. *arXiv preprint arXiv:2009.00269*, 2020.

[190] Vladimir Iosifovich Karpman and EM Krushkal. Modulated waves in nonlinear dispersive media. *Journal of Experimental and Theoretical Physics*, 28(2):277–281, 1969.

[191] RH Hardin. Applications of the split-step fourier method to the numerical solution of nonlinear and variable coefficient wave equations. *SIAM Review (Chronicles)*, 15, 1973.

[192] Robert A Fisher and William K Bischel. Numerical studies of the interplay between self-phase modulation and dispersion for intense plane-wave laser pulses. *Journal of Applied Physics*, 46(11):4921–4934, 1975.

[193] Jr A Fleck, JR Morris, and MD Feit. Time-dependent propagation of high energy laser beams through the atmosphere. *Applied Physics*, 10(2):129–160, 1976.

[194] Bengt Fornberg and Gerald Beresford Whitham. A numerical and theoretical study of certain nonlinear wave phenomena. *Philosophical Transactions of the Royal Society of London. Series A, Mathematical and Physical Sciences*, 289(1361):373–404, 1978.

[195] M Delfour, M Fortin, and G Payr. Finite-difference solutions of a non-linear schrödinger equation. *Journal of Computational Physics*, 44(2):277–288, 1981.

[196] Thiab R Taha and Mark I Ablowitz. Analytical and numerical aspects of certain nonlinear evolution equations. ii. numerical, nonlinear schrödinger equation. *Journal of Computational Physics*, 55(2):203–230, 1984.

[197] D Pathria and J Ll Morris. Pseudo-spectral solution of nonlinear schrödinger equations. *Journal of Computational Physics*, 87(1):108–125, 1990.

[198] Lionel R Watkins and Yu Rong Zhou. Modeling propagation in optical fibers using wavelets. *Journal of Lightwave Technology*, 12(9):1536–1542, 1994.

[199] Dietrich Marcuse, CR Manyuk, and PKA Wai. Application of the manakov-pmd equation to studies of signal propagation in optical fibers with randomly varying birefringence. *Journal of Lightwave Technology*, 15(9):1735–1746, 1997.

[200] EH Twizell, AG Bratsos, and JC Newby. A finite-difference method for solving the cubic schrödinger equation. *Mathematics and Computers in Simulation*, 43(1):67–75, 1997.

[201] Kumar V Peddanarappagari et al. Volterra series approach for optimizing fiber-optic communications system designs. *Journal of Lightwave Technology*, 16(11):2046, 1998.

[202] Wen-ping Zeng. A leap frog finite difference scheme for a class of nonlinear schrödinger equations of high order. *Journal of Computational Mathematics*, pages 133–138, 1999.

[203] AG Shagalov. Symplectic numerical methods in dynamics of nonlinear waves. *International Journal of Modern Physics C*, 10(05):967–980, 1999.

[204] Qianshun Chang, Erhui Jia, and W Sun. Difference schemes for solving the generalized nonlinear schrödinger equation. *Journal of Computational Physics*, 148(2):397–415, 1999.

[205] Wei-zhong Dai and Raja Nassar. A finite difference scheme for the generalized nonlinear schrödinger equation with variable coefficients. *Journal of Computational Mathematics*, pages 123–132, 2000.

[206] SRK Iyengar, G Jayaraman, and V Balasubramanian. Variable mesh difference schemes for solving a nonlinear schrödinger equation with a linear damping term. *Computers & Mathematics with Applications*, 40(12):1375–1385, 2000.

[207] Q Sheng, AQM Khaliq, and EA Al-Said. Solving the generalized nonlinear schrödinger equation via quartic spline approximation. *Journal of Computational Physics*, 166(2):400–417, 2001.

[208] Jing-Bo Chen, Meng-Zhao Qin, and Yi-Fa Tang. Symplectic and multi-symplectic methods for the nonlinear schrödinger equation. *Computers & Mathematics with Applications*, 43(8-9):1095–1106, 2002.

[209] Juan I Ramos. Linearly implicit methods for the nonlinear schrödinger equation in nonhomogeneous media. *Applied Mathematics and computation*, 133(1):1–28, 2002.

[210] Xueming Liu and Byoungho Lee. A fast method for nonlinear schrodinger equation. *IEEE Photonics Technology Letters*, 15(11):1549–1551, 2003.

[211] Whye-Teong Ang and Keng-Cheng Ang. A dual-reciprocity boundary element solution of a generalized nonlinear schrödinger equation. *Numerical Methods for Partial Differential Equations: An International Journal*, 20(6):843–854, 2004.

[212] Malin Premaratne. Split-step spline method for modeling optical fiber communications systems. *IEEE Photonics Technology Letters*, 16(5):1304–1306, 2004.

[213] Gulcin M Muslu and HA Erbay. Higher-order split-step fourier schemes for the generalized nonlinear schrödinger equation. *Mathematics and Computers in Simulation*, 67(6):581–595, 2005.

[214] Tristan Kremp and Wolfgang Freude. Fast split-step wavelet collocation method for wdm system parameter optimization. *Journal of Lightwave Technology*, 23(3):1491, 2005.

[215] MS Ismail. Numerical solution of coupled nonlinear schrödinger equation by galerkin method. *Mathematics and Computers in Simulation*, 78(4):532–547, 2008.

[216] Paulsamy Muruganandam and Sadhan K Adhikari. Fortran programs for the time-dependent gross–pitaevskii equation in a fully anisotropic trap. *Computer Physics Communications*, 180(10):1888–1912, 2009.

[217] James W Cooley and John W Tukey. An algorithm for the machine calculation of complex fourier series. *Mathematics of Computation*, 19(90):297–301, 1965.

[218] Partha P Banerjee. *Nonlinear optics: theory, numerical modeling, and applications*. CRC Press, 2003.

[219] J Van Roey, J Van der Donk, and PE Lagasse. Beam-propagation method: analysis and assessment. *JOSA*, 71(7):803–810, 1981.

[220] J Saijonmaa and D Yevick. Beam-propagation analysis of loss in bent optical waveguides and fibers. *JOSA*, 73(12):1785–1791, 1983.

[221] Oleg V Sinkin, Ronald Holzlohner, John Zweck, and Curtis R Menyuk. Optimization of the split-step fourier method in modeling optical-fiber communications systems. *Journal of lightwave technology*, 21(1):61–68, 2003.

[222] George H Weiss and Alexei A Maradudin. The baker-hausdorff formula and a problem in crystal physics. *Journal of Mathematical Physics*, 3(4):771–777, 1962.

[223] Fredric J Harris. On the use of windows for harmonic analysis with the discrete fourier transform. *Proceedings of the IEEE*, 66(1):51–83, 1978.

[224] Richard G Lyons. *Understanding digital signal processing, 3/E*. Pearson Education India, 2004.

[225] M Crisp, Richard V Penty, Ian H White, and A Bell. Wideband radio over fiber distributed antenna systems for energy efficient in-building wireless communications. In *2010 IEEE 71st Vehicular Technology Conference*, pages 1–5. IEEE, 2010.

[226] Kun Xu, Ruixin Wang, Yitang Dai, Feifei Yin, Jianqiang Li, Yuefeng Ji, and Jintong Lin. Microwave photonics: radio-over-fiber links, systems, and applications. *Photonics Research*, 2(4):B54–B63, 2014.

[227] Sergey I Ivanov, Alexander P Lavrov, and Igor I Saenko. Application of microwave photonics components for ultrawideband antenna array beamforming. In *Internet of Things, Smart Spaces, and Next Generation Networks and Systems*, pages 670–679. Springer, 2016.

[228] Jianping Yao. Microwave photonics. *Journal of Lightwave Technology*, 27(3):314–335, 2009.

[229] Jianping Yao. A tutorial on microwave photonics. *IEEE Photonics Society Newsletter*, 26(2):4–12, 2012.

[230] William SC Chang. *RF photonic technology in optical fiber links*. Cambridge University Press, 2002.

[231] Anne Vilcot, Béatrice Cabon, and Jean Chazelas. *Microwave photonics: from components to applications and systems*. Springer Science & Business Media, 2003.

[232] Xiaojun Xie, Kejia Li, Qiugui Zhou, Andreas Beling, and Joe C Campbell. High-gain, low-noise-figure, and high-linearity analog photonic link based on a high-performance photodetector. *Journal of Lightwave Technology*, 32(21):4187–4192, 2014.

[233] Anjali Agarwal, Tom Banwell, and Ted K Woodward. Optically filtered microwave photonic links for rf signal processing applications. *Journal of Lightwave Technology*, 29(16):2394–2401, 2011.

[234] Samuel LI Olsson, Henrik Eliasson, Egon Astra, Magnus Karlsson, and Peter A Andrekson. Long-haul optical transmission link using low-noise phase-sensitive amplifiers. *Nature Communications*, 9(1):1–7, 2018.

[235] Paolo Ghelfi, Francesco Laghezza, Filippo Scotti, Giovanni Serafino, Amerigo Capria, Sergio Pinna, Daniel Onori, Claudio Porzi, Mirco Scaffardi, Antonio Malacarne, et al. A fully photonics-based coherent radar system. *Nature*, 507(7492):341–345, 2014.

[236] Valentina Cristofori, Zohreh Lali-Dastjerdi, Toke Lund-Hansen, Michael Galili, Christophe Peucheret, and Karsten Rottwitt. Saturation effect on pump-to-signal intensity modulation transfer in single-pump phase-insensitive fibre optic parametric amplifiers. In *IEEE Photonic Society 24th Annual Meeting*, pages 314–315. IEEE, 2011.

[237] Carl Lundström, Bill Corcoran, Magnus Karlsson, and Peter A Andrekson. Phase and amplitude characteristics of a phase-sensitive amplifier operating in gain saturation. *Optics Express*, 20(19):21400–21412, 2012.

[238] Valentina Cristofori, Zohreh Lali-Dastjerdi, Toke Lund-Hansen, Christophe Peucheret, and Karsten Rottwitt. Experimental investigation of saturation effect on pump-to-signal intensity modulation transfer in single-pump phase-insensitive fiber optic parametric amplifiers. *JOSA B*, 30(4):884–888, 2013.

[239] E Voges and K Petermann. Abkürzungsverzeichnis, physikalische konstanten und materialdaten. In *Optische Kommunikationstechnik*, pages 1–11. Springer, 2002.

[240] RP Photonics. Rp photonics encyclopedia-pockel's effect. `http://www.rp-photonics.com/pockels_effect.html`.

[241] Matthias Seimetz. *High-order modulation for optical fiber transmission*, volume 143. Springer, 2009.

[242] Keye Sun and Andreas Beling. High-speed photodetectors for microwave photonics. *Applied Sciences*, 9(4):623, 2019.

[243] Vincent J Urick, Frank Bucholtz, Jason D McKinney, Preetpaul S Devgan, Anthony L Campillo, James L Dexter, and Keith J Williams. Long-haul analog photonics. *Journal of Lightwave Technology*, 29(8):1182–1205, 2011.

[244] Tarek Labidi. *Amplification sensible à la phase de signaux analogiques sur porteuse optique*. PhD thesis, 2016.

[245] Jian Li, Yi-Chen Zhang, Song Yu, and Wanyi Gu. Optical sideband processing approach for highly linear phase-modulation/direct-detection microwave photonics link. *IEEE Photonics Journal*, 6(5):1–10, 2014.

[246] Pantelis Velanas, Adonis Bogris, and Dimitris Syvridis. Impact of dispersion fluctuations on the noise properties of fiber optic parametric amplifiers. *Journal of lightwave technology*, 24(5):2171, 2006.

[247] He Wen, Hongjun Zheng, Qi Mo, Amado Manuel Velázquez-Benítez, Cen Xia, Bin Huang, Huiyuan Liu, Huang Yu, Pierre Sillard, Jose Enrique Antonio Lopez, et al. Few-mode fibre-optic microwave photonic links. *Light: Science & Applications*, 6(8):e17021–e17021, 2017.

[248] Ron R Nissim, Evgeny Myslivets, and Stojan Radic. Performance limits of inhomogeneous fiber optic parametric amplifiers operated in saturated regime. *Journal of Lightwave Technology*, 32(21):3552–3559, 2014.

[249] M Bagheri, H Pakarzadeh, and A Keshavarz. Gain-saturated one-pump fiber optical parametric amplifiers in presence of longitudinal dispersion fluctuations. *Applied optics*, 55(13):3368–3372, 2016.

[250] Jitao Gao, Yan Meng, Songnian Fu, Magnus Karlsson, Peter A Andrekson, Ming Tang, and Deming Liu. Theoretical investigation of longitudinal dispersion fluctuations on all-fiber phase-sensitive parametric optical switch. *Journal of Lightwave Technology*, 35(9):1646–1653, 2017.

[251] Arnaud Mussot, Matteo Conforti, Stefano Trillo, Francois Copie, and Alexandre Kudlinski. Modulation instability in dispersion oscillating fibers. *Advances in Optics and Photonics*, 10(1):1–42, 2018.

[252] CS West and TAB Kennedy. Optical multiwave mixing: Dark solitary wave trains and quasiperiodic dynamics. *Physical Review A*, 47(2):1252, 1993.

[253] Wolfram Research, Inc. Mathematica, Version 11.3. Champaign, IL, 2018.

université
PARIS-SACLAY

ÉCOLE DOCTORALE
Ondes et matière
(EDOM)

Titre : Etude Théorique des Amplificateurs Sensibles à la Phase des Fibres pour les Applications

Mots clés : fibre optique, amplification paramétrique, amplificateur sensible à la phase, photonique hyperfréquence

Résumé : Les amplificateurs paramétriques à fibre optique (FOPA) sont prometteurs pour les systèmes de communication de demain. En particulier, les amplificateurs sensibles à la phase des fibres offrent des fonctionnalités intéressantes comme un faible bruit et un gain élevé, ce qui en fait des candidats potentiels pour des applications dans les liaisons photoniques micro-ondes. Cette thèse propose une étude théorique de tels amplificateurs sensibles à la phase destinés à certaines applications.

La première partie de la thèse est consacrée au développement d'un modèle analytique pour la propagation de sept ondes continues à travers un FOPA. Le système est résolu lorsque les effets non linéaires de la fibre ne sont pas trop forts. Le modèle développé révèle le rôle important des ondes d'ordre supérieur dans la détermination des performances d'amplification du FOPA. Des stratégies sont formulées pour améliorer l'amplification. La possibilité d'une conversion de fréquence sensible à la phase avec seulement deux ondes de pompe est également prédite.

Dans la deuxième partie de cette thèse, la possibilité d'introduire un amplificateur sensible à la phase dans une liaison photonique hyperfréquence pour la distribution de signaux analogiques est étudiée. Un modèle numérique est utilisé pour simuler comment les non-linéarités RF dans une liaison photonique hyperfréquence sont amplifiées par le FOPA. Les performances de la liaison lorsque le FOPA atteint la saturation du gain sont également étudiées. L'étude révèle la possibilité d'une atténuation de la non-linéarité RF en utilisant la non-linéarité de la fibre. La mise en œuvre de telles techniques pourrait conduire à la réalisation de liaisons photoniques hyperfréquences à longue portée et hautement linéaires pour les applications de déport d'antenne.

Title :

Keywords : fiber optics, parametric amplification, phase sensitive amplifier, microwave photonics

Abstract : Fiber optic parametric amplifiers (FOPA) are promising for tomorrow's communication systems. In particular, fiber phase sensitive amplifiers offer attractive functionalities like low noise and high gain which makes it a potential candidate for applications in microwave photonic links. This thesis provides a theoretical investigation of such fiber phase sensitive amplifiers aimed towards applications.

The first part of the thesis is dedicated towards development of an analytical model for propagation of seven CW waves through a FOPA. The system was solved exactly when nonlinear effects of the fiber are not strong. The developed model unravelled the important role of the higher order waves in determining the amplification performance of the FOPA. Strategies were formulated to enhance the amplification and the possibility of a phase sensitive frequency conversion with just two pump waves was also predicted.

In the second part of this thesis, the possibility of introducing a fiber phase sensitive amplifier in a microwave photonic link for analog signal distribution was investigated. A numerical model was utilized to simulate how the RF nonlinearities in a microwave photonic link are amplified by the FOPA. The performance of the link when the FOPA attains a gain saturation was also studied. The study revealed the possibility of RF nonlinearity mitigation using the fiber nonlinearity. Implementation of such techniques could lead to realization of long-range and highly linear microwave photonic links for antenna remoting applications.

Université Paris-Saclay
Espace Technologique / Immeuble Discovery
Route de l'Orme aux Merisiers RD 128 / 91190 Saint-Aubin, France